DNA Nanostructures for Nanopore-based Digital Assays

Liqun He

A thesis submitted in partial fulfillment of the requirements for the

Doctorate in Philosophy in Physics

Ottawa-Carleton Institute for Physics

Department of Physics

Faculty of Science

University of Ottawa

Table of Contents

Abstract

Solid-state nanopores are a versatile class single-molecule sensors to electrically characterize a range of biological molecules. Nanopores operate on the simple premise that when a voltage is applied across a pore immersed in a salt solution, the passage of a biomolecule results in a transient blockage in the ionic current that provide information about the translocating molecule. This thesis presents studies employing various DNA nanostructures with solid-state nanopore electrical readout for the development of high sensitivity digital single-molecule assays to detect low-abundance biomarkers. Toward this ultimate goal, work presented in this thesis use nanopores to probe DNA nanostructures, their assembly, mechanical properties, and monitor their dynamics with time and temperature. DNA nanostructures are self-assembled via specific base pairing of DNA, their programmability make them particularly useful for applications including drug delivery, molecular computation and biosensing. Here, I first show results of translocation profiles and discuss folding characteristics, mobility, and molecular configuration during passage for different DNA nanostructures such as the short star-shaped DNA nanostructures and large helix-bundle DNA origami structures under various experimental conditions in an effort to understand the passage characteristics through nanopores of these structures before using them in biological assays. I conclude by presenting a magnetic bead-based immunoassay scheme using a digital solid-state nanopore readout. Nanopore has the ability to count molecules one at a time, this allows accurate and precise determination of the concentration of a biomarker in solution. Coupled with the use of specific choice of DNA nanostructures, as proxy labels for proteins of interest, I establish that nanopores sensors can reliably quantify the concentration of a protein biomarker from complex biofluids and overcome the traditional challenges associated with nanopore-based protein sensing, such as specificity, sensitivity, and consistency. I demonstrate the quantification of thyroid stimulating hormone (TSH) with a high degree of precision down to the femtomolar range by using a nanoparticle-based signal amplification strategy. The proposed assay scheme is generalizable to a framework for the detection and quantification of a wide range of target proteins, and given that its performance can further be improved with the use of parallelization, preconcentration, or miniaturization, it opens up exciting opportunities for the development of ultra-sensitive digital assay in a format that is compatible for point-of-care.

Résumé

Les nanopores à l'état solide constituent une classe polyvalente de capteurs à molécule unique permettant de caractériser électriquement une série de molécules biologiques. Les nanopores fonctionnent sur le principe simple que lorsqu'une tension est appliquée à travers un pore immergé dans une solution saline, le passage d'une biomolécule entraîne un blocage transitoire du courant ionique qui fournit des informations sur la molécule qui transite. Cette thèse présente des études employant diverses nanostructures d'ADN avec une lecture électrique des nanopores à l'état solide pour le développement de tests numériques à molécule unique de haute sensibilité pour détecter des biomarqueurs peu abondants. Pour atteindre ce but ultime, les travaux présentés dans cette thèse utilisent des nanopores pour sonder les nanostructures d'ADN, leur assemblage, leurs propriétés mécaniques, et suivre leur dynamique en fonction du temps et de la température. Les nanostructures d'ADN sont auto-assemblées via un appariement spécifique des bases de l'ADN, leur programmabilité les rend particulièrement utiles pour des applications telles que l'administration de médicaments, le calcul moléculaire et la biodétection. Ici, je montre d'abord les résultats des profils de translocation et je discute des caractéristiques de pliage, de la mobilité et de la configuration moléculaire pendant le passage pour différentes nanostructures d'ADN telles que les courtes nanostructures d'ADN en forme d'étoile et les grandes structures d'origami d'ADN en forme d'hélice dans diverses conditions expérimentales dans le but de comprendre les caractéristiques de passage à travers les nanopores de ces structures avant de les utiliser dans des tests biologiques. Je termine en présentant un schéma d'immunodosage à base de billes magnétiques utilisant une lecture numérique avec des nanopores. Les nanopores ont la capacité de compter les molécules une par une, ce qui permet de déterminer de manière exacte et précise la

concentration d'un biomarqueur en solution. Couplé à l'utilisation d'un choix spécifique de nanostructures d'ADN, comme marqueurs de substitution pour les protéines d'intérêt, j'établis que les capteurs à nanopores peuvent quantifier de manière fiable la concentration d'un biomarqueur protéique dans des biofluides complexes et surmonter les défis traditionnels associés à la détection des protéines par nanopores, tels que la spécificité, la sensibilité et la fiabilité. Je démontre la quantification de l'hormone thyréostimulante (TSH) avec un haut degré de precision jusque dans les femtomolaire en utilisant une stratégie d'amplification du signal basée sur les nanoparticules. L’approche expérimentale propose peut être généralisé pour la détection et la quantification d'une large gamme de protéines cibles et, étant donné que ses performances peuvent être améliorées par la parallélisation, la préconcentration ou la miniaturisation, cela ouvre des perspectives intéressantes pour le développement d'analyses numériques ultra-sensibles avec des nanopores dans un format portatif, pouvant être utilisé sur les lieux de soins.

Acknowledgement

First and foremost, I am deeply indebted to my supervisor, Dr. Vincent Tabard-Cossa for the opportunity to pursue my degree here at the University of Ottawa. Thank you, Vincent, for dedicated supervision, patience, and encouragement throughout my time as a PhD student. I have been incredibly lucky to have you as my supervisor, your immense knowledge and insight have encouraged me through all stages of my study, and it was a great delight to have been your student.

My gratitude extends to all members of the Tabard-Cossa lab, this thesis was a collaborative work throughout. It has been a privilege to work with all of you, collaborating with you has kept me motivated and made research a lot more enjoyable. I would like to make special mention of a few of my colleagues: Dr. Daniel Tessier, it was a pleasure to work with you in the lab and to enjoy our fresh air break, your input and mentorship in and outside of the lab was immeasurable. Dr. Kyle Briggs, your expertise in just about everything made a huge difference in improving the quality of my research. Philipp Karau, who showed me the ropes to the whole star thing, the skills I learnt from your during the first week of my degree has served me well. Martin Charron, who did not mind showing me how to make gels in the middle of the night, what you can do with data analysis continuously impressed me. Dmytro Lomovtsev, the engineering wizard who joined the lab on the same day and beat me to graduation, your brilliant engineering skills really made my day-to-day life a lot easier towards the second half of my degree, our friendship helped me through the ups and downs during my time here.

Finally, I would like to express my deepest gratitude to my wife, Sishi Xu, for her patience and unconditional support over the last four years. My parents, Houguang He, and Fengling Yin, and my grandparents who I spent a good portion of my childhood with, I could not be able to finish this work without your unconditional support. Thank you for being here for me and for your appreciated sacrifices. Thank you to our newborn baby, William, for being a good kid with your mother when I was busy pipetting.

Statement of Originality

The material herein presented was conducted during my work as a Ph.D. student under the supervision of Dr. Vincent Tabard-Cossa in the Department of Physics at the University of Ottawa, the work contains adaptations of articles published or submitted to peer-reviewed journals at the time of submission. I contributed the majority of the work presented in this thesis, including experiment design and execution, data analysis, and the writing of this thesis.

Chapter 1 serves as an introductory overview and a literature review of nanopore technology, DNA origami, and nanopore assay for protein detection. Nanopore was the primary tool for all the research results shown in this thesis, nanopore label design using DNA nanotechnology was the focus of the first half of my doctoral research, which led to the articles covered in Chapter 2 and 3. Chapter 4 consists of a practical implementation of those label design projects as well as an adaptation of an immunoassay scheme for the nanopore platform.

Chapters 2 contains work from a peer-reviewed article published in *Nanoscale*, it was a collaboration between me and Phillip Karau, a graduate student in our lab. The experimental design was done by Phillip Karau and Vincent Tabard-Cossa. My nanopore journey started by shadowing Phillip, who collected the initial datasets and first saw multiplexing using star-shaped DNA nanostructures upon his M.Sc. graduation. I then performed the rest of the experiments and collected all the data for salt asymmetry experiments and the analysis.

Chapter 3 is a version of a manuscript submitted to *Nanoscale*; it represents my second label design which turned into a comprehensive study of transport properties of DNA nanostructures.

Dr. Vincent Tabard-Cossa and I designed the nanostructures and experiments, I performed all the experiments, Martin Charron contributed to data analysis and interpretation of the folding section.

Chapter 4 contains research from a peer-reviewed article published in *Nature Communications*, the project was the focus of the second half of my graduate studies, a collaboration with Dr. Daniel Tessier, a postdoctoral fellow in the research group at the time. The assay design was done by Daniel and Vincent Tabard-Cossa, Daniel performed the majority of the 1 to 1 assay. I performed all the nanopore experiments, data analysis, and adapted the amplification assay using gold nanoparticles.

Finally, Chapter 5 contains a summary and outlook for the work presented in Chapters 2-4.

A list of all articles published, submitted or in preparation over the course of my doctoral studies, either as part of my main doctoral projects or collaborative work is available in my List of Publications below.

Statement of Contributions

Publications

1. **He, L.**,* Charron, M.,* Karau, P., Briggs, K. & Tabard-Cossa, V. Dynamics of passage of DNA nanostructures through solid-state nanopores gives insights on complexities of macromolecular assembly. *To be submitted to: Nanoscale* (2022).
2. Charron, M.,* Philipp, L.,* **He, L.** & Tabard-Cossa, V. Elucidating the dynamics of polymer transport through nanopores using asymmetric salt concentrations. *Nano Res.* **15**, 9943-9953 (2022).
3. **He, L.**, Tessier, D. R., Briggs, K., Tsangaris, M., Charron, M., McConnell, E., Lomovtsev, D. & Tabard-Cossa, V. Digital immunoassay protocol for solid-state nanopore sensing. *Protoc. Exch.* (2021)
4. **He, L.**,* Tessier, D. R.,* Briggs, K., Tsangaris, M., Charron, M., McConnell, E., Lomovtsev, D. & Tabard-Cossa, V. Digital immunoassay for biomarker concentration quantification using solid-state nanopore sensing. *Nat. Commun.* **12**, 5348 (2021).
5. Briggs, K., Bouhamidi, M. Y., **He, L.** & Tabard-Cossa, V. Efficient simulation of arbitrary multicomponent first-order binding kinetics for improved assay deign and molecular assembly. *Meas. Sci. Au* **2**, 139-146 (2021).
6. **He, L.**,* Karau, P.* & Tabard-Cossa, V. Fast capture and multiplexed detection of short multi-arm DNA stars in solid-state nanopores. *Nanoscale* **11**, 16342–16350 (2019).

Conference Presentations

7. **He, L.**, Charron, M., Karau, P., Briggs, K., Adams, J., de Haan, H. & Tabard-Cossa, V. Poster: Characterization of DNA nanostructures using solid-state nanopores. *Biophysical Society of Canada Annual Meeting*, Ottawa, ON, Canada (2022).
8. **He, L.**, Tabard-Cossa, V. Talk: Characterization of DNA Nanostructures for the Development of Digital Immunoassays using Solid-state Nanopore Sensors. *DNA Nanotechnology for Medicine & Biology Webinar series*, University of Edinburgh, Edinburgh, UK, virtual (2021).
9. **He, L.**, Tabard-Cossa, V. Talk: Digital Immunoassay for Quantification of Specific Target Proteins using Solid-state Nanopores. *International Conference on Nanoscience and Technology*, Vancouver, BC, Canada, virtual (2021).
10. **He, L.**, Tabard-Cossa, V. Talk: Characterization of DNA Nanostructures using Solid-state Nanopores. *Chemical Institute of Canada IUPAC|CCCE conference*, virtual (2021).
11. **He, L.**, Charron, M, Tessier, D. R., Briggs, K, Tabard-Cossa, V. Poster: Capture and Translocation Characteristics of DNA Nanostructures through Solid-state Nanopores. *Biophysical Society Annual Meeting*, San Diego, CA, USA (2020).

*These authors contributed equally to this work.

List of Figures

List of Tables

List of Abbreviations

- Ab: Antibody
- AFM: Atomic Force Microscopy
- Ag/AgCl: Silver/Silver Chloride
- bp: basepair
- CBD: Controlled Dielectric Breakdown
- DR: Dynamic Range
- dsDNA: double-stranded DNA
- ELISA: Enzyme-linked Immunosorbent Assay
- fM: femtomolar
- I-V curve: Current *versus* Voltage curve
- KCl: Potassium Chloride
- kbp: kilobasepair
- LiCl: Lithium Chloride
- LoB: Limit of Blank
- LoD: Limit of Detection
- LoQ: Limit of Quantification
- nm: nanometre (10^{-9} m)
- nM: nanomolar (10^{-9} moles/L)
- nt: nucleotide
- oligo: oligonucleotide

- PDMS: Polydimethylsiloxane
- pM: picomolar
- PMB: Paramagnetic Beads
- PSD: Power Spectral Density
- RMS: Root-Mean-Square
- ssDNA: single-stranded DNA
- SNR: Signal-to-Noise Ratio
- SiN: Silicon Nitride
- SD: Standard Deviation
- SEM: Scanning Electron Microscope
- TEM: Transmission Electron Microscope

Chapter 1 – Introduction

1.1 Nanopore Sensing

1.1.1 Basics of Nanopores

A nanopore is a nanoscale aperture in a thin membrane connecting two reservoirs of electrolyte solutions (e.g. 1 M KCl or 3.6 M LiCl). A nanopore typically ranges between one and tens of nanometres in diameter, about the size of a single molecule of DNA a protein or a bio-molecular complex. When a voltage is applied across the membrane, as illustrated in **Figure 1.1**, an ionic current is established and molecules in solution are captured and driven to translocate through the nanopore. During their passage through the nanopore, information about their size, shape, charge, and conformation can be obtained from the changes in ionic current. This makes nanopores ideal for a wide range of applications, such as molecular characterization, polymer sequencing, and bio-sensing. The details of the sensing process will be discussed further in the sections below.

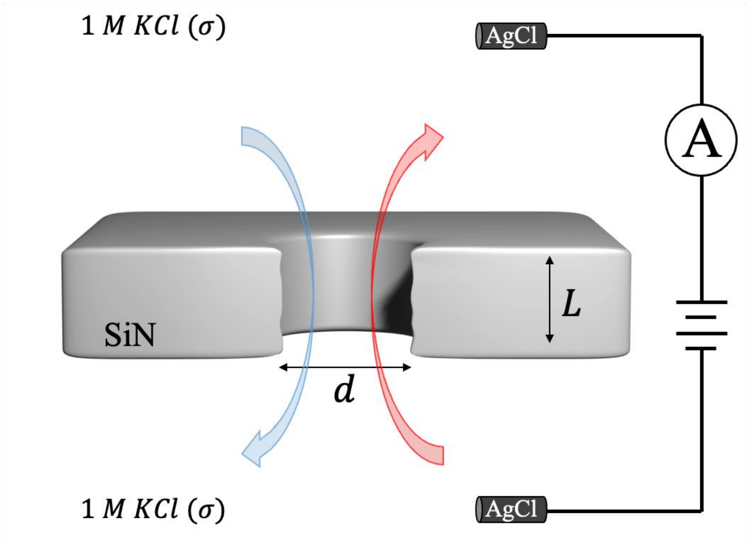

Figure 1.1. An illustration of a nanopore.

1.1.2 Types of Nanopores

There are two classes of nanopores: organic nanopores and synthetic nanopores that share the same basic sensing principles. Organic pores, are often biological pores consisting of transmembrane protein channels embedded in a lipid bilayer, as shown in **Figure 1.2**a. While much engineering effort has been put into the development of nanopore DNA sequencing to package it into a cell phone-sized instrument, it was not until the introduction of an enzyme (helicase or polymerase) to ratchet the DNA and slow down its translocation that long-read sequencing, the ability to reliably read long sequences of DNA, became possible.[1] These protein-based nanopores are finding increasingly broad applications. Single-molecule sensors are a great representative of 4th-generation sequencing technology, and they have demonstrated excellent miniaturization, scalability, parallelization, and cost-effectiveness capabilities.[2,3] While biological pores have been the method of choice for many areas of research thanks to their angstrom-level precision, excellent noise performance, and pore-to-pore consistency, they have drawbacks as well. They suffer from their inherently high sensitivity to experimental conditions and the inability to control pore size (requiring different protein pores to be found and mutated each desired size), limiting the types and sizes of molecules they are able to sense.

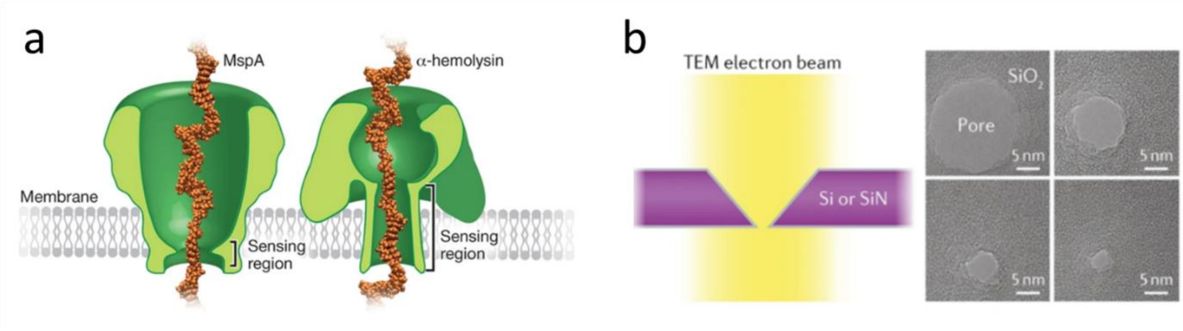

Figure 1.2. Illustration of biological and solid-state nanopores.

(a) MspA and α-hemolysin biological nanopore embedded in a lipid bilayer, with MspA having a shorter sensing region. α-hemolysin in particular was among the first proteins to be experimented with for nanopore DNA sensing. [Image taken from *Three Decades of Nanopore Sequencing* (Nat. Biotechnol.) with permission][4] **(b)** Illustration and TEM images of a silicon nitride (SiN) solid-state nanopore. [Image taken from *Solid-state Nanopore Sensors* (Nat. Rev. Mater.) with permission][5] These nanopores are typically cylindrical with a diameter larger than 2 nm. The length of a nanopore is defined by the thickness of the SiN membrane and they can range from tens to hundreds of nanometers.

The development of synthetic nanopores, primarily solid-state nanopores has address some of the issues associated with biological pore sensing, in particular limitations in and sensitivity to sensing conditions.[6] Solid-state nanopores are produced in more mechanically stable membranes typically made from Si-based materials. They are available in various geometries such as conical nanopipettes,[7–10] planar membrane-cased silicon nitride (SiN) nanopores,[6,11–13] and even ultra-thin 2D material pores.[14,15] The most popular among these are nanopipettes and SiN nanopores. Nanopipettes are fabricated by heating and pulling using glass capillary pullers. **Figure 1.3**a shows SEM images of a nano-pipette. A glass or quartz tubes are heated with a laser to above its softening temperature and subsequently pulled from both ends till separation to produce two nanoscale apertures, often larger than 10 nm in diameter.[10,16–21] While the nanopipettes suffer from limited spatial resolution due to their unique conical shape and there is little control over pore size during fabrication, the material of choice, quartz, provides very low dielectric and capacitance noise.

While nanopores in organic and inorganic membranes have both shown great potential, another interesting possibility is a hybrid system. Researchers have been able to dock a DNA origami structure onto a solid-state nanopore,[22–24] which in turn acts as a nanopore, as shown in **Figure 1.3**b. These DNA origami pores take advantage of the excellent programmability of DNA, which allows for highly customized geometry and chemical modifications.

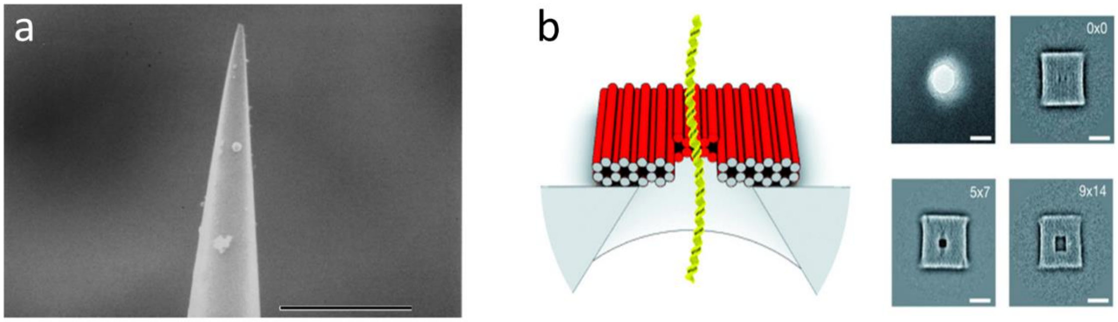

Figure 1.3. Nano-pipette and DNA origami pores.

(a) An SEM image showing a nano-pipette, scale bar = 2 μm. [Image take from *Single DNA Molecule Detection Using Nanopipettes and Nanoparticles* (Nano Lett.) with permission][10] **(b)** Illustration and TEM images of a DNA origami nanopore. Left panel shows DNA translocating through a DNA origami pore which is docked onto a solid-state nanopore. [Image taken from *DNA Origami Gatekeepers for Solid-State Nanopores* (Angew. Chem. Int. Ed.) with permission][23]

Of these alternatives, a particularly promising class of nanopores are SiN solid-state nanopores, as shown in **Figure 1.2**b. A silicon chip containing a free-standing SiN membrane is mounted in a fluidic cell submersed in two reservoirs of electrolyte solution (typically 1M KCl). Two Ag/AgCl electrodes are inserted in both reservoirs, allowing the application of a voltage potential across the membrane. Compared to biological nanopores, nanopores of this type offer more flexible pore sizes and lengths and by virtue of their robust inorganic membrane, they can sustain higher voltages and operate in a much wider range of experimental conditions including pH, mechanical pressure, and temperature. These nanopores are traditionally fabricated by TEM drilling or ion beam sculpting,[6,11,25] which typically involve complex material preparation, expensive equipment, and highly trained personnel. More recently, however, a simpler, and much more cost-effective technique called controlled breakdown (CBD), introduced by the Tabard-Cossa Lab at the University of Ottawa is growing in popularity (see section below).[12,13,26–28]

1.1.3 Nanopore Ionic Current Sensing

While nanopores can be characterized by TEM imaging, the dimensions of a pore can be calculated through electrical measurements and a simple conductance model assuming a cylindrical shape (**Figure 1.4**).

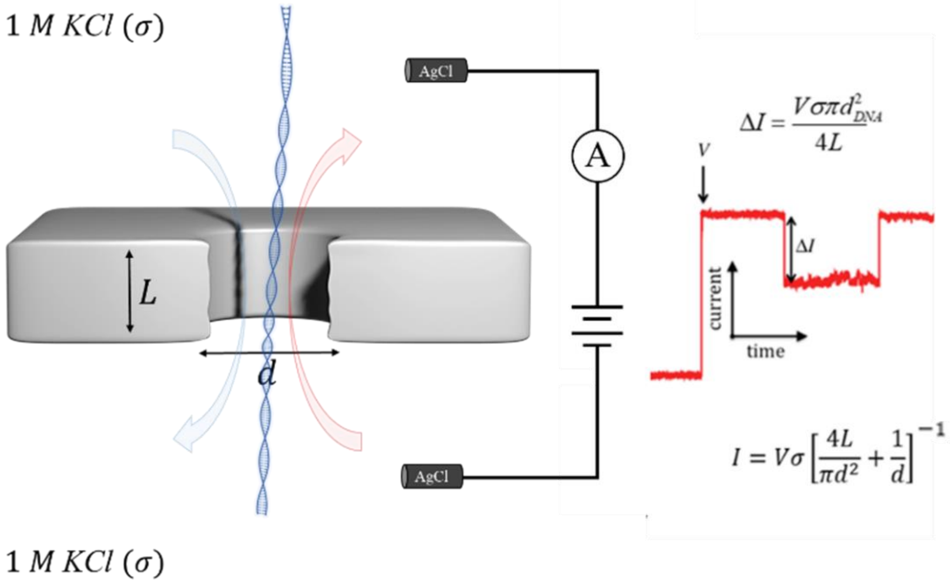

Figure 1.4. Schematic illustration of nanopore sensing.

When a bias voltage is applied, electrolyte ions travel through the nanopore. A DNA polymer translocating through a nanopore with a diameter d and length L, immersed in 1 M KCl, with a conductivity σ and applied bias of V.

By applying an electric potential across the membrane, the charged ions travel through the nanopore, producing an ionic current. The conductance is given by:[29]

$$G = \frac{I}{V} = \left[\left[\sigma\frac{\pi d^2}{4\,L} + \frac{\mu_+\gamma\pi d}{L} + \frac{\pi\gamma^2\lambda_D d}{\eta L}\right]^{-1} + \frac{1}{\sigma\,d}\right]^{-1} \qquad 1.1$$

Where L is the length of the nanopore, V is the applied potential, σ is the conductivity of the bulk solution, η is the viscosity of the solution, $\mu_+$is the electrophoretic mobility, γ is the surface charge density of the nanopore walls, λ_D is the Debye length, and d is the diameter of the nanopore. The Debye length is the characteristic distance of a potential decay in electrolyte solutions, it defines the thickness of the electric double layer and is also known as the shielding distance, over which the charged surface is effectively shielded by the counter-ions. The first term comes from the bulk conductance of the pore, as the conductance of a cylinder with length L and diameter d can be written as $G_{bulk} = \sigma\frac{\pi d^2}{4L}$, where the solution has a uniform conductivity σ. The second and third term arise from the surface charge of the nanopore $G_{surf} = \frac{\mu_+ \gamma \pi d}{L}$, and the electroosmotic flow (EOF) $G_{EOF} = \frac{\pi \gamma^2 \lambda_D d}{\eta L}$.[30] An equivalent circuit of the nanopore system (**Figure 1.5**) helps illustrate the contribution from each term. Unlike the first three terms, which originate from the cylindrical shape inside the nanopore, the fourth term comes from the access regions, calculated as $G_{access} = 2\sigma d$.[31]

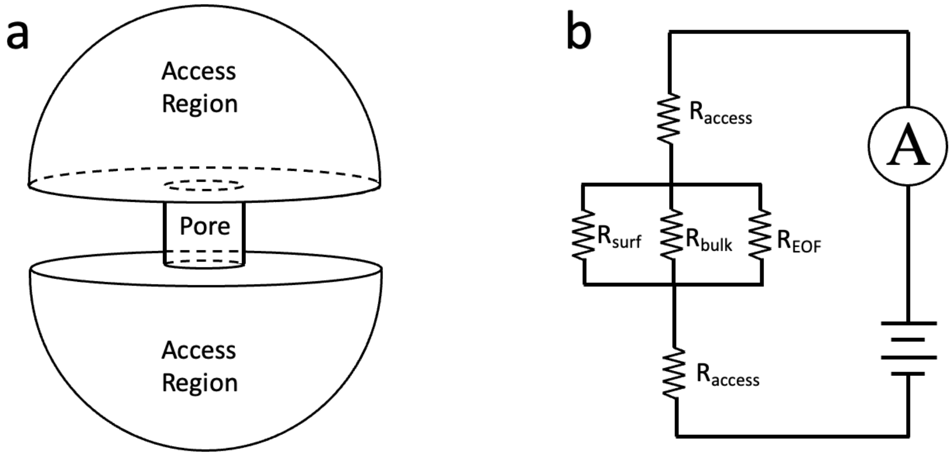

Figure 1.5. The equivalent circuit of the nanopore system.

(a) The conductance contributions of the pore and two access regions of the nanopore. **(b)** The equivalent circuit of the nanopore system.

Since typical nanopore experiments are performed in high-salt conditions, which effectively screen surface charge (Debye length ≈ 0.1 nm), this open pore current can therefore be reduced to voltage divided by resistance:

$$G = \sigma \left[\frac{4L}{\pi d^2} + \frac{1}{d} \right]^{-1} \qquad 1.2$$

The first component $R_{bulk} = 4L/\sigma\pi d^2$ corresponds to the geometry of the nanopore itself, and the second component $R_{access} = 1/2\sigma d$ is the access resistance which comes from the ionic current converging from two hemispheres of bulk solution into the pore.

The size of the nanopore d can be easily estimated from the measured conductance (obtained by measuring the pore current *versus* applied voltage) and known parameters using the following conductance equation.

When a molecule, such as a double-stranded DNA molecule, is passing through a nanopore, a portion of the open pore ionic current is blocked. Assuming small pore sizes of aspect ratio $d/L \leq 1$, the DNA molecule's impact on access resistance is negligible, and the change in conductance ΔG is given by

$$\Delta G = \sigma \frac{\pi d_{DNA}^2}{4L} \qquad 1.3$$

The conductance blockage equation in turn provides an estimate of nanopore length, based on the assumption that surface charges and access resistance can be neglected, as the hydrodynamic diameter of double-stranded DNA has been well characterized to be $d_{DNA} = 2.2$ nm. By running

DNA molecules through the nanopore and measuring its conductance blockage, equation 1.3 allows a good approximation of the nanopore effective length:

$$L_{eff} = \sigma \frac{\pi d_{DNA}^2}{4\,\Delta G} \qquad 1.4$$

This expression provides an improved estimate of the effective nanopore length in high salt conditions compared to the nominal membrane thickness and helps account for slight variation from a cylindrical geometry. This L_{eff} can be used in Equation 1.4 to obtain a more accurate pore size from conductance measurements. This approach has been confirmed to be reasonably accurate as confirmed through TEM imaging.[13,27,32]

The motion of a charged molecule through the electric field outside the nanopore is considered the primary driving force for the capture process.[33,34] The electrophoretic velocity of the molecules v_E in response to the electric field is given by $v_E = \mu_e E$, where E is the magnitude of the electric field, and μ_e is the electrophoretic mobility of the molecule. A molecule's electrophoretic mobility is defined as $\mu_e = q/6\pi\eta r$, where q is the molecule's charge, η is the buffer's viscosity, and r is the radius of the molecule. Electroomsmotic flow is the motion of fluid in response to the applied electric field. Electroosmotic flow takes place since the walls of the capillary carry charges, when an electric field is applied, the ions in the buffer migrate due to the field towards the cathode.

With an applied bias across a nanopore, a molecule undergoes a combination of drift and diffusion, the capture and translocation of a molecule through the nanopore is described by three main steps: 1) drift-diffusion, 2) capture, and 3) translocation, as illustrated in **Figure 1.6**.[35–37]

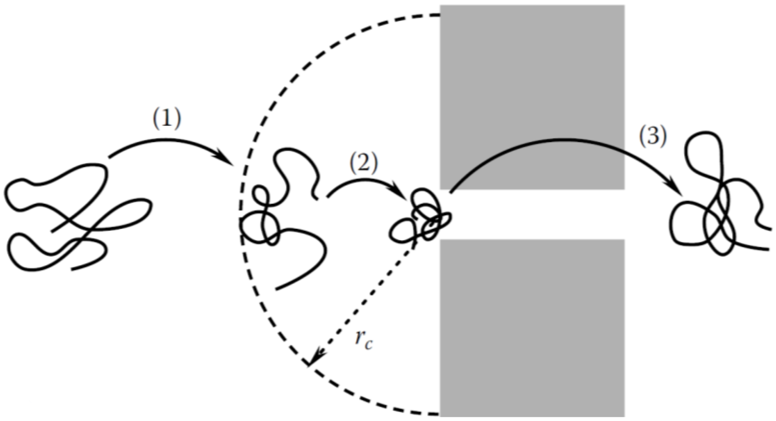

Figure 1.6. **Illustration of the main stages of polymer translocation**. 1) drift and diffusion, 2) capture, and 3) translocation. [Image taken from *Polymer Translocation* (2011) with permission][36]

A molecule diffuses freely until it enters a distance r_c from the nanopore, where r_c is defined as the capture radius of the nanopore. The diffusion arises from collisions with the solvent molecules in the solution. The molecule then undergoes drift and is brought close to the nanopore mouth due to the externally imposed field, namely, the electric field. At the nanopore mouth, the molecule may undergo conformation deformation to enter the nanopore and begin translocation. Generally, when a polymer is captured at the nanopore mouth, it is in a jammed state.[36] The translocation is believed to consist three stages: a) chain-end localization, b) nucleation, and c) threading. The eventual single-file translocation involves overcoming an entropic barrier in localizing one of the chain ends at the nanopore mouth from the jammed coil state. This entropic barrier arises from the requirement that one of the chain end must be at the nanopore mouth, instead of all possible locations, therefore reducing its translational entropy.[36] Upon the completion of localization, another entropic barrier must be overcome for the chain to thread through the nanopore, which comes from the reduction of conformational degrees of freedom. A sufficient number of monomers must cross this nucleation barrier before further translocation takes place. The final threading process is a drift-diffusion process on its own, the chain then exists the nanopore and completes the translocation.[36]

1.1.4 Nanopore Fabrication by Controlled Breakdown (CBD)

While all solid-state nanopore systems share very similar principles, the nanopores used in this study were fabricated on thin dielectric SiN membranes using the controlled dielectric breakdown technique. In addition to greater simplicity and cost-effectiveness compared to traditional TEM drilling or ion beam sculpting, nanopores fabricated by CBD have the unique advantage of being formed *in situ* in sensing electrolyte solution. All the nanopores presented in this thesis were approximately 5 - 15 nm in diameter and 10 - 12 nm in length.

The CBD technique consists of the application of a voltage potential across the SiN membrane in electrolyte solution. A leakage current is produced by the electric field; this leakage current is believed to be due to tunnelling of charges through defects in the SiN membrane. These defects accumulate and eventually cause a breakdown in the membrane, leaving a hole typically 1-2 nm in diameter. This nanopore can subsequently be fine-tuned and enlarged to the desired size by applying alternating voltage potentials using a process called “conditioning”, all *in situ* in sensing conditions. An I-V curve can be constructed by measuring the current at various voltages, and the conductance can then be determined from the slope of the linear fit of the I-V curve, as shown in **Figure 1.8**b.

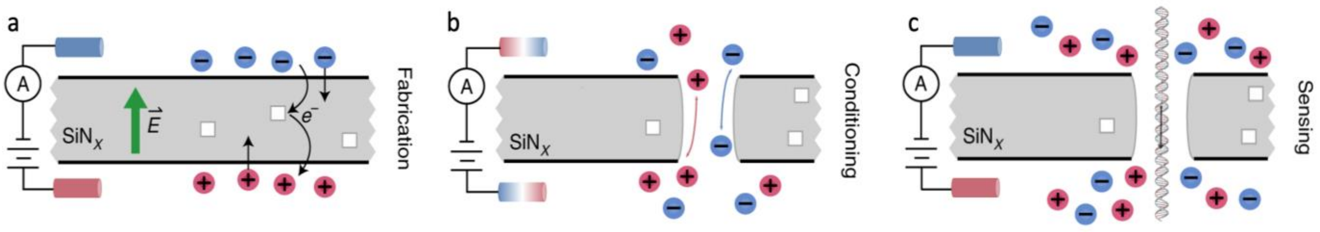

Figure 1.7. Schematic of controlled breakdown (CBD).

(a) A strong electric field is applied across the thin SiN membrane, damaging the membrane, and generating leakage current. This high electric field forms charged traps in the material. The traps accumulate until they form a localized conductive path, which leads to a breakdown event. **(b)** Conditioning of a nanopore. After fabrication, alternating voltages are applied following fabrication, to enlarge the nanopore to the desired size. **(c)** The nanopore can be used for single-molecule sensing, such as the detection of DNA molecules. [Image taken from *Solid-state Nanopore Fabrication by Automated Controlled Breakdown* (Nat. Protoc., 2020) with permission][12]

A typical workflow for nanopore fabrication by CBD is as follows. A silicon chip containing a SiN membrane is sandwiched between two elastomer gaskets and packed into a fluidic flow cell. The assembled flow cell is inserted into the fabrication unit, which contains a Faraday cage to minimize electrical noise. This fabrication unit applies a gradual voltage ramp, typically from $0\ V$ to up to $14\ V$ across the SiN membrane, during which, increasing leakage is observed (shown in **Figure 1.8**). When a breakdown event occurs, a sudden increase in leakage current is detected as a threshold is crossed. This is the indication of the formation of a nanopore, and the voltage is switched off immediately. A typical breakdown voltage is between $8 - 13\ V$ using a 12 nm thick SiN chip in 1 M KCl salt.

The software performs a current-voltage (I-V) curve to calculate the initial pore size immediately after the breakdown, which is generally less than 2-3 nm. The nanopore is then gradually enlarged to the desired size by applying an alternating voltage of ~ 40% of the breakdown voltage in 3.6 M LiCl salt. The software measures the pore size and performs noise checks after each series of voltage pulses to ensure that the nanopores are conditioned to the correct size and performance. In following sections, I will describe the nanopore fabrication instrumentation and workflow in detail, then briefly discuss the noise, capture rate, and signal analysis.

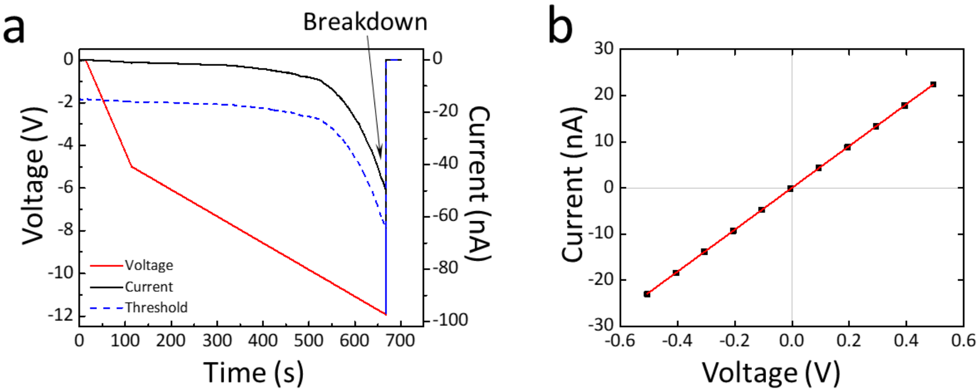

Figure 1.8. Nanopore fabrication using CBD.

(a) The fabrication curves: voltage (red), current (black), and threshold (blue dashed line). As a gradual voltage ramp is applied, increasing leakage is detected, followed by a sudden spike when a nanopore is formed. **(b)** Example current-voltage (I-V) characteristics of the nanopore from -500 mV to + 500 mV. The fitted slope of the I-V curve is the conductance of the nanopore, which can be used to calculate nanopore size from equation 1.2.

1.1.5 Nanopore Instrumentation

The custom nanopore fabrication instrumentation and software setup used in my studies was developed by the team at T.-Cossa Lab at the University of Ottawa.[6,11–13] A silicon chip containing a free-standing 40 μm × 40 μm SiN window with a thickness of approximately 10 nm is supported by 5 mm × 5 mm Si substrate, as shown in **Figure 1.9**. Some chips have additional layers of SiO_2, which has demonstrated better noise performance as discussed in next subsection.

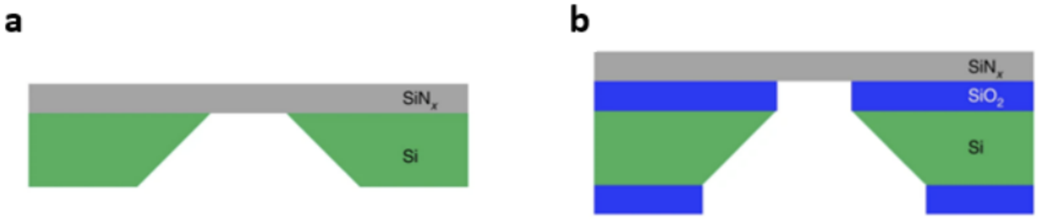

Figure 1.9. Types of silicon chips.

Schematic representation of **(a)** SiN membrane and **(b)** SiN membrane with SiO_2 under-layer. [Image taken from *Solid-state Nanopore Fabrication by Automated Controlled Breakdown* (Nat. Protoc., 2020) with permission][12]

A typical nanopore fabrication setup is shown in **Figure 1.10**. The chip is enclosed in a pair of elastomer gaskets with pre-punctured apertures to allow fluidic contact with the membrane. The gasket/chip sandwich is then clamped together in the flow cell as shown in **Figure 1.10**a), which ensures a fluidic seal between the surface of the chip and the flow channels.

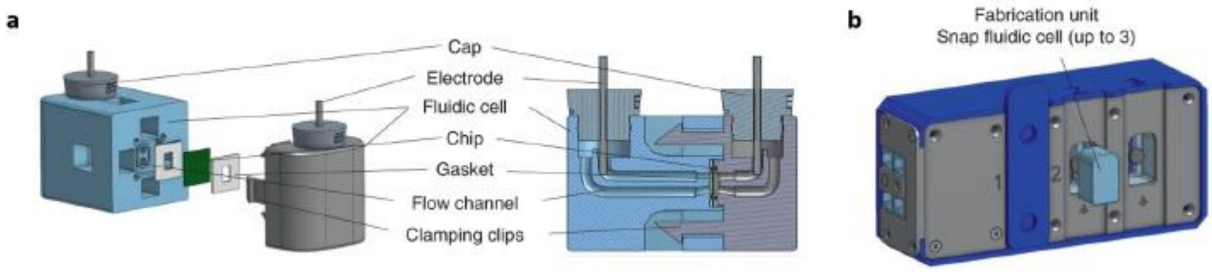

Figure 1.10. Schematic design of the nanopore fluidic flow cell and the fabrication unit.

(a) CAD drawing of the snap flow cell, and the assembly of the silicon chip supporting the SiN membrane, elastomer gaskets, Ag/AgCl electrodes, and caps. **(b)** The assembled fluidic cell inserted into one of the three channels on the Spark-E nanopore fabrication device. [Image taken from *Solid-state Nanopore Fabrication by Automated Controlled Breakdown* (Nat. Protoc., 2020) with permission][12]

Once the chip is mounted in the flow cell, the flow channels are then flushed with isopropl alcohol (IPA), de-ionized water, and fabrication electrolyte (1 M KCl). Ag/AgCl electrodes are inserted into the flow channels containing electrolyte solution, then sealed with rubber or 3D printed caps to prevent evaporation during experiments.

Once the nanopore is made and characterized, samples are mixed with sensing electrolyte solutions, typically in higher salt concentrations such as 1 M KCl or 3.6 M LiCl. For the experiments performed for this thesis, the samples were mixed in 3.6 M LiCl with a final volume of roughly 40 μL (larger than the volume of the fluidic channels of the flow cell) and loaded on the nanopore by flushing through the flow cell with a pipette.

To sense the molecules using the nanopore, the flow cell containing the nanopore is inserted into another Faraday cage and connected to a low-noise high-bandwidth current amplifier, as shown in

Figure 1.11. For the results shown in this thesis, a Chimera VC 100 was used. The Chimera VC100 (Chimera Instruments LLC, RI) has a much higher bandwidth of up to 1 MHz and a sampling rate of 4.167 MHz compared to 100 kHz on the more commonly used Axopatch 200B current amplifier, providing a higher temporal resolution for the shorter molecules used in these experiments.

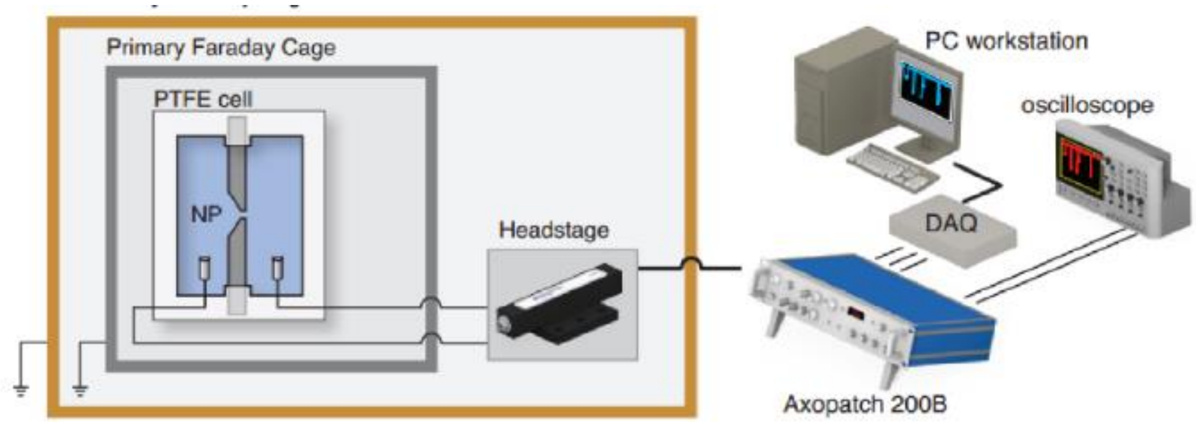

Figure 1.11. Schematic overview of the nanopore sensing apparatus.

The fluidic cell containing the nanopore is enclosed in a Faraday cage and connected to a current amplifier and a data acquisition card (DAQ) allowing computer control. The figure shows the Axopatch 200B. The data shown in this thesis were collected using the Chimera VC100, which allows for a higher bandwidth recording of 1 MHz. [Image taken from *Instrumentation for Low-Noise High-Bnadwidth Nanopore Recording* in *Engineered Nanopores for Bioanalytical Applications: A Volume in Micro and Nano Technologies* (Elsevier Inc., 2013) with permission][38]

1.1.6 Nanopore Electrical Noise

Due to the need for higher-bandwidth measurements to detect fast-translocation molecules, is important to characterize and control the noise profile of solid-state nanopores. For the work shown in this thesis, the experiments were performed at a high bandwidth of 1 MHz, where capacitive noise dominates.

Noise is characterized by its power spectral density (PSD), which reveals the sources of noise and how they scale with frequency. Noise PSD can be expressed in the following polynomial form:

$$S_1(f) = \frac{a_0}{f} + a_1 + a_2 f + a_3 f^2 \qquad 1.5$$

Where f is the frequency and the constants represent different contributions of noise. a_i are the coefficients of the distribution from each term. The a_0/f term describes the flicker noise, also known as the $1/f$ noise. This term dominates at lower frequencies. The second term relates to the thermal and shot noise, which does not scale with frequency but is dependent on the temperature, resistance of the medium, and current flowing through the nanopore. At higher frequencies (>100 kHz), the dielectric and capacitive noise begin to dominate the spectrum. These are described by the third and fourth terms. a_2, and a_3 are related to the capacitance of the chip.

The level of noise in a current can be represented by the root-mean-square (RMS) noise, which is essentially the square root of the integral of the PSD:

$$RMS = \sqrt{\int S_1(f)\, df} \qquad 1.6$$

Therefore, the total RMS noise will depend on the bandwidth of the current recording. **Figure 1.12** shows an example plot of PSD and the RMS noise. The data shown in this thesis were all collected using the Chimera VC100 current amplifier (Chimera Instruments LLC, RI) for better temporal resolution.

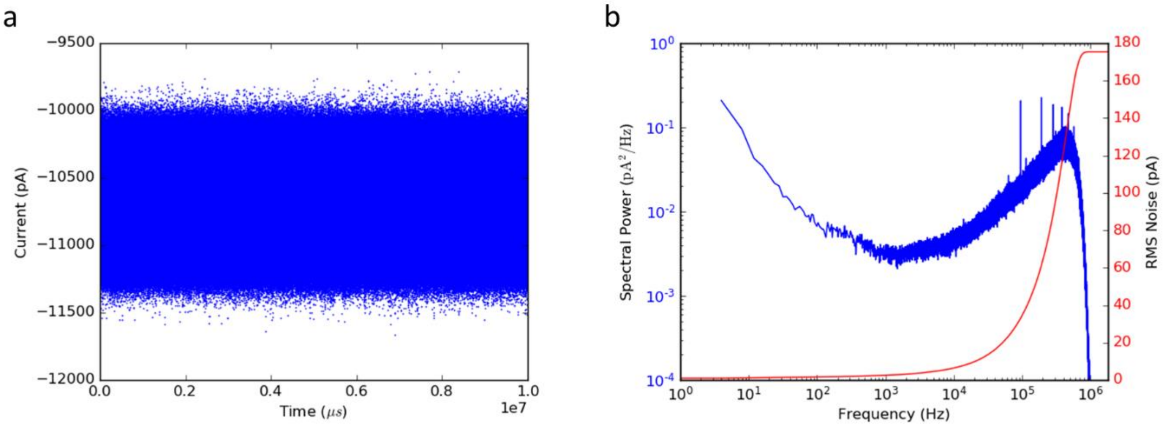

Figure 1.12. Current trace and power spectra for a nanopore.

a) 10 second current trace and b) Power spectral density (PSD) of a PDMS painted nanopore (left axis) and root-mean-square (RMS) noise (right axis) of a nanopore with an applied bias of 200 mV in 3.6 M LiCl. The data was digitally low-pass filtered at 900 kHz.

Capacitance noise dominate at higher frequencies due to its high bandwidth capabilities, as it scales quadratically with frequency:

$$S_{capacitance} \propto (C_{total}\, f)^2 \qquad 1.7$$

Where C_{total} is the total capacitance of the system. Noise in nanopore systems has been well characterized,[25] and for the purpose of the work done in this thesis, capacitance noise is the dominant source. Coating the silicon chip with a silicon elastomer polydimethylsiloxane (PDMS) has been proven to reduce C_{total} to help achieve better overall noise performance. The work shown in this thesis were done using PDMS painted chips. Alternatively, the use of oxide-coated chips, which introduce an underlayer of SiO_2 between the SiN layer and the supporting Si frame, as shown in **Figure 1.9**, is an effective way to reduce capacitance noise.

1.1.7 Nanopore Translocation Signal Analysis

Data analysis of translocation events was performed using the cumulative sum (CUSUM) algorithm, which is widely used for change detection. The custom CUSUM analysis software used in this these was implemented by Dr. Kyle Briggs at the University of Ottawa.[39] Once the individual event has been detected and fitted, various useful information about the event or the molecule can then be extracted. The raw current is plotted in blue, and green curve is the fit. Some of the most important parameters include maximum blockage level, maximum deviation, and dwell time. **Figure 1.13**a shows a nanopore current trace of a DNA event.

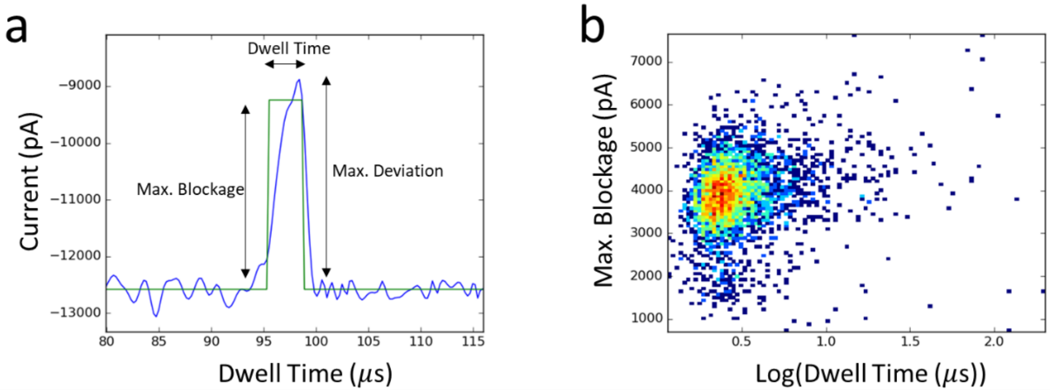

Figure 1.13. Nanopore translocation event and distribution.

(a) Current trace of a translocation event (blue) and its CUSUM fit (green). **(b)** Scatter plot of the extracted maximum blockage level *versus* dwell time.

Maximum blockage level is the difference in current between the local baseline and the deepest fitted level. These are shown in **Figure 1.13**a. Maximum deviation is the largest difference between the local baseline and the actual event. The maximum deviation is almost always larger than the maximum blockage, especially in the case of faster translocation events. Therefore, the difference between maximum deviation and maximum blockage can be calculated, and this residual value serves as an indicator of the goodness CUSUM fit. The dwell time is the total duration of all fitted levels, which corresponds to the amount of time a molecule spends inside (translocating) or interacting with a pore. Once the analysis and fitting are completed, a scatter plot can be constructed. **Figure 1.13**b shows a heat map of the extracted maximum blockage *versus* the logarithmic of dwell time. Each dot on the plot represents a single-molecule translocation event, with its own specific blockage level and translocation time. This plot helps visualize the distribution of the translocation events. Together, these values reveal information about the molecule's size, conformation, and charge.

1.1.8 Nanopore Capture Rate

The capture rate is defined as the number of translocation events over a fixed period of time. It is the rate at which molecules arrive at and are captured by the nanopore. This value is related to the concentration of the sample molecules, which can be used as a valuable metric for bio-sensing. When applying a bias across a nanopore, it is believed that the capture process relies on the balance between electrophoresis and thermal forces, electrostatic and electro-osmotic forces are negligible due to the shielding of surface charge in high salt, where nanopores typically operate in.[35,37,40–42] By considering the entropic barrier at the nanopore mouth and the drift of molecule under an electric field, two capture regimes can be described: barrier-limited regime and diffusion limited regime or drift regime. In barrier-limited regime, a molecule must overcome an entropic barrier to begin translocation process,[37] the capture rate increases non-linearly with voltage and molecule length.[35] In the diffusion-limited regime, the entropic barriers can be negligible due to the applied voltage (electric field).[35,37,42] Without the rate limiting energy barriers, the capture rate increases linearly with voltage and it is independent of molecule length.[35]

Nanopores have the advantage of sensitivity by virtue of single-molecule detection, which, when operating in a diffusion-limited capture regime, does not depend on the absolute mass of the sample but on its concentration. Studies have shown that the capture rate is directly proportional to the sample concentration, assuming dilute solutions where inter-molecular interactions can be neglected.[43,44]

The capture rate R_C can be experimentally determined by calculating the inter-event time τ. Since the nanopore capture is a Poisson process, the survival probability of an inter-event time can thus be written as

$$P(\tau) \propto R_C \, e^{-R_c \tau} \qquad 1.8$$

Survival probability *versus* inter-event time can be plotted on a semi-log plot, as shown in **Figure 1.14**. The capture rate of an experiment can be determined by simply fitting the distribution of inter-event times. The linear curve on this plot agrees with the exponential relationship between survival probability and inter-event time as expressed in Equation 1.8, and the capture rate R_C is simply $R_C \propto \tau^{-1}$.[37,44] However, this value depends heavily on experimental conditions, such as the applied voltage, the geometry of the nanopore, the charge of the molecule, the electrolyte solution, and the mobility of the target molecule. Because capture is a stochastic process, typically hundreds of translocation events are needed to draw a statistically meaningful conclusion and internal calibration is often required for precise quantification.[44]

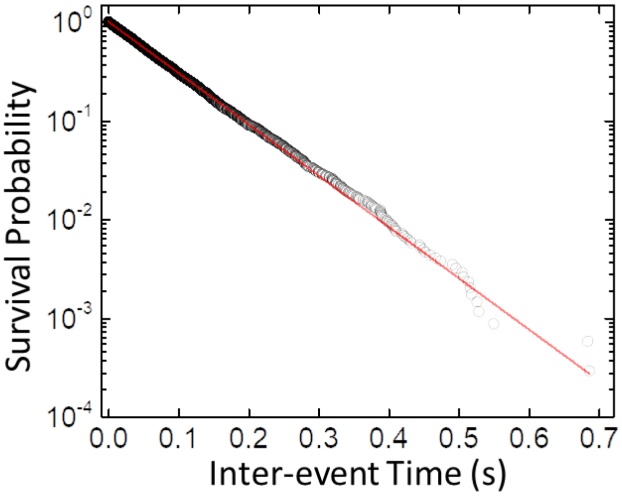

Figure 1.14. An example of capture rate determination.

A scatter plot of survival probability *versus* inter-event time. The capture rate was determined to be $R_C = 11.8\ s^{-1}$.

1.2 DNA Nanotechnology

1.2.1 Background of DNA Nanotechnology

Deoxyribonucleic acid (DNA) is a molecule which carries genetic information in all living organisms and many viruses. The principle of Watson-Crick complementary base pairing has laid the groundwork for the field of DNA origami, in which DNA strands can be used as building blocks to form different shapes. This idea was first proposed by Seeman in 1982,[45] which set the cornerstone of this emerging field of research. In recent years, the field has advanced from building smiley faces to practical applications using DNA nanotechnology. Numerous novel techniques have been developed as shown in **Figure 1.15**, such as a DNA nanoswitch as a diagnostics device,[46–49] DNA origami-based lithography for nano-fabrication,[50] and a DNA origami box with a controllable lid for drug delivery.[51]

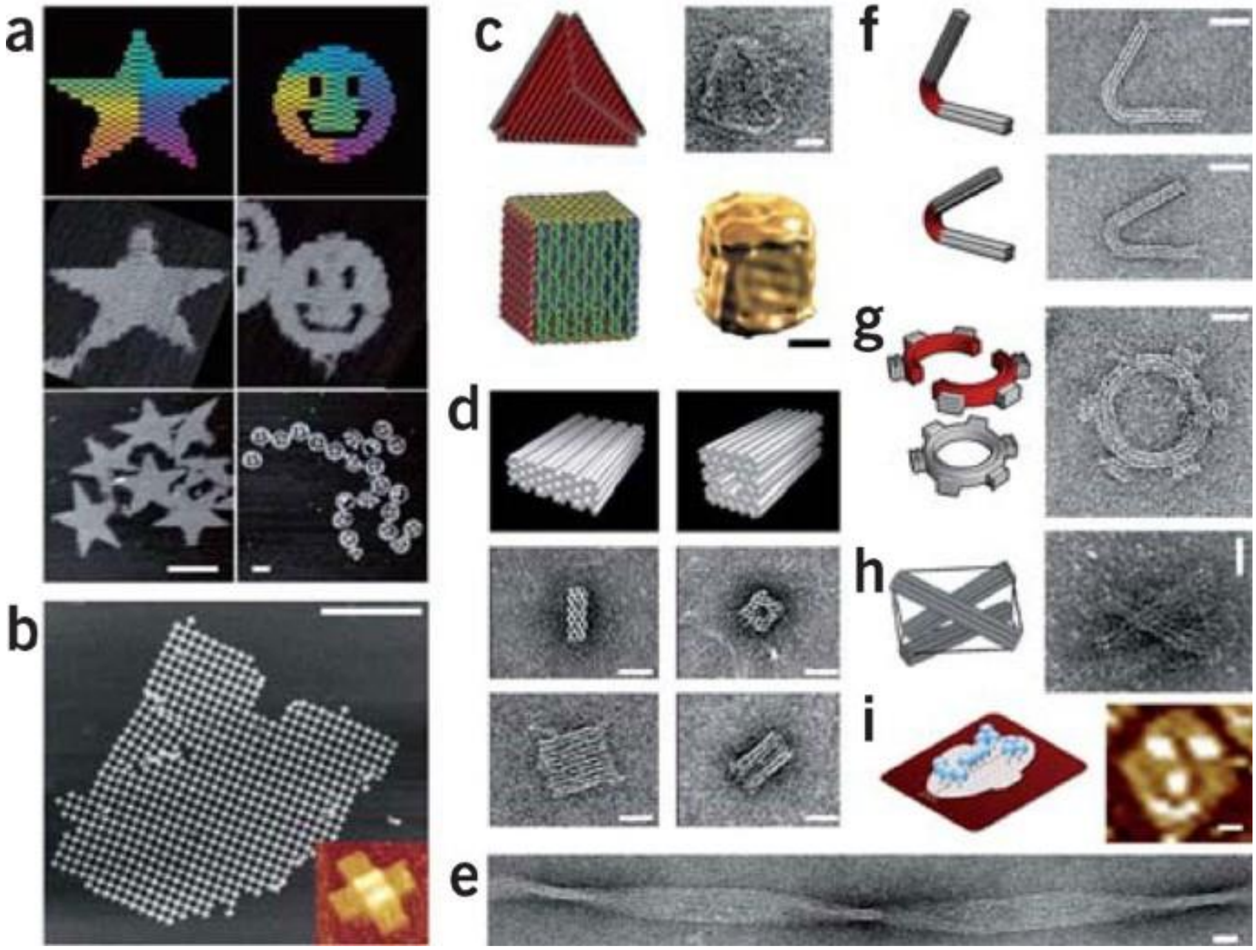

Figure 1.15. DNA origami structures. (a) Designs of DNA origami (top) and AFM images of these objects (middle and bottom). Scale bar, 100 nm. **(b)** AFM image of crystalline DNA origami arrays formed from hundreds of a cross-shaped single-layer DNA origami object. (Inset, a 100-nm-long origami monomer). Scale bar, 1000 nm. **(c)** Container-shaped DNA origami objects (left) imaged with negative-stain TEM (top) and cryogenic TEM (bottom). **(d)** Designs and images of multilayer DNA origami structures. **(e)** Image of a multimeric multilayer DNA origami object with global twist deformation. **(f-g)** Design and images of objects with custom curvatures, bent bars in **(f)** and a gear with square teeth in **(g)**. **(h)** Tensegrity prism created by combining multilayer DNA origami struts and ssDNA strings. **(i)** Design and image of a single-layer DNA origami shape with protein attachments. Scale bar, 20 nm **(c-i)**. [Image taken from *A primer to scaffolded DNA origami* (Nat. Methods, 2011) with permission][52]

The sugar-phosphate backbone is the structural component of the DNA double helix. It consists of deoxyribose and phosphate groups, which together form the supporting framework of the molecule. The alternating sugar and phosphate groups gives the direction of the molecule, namely, the 5’ (phosphate) and the 3’ (sugar) end. DNA molecules are composed of monomer units called nucleotides, which are connected covalently through phosphate-diester bonds. Each nucleotide is linked to the sugar of one nucleotide and the phosphate of another nucleotide, as shown in **Figure 1.16**.

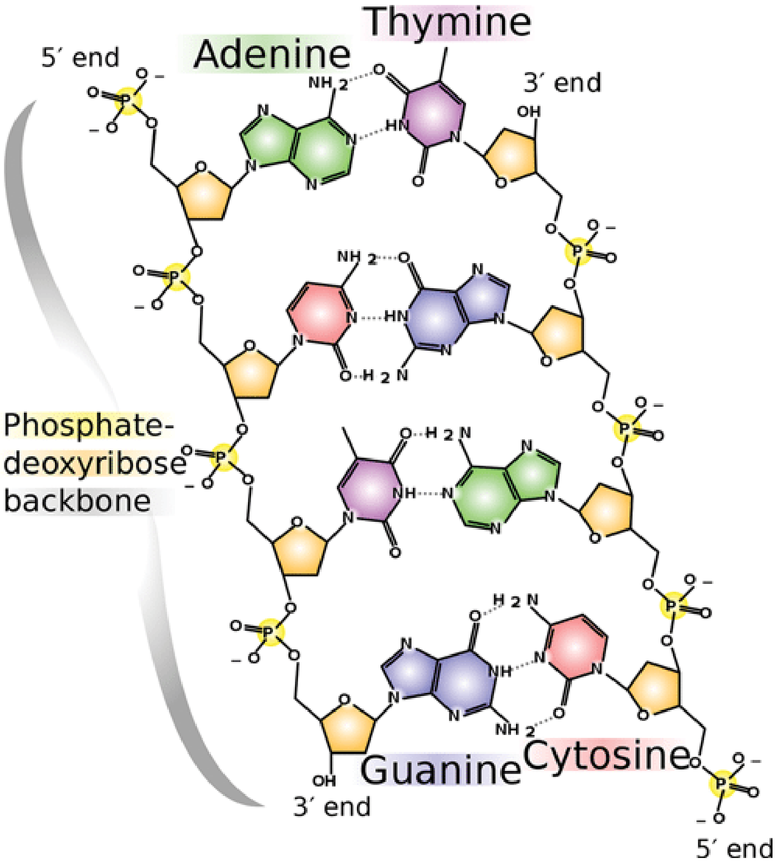

Figure 1.16. Illustration of the sugar-phosphate backbone and complementary base pairing between DNA bases. [Image created by Madeleine Price Ball]

There are four types of nucleotides, adenine (A), cytosine (C), guanine (G), and thymine (T). The nucleotides bind to one another (through non-covalent hydrogen bonds of medium to low strength) according to DNA base-pairing or complementarity, namely, A to T and C to G, to form double-stranded DNA. This base-pairing complementarity forms the basis of DNA hybridization, which is itself the basis of DNA origami. The complexity of DNA is described by its $c_0 t$ curves, as given by:[53]

$$\frac{c(t)}{c_0} = \frac{1}{1 + k\, c_0 t} \qquad 1.9$$

Where c_0 is the concentration of single-stranded DNA at time 0, $c(t)$ is the concentration of single-stranded DNA at time t, and k is the association constant.

The specificity of DNA hybridization depends on the stability of the complex, and the stringency of the reaction. The stability of the hybrid depends on the melting temperature (T_m), which is the temperature at which half of the molecules are dissociated. This value is related to the length of the molecule, the G/C content, and the salt concentration of the solution as given by:[53]

$$T_m = 81.5\,^\circ C + 16.6 \log[c(\mathrm{Na}^+)] + 0.41\ (\%\ \mathrm{G} + \mathrm{C}) - \frac{500}{n} \qquad 1.10$$

Where $c(\mathrm{Na}^+)$ is the concentration of Na^+ and n is the number of base pairs in the sequence. The G/C content of the sequence has an effect on the melting temperature because G and C each contain three hydrogen bonds compared to only two in A and T, which makes G/C bonds more stable.

Stringency describes the conditions under which a target is exposed to a probe, indicating the proportion of correctly hybridized molecules. Under stringent conditions, only perfectly matching nucleic acids hybridize and remain stable. The higher the stringency, the more specific the hydrogen bonding between the oligonucleotides (short DNA sequences). Numerous factors affect the stringency, most notably the temperature and salt concentration of the medium. Most hybridization experiments are performed at fixed salt concentrations, making temperature the dominant factor influencing in the degree of stringency. Since the melting temperature of a complex T_m decreases by up to $5\,^{\circ}C$ for every 1% base-pair mismatch, it is possible to differentiate a single base mutation with oligonucleotides under stringent conditions.[53] Therefore, heating a sample up and then ramping down the temperature (thermal annealing) is a commonly used technique in the hybridization of DNA origami structures.

1.2.2 Design and Methods

Since Nadrian Seeman laid the framework for the use of DNA nanostructure in 1982,[45] DNA has been used to construct increasingly complex shapes. There are two main approaches to DNA origami, the multi-stranded approach and the scaffold-based approach.[54] The multi-stranded approach makes use of the DNA complementarity rule by mixing pieces of DNA oligonucleotides and forming “Holliday junctions”, as shown in **Figure 1.17**.This approach has been widely used in the field including some of the work shown in this thesis.

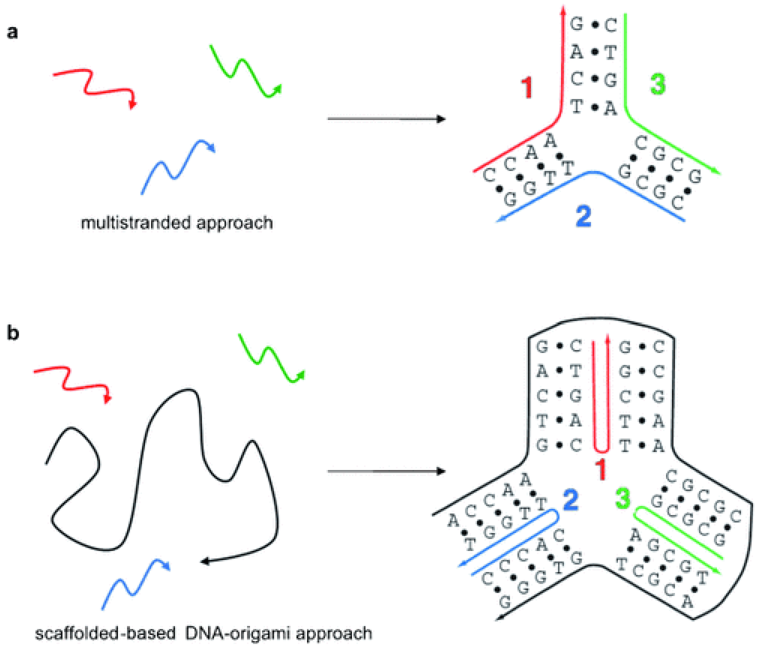

Figure 1.17. Schematic representation of the two main approaches used for the construction of DNA-based architectures. (a) The multi-stranded approach, in which the oligonucleotides bind to each other. **(b)** The scaffold-based DNA origami approach, in which a long single-stranded scaffold is folded into shapes by hundreds of “staple” strands. [Image taken from *DNA Origami: The Art of Folding DNA* (Angew. Chem., 2012) with permission][54]

In 2006, Paul Rothemund introduced DNA origami for the construction of arbitrary 2D shapes, which involves the use of a “scaffold” strand and hundreds of “staple” strands to fold into desired shapes.[55] Rothemund presented large two-dimensional nanostructures by mixing hundreds of short ~40-mer oligonucleotides with a 7249 nt long sequence of M13 viral DNA, as shown in **Figure 1.15** a-c. This approach was further developed by Shih and coworkers at Harvard, where they developed a computer-aided design (CAD) software called caDNAno. This software extends the DNA origami into 3D shapes, making the prototyping of DNA origami even more accessible.[52,56–58]

In a honeycomb lattice, the assembly of the target shape can be visualized by laying down the "scaffold" strand into an array of anti-parallel helices, as shown in **Figure 1.18**c.[56] Helix $m+1$ has a preferred attachment angle to helix $m \pm 120°$. The complementary "staple" strands bind in the antiparallel direction around the scaffold to hold the structure in place. The rule of thumb is that antiparallel crossovers are permitted between staple helices where the strand backbones arrive at points of closest proximity; as the DNA double helix twist averages 10.5 base pairs per turn, this repeats every 21 base pairs. This rule implies that potential crossover positions are only available every 7 base pairs or 2/3 of a turn.

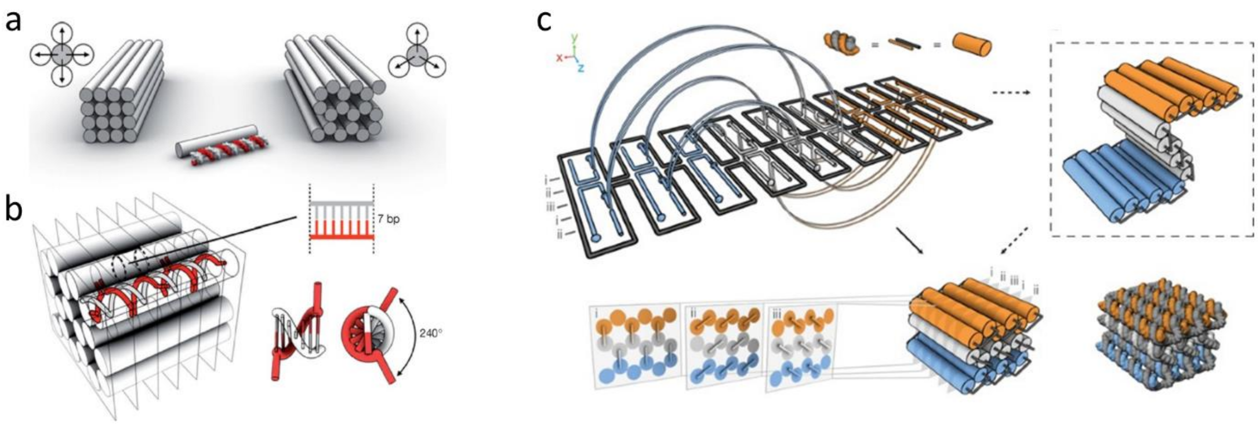

Figure 1.18. Designing multilayer DNA origami. (a) Cross-sectional view of multilayer DNA origami objects in square lattice (left) and honeycomb lattice (right) packing. **(b)** Cross-overs in multilayer objects with honeycomb lattice packing. [Image taken from *A Primer to Scaffolded DNA Origami* (Nat. Methods,

2011) with permission][52] **(c)** Design of three-dimensional DNA origami using caDNAno. [Image taken from *Self-assembly of DNA into nanoscale three-dimensional shapes* (Nature, 2009) with permission][56]

The design process for DNA origami objects typically involves four steps. The first step is to build a raster-style fill pattern to establish the target shape. The constraint at this step is that the antiparallel crossovers are only allowed at those locations where the DNA twist places it at a tangent point between helices. Second, the staple paths are assigned according to the scaffold paths. Third, the staple paths are broken into smaller pieces, typically 18 to 49 bases in length, with a mean of 30 - 35 bases. Finally, the scaffold path is filled with the desired DNA sequence, the most widely used template being the 7249 nt M13mp18, and its complementary staple strands are generated accordingly.

Before ordering or synthesizing staple oligonucleotides to perform the assembly, which can be expensive and very labor-intensive, a more cost-effective approach is to use computational tools to predict and model the DNA origami designs. A computational tool named Computer-aided Engineering for DNA Origami (CanDo) was developed.[52,59] CanDo models the DNA origami shapes using the finite element method based on caDNAno designs. CanDo simulations can provide valuable feedback such as the local root-mean-square fluctuations (RMSFs), as shown in **Figure 1.19**.

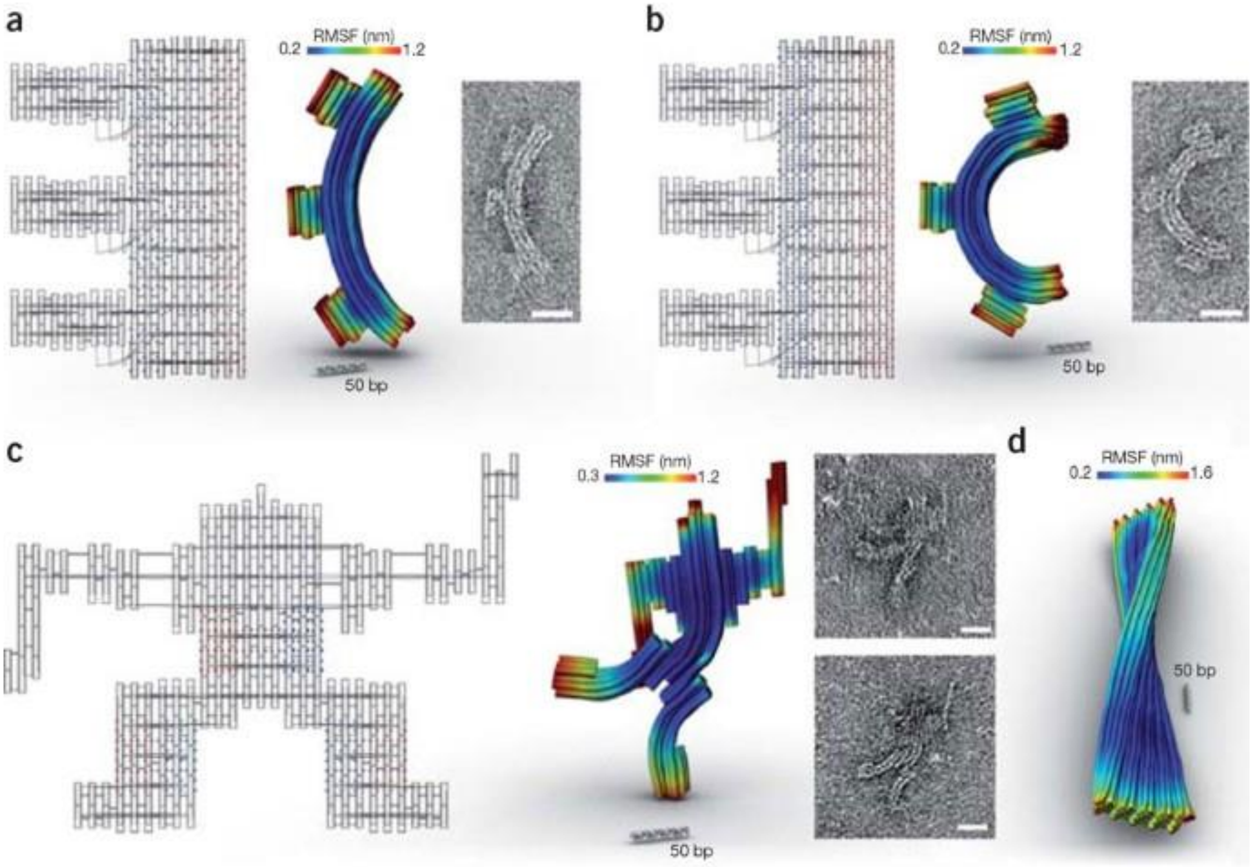

Figure 1.19. Designing and imaging of DNA origami. Examples of caDNAno design diagrams of DNA origami structures, their CanDo 3D structures shown as heatmaps, and the representative negative-stain TEM images of the structures. Scale bar is 20 nm for TEM images. [Image taken from *A primer to scaffolded DNA origami* (Nat. Methods, 2011) with permission][52]

Samples are typically prepared by mixing scaffold strands and staple strands at a ratio of 1:5, for example, 20 nM of M13mp18 in mixture with 100 nM of each staple nucleotide, buffer and salts containing 5 nM Tris, 1 mM EDTA (pH 7.9), and 10 mM or more $MgCl_2$ or MgAc. The annealing is carried out by rapid heat denaturation and slow cooling down to room temperature (22 ℃) over the course of a few hours to up to a week. The concentration of $MgCl_2$ and the cooling down speed can play a major role in the yield of the assembly.[57,58,60]

1.2.3 Characterization of DNA Origami Structures

Once the samples are assembled, the quality of the assembly can be assessed by agarose gel electrophoresis, which is a most widely used method for high-resolution separation of objects. In an agarose gel electrophoresis, charged molecules are driven though a gel medium by an applied electric field, separating by their size.[52,56,61]

Because DNA molecules are negatively charged, DNA origami structures are as well, and under the applied electric field they migrate towards the anode. Since the charge distribution of DNA is uniform, the charge of the origami structure is proportional to its mass. Smaller structures generally migrate faster than bigger ones in gel electrophoresis. The aggregates, or so called “multi-mers” are typically stuck in the loading wells, while correctly folded origami structures normally result in a sharp and fast migrating band, as shown in **Figure 1.20**.

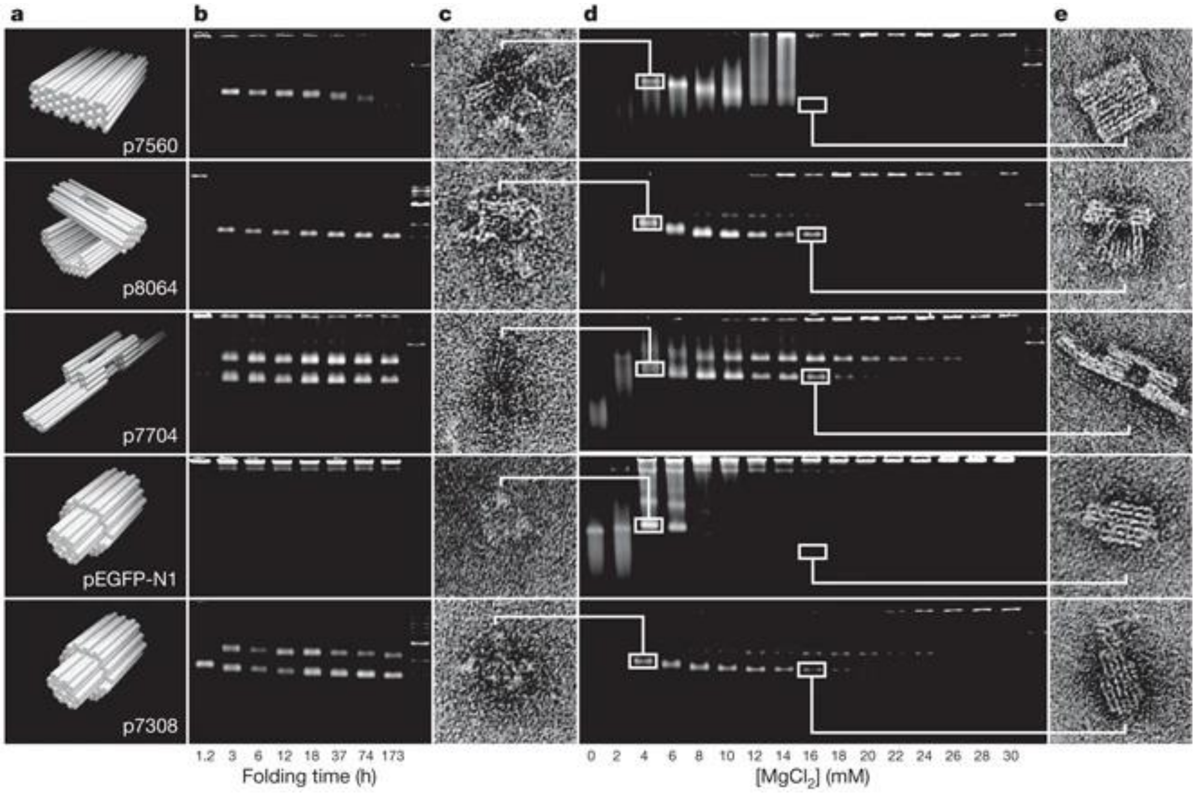

Figure 1.20. Characterization of DNA Origami Structures. (a) Cylinder models of shapes: monolith, stacked cross, railed bridge, and two versions of genie bottle. **(b)** Shapes were folded in 5 mM Tris + 1 mM EDTA (pH 7.9 at 20 °C) and 16 mM $MgCl_2$ and analyzed by gel electrophoresis using different thermal-annealing ramps. **(c–e)** TEM and gel analysis of influence of $MgCl_2$ concentration on folding quality. [Image taken from *Self-assembly of DNA into Nanoscale Three-Dimensional Shapes* (Nature, 2009) with permission][56]

Structural analysis of DNA origami structures on a per-molecule basis can be performed by microscopy techniques such as negative-stain transmission electron microscopy (TEM) or atomic force microscopy (AFM), , where the background is stained to contrast the unstained sample specimen, it is particularly useful for 3-dimensional structures.[62,63] TEM is a powerful tool in material science in which electrons are used to image objects. With TEM, a high-energy beam is shone at the sample and transmits through to a detector below. The basic principle is similar to light microscopes but with electrons. Since electrons have much shorter wavelength than light, TEM offers far superior resolution. **Figure 1.20** shows examples of TEM imaging of 5 different Origami shapes. AFM, on the other hand, uses a cantilever with a very small very sharp tip to probe the topology of a sample surface. As the cantilever scans the surface, the deflection of the cantilever changes according to the raised or lowered features on the surface, which changes the direction of the laser beam reflected off the cantilever. By monitoring these changes with a position-sensitive photo diode the AFM can generate a topographical map of the sample surface. Both TEM and AFM are commonly used in the DNA origami field.[52,56,57]

1.2.4 Use of Nanopore as an Analytical Tool

While gel electrophoresis and microscopy techniques are effective, nanopore sensing has distinct advantages. It enables sensing on the single-molecule level, as the blockage depth, duration, and frequency of translocation events reveal information about a nanostructure’s size, charge, and shape. Nanopore sensing also enables detection in buffer solution, rather than immobilizing the sample on the surface. These characteristics make nanopores an emerging class for DNA nanostructures sensing and characterization.[64] A number of research groups have work involving sensing DNA nanostructures using solid-state nanopores, ranging from ring-/cube-shaped structures and branched DNA structures of tens of nm in diameter to DNA nanocarriers and DNA helix bundle structures of hundreds of nm in length.[65–69] Apart from sensing, there are other interesting approaches, such as the NEOtrap and synthetic DNA-nanopores.[70,71]

Alibakhshi *et al* at Northeastern University presented the use of nanopores to study two different nucleic acid structures, the ring-shaped RNA (15 nm) and the cube-shaped DNA (8 nm) nanostructures, as shown in **Figure 1.21**.[65] They studied the electrophoretic transport of individual shapes and optimized for a range of pore sizes which ensures the deformation of their nanostructures during translocation. The squeezing of the molecules considerably increases the translocation time, the extended translocation time ensures that the translocation of the molecules are correctly resolved by the current recording device. Without sequeezing, the small nucleic acid nanostructures are likely too fast, the events are either truncated or even missed entirely. Fully resolved translocation events show tighter distribution of blockage levels of the nanostructures as truncated events may lead to misfits, this permits the detection of these nanostructures at picomolar concentration.

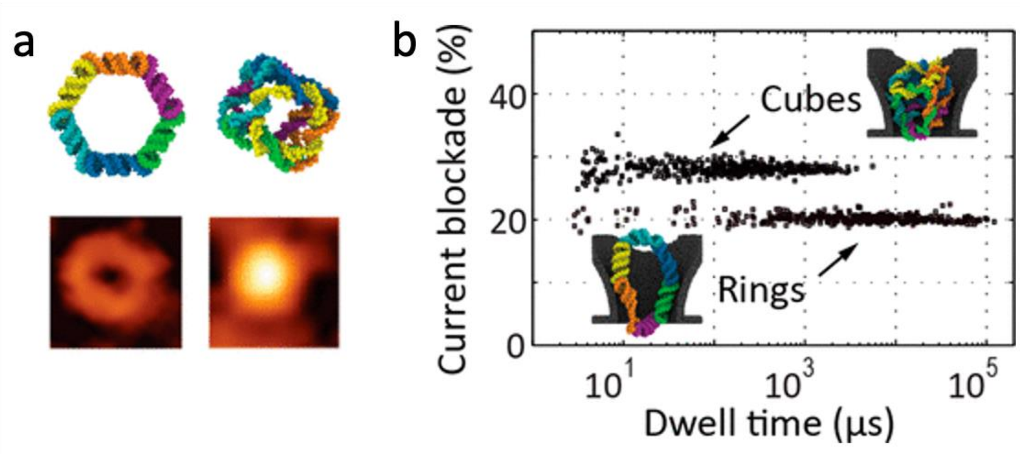

Figure 1.21. Assembly, visualization, and nanopore sensing of nucleic acid nanoparticles (NANPs). (a) Assembly and AFM imaging of ring-shaped RNA and cube-shaped DNA. **(b)** Scatter plot of the fractional blockade *versus* dwell time measured at 500 mV applied bias displays two distinct populations

corresponding to the DNA cubes and the RNA rings. [Image taken from *Picomolar Fingerprinting of Nucleic Acid Nanoparticles Using Solid-State Nanopores* (ACS Nano, 2017) with permission][65]

Wang *et al* at Cambridge University demonstrated the characterization of large DNA origami structures using nanopores.[66] In their work, they deployed the 4-helix bundle (4HB) and the 16-helix bundle (16HB) origami shapes, which are ~630 nm and ~151 nm in length, respectively, as shown in **Figure 1.22**. These structures are considerably larger than the cube-shaped and ring-shaped shapes; when they translocate through a nanopore, they produce current blockages 4 and 16 times that of double-stranded DNA (dsDNA). They further demonstrated that introduction of polyethylene glycol (PEG) into the sensing solution enables translocation of large DNA origami structures by reducing the electroosmotic flow.

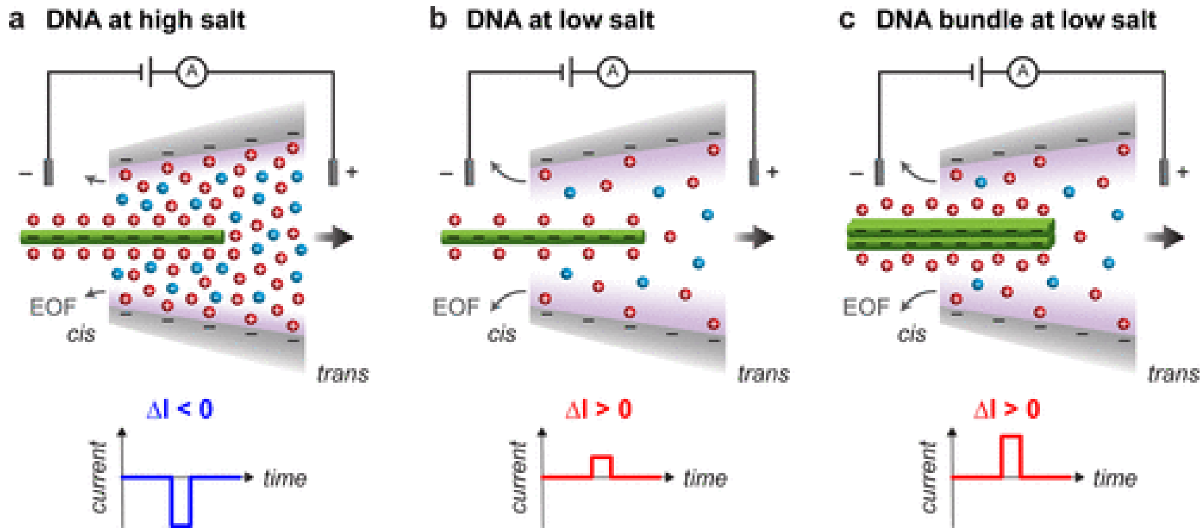

Figure 1.22. Nanopore sensing in high and low salt environments. DNA nanostructures are added to the tip side of the nanocapillary. As each DNA nanostructures translocate through the pore, a transient ionic current modulation ΔI is observed. **(a)** At high salt concentrations, counterions screen the glass nanopore

surface charge within a region close to the pore (purple shading), generating small electroosmotic flow (EOF) out of the pore. Negative current changes, or blockades, are observed upon translocation of a single dsDNA strand. **(b)** At low salt concentrations, counterions screen the glass surface charge within a region further from the pore, leading to higher EOF. The introduction of mobile counterions by DNA outweighs frictional current reduction in the presence of a low background concentration of ions. Positive current changes, or enhancements, are observed upon translocation of a single dsDNA strand. **(c)** At low salt concentrations, the translocation of DNA bundles (composed of multiple dsDNA strands) leads to larger positive current changes compared to that of a single dsDNA strand. [Image taken from *Current Enhancement in Solid-State Nanopores Depends on Three-Dimensional DNA Structure* (Nano Lett., 2019) with permission][66]

There are other interesting applications with emerging nanopore and DNA nanotechnology, such as the NEOtrap presented by Schmid *et al*.[70,72] The nanopore electro-osmotic trap (NEOtrap) allows long-term trapping (hours) and observing single proteins with sub-millisecond time resolution. They built the NEOtrap by docking a DNA-origami sphere onto a passivated solid-state nanopore, as shown in **Figure 1.23**, which creates an electro-osmotic flow that traps nearby protein molecules regardless of their charge. They further demonstrated the ability to use the NEOtrap to distinguish proteins according to their size and shape.

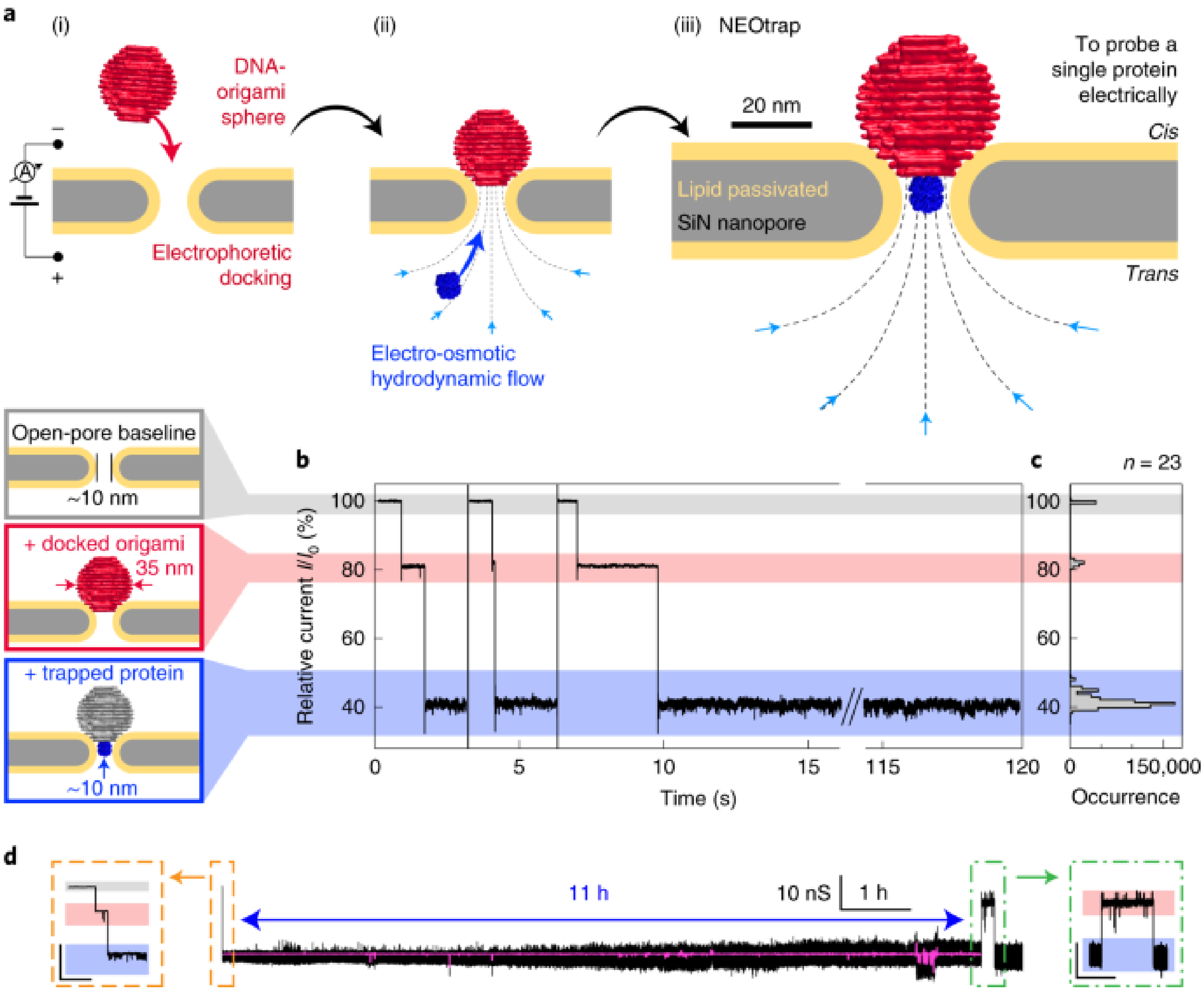

Figure 1.23. Working principle of the NEOtrap. (a) Illustration of the trapping process: a DNA-origami sphere is electrophoretically docked onto a solid-state nanopore. *Cis* and *trans* reservoirs are defined in **(iii)**. **(b)** Current recordings starting with a open-pore baseline (grey); the origami docking blocks 20% of the current (red); and the induced EOF traps a ClpP protein leading to further current blockage (blue). **(c)** Histogram of 23 current traces similar to ones shown in **(b)**. **(d)** One ClpP protein was trapped and recorded for 11 hours. Insets show zoomed current traces of ClpP trapping (orange, left, scale bar 10 nS *versus* 10 s) and spontaneous escape after 11 hours (green, right, scale bar 10 nS *versus* 500 s). [Image taken from *Nanopore electro-osmotic trap for the label-free study of single proteins and their conformations* (Nat. Nanotechnol. 2021) with permission][70]

Seifert *et al.* created a nanoscale device by combining nanopores and DNA nanotechnology.[73] They described the assembly of a DNA-based nanopore that structurally mimics the amphiphilic characteristics of biological nanopores and inserts them into bilayers, as shown in **Figure 1.24**. These synthetic nanopores are made from DNA with hydrophobic lipid anchors attached to insert the hydrophilic structures into lipid bilayer membranes, which are otherwise energetically unfavorable.[71,73,74]

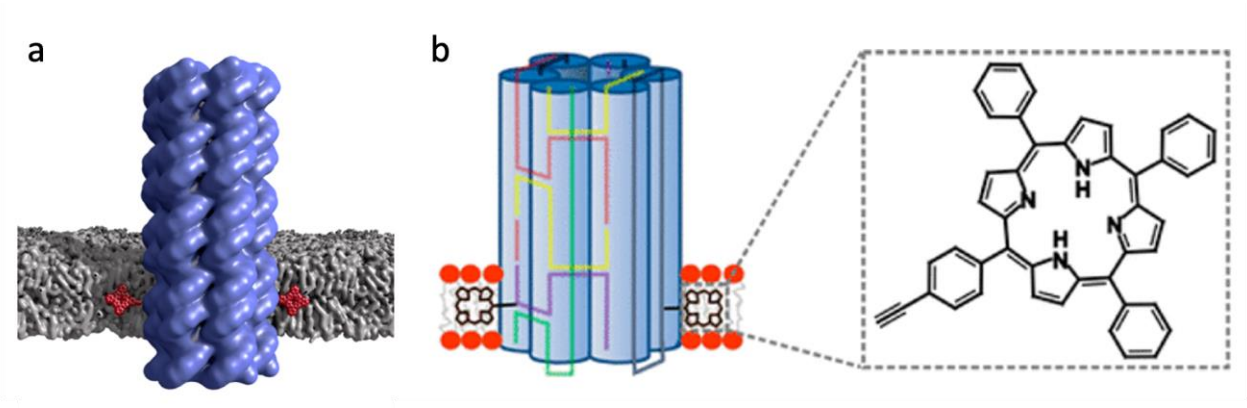

Figure 1.24. Synthetic nanopores from self-assembled DNA. (a) Illustration of DNA-based membrane-spanning pore and the two recording setups used to measure the conductance properties of the nanopore. **(b)** Schematic drawing of a six-duplex-bundle nanopore composed of six DNA oligonucleotides (colored) carrying two tetraphenyl porphyrin tags (black, inset), which anchor the pore into the lipid bilayer. [Image taken from *Bilayer-Spanning DNA Nanopores with Voltage-Switching between Open and Closed State* (ACS Nano, 2015) with permission][73]

1.3 Nanopore assay for detecting proteins

1.3.1 Challenges with Direct Sensing

Having established nanopore fabrication and the means to reliably sense DNA nanostructures, we set out to develop an assay scheme to quantify proteins using solid-state nanopores. Direct sensing of the molecules would be the first method of choice; however, their behaviors on nanopore platforms are not only less understood, but also difficult to sense reliably and with high specificity. While researchers have successfully characterized certain protein molecules using nanopores,[75–78] challenges associated with direct protein sensing remain, namely, charge effects, translocation velocity, and clogging.[79–82]

Unlike DNA molecules, proteins have charge distributions that are not uniform, which makes them less suitable for nanopore sensing using electrophoresis due to their inconsistency in translocation speed and direction. Furthermore, there are hardware limitations. Studies have shown that the electrical bandwidth of the current recording is not sufficient to correctly resolve most protein translocations, as shown in **Figure 1.25**a,[83] further development would be needed towards higher recording bandwidths and to slow protein translocation.

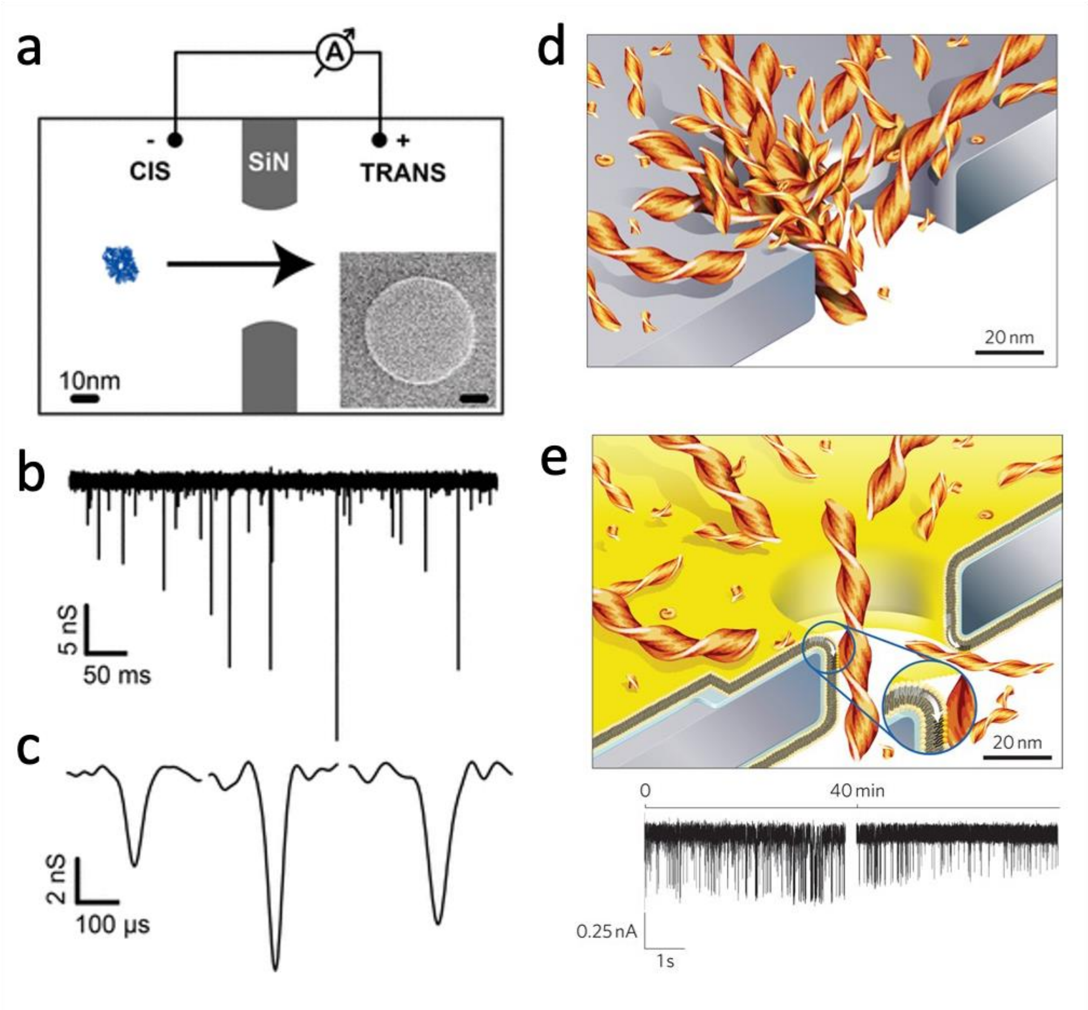

Figure 1.25. Solid-state nanopore for protein analysis. (a) Schematic illustration of the nanopore setup, with the 20 nm thick SiN membrane and a β-galactosidase protein shown to scale. Insert: TEM image of one of the 40 nm nanopores used in this study. **(b)** Current trace of β-galactosidase translocating through a 40 nm pore. **c)** Representative translocation events, shown at better temporal resolution. [Image taken from *Fast Translocation of Proteins through Solid State Nanopores* (Nano Lett., 2013) with permission][79] **(d)** Representation of clogging of uncoated nanopores and a typical current versus time trace during clogging of a nanopore. (**e)** Representation of translocation of individual aggregates through a bilayer-coated nanopore with a fluid wall (white arrow in the inset) and a typical current versus time trace of translocation

events. [Image taken from *Controlling Protein Translocation Through Nanopores with Bio-inspired Fluid Walls* (Nat. Nanotech., 2011) with permission][82]

Another issue associated with direct sensing is clogging, as most applications require hundreds of thousands of translocation events to be able to draw statistically meaningful conclusions. **Figure 1.25**e shows a different strategy for functionalizing nanopore that researchers have implemented to mitigate nanopore clogging.[82–84] While several different approaches have been attempted, successfully reducing protein clogging while maintaining sufficient signal-to-noise ratio (SNR) remains a challenging task for the reasons discussed above, a different strategy must be developed to achieve the goal of reliably counting protein biomarkers to determine their concentrations. Since the translocation properties of DNA molecules have been proven to be well behaved on nanopore platforms and have been thoroughly characterized, an indirect strategy would be more suitable, such as the use of DNA molecules as proxy labels unique to each of the protein biomarkers of interest, or the use of DNA as nano-carriers.[69,85–87] Such indirect strategy translates protein sensing to DNA sensing

1.3.2 Protein Detection Using Nanopores

The development of effective bioassays has been of great importance in diagnostics over the last decade. Sensitivity, limit of blank (LoB), limit of detection (LoD), and limit of quantification (LoQ) are often used to describe the lowest concentration of an analyte needed for reliable measurement. Sensitivity is the lowest concentration of analyte that the assay can distinguish from background. LoB is the highest apparent concentration of an analyte measured of a blank sample, which contains no analyte. LoB can be calculated by measuring replicates of a blank sample and calculating the mean and standard deviation (SD), it is given by Equation 1.11:[88]

$$\mathrm{LoB} = \mathrm{mean}_{\mathrm{blank}} + 1.645(\mathrm{SD}_{\mathrm{blank}}) \qquad 1.11$$

Where 1.645 comes from the fact that to achieve 90 % confidence interval, the central 90 % of the normal distribution must be included. And to capture the central 90 %, one must include 1.645 standard deviations from the mean from either side of the calculated mean value.

LoD is the measure of the lowest possible concentration of an analyte which is detectable from a sample, namely, the lowest analyte concentration to be reliably differentiated from LoB. LoD can be calculated by using the calculated LoB and replicates of a sample containing low concentration of the analyte, it is given by Equation 1.12:[88]

$$\mathrm{LoD} = \mathrm{LoB} + 1.645(\mathit{S}\mathrm{D}_{\mathrm{low\ concentratiom\ sample}}) \qquad 1.12$$

LoD is separate from LoQ, at which an analyte can be accurately quantified.[88] LoQ can be estimated by an SNR of 10, or multiplying LoD by 3.3.[89] Apart from these, there are several key aspects to consider. Accuracy and precision give insights on the reliability of an assay. Accuracy is a measure of the closeness of the experimental measurement to the actual amount of analyte present. While precision measures of close the individual measurements are.[90] Spike recovery experiment of the most common technique to determine accuracy, where a known amount of analyte is added to the sample (spiked) and the percentage is determined from experimental and theoretical values.[90]

There are two most prominent aspects when it comes to the effectiveness of a biosensor, the limit of detection (LoD) and the dynamic range of an assay.[91] Dynamic range (DR) represents the concentration range from the lowest to the highest concentration of an analyte which can be reliably detected by an assay. The DR is limited at the lower end by the LoD and the saturation of the sensor at the higher end. For instance, for a binding assay, the sensor surface is saturated when there are no binding sites left, this produces a hyperbolic dose response curve. It is advantageous to extend the DR of an assay, as it broadens the sensing range of an analyte. However, biosensors with large DR often suffer from limited precision, while precise sensors are often limited from poor dynamic range.[92,93] Along with sensitivity, specificity reveals the likelihood of the assay giving false positive and false negative results. It refers to the ability to undisturbedly measure a specific analyte, rather than other substances present in the sample.[94] While selectively refers to the ability to accurately measure a number of given analytes individually without interferences by other components.[94]

In the last few years, motivated by the need for novel digital diagnostic technologies, the bio-sensing field has seen important advances in nanopore detection of proteins. The detection of specific biomarkers is an essential part of diagnostics, traditional assays have utilized single assay techniques, where one analyte is measured at a time. In comparison, multiplexing assays allow simultaneous detection of multiple analytes in a single experiment.[95] With a growing need in high throughput assays, multiplexing becomes the clear choice. Multiplexing comes with several perks, such as faster data generation while reducing cost per sample, it also minimizes sample handling. Although advantageous, there are many hurdles to overcome before multiplexing can be realized. One major challenge to overcome is non-specific binding and associated cross-reactivity. Non-specific binding takes place when the unintended biomarker is bound and detected, this can result in false positives, in which the result falsely reports the presence of a biomarker thus negatively impacting the diagnosis.[96]

One of the most-used methods of protein biomarker quantification in the nanopore field is perhaps the DNA nano-carriers, first proposed by Keyser group at Cambridge.[68,86,97] The DNA carrier barcode scheme improves specificity for multiplexed sensing, where a library of DNA carriers assembled from M13mp18 is used, each carrying a unique 3-bit barcode and binding site to a specific protein. They demonstrated multiplexed detection of four different designs of barcoding, which can be distinguished with 94% accuracy on a nanopore platform, as shown in **Figure 1.26**a. The carriers were then functionalized to detect an antibody through antigen presentation on specific oligonucleotides on the DNA carrier. This enabled multiplexed detection of four different antibodies at nanomolar levels.[68]

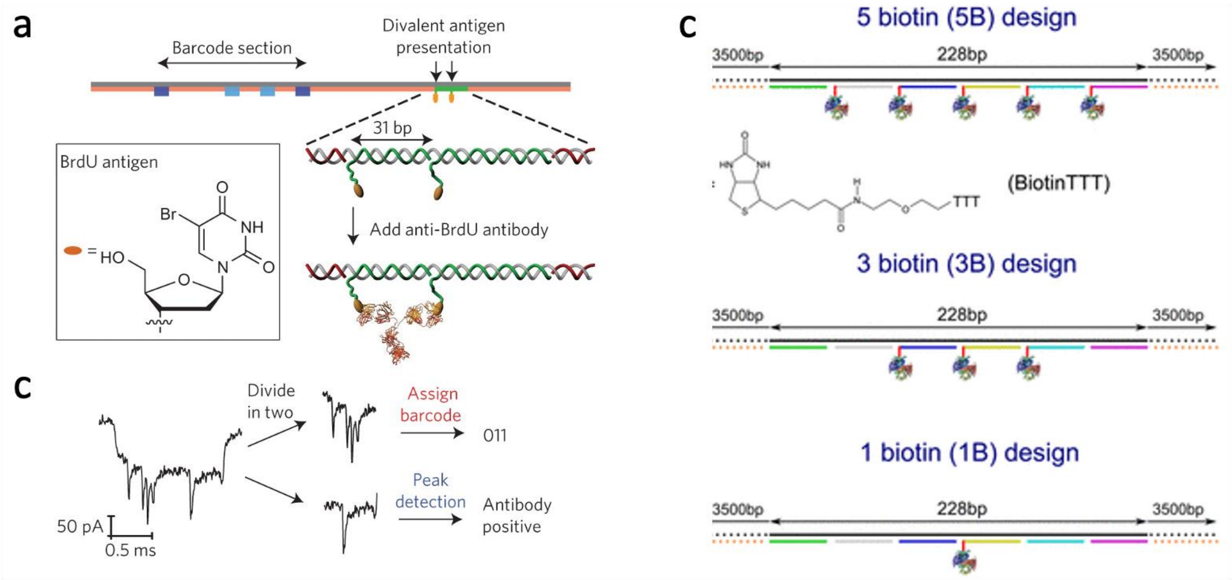

Figure 1.26. Multiplexed protein detection using DNA carriers. (a) DNA carrier barcode design. Two oligonucleotides (green) overhang conjugated to the antigen at three-quarters of the DNA contour length.

(b) Translocation events of the DNA after incubation with the anti-BrdU antibody. [Image taken from *Digitally encoded DNA nanostructures for multiplexed, single-molecule protein sensing with nanopores* (Nat. Nanotechnol., 2016) with permission][68] **(c)** Schematics of DNA carrier designs with 5, 3, and 1 biotin groups after incubation with streptavidin. [Image taken from *Specific Protein Detection Using Designed DNA Carriers and Nanopores* (J. Am. Chem. Soc., 2015) with permission][87]

Similar DNA nano-carrier schemes were employed by the groups of Edel and Ivanov at Imperial College to detect proteins and antibodies from serum. The DNA carrier approach can be used by directly the attachment of proteins.[69,85] **Figure 1.27** shows a DNA carrier with up to three protein binding sites along its contour.[69] The ionic current signal of translocating DNA carriers can be measured as a function of the number of binding sites and achieve detection down to the single-protein level.

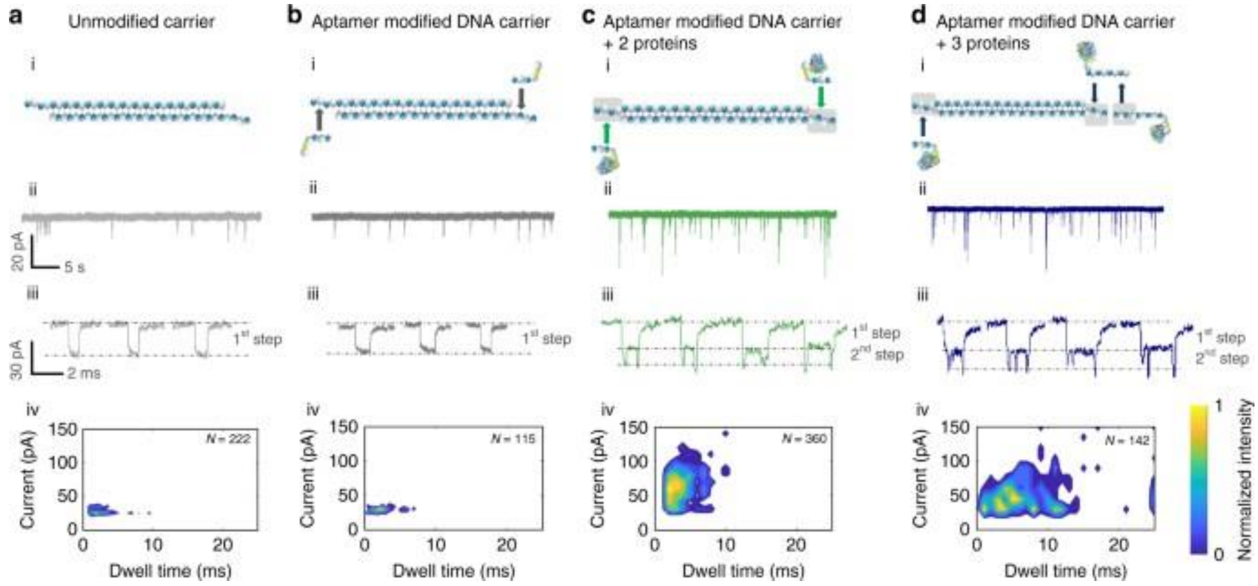

Figure 1.27. Aptamer-based multiplexed detection of proteins using DNA carriers on a nanopore. (a) Current-time trace and statistics for sensing proteins bound to a modified carrier. Translocation and

statistics for a 100 pM of unmodified λ-DNA, **(b)** 100 pM aptamer modified λ-DNA, **c)** 100 pM aptamer modified λ-DNA with two probes for the detection of thrombin (1.6 nM each), **(d)** 100 pM aptamer modified λ-DNA with three probes for the detection of three thrombin targets. [Image taken from *Single molecule multiplexed nanopore protein screening in human serum using aptamer modified DNA carriers* (Nat. Comm., 2017) with permission][69]

Although proteins can be attached to a nano-carrier through modification of the oligonucleotides, the simplicity of using nucleic acid aptamers on DNA carriers has led several groups to study this alternative method. Multiplexed detection of protein biomarkers can be achieved by directly attaching multiple proteins onto the carrier via aptamers, without the need for extensive labelling.[69,85,98] One example of this is shown in **Figure 1.27**. This method allows differentiation of individual protein sizes according to the peak blockage levels produced. Furthermore, the experiments can be performed in human serum at pM (10^{-12} M) protein concentrations. This approach offers a fast and flexible method to selectively detect proteins, the selectivity comes from the use of aptamers, which are engineered to optimize for the selectivity and binding affinity. However, aptamer-based assays are intrinsically limited in pM to nM range due to the binding affinity of the aptamers. The detection relies on the identification of the peak produced by the target attached to the nano-carrier, which makes it sensitive to pore size and unsuitable to proteins that are too big or too small.

This combination of DNA nanotechnology and aptamers is not limited to linear DNA nano-carriers. Raveendran *et al* at Leeds University presented individual biomarker detection using DNA origami structures with central cavities for a target-specific DNA aptamer for nanopore sensing,[99] as shown in **Figure 1.28**. The use of large DNA nanostructures with cavities provides an improved SNR and uniqueness of the nanopore translocation signature. Similar to the other aptamer schemes, although this scheme benefits from the simplicity, which is advantageous, the binding affinity of the aptamer of choice remains the limiting factor to the ability to detect at lower concentrations. Moreover, aptamer-based assays require sensing in complex fluids when sensing serum or plasma samples, which can be problematic for nanopore sensing.

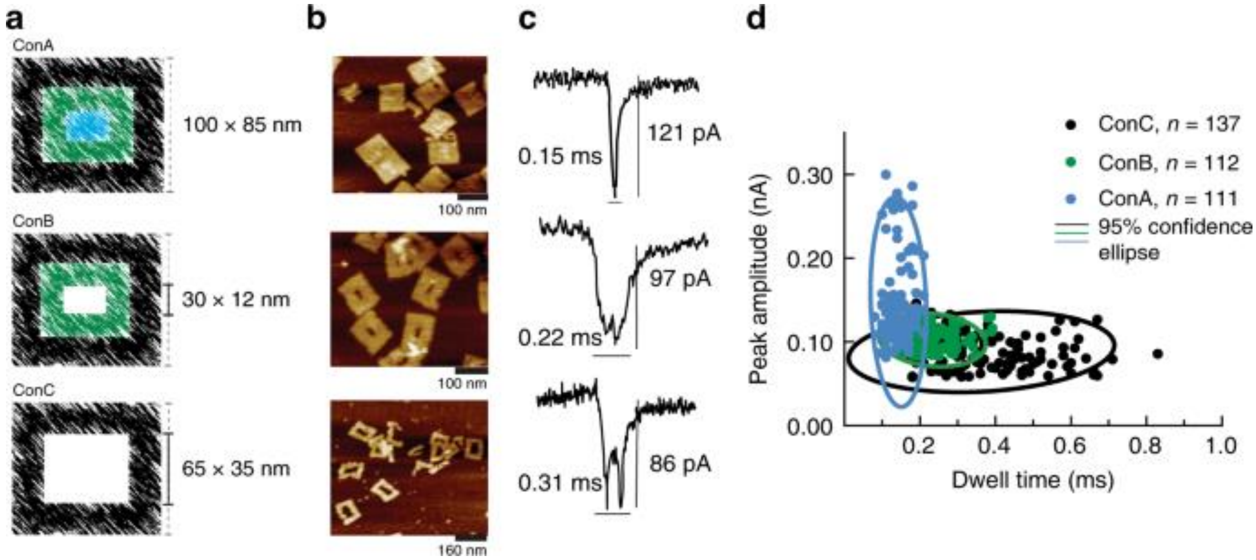

Figure 1.28. Nanopore protein detection using DNA nanostructures with central cavity. (a) Schematic representation of DNA nanostructure designs – ConA is a solid tile and ConB and ConC are frame-like with different central cavities. **(b)** AFM images of the respective nanostructures and **(c)** their typical translocation ion current signatures. [Image taken from *Rational design of DNA nanostructures for single molecule biosensing* (Nat. Comm., 2020) with permission][99]

1.3.3 Enzyme-linked Immunosorbent Assay

While nanopore-based assays employing DNA carrier equipped with receptors (often aptamers, or antibodies) have shown great promise towards a rapid diagnostics tool and demonstrated advantages such as assay time and ease of use due to its simplicity, as discussed previously, their sensitivity is fundamentally limited by their affinity. Affinity is the measure of the binding of a molecule to its ligand, this value is typically represented by the equilibrium dissociation constant K_D. Binding is a reversible process; the rate of binding is directly related to the concentration of molecules. K_D is defined as a ratio of k_{on}/k_{off} for a pair of receptor and ligand (e.g. antigen and its antibody), given in the units of molar concentration.[100] K_D is the reciprocal of association constant K_A, $K_D = [P][L]/[PL] = 1/K_A$, it is more common and intuitively simpler. At equilibrium, half the ligand-binding sites are occupied, such that the rate of bound complex [PL] formation is equal to the dissociation rate into individual components [P] and [L]. As the concentration of ligand falls below K_D, less protein has ligand bound to it. Most antibodies and aptamers have K_D in μM (10^{-6} M) to nM (10^{-9} M) range, high affinity antibodies can be in the low nM to even pM (10^{-12} M) range.[101–103] Therefore, the detection of biomarkers in the fM range (10^{-15} M) with DNA carrier schemes is fundamentally limited, as fM concentration is orders of magnitude below the typical dissociation constant for most receptor-ligand interactions. Furthermore, most DNA carrier schemes are aptamer-based and rely on the the detection of the protein itself, this is potentially limited by the ability of the ionic current recording instrument to reliably detect the fast current blockages of the target proteins bound (or unbound) to receptors anchored along a DNA carrier. Indeed, while aptamers can be comparable in size to the target, antibody can be much larger and obscure the presence or absence of the target protein, thus limiting the choice of targets. In addition, the high salt concentrations ($>$ 1M salt) in which nanopores are optimally operated at, are incompatible with the lower salt concentrations necessary to maintain a good affinity for the receptor/target interaction. Finally, studies have shown that folding of the DNA carriers does happen when translocating through nanopores, this could add to false positive rates when the folded portion is misinterpreted to be target bound to receptor and classifying folding could add another layer of complexity. To push the limits of nanopore-based assays further, another assay scheme must be implemented.

Enzyme-linked immunosorbent assay (ELISA) is a well-known assay technique for the detection and quantification of proteins.[104] In an ELISA, sample is added and target protein is immobilized to the plate surface or micro-sized magnetic beads which are coated with capture antibodies specific to that target protein; the secondary, detection antibody conjugated with a reporter molecule is then introduced and binds to the target protein captured by the beads, forming a "sandwich" complex, as illustrated in **Figure 1.29**.[104] Detection is then carried out by measuring the activity of this label instead of the actual target protein, where the enzyme converts the substrate into a fluorescent or colourimetric signal, and the absorbance or the fluorescence is measured to detect the antigen.[105]

The use of an ELISA on paramagnetic microbeads scheme can address some of the challenges that inherently come with nanopore approaches employing DNA carriers with single isolated receptors, such as LoD and complications from biofluids.

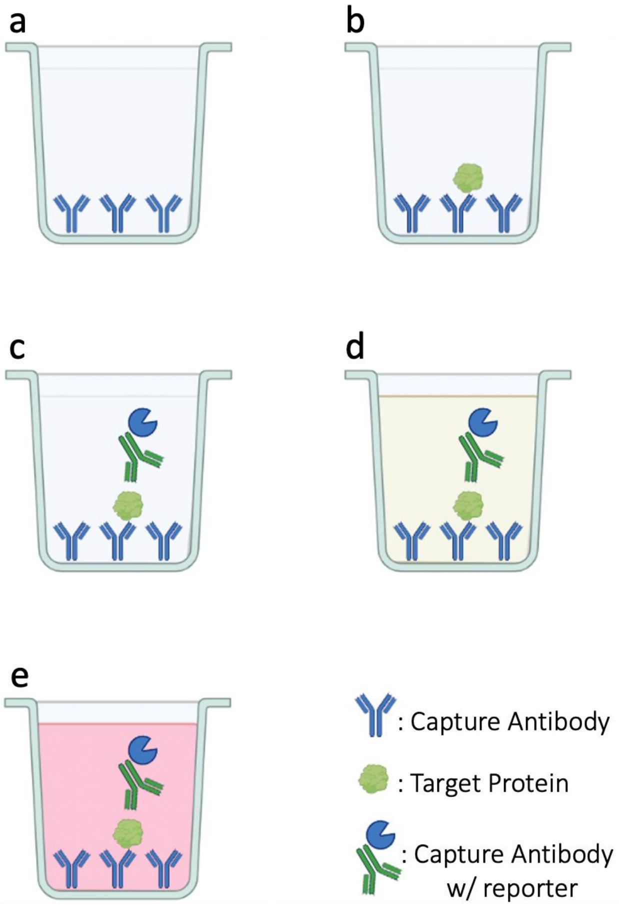

Figure 1.29. Illustration of a sandwich ELISA. (a) Plate is coated with a capture antibody. **(b)** Target protein is captured by the capture antibody. **(c)** Detection antibody conjugated with a reporter molecule is added, and binds to target protein. **(d)** Substrate is added. **(e)** Substrate is catalyzed by reporter molecule to generate readout. [The illustration was drawn on biorender]

While the sandwich assay typically involves coating the wells with millions of capture antibodies, bead-based immunoassay is similar to the principle, having each paramagnetic micron-sized bead (PMB) conjugated with capture antibodies. Bead-based immunoassay employs the brad as a 3D carrier as opposed to the planar 2D format of the plate-based, increasing the surface to volume ratio and minimizing spatial hindrance, therefore increasing the sensitivity of the assay.[106] The paramagnetic beads (PMB) are each coated with hundreds of thousands of capture antibodies, turning each bead into a capture antibody with a significantly higher on-rate than that of individual antibodies, yet while maintaining the same off-rate, allowing detection of targets at a much lower concentration. The assay and (nanopore) sensing take place in separate buffers, which allows the sensing to be carried out in its optimal salt conditions without affecting the affinity of the interactions in the assay itself. Finally, magnetic beads simplify washing, and the wash steps can remove most unwanted molecules in complex biofluids, such as serum.

1.3.4 Digital Scheme

ELISA has been the method of choice for early detection of disease biomarkers, which can able early intervention, but traditional analog ELISA is limited to pico-molar sensitivity, which is often insufficient to quantify biomarkers of some diseases at clinically relevant concentrations (e.g. traumatic brain injury markers in blood instead of cerebral spinal fluids). This is due in part to the affinity of antibodies, since the dissociation constants for the available antibodies are typically larger than the clinically relevant concentration of the target in clinical samples, and in part to the inadequate SNR of standard optical readouts.[107,108] The introduction of a digital scheme made it possible to count proteins at the single-molecule level, enabling detection at femtomolar concentrations.

Despite the efforts made to reduce instrumental noise and increase signal strength, analog detection relies on intensity-based optical readout, its sensitivity is often insufficient to quantify at clinically relevant at ultra-low concentrations.[109] The Quanterix SiMoA (single-molecule array) has achieved sub-fM sensitivity by using a ‘digital detection’ scheme, as illustrated in **Figure**

1.30.[108,110] Ultrasensitive biomarker detection allows the detection of disease biomarkers at an early stage, a digital approach is needed in the limit of low target concentration.

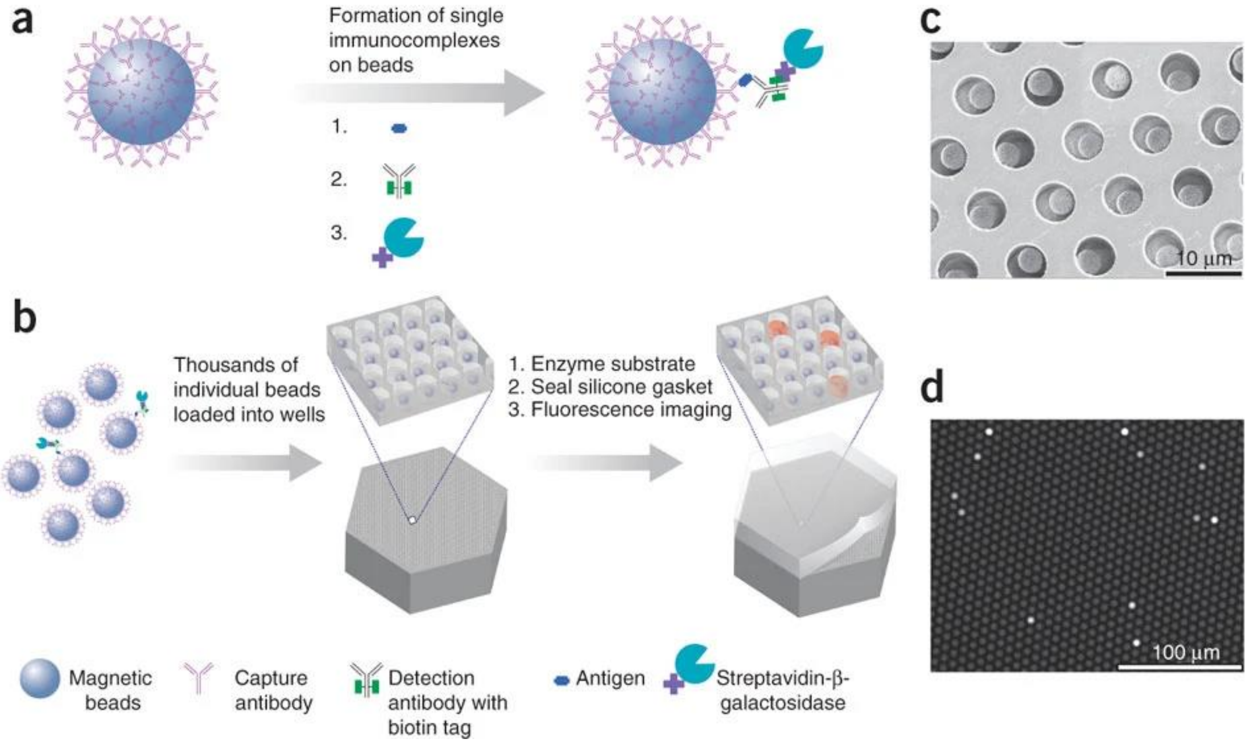

Figure 1.30. Digital ELISA on microwell arrays. (a) Single protein molecules are captured and labeled on beads using standard ELISA reagents. **(b)** Labeled molecules are loaded into femtoliter-volume well arrays for isolation and detection of single molecules by fluorescence imaging. **(c)** SEM image of a small section of a femtoliter-volume well array after bead loading. **(d)** Fluorescence image of the femtoliter-volume well array after signals from single enzymes are generated. [Image taken from *Single-molecule enzyme-linked immunosorbent assay detects serum proteins at subfemtomolar concentrations* (Nat. Biotechnol, 2010) with permission][110]

By counting samples in a single molecule manner, digital detection has pushed sensitivity further, now the only limiting factor is the ability to acquire enough molecules in a given volume in a reasonable amount of time, to be able to draw statistically meaningful conclusions from it. As an example, a single-molecule immunoassay method employing high affinity antibodies and optimized to minimize non-specific binding will reach a fundamental limit of quantification, LoQ of ~3 aM in 100 μL (60,000 copies) when a few hundred molecules are counted.[108,110] Despite the remarkable achievement, these single-molecule technologies will have difficult time translating to clinical applications at the point-of-care due in part to their size, cost and complexity, originating from their dependence on optical detection. Ultrasensitive performance relies on the use of costly and complex instruments that are operated in a centralized setting.

The Quanterix's approach to count individual proteins bound to paramagnetic microbeads (PMB) is by partitioning the PMB, carrying the sandwich complex into individually optically addressable micro-wells for digital readout, overcoming analog error modes by transitioning to a digital scheme, as shown in **Figure 1.30**.[108,110,111] Partitioning the samples ensures a single PMB carrying zero or one target molecule exist in a well (not all well will be occupied by beads), and is spatially separated to facilitate optical detection without being diffraction limited. The occupancy of well can be described using Poisson statistics, such that an occupied compartment contains either "0" or "1" molecule of the target analyte.[112] This binary output, in principle, provide a wide dynamic range compared to the traditional bulk measurements.[112] Compared to traditional measurements, a digital counting scheme provides an absolute number by counting target molecules in a digital manner, and eliminating interfering factors.[110,113] In principle, nanopores, thanks to its electrical nature, are immune to background fluorescence that come with optical schemes and their intrinsic single molecule sensitivity makes them ideal candidates for the development of a technology platform that can be miniaturized to operate point-of-care and decentralized setting to perform ultra-high sensitivity measurements, as embodied by the cell phone-sized MinION DNA sequencer by Oxford Nanopore.

Chapter 4 of this thesis combines the approach of bead-based ELISA assays and DNA nanostructures detection with the nanopore single-molecule electrical readout platform, to develop a digital immunoassay scheme, as illustrated in **Figure 1.31**. Briefly, the digital nanopore assay works as follows: The sandwich assay is performed as usual, with one difference: the reporter molecule is replaced with a single-stranded DNA (ssDNA) linker strand.

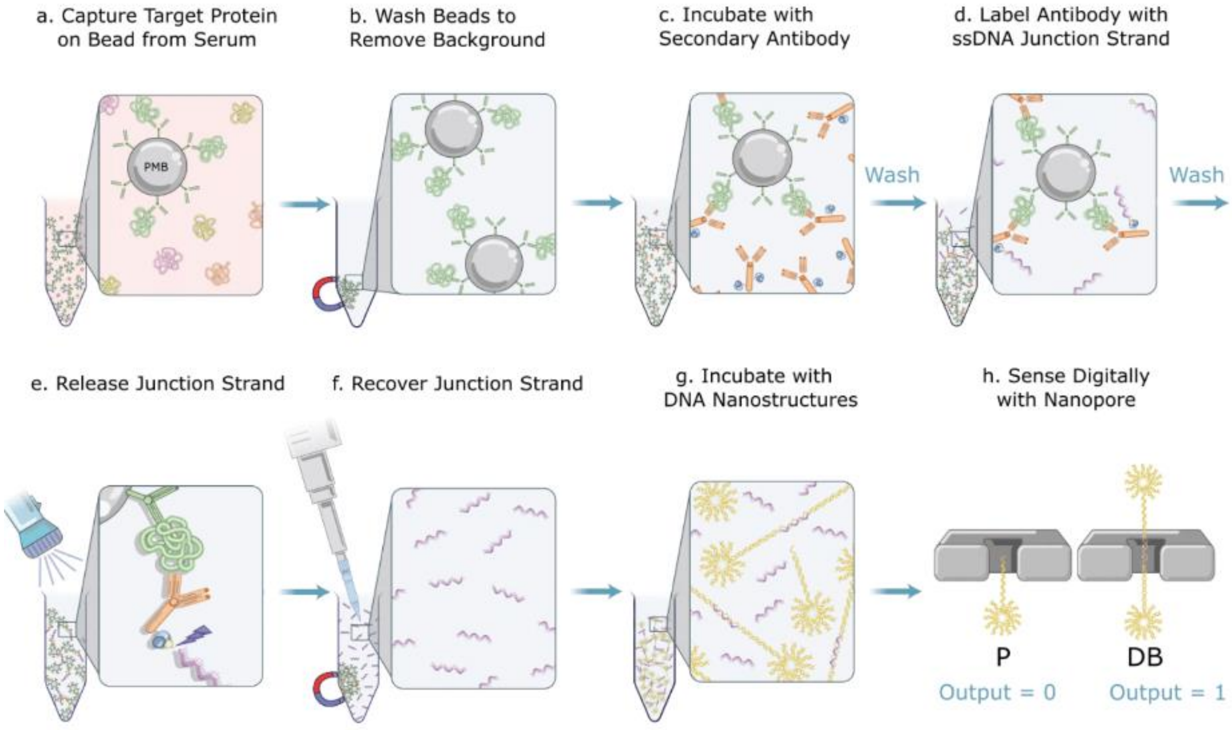

Figure 1.31. Bead-based ELISA on nanopores. (a-c) The steps of bead-based sandwich assay. **(d)** A 50 nt long ssDNA junction strand with a photocleavable linker is added, it binds to the detection antibody through biotin-streptavidin interaction, serving as the reporter molecule. **(e-f)** The reporter molecule (junction strand) is UV released and the supernatant containing the junction strand is collected. **(g)** The

probes are added to the solution containing the recovered junction strand from **(f)** The probes undergo shape transformation with the presence of the junction strand. **(h)** The final product is sensed on a nanopore. [Image taken from *Digital Immunoassay for Biomarker Concentration Quantification using Solid-State Nanopores* (Nat. Comm., 2021) with permission][114]

Ideally the linker strand recovered from the assay is at a 1 to 1 ratio with the protein of interest, so that the concentration of the target protein is simply the concentration of the linker strand. The DNA nanostructured probes are designed in such a way that with the presence of a linker strand, they will bind and form a different structure, which is easily distinguishable from the probe itself (with report ssDNA molecule unbound). Since the probes are added at a fixed concentration, the concentration of the target protein is then proportional to the fraction of binding events. In Chapter 4, I will present in more detail our approach to digitally detection using nanopores, as well as how an amplification scheme can be implemented to extend the LoD into femtomolar range with a single nanopore.

Chapter 2 – Nanopore Characterization of Multi-Way Junction DNA Nanostructures

This chapter is published as:

Fast Capture and Multiplexed Detection of Short Multi-Arm DNA Stars in Solid-State Nanopores

Liqun He,* Philipp Karau,* Vincent Tabard-Cossa

Department of Physics, University of Ottawa, Ottawa, ON, Canada

* These authors contributed equally

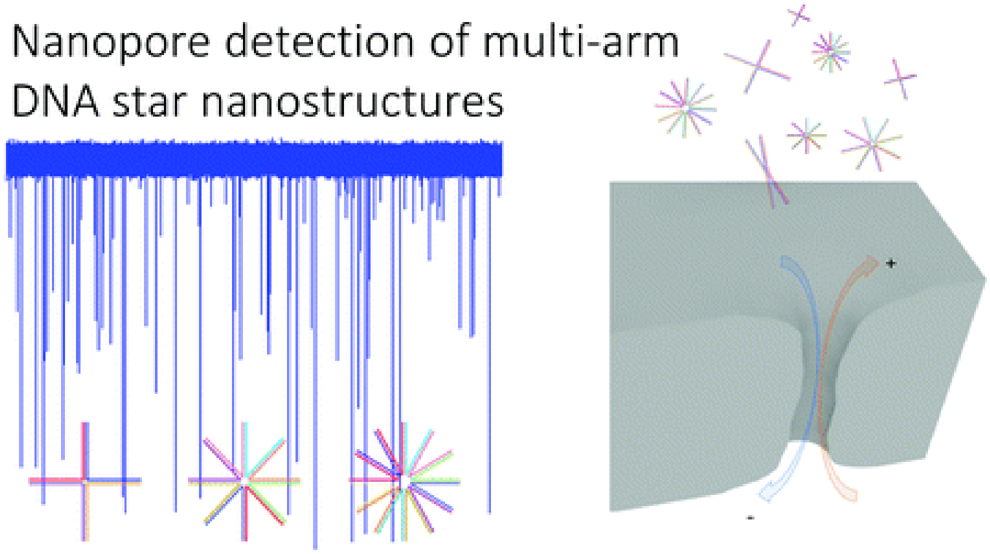

Adapted with permission from [L. He, P. Karau, and V. Tabard-Cossa, “Fast capture and multiplexed detection of short multi-arm DNA stars in solid-state nanopores,” *Nanoscale*, **11**, 16342, 2019]

Abstract

Fast and multiplexed detection of low-abundance disease biomarkers at the point-of-need would transform medicine. Nanopores have gained attention as single-molecule counters to electrically detect a range of biological molecules in a handheld format, but challenges remain before diagnostic applications can emerge. For solid-state nanopore sensors, the specificity of the ionic current signatures and the rate of target capture required to simultaneously recognize and rapidly count a mixture of molecular targets in a complex sample are active areas of research. Herein, we study the capture and translocation characteristics of short *N*-arm star shaped DNA nanostructures to evaluate their potential as a family of surrogate label molecules for biomarkers of interest designed for fast and reliable multiplexed detection based on conductance blockages. Simple hybridization of a varying number of short, easily synthesized, 50bp ssDNA strands allows the number of arms in the star shape DNA to be controlled from $N = 3$ to 12. By introducing more arms to the nanostructures, we show that we can controllably increase the nanopore signal-to-noise ratio for a range of pore sizes, producing conductance blockages which increase linearly with the number of arms, and we demonstrate conductance-based multiplexing through simultaneous detection of three such nanostructures. Moreover, the increased molecular signal strength facilitates detection under salt concentration asymmetries, allowing for a capture rate enhancement of two orders of magnitude without compromising the nanopore temporal and ionic signals. Together these attributes (strong signal, multiplexing potential and increased counting rate) make the *N*-arm star DNA-based nanostructures promising candidates as proxy labels for the detection of multiple biomarkers of interest in future high sensitivity single-molecule solid-state nanopore-based assays.

2.1 Introduction

Advances in medicine demand the development of high-performance detection technologies for the rapid, sensitive and accurate quantification of disease biomarkers.[112] Of the emerging single-molecule platforms, electrical nanopore sensing is a promising technology that is amenable to miniaturization, and can democratize single molecule detection, by moving from a centralized core laboratory to a more rapid, mobile testing on site. Nanopores inherently sense individual molecules electrically by electrophoretically capturing and translocating one molecule at a time while measuring the changes in ionic current through the nanopore. Whereas this concept has been demonstrated in the form of a hand-held DNA sequencer,[115,116] several hurdles still need to be overcome for the detection of various disease biomarkers (e.g. proteins, RNA), and in particular for the development of quantitative bioassays from complex clinical samples.

On the solid-state nanopore platform, one such challenge is achieving the high specificity required to distinguish targets of interest in a complex mixture. To tackle this issue, different assay schemes have been proposed in recent years,[117–123] primarily based on the use of long linear DNA fragments acting as carriers for specific receptors or bulky side attachments labels located at different position along its length, so as to produce unique barcoded electronic signatures for each targets. [68,69,86,124–128] Alternatively, as in many optical-based bioassays,[107] the use of surrogate labels linked to high affinity receptors (e.g. nucleic acid probes complementary to a region of a DNA or RNA target or detector antibodies specific to a protein), in place of the direct detection of the biomarker of interests may be advantageous to improve the nanopore sensing performance.[107,112] Indeed, solid-state nanopore sensors would benefit from advanced labels engineered so as to be detected more accurately and rapidly than for example free proteins or mRNAs, and to produce more robust and easily distinguishable signatures from other background molecules.

DNA-based nanoparticles assembled from hybridized ssDNA strands have previously been studied with solid-state nanopores and have shown promise as advanced labels towards this type of goal. Nevertheless, operating conditions for achieving a 2-plex multiplexing levels were stringent, requiring a fixed pore size that restricted full translocation, thus limiting the utility of these structures for the development of versatile nanopore-based bioassays[65]. Recently, we characterized the translocation characteristics of a short 3-arm dsDNA branched structure, as an improved label candidate over linear 50bp dsDNA, which allowed operation of the nanopore sensor at a higher detection rate while limiting the passage speed so as to permit reliable detection over a wide range of pore sizes and improving the signal-to-noise ratio (SNR).[129] Here, building from this previous work, we describe the capture and translocation kinetics of short N-arm star shaped dsDNA structures[130] (N = 3, 4, 6, 8, 12). By introducing more arms to the star-shaped nanostructure design, we show that we can linearly increase the SNR so as to further improve specificity of the nanopore signal and more importantly enable conductance-based multiplexing while simultaneously enhancing the detection rates (i.e. capture rates of resolvable events) for a range of pore sizes.

2.2 Results and Discussion

2.2.1 Star Shape Results

We studied four star-shaped nanostructures, with different numbers of short 25bp essentially rod-like arms. Their assembly strategy is described in the Experimental section. **Figure 2.1**a shows the different multi-arm nanostructures (*N* = 4, 6, 8, 12) that were assembled and characterized by solid-state nanopore ranging in size from 4 nm to 13 nm on nominally 12 nm thick SiN_x membranes. Their sequences are available in Section 2.3.1.

The majority of DNA nanostructures are correctly assembled, as demonstrated by the gel electrophoresis results presented in **Figure 2.1**b. However, as expected thermodynamically, the likelihood of misassembly increases with the number of arms in the nanostructure. In particular, for the 12-arm star structure, faint streaking and faster migrating bands can be observed (see Section 2.3.2 **Figure 2.7**c), indicating that a significant portion can be misassembled (between 10-50% depending on the batch). This is confirmed following a gel band purification method (see Section 2.3.2) to remove partially formed structures for the 12-arm star. Therefore, results shown below for the *N*-arm stars are for batches featuring low levels (<20%) of misassembled nanostructures or from purified samples.

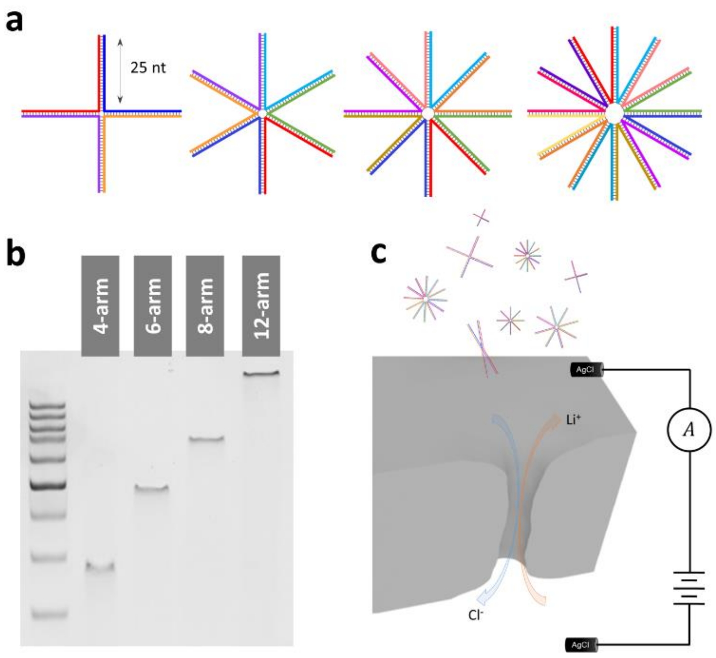

Figure 2.1. Schematic representation and gel electrophoresis of multi-arm stars. **(a)** Schematic of the multi-arm star nanostructures, from left to right: 4-arm, 6-arm, 8-arm, and 12-arm. **(b)** Gel electrophoresis of DNA stars (25 ng loaded) using Bio-Rad 5% precast polyacrylamide in 0.5x TBE. The ladder GeneRuler 100 bp DNA Ladder (Thermo Scientific, SM0241) shows at the bottom the 200 bp band. **(c)** Schematics of the nanopore setup. Typical operating condition, involved pore ranging from 4 to 13 nm, immersed in 3.6 M or 2.8 M LiCl pH8, with the ionic current signal recorded at an applied voltage typically ranging from 200 to 300 mV with a Chimera VC100 amplifier operated at 1 MHz bandwidth (4.17 MHz sampling rate). Analysis was typically performed after Bessel filtering at 500 kHz bandwidth to reduce high frequency noise and facilitate event detection and level fitting.

Once assembled, the DNA nanostructures are immersed in 3.6 M or 2.8 M LiCl pH8 and electrophoretically captured with an applied voltage of 200 or 300 mV, as depicted in **Figure 2.1**c, unless otherwise noted. **Figure 2.2** shows the resulting translocation characteristics (maximum blockage depth and dwell times) through 9.0, 9.5 and 11.5 ± 0.5 nm pores for the 4-arm, 8-arm, and 12-arm dsDNA star shape molecules respectively (data for the 6-arm DNA star is available in Section 2.3.3). While the translocation of nanostructured DNA molecules can produce event signatures with multiple sub-levels[126,129,131] depending on the orientation of the arms during translocation (see Section 2.3.3), here we focus on extracting the maximum blockage depth of a given event, i.e. the deepest level fitted by our analysis algorithm (see Section 2.2). To compare results between experiments performed on different pores with potentially different effective length, applied voltages and solution conductivities, we normalize the measured maximum blockage by the mean blockage produced by the passages of 2 kbp linear dsDNA fragments. This calibration of the blockage level of single-file dsDNA was done on every pore, before running the DNA nanostructures. It follows that to first order, the blockage level of one dsDNA fragment is equal to 1, and that of two non-interacting dsDNA fragments simultaneously spanning the pore is equal to 2, and so on.

In addition, while many events are relatively fast, ca. 10 μs, if the applied voltage is kept below 300 mV, they appear to be all detected by the bandwidth of our recordings, which has a typical response time of ~1 μs. However, sub-levels within events may not all be resolved especially if they are short-lived. Furthermore, these events are fully translocating rather than just colliding with the nanopore, as a decrease in passage times is observed with increasing voltage for the range of pore sizes and the different DNA nanostructures studied here (data shown in **Figure 2.8** in Section 2.3.2 and **Figure 2.14** in Section 2.3.5). Indeed, unlike more rigid DNA structures previously studied, which require a certain applied voltage threshold in order to locally bend and squeeze through the nanopore,[65] these *N*-arm star structures are more easily compressible since the arms can rearrange to facilitate translocation.

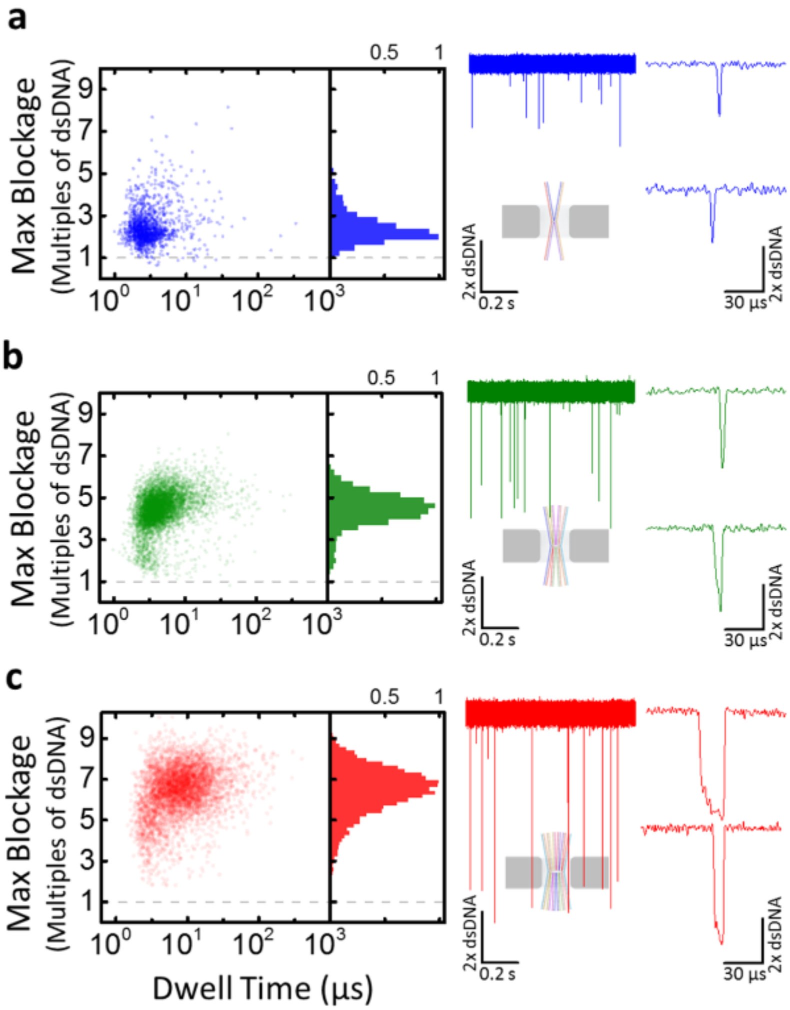

Figure 2.2. Scatter plots of 4-arm (blue), 8-arm (green) and 12-arm (red) individually. (a) Scatter plot of maximum blockage *versus* dwell time, histogram of the maximum blockage distribution, and representative 1 s current trace for 4-arm structure (unpurified) using a 9 nm pore at 200 mV. **(b)** For 8-arm (unpurified) using a 9.5 nm pore at 200 mV. **(c)** For 12-arm (purified) using an 11.5 nm pore at 200 mV. All experiments are performed in 3.6 M LiCl pH 8.0, except for the purified experiments performed in 2.8 M LiCl. Horizontal grey dash line represents the measured level of a single-file dsDNA molecule. Displayed current traces and events are filtered at 900 kHz.

The 4-arm star (**Figure 2.2**a) shows a mean blockage of 2.2 ± 0.5 multiples of dsDNA blockage (extracted from Gaussian fit). This is ~2x deeper than the unfolded blockage of a linear fragment of dsDNA. The 8-arm star (**Figure 2.2**b) shows a mean blockage of 4.5 ± 0.7 multiples of dsDNA blockage. This is ~4x deeper than the unfolded blockage of a linear fragment of dsDNA. A low number of events (< 6.5%) exhibit a faster passage time and a shallower blockage amplitude, which we attribute to incomplete assembly of the nanostructures. The 12-arm star (**Figure 2.2**c) shows a mean blockage of 6.7 ± 0.8 multiples of dsDNA blockage, more than 6x deeper than linear dsDNA, leading to a remarkable SNR of >10 at 500 kHz bandwidth. This nanostructure, while purified, also displays a fraction of events (~7%) with faster passage times and shallower blockage levels. We attribute these events to low amounts of partly assembled nanostructures remaining in the purified sample (e.g. nanostructure with missing strands) rather than collisions of the star-shaped DNA with the pore due to steric hindrance or attenuated events by the response time of our measurements system. This is supported by further experiments shown in Section 2.3.2, which show that the number of low-level events is dramatically reduced following purification, and that these events can by increasing the applied voltage for a range of pore sizes.

All blockage depth histograms were fitted with a single peak Gaussian to extract the mean maximum blockage. The resulting mean maximum blockage depth as a function of number of arms in the star-shape DNA nanostructures is shown in **Figure 2.3**a. These results are averaged over 58 experiments performed on 30 pores and are comprised of ~10^6 single-molecule events. As expected, the mean maximum blockage depth shifts to larger values as the number of arms increases. It appears to follow a linear trend, as is expected from simple considerations of the geometric properties of the number of dsDNA arms inside the pore and their configuration during translocation. On average, the 4-arm, 6-arm, 8-arm and 12-arm stars produce blockages of 2.1 ±

0.2, 3.5 ± 0.3, 4.5 ± 0.3, 6.4 ± 0.4 multiples of dsDNA blockage respectively. We attribute these maximum blockage values and the spread in their distribution to the number of possible molecular conformations of the arms during translocation. Using this simple geometric argument, it follows that the 4-arm star must be translocating primarily in a 2-arm/2-arm configuration, with some events oriented 3-arm/1-arm. We note that the largest number of arms in any configuration defines the maximum blockage observed, so that a 3-arm/1-arm orientation would provide the same maximum blockage amplitude as molecule oriented 1-arm/3-arm. This is particularly clear for the 4-arm case translocating sub-6 nm nanopores, where the kinetics are slower, the conformations more restricted, and discrete orientations forced, allowing us to resolve quantized sublevels for all translocation signatures (see Section 2.3.3 **Figure 2.11**). Unfortunately, we cannot fully resolve all the multiple sub-levels on all pores, especially when the number of arms increases, since larger pores are used, resulting in faster kinetics of passage.

Consistent with this picture, the distribution of 12-arm star is composed of a larger superposition of the maximum number of arms during translocations, including a majority 6-arm/6-arm configuration, but also 7-arm/5-arm, and so on, with the size of the pore restricting the maximum number of arms in the pore at the same time and therefore the observed spread in the distribution. For example, the 11.5 nm pore of **Figure 2.2**c shows nanostructures oriented in a 9-arm/3-arm configuration for the high tail end of the distribution, while an 8.8 nm pore in supplementary **Figure 2.8**a shows a tighter distribution, fitting at maximum nanostructures oriented in an 8-arm/4-arm configuration. In support of this, **Figure 2.10** shows that multiple quantized sub-levels can be observed in some of the 12-arm events, in particular those lasting longer than ~10 μs, where enough data points are present to resolve them. Furthermore, the observed spread in the distribution of the maximum blockage is also affected by the quality of the fits during analysis and by the ability of our measurement system to resolve the deepest level, in particular for those fast events < 10 μs. Therefore, while we expect the lowest observable value of the maximum blockage of an *N*-arm star to be *N*/2, a small fraction (~4%) of events below this minimal expected value can be seen in the scatter plots of **Figure 2.2**c and are attributed to inaccurate fits, unresolved sublevels, or misassembled structures. These different cases are highlighted in **Figure 2.10** in Section 2.3.2.

Figure 2.3b shows the mean maximum blockage depth for different pore sizes. For a given *N*, the measured mean maximum blockage is consistent for the relatively large range of pore sizes studied here, with a coefficient of variation of less than 21% for the different star-shape molecules. The minimum pore size used is often limited by the physical size and deformability of the star-shape DNA nanostructures.

The results in **Figure 2.3** highlight the robustness of the maximum blockage signals produced for these nanostructures for a wide range of pore sizes and show clearly distinguishable blockage levels for the different arm counts. As such these DNA nanostructures are good candidates for multiplexed detection based on conductance blockages.

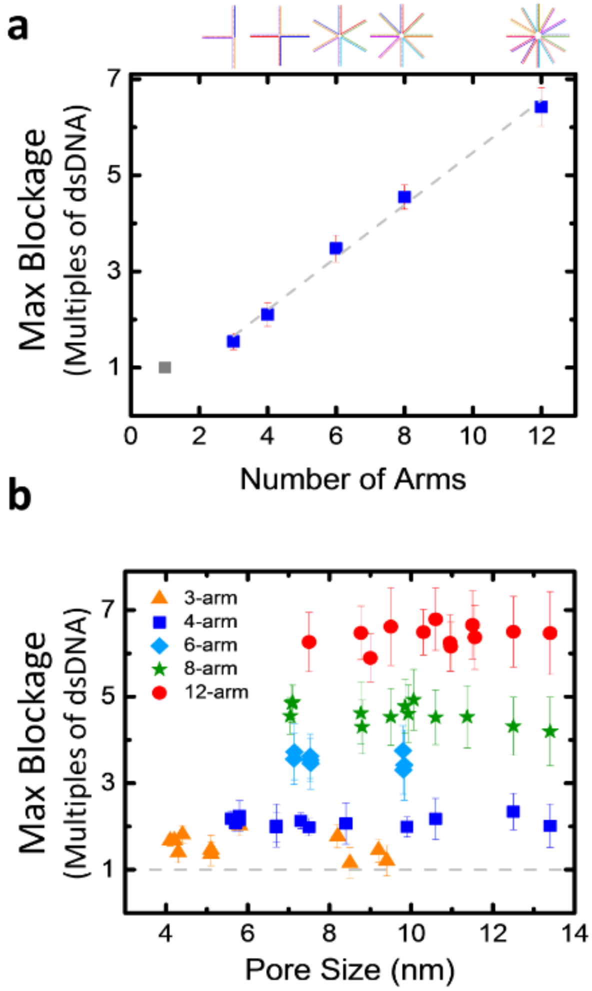

Figure 2.3. Mean maximum blockage of star-shaped DNA nanostructures. (a) Mean maximum blockage of 3-arm, 4-arm, 6-arm, 8-arm and 12-arm stars as a function of the number of arms. Grey dash line is a fit to the N-arm data points. **(b)** Mean maximum blockage of 3-arm (n= 11), 4-arm (n=13), 6-arm (n=9), 8-arm (n=13) and 12-arm (n=12) stars as a function of pore size. The error bars represent the standard deviation of the Gaussian fit. Data collected in either 3.6 M or 2.8 M LiCl pH8. Horizontal grey dash line represents the expected level of a single-file dsDNA molecule.

2.2.2 Mixtures of DNA structures

A major challenge in single-molecule detection with solid-state nanopores lies in the reliable distinction of multiple different analytes in a mixture. Previous studies have demonstrated multiplexing by dwell time,[125,132] event shape,[68,97,124] and by blockage depth.[65] Each of these strategies come with their own set of advantages and drawbacks. While dwell times (when not too fast so as to be fully resolved) can be very precisely determined on a per-event basis, the wide distribution of the ensemble of passage times for a given molecule limits the number of molecules that can be differentiated. In particular for linear dsDNA, fragments need to be >1kbp apart to be distinguished unless a very precise pore size is used[133] or the conformation of the polymers controlled[132].

Differentiating molecules according to the event shape has the advantage of potentially removing this constraint by allowing the overall length of the molecules to be similar, while adding small side branches along its length at precise locations to produce unique barcoded event signatures. This strategy possesses a high multiplexing potential and can be independent of any pore characteristics, as long as the barcodes on the carrier molecule can be resolved, but it is highly susceptible to the noise level and bandwidth of the ionic current measurements as well as the transport kinetics and the folding state of the carrier molecule.[134] A more straightforward method, when low levels of the multiplexing are acceptable, lies in the distinction of electrical signatures based purely on their blockage depths. This can be achieved using different strategies for molecular assembly, as presented in previous studies.[65,126,129]

In order to explore the multiplexing potential of these nanostructures, we first recorded the ionic current signal from a mixture of 4-arm and 8-arm stars translocating a 9 nm pore immersed in 3.6M LiCl. **Figure 2.4**a shows the results of this 2-plex measurement. Prior to running the mixture experiment, the pore dimensions were calibrated using 2 kbp linear dsDNA as a molecular ruler. It was then flushed out with fresh solution and the 8-arm star alone was introduced to characterize the signature of the translocation events in order to facilitate analysis of the subsequent mixture experiment. Analysis of this control experiment revealed the presence of a clear peak with a mean maximum blockage depth of 4.5 ± 0.6 multiples of dsDNA as expected from **Figure 2.3**. The scatter plot of the maximum blockage versus dwell times for each event also shows the presence of very few shallow events (<5%) from misassembled nanostructures of the unpurified 8-arms that would overlap with the signal from the 4-arm star. Note that in the normalized histogram plot, this sub-population of events is barely visible. Additional 2-plex results from different pores are shown in the Section 2.3.4 **Figure 2.12**.

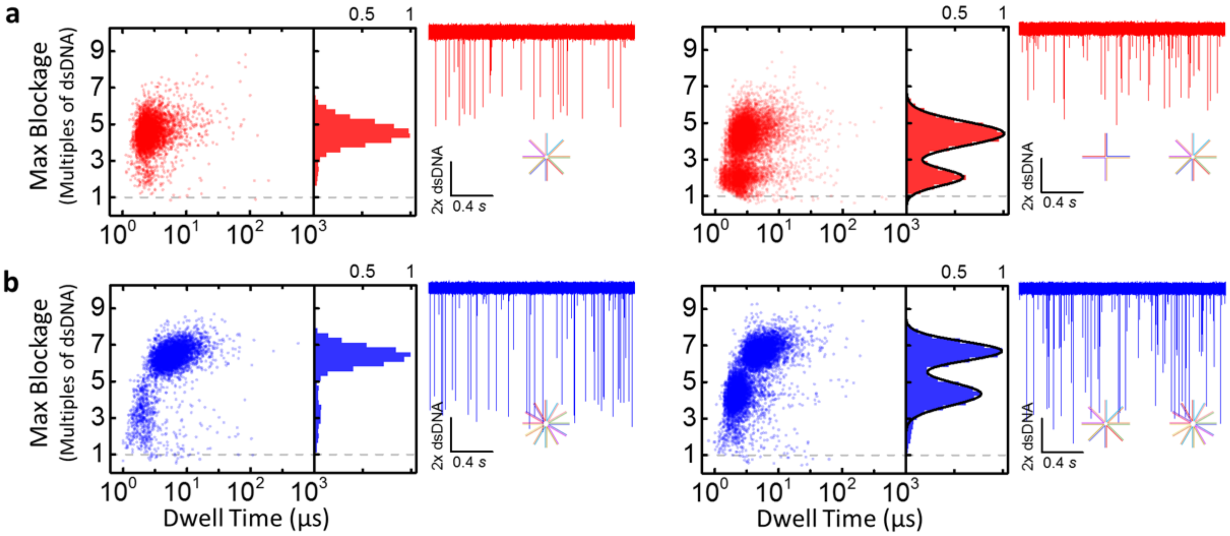

Figure 2.4. Scatter plots of 2-plexing experiments. (a) Scatter plot of normalized maximum blockage *versus* dwell time for the unpurified mixture of 4-arm and 8-arm stars using a 9 nm pore at 200 mV in comparison with the scatter plot of 8-arm alone on the left. **(b)** Scatter plot of normalized maximum blockage *versus* dwell time for the unpurified mixture of 8-arm and 12-arm stars using an 8.8 nm pore at 300 mV in comparison with the scatter plot of 12-arm alone on the left. Distributions of corresponding maximum blockage and 2 s current traces filtered at 900 kHz are attached to each scatter plots. Horizontal grey dash line represents the expected level of a single-file dsDNA molecule. Experiments are performed in 3.6 M LiCl, pH 8.0, and analyzed at 500 kHz.

The analysis of the 2-plex experiments each revealed two well-resolved peaks in the distribution of maximum blockage amplitude. These results show that we can distinguish with a confidence interval of 97% or better 4-arm from 8-arm, and 8-arm from 12-arm. This is achieved without purification of the DNA nanostructures by gel band excision and is anticipated to be further improved by removing the small percentage of overlapping events. Consequently, we increased the mixture complexity and performed multiplex experiments composed of 4-arm, 8-arm, and 12-arm, as well as 2kbp linear dsDNA fragments, to assess the ability of these nanostructures to be distinguished by our nanopore sensing system.

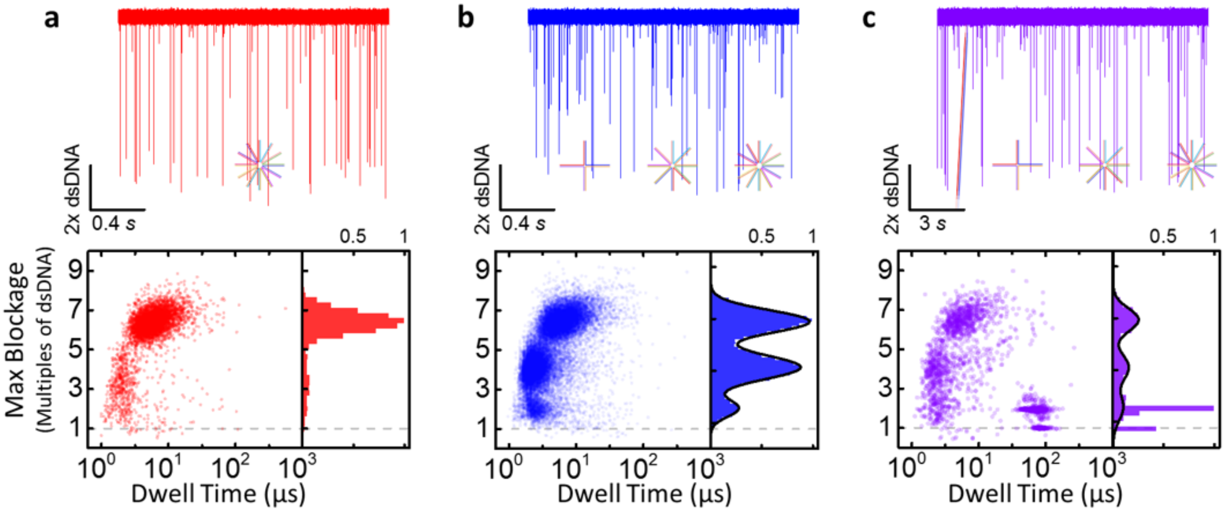

Figure 2.5. Scatter plots of mixtures of star-shaped molecules. (a) 2 s current trace of 12-arm star alone; Scatter plot of normalized maximum blockage *versus* dwell time for 12-arm alone (unpurified). **(b)** 2 s current trace of the mixture of 4-arm, 8-arm and 12-arm stars; Scatter plot of normalized maximum blockage *versus* dwell time for the mixture of 4-arm, 8-arm and 12-arm stars (all unpurified), with three distinguishable populations of 4-arm (n = ~2,500), 8-arm (n = ~10,000) and 12-arm (n = 10,000) stars. **(c)** 15 s current trace of the mixture of 2 kbp dsDNA, 4-arm, 8-arm and 12-arm stars; Scatter plot of normalized maximum blockage *versus* dwell time for the mixture of 2 kbp dsDNA, 4-arm, 8-arm and 12-arm stars, with four distinguishable populations of 2 kbp dsDNA (n = ~800), 4-arm (n = ~300), 8-arm (n = ~500) and 12-arm (n = ~800) stars. All experiments are performed in 3.6 M LiCl (pH 8.0), with 300 mV applied bias. Distributions of maximum blockage are attached to the scatter plots. Horizontal grey dash line represents

the expected level of a single-file dsDNA molecule. All current traces shown are filtered at 900 kHz and analyzed at 500 kHz.

Figure 2.5b, and **Figure 2.5**c show the results of this 3-plex and 4-plex experiment respectively. In both cases, three peaks in the maximum blockage depth histogram are observed, aligned with the expected values for the 4-arm, 8-arm and 12-arm stars. For the data in **Figure 2.5**b, using Gaussian fits to extract the mean and standard deviation of each star population, a mean blockage level of 6.5 ± 0.6, 4.1 ± 0.6 and 2.0 ± 0.4 multiples of dsDNA is obtained for 12-, 8-, and 4-arm stars respectively. The distributions of the 12-arm star and the 8-arm star intersect at 5.3x dsDNA, while the distributions of the 8-arm star and the 4-arm star intersect at 2.7x dsDNA. We can then calculate the confidence interval (CI) by dividing the mean-intersections distance with the standard deviation of each. In the 3-plex experiment, these results show that the 12-arm star can be distinguished from the rest with a CI > 95% and the 4-arm star can be distinguished from the rest with a CI > 85%. Furthermore, while the maximum blockade depths of the linear dsDNA fragment overlap with that of the 4-arm, the datasets can be easily separated by dwell time, since the translocation timescales differ by an order of magnitude between the various constituents of the mixture, as shown in **Figure 2.5**c, bringing the multiplexing level to 4.

Overall, these multi-arm star-shaped DNA nanostructures are able to provide a multiplexing level of up to 3, given their distinguishable conductance blockages, when using ~10 nm pore size in nominally 12 nm thick membranes immersed in LiCl. Nevertheless, accurate quantification of the mixtures above the 2-plex level, and in particular when employing the 12-arm, remains a challenge. This is in part due to the fraction of misassembled molecules for each nanostructure, which produce events with shallower blockage levels, with the consequence of having some overlap in the conductance blockage distributions for the different star molecules. This can be tackled by employing a gel band purification method to increase the purity of the fully formed nanostructures as describe in Section 2.3.2. We note that much of the variation in single-molecule counts between nanostructures is most likely a result of pipetting errors when handling small volumes (~μL) which can lead to significant uncertainty in the concentration of each star molecule. Future work will address these issues to extract quantitative nanopore concentration measurements from capture rate data and single-molecule counts of nanostructured DNA molecules.

2.2.3 Capture Rates

An added advantage of the deep conductance blockages provided by these star-shaped DNA nanostructures is to enable operation under reduced salt concentrations compatible with many biomolecular targets of interest, while maintaining a high SNR. In particular, when employing a salt concentration asymmetry across the membranes, one can gain a significant increase the nanopore capture rate. Wanunu *et al.*[37] first showed an improvement by up to 40-fold can be achieved for long linear 3,500 bp DNA molecules by applying a salt gradient factor of 30 (C_{cis} = 0.2 M KCl on the capture side and C_{trans} = 4 M KCl on the other side of the membrane), compared to the value measured under 1M KCl symmetric conditions. The potential outside of the nanopore mouth is proportional to the ratio of the bulk ion concentrations in the *cis* and *trans* chambers, therefore, the capture radius is also proportional to C_{trans}/C_{cis}.[37] There is a higher voltage drop in the solution of lower conductance, therefore, a C_{trans}/C_{cis} salt gradient will yield an asymmetric potential, thus a larger voltage drop in the *cis* side than the *trans* side when $C_{cis} < C_{trans}$. Studies have shown that asymmetric salt conditions (when C_{cis} is lower salt) promote capture, due to the increased external field E_{cis} on the *cis* side, while the opposite is true for capture-opposing conditions, where C_{cis} is higher salt.[135,136] Charron *et al.* showed that the external field E_{cis} increases monotonically with C_{trans}/C_{cis}; and translocation time increases with C_{trans}/C_{cis} due to the effective pulling force decreasing monotonically with C_{trans}/C_{cis}. [135] Fast capture is of particular importance when trying to quantitate low abundance molecular targets, to speed up the detection of a statistically relevant number of copies, and thus lower the limit of detection for a fixed assay time. Here, we demonstrate that the capture rate of the 12-arm DNA star can be increased by >200-fold compared to the symmetric 3.6M LiCl case, for the range of pore size and applied voltages used. **Figure 2.6**a-d shows representative current traces with the number of single-molecule events increasing by ~5,000x with rising salt concentration ratio from 0.2 (corresponding to a C_{cis} = 3.6M LiCl and C_{trans} = 0.72M LiCl, in which the salt gradient hinders capture) to 20 (corresponding to a C_{cis} = 0.18M LiCl and C_{trans} = 3.6M LiCl, in which capture rates are enhanced). The data show that deep blockage levels and high SNR of the 12-arm star are maintained throughout the salt concentration ratio sweep. **Figure 2.6**e shows the concentration-normalized capture rate enhancement as a function of the salt concentration gradient C_{trans}/C_{cis}. Using a 20-fold salt concentration gradient between the capture side (C_{cis} = 0.18 M) and the translocating side (C_{trans} = 3.6 M) of the membrane, a capture rate of R_c = 30.5 Hz/nM is achieved for the 12-arm star, in comparison to R_c = 0.13 Hz/nM in symmetric salt (C_{cis} = C_{trans} = 3.6 M). This 235x increase in capture rate is somewhat surprising, and similar enhancement factors have been observed on multiple nanopores (see **Figure 2.13**). It is an order of magnitude larger than predicted by the proposed capture model of Wanunu *et al.*[37], which explains the physical origin of the capture rate enhancement under salt asymmetry. Their model states that the ratio of electric fields outside the pore is expected to scale with the ratio of the conductivities of the electrolyte solutions, which to first order can be approximated by the salt concentration, *i.e.* $E_{\mathrm{asym}}/E_{\mathrm{sym}} = \sigma_{trans}/\sigma_{cis} \approx C_{trans}/C_{cis}$. We speculate that the additional 10-fold enhancement observed in our data is a result of the nature of the multi-arm DNA nanostructures used here. Indeed, the existing theoretical framework applies to linear DNA in the diffusive capture regime, whereas the physics of the capture process for these DNA nanostructures are clearly different. In particular, the transition between the barrier limited capture regime[37] and the diffusion-limited capture regime is less clear, and the effects of electroosmotic flow may be more pronounced since the star structures likely sample the entire volume of the pore. We hope that this unexpected deviation in behavior between the multi-arm star structures and linear dsDNA will inspire theoretical work dedicated to understanding how the topology of these nanostructures affects nanopore capture and translocation kinetics. Because of this additional capture rate enhancement, DNA star nanostructures can in principle be detected in the picomolar concentration range under reasonable measurement time using a salt concentration gradient.

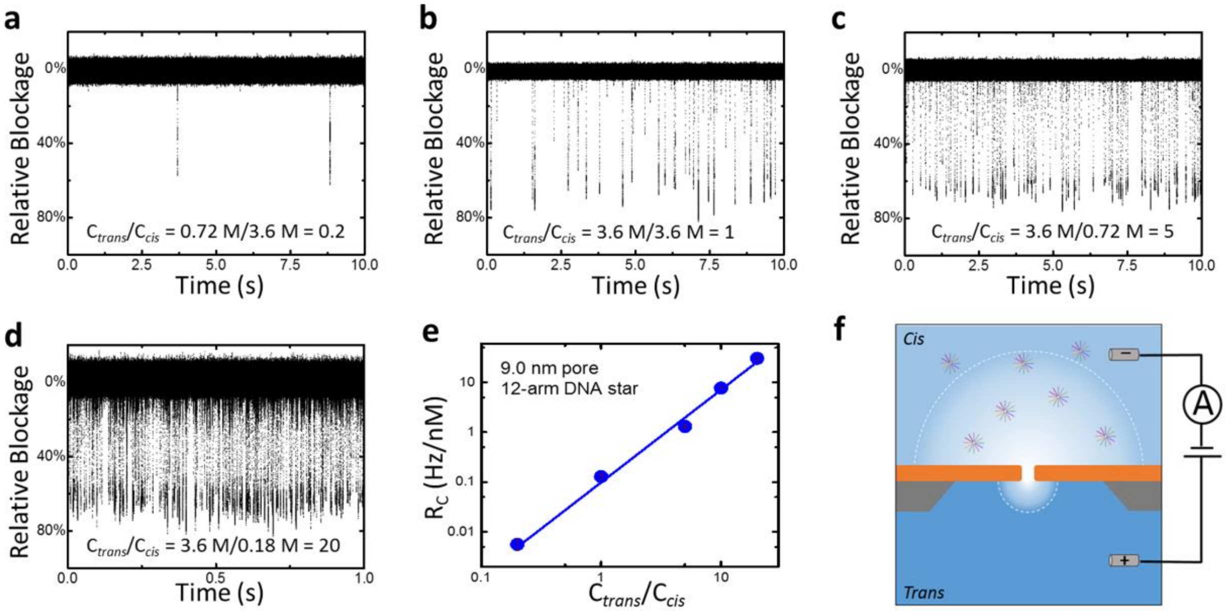

Figure 2.6. Capture rate improvement for the 12-arm star. (a-d) Current traces of 20 nM 12-arm star in asymmetric salt conditions (LiCl) with concentration-normalized capture rates from: 0.0056 Hz/nM to 30.5 Hz/nM. All current traces are displayed at 500 kHz. **(e)** Capture rate as a function of salt gradient (C_{trans}/C_{cis}) on a log-log scale. **(f)** Schematic of nanopore and translocations of 12-arm star molecules in asymmetric salt conditions. Experiments are performed at 200 mV using a 9.0 nm pore with an effective thickness of 12.5 nm.

Interestingly, in high C_{trans}/C_{cis} conditions, while significantly enhancing the capture rate, the kinetics of translocations are also affected.[137,138] This increase in passage times in asymmetric salt has previously been reported for linear dsDNA.[37,139,140] Here, an average 5-fold increase in translocation time is observed, which offers an improved time resolution that facilitates analysis (see Section 2.3.5 **Figure 2.13**b). For the particular experiment shown in **Figure 2.6** on a 9.0 nm pore at 200 mV, the 12-arm stars translocated with a mean passage time of 8.5 ± 1.6 μs under the symmetric case, $C_{cis} = C_{trans} = 3.6$ M, while the mean passage time was increased to 25.1 ± 2.2 μs under the asymmetric condition $C_{cis} = 0.18$ M and $C_{trans} = 3.6$ M. Similar improvements are obtained for different nanopore sizes, and for different DNA star molecules (see Section 2.3.5 **Figure 2.13**).

2.3 Conclusions

We have investigated the capture and translocation characteristics as well as the multiplexing capability of DNA-based multi-arm nanostructures to evaluate their potential as a class of molecules that could serve as advanced labels engineered for improved solid-state nanopore sensing performance. The translocation characteristics of 4-, 6-, 8-, and 12-arm star shaped DNA were studied with 30 different nanopores ranging in size from 4 nm to 13 nm, producing unique deep electrical signatures for all four nanostructures. The observed maximum blockage follows a predictable trend that is readily explained by the molecular geometry during passage through the nanopore. We demonstrated that these DNA nanostructures can be used to perform a 3-plex detection in a mixture by relying on their distinct maximum conductance blockages. Finally, the increased SNR is leveraged by operating the nanopore under salt concentration asymmetry to enhance the observed capture rate of the multi-arm DNA stars by two orders of magnitude compared to the symmetric case, opening up interesting future biosensing applications related to the rapid and multiplexed detection of low abundance disease biomarkers.

2.4 Experimental Methods

2.4.1 Nanopore Fabrication

Nanopores are fabricated using controlled breakdown (CBD)[13], in nominally 12 nm thick SiN_x membranes supported by a silicon support structure in either 3 mm or 5 mm chip format (Norcada Inc, NT005Z and NPBX5004Z). Before assembly in a custom fluidic flow cell, the membranes are painted with a layer of polydimethylsiloxane (PDMS) to reduce the device capacitance[141]. The chips are cleaned using air plasma for 20 s at 30 W. CBD is performed in 1 M KCl buffered with 10 mM $NaHCO_3$ at pH 8 using custom instrumentation controlled with LabView software. Following dielectric breakdown, the pore is conditioned to the desired size using a series of voltage pulses (±3.5 V square pulses with 8 s period). After changing the electrolyte solution to 3.6 M LiCl buffered with 10 mM HEPES at pH 8 ($\sigma = 16.1$ S/m), the pore size is extracted from the measured value of the pore conductance, G, as determined by I-V measurements obtained by applying voltages ranging from -500 mV to +500 mV and performing a linear fit of the resulting curve. Assuming cylindrical geometry and accounting for access resistance, the pore diameter can be extracted from the slope of the linear fit using:[29]

$$G = \sigma\left[\frac{4h}{\pi d^2} + \frac{1}{d}\right]^{-1}$$

where σ is the solution conductivity, h the effective height of the membrane at the pore, and d the effective pore diameter.

2.4.2 Structure Assembly

Four different designs of short multi-arm DNA structures have been assembled (**Figure 2.1**a). The nanostructures rely on complementary base-pairing of different ssDNA oligos for assembly (see Section 2.3.1 for their sequence). In this design, each 25 bp arm is formed by hybridizing 50 nt oligos between two adjacent arms, as shown schematically in **Figure 2.1**a. DNA were purchased from Integrated DNA Technologies (IDT). DNA sequences have been adapted from Wang *et al.*[130] Oligos are mixed in 1:1:…:1 ratio and the mixture is heated to 90 °C for 5 minutes, then slowly cooled at a rate of 0.2 °C/min. The resulting solution is run on a 5% PAGE gel (Bio-Rad 5% precast polyacrylamide gel) to confirm correct assembly. A single band is interpreted as correct assembly of the majority of the product and the solution is used without further purification unless otherwise noted (**Figure 2.1**b and Section 2.3.4 **Figure 2.9**c). Purification by gel band excision, as described in Section 2.3.4, is recommended for improving the detection of nanostructures in a mixture.

2.4.3 Nanopore Sensing

Sensing of DNA star shape molecules was performed in 3.6M LiCl buffered with 10 mM HEPES at pH 8 with applied voltages ranging from 200 to 400 mV, except for purified molecules which were performed in 2.8 M LiCl pH8. A high molarity LiCl salt was chosen so as to produce longer lasting translocations than in KCl, while also effectively shielding the pore surface charges.[142] The applied voltage range was limited by the maximum current readout of the current amplifier under these experimental conditions. Samples were introduced on the *cis* side of the chip (membrane side) with the *trans* side grounded (etch pit side), and a negative voltage was applied to the *cis* side

(**Figure 2.1**c). The current recordings were performed using the Chimera VC100 (Chimera Instruments) with a sampling frequency of 4.17 MHz and a bandwidth of up to 1 MHz. In this study, we show results acquired on multiple pores (n = 30) ranging in size from 3.6 ± 0.1 (2.5 nm for linear dsDNA) to 13.4 ± 0.3 nm. The uncertainty is calculated from the uncertainties of the effective thickness of the membrane as shown in the Section 2.3.6 and the standard deviation of the baseline current.

2.4.4 Data Analysis

Translocation events in the recorded current traces were located and fitted using the ADEPT algorithm implemented in MOSAIC[143,144] (https://pages.nist.gov/mosaic/). The details of the analysis can be found in Karau *et al.*[129]. For all data shown here, events are fitted and the maximum blockage is detected with a digital lowpass filter set at 900 kHz or 500 kHz depending on the SNR (an event is called when a point in the current trace deviates from the local mean by a minimum of 6x the local standard deviation).

2.5 Supplementary Information

2.5.1 Assembly and Sequences for Star-shaped Structures

Following Wang *et al.* [130] the sequences for the N-arm star nanostructures are:

4-arm star:

strand 1	5'	GTGTCTTGAAGAAGGACCAGGGAACGTATTTGCCTTGTCTGGGAAATCGT	3'
strand 2	5'	ACGATTTCCCAGACAAGGCAAATACGGACTTATCGTTTGCTAATACTACA	3'

strand 3	5'	TGTAGTATTAGCAAACGATAAGTCCCCAACTGGTTGTGGCCTATCGAAAA	3'
strand 4	5'	TTTTCGATAGGCCACAACCAGTTGGGTTCCCTGGTCCTTCTTCAAGACAC	3'

Table 2.1. Sequences for 4-arm star.

6-arm star:

strand 1	5'	AGGCACAGCTATAATAACGCAATCCTCTCCGGCCTCAAACTACTTTACCT	3'
strand 2	5'	AGGTAAAGTAGTTTGAGGCCGGAGACCGAATGGAGTCTGTTCTCGACGCT	3'
strand 3	5'	AGCGTCGAGAACAGACTCCATTCGGACAATTACGAACCAACTTAGGACCT	3'
strand 4	5'	AGGTCCTAAGTTGGTTCGTAATTGTGGTCATCGTGGCGTACCATATACCT	3'
strand 5	5'	AGGTATATGGTACGCCACGATGACCTCTTCGATCTACCCGATAGGCTCCT	3'
strand 6	5'	AGGAGCCTATCGGGTAGATCGAAGAGGATTGCGTTATTATAGCTGTGCCT	3'

Table 2.2. Sequences for 6-arm star.

8-arm star:

strand 1	5'	AGGCACAGCTATAATAACGCAATCCTCTCCGGCCTCAAACTACTTTACCT	3'
strand 2	5'	AGGTAAAGTAGTTTGAGGCCGGAGACCGAATGGAGTCTGTTCTCGACGCT	3'
strand 3	5'	AGCGTCGAGAACAGACTCCATTCGGACAATTACGAACCAACTTAGGACCT	3'
strand 4	5'	AGGTCCTAAGTTGGTTCGTAATTGTGGTCATCGTGGCGTACCATATACCT	3'
strand 5	5'	AGGTATATGGTACGCCACGATGACCTCTTCGATCTACCCGATAGGCTCCT	3'
strand 6	5'	AGGAGCCTATCGGGTAGATCGAAGACGTACAGGTGTGACTTGAATTTGCT	3'
strand 7	5'	AGCAAATTCAAGTCACACCTGTACGAGTGTTAGAATACAACAAGCGACCT	3'
strand 8	5'	AGGTCGCTTGTTGTATTCTAACACTGGATTGCGTTATTATAGCTGTGCCT	3'

Table 2.3. Sequences for 8-arm star.

12-arm star:

strand 1	5'	AGGCACAGCTATAATAACGCAATCCTCTCCGGCCTCAAACTACTTTACCT	3'
strand 2	5'	AGGTAAAGTAGTTTGAGGCCGGAGACCGAATGGAGTCTGTTCTCGACGCT	3'
strand 3	5'	AGCGTCGAGAACAGACTCCATTCGGACAATTACGAACCAACTTAGGACCT	3'
strand 4	5'	AGGTCCTAAGTTGGTTCGTAATTGTGGTCATCGTGGCGTACCATATACCT	3'
strand 5	5'	AGGTATATGGTACGCCACGATGACCTCTTCGATCTACCCGATAGGCTCCT	3'
strand 6	5'	AGGAGCCTATCGGGTAGATCGAAGACGTACAGGTGTGACTTGAATTTGCT	3'
strand 7	5'	AGCAAATTCAAGTCACACCTGTACGAGTGTTAGAATACAACAAGCGACCT	3'
strand 8	5'	AGGTCGCTTGTTGTATTCTAACACTGCATCTCATACGGCAGTATCCGCCT	3'
strand 9	5'	AGGCGGATACTGCCGTATGAGATGCTGAGCACGGAACTGTCAACCTTGCT	3'
strand 10	5'	AGCAAGGTTGACAGTTCCGTGCTCACGTTCATTAAGATAAATCTGATCCT	3'

strand 11	5'	AGGATCAGATTTATCTTAATGAACGACTATGCCTGCTACATGCACTTCCT	3'
strand 12	5'	AGGAAGTGCATGTAGCAGGCATAGTGGATTGCGTTATTATAGCTGTGCCT	3'

Table 2.4. Sequences for 12-arm star.

2.5.2 Investigation of Shallow Events from 12-arm

For the 12-arm star nanostructure, a faster migrating streaking band is often present, indicating up to 45% of the portion could be misassembled depending on the production batch. This streaking band is less pronounced when a small mass of the 12-arm star is loaded into the gel (500 ng compared to 25 ng), due to the limitation in the resolution of the gel imaging device.

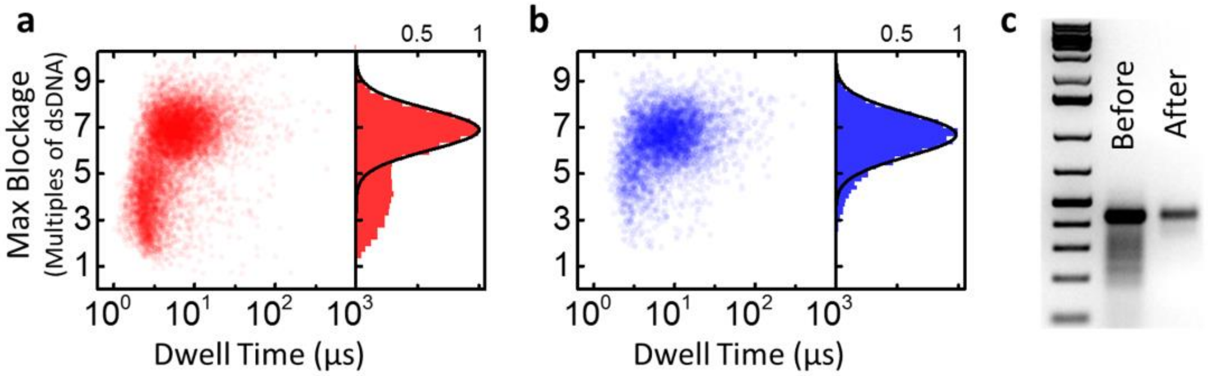

Figure 2.7. Purification results of 12-arm. (a) Scatter plot of unpurified 12-arm star showing 29% shallow events. **(b)** Scatter plot of purified 12-arm star with 7% shallow events. Both experiments are performed in LiCl pH 8.0, using the same pore of 11.5 nm in diameter with an applied bias of 200 mV. **(c)** Gel electrophoresis results in 2% agarose gel in 1xTAE, from left to right: GeneRuler 1 kb Plus DNA Ladder (Thermo Scientific, SM1331), 12-arm star following assembly, and 12-arm star after purification. On the ladder lane of the gel image shows from bottom to top: 200, 300, 400, 500, 700, 1000, 1,500 bp, etc.

Misassembled products account for the major portion of the shallow events observed (**Figure 2.4**b). **Figure 2.7**a shows the scatter plot of 12-arm star before purification showing 29% of such shallow events (extracted from the Gaussian fit of the histogram). The crude products can then be purified using a method described by Sun *et al.*[145], as commercial gel extraction kits have been observed to disassemble DNA origami structures. Briefly, the desired band is visualized using UV light and extracted from a 2% agarose gel. The excised band can be purified using the diffusion method as described by Alibakhshi *et al.*[65]. The gel image of the purified 12-arm shows that most of the streaking is removed in comparison to the unpurified 12-arm (**Figure 2.7**c).

Figure 2.7b shows the scatter plot of purified 12-arm star with only ~7% shallow events, indicating that the purification step significantly reduced the rate of shallow events. The remaining shallow events could be explained by a combination of factors such as the bandwidth of the recording device producing truncated events when the passage times are short and approaching the ~1 μs response time of our system, or the possibility of collisions of labels that do not fully translocate. However, the dramatic reduction in the shallow event rate after purification strongly suggests that these events are due to remaining misassembled products, as a faint streak can be still be seen on **Figure 2.7**c, either due to partial dissociation of nanostructures during or after the purification step or remaining misassembled products in the excised gel as due to the limitation of this manual band cutting step.

To further highlight the effect of the time resolution of our measurements system (nanopore device + sensing electronics) on the ability to detect these shallower events, we show translocation results from 4 additional pores ranging in size from 7.5 to 10.5 nm, each at two different voltages. The results shown in **Figure 2.8** demonstrate how some of the shallow events can be missed by our measurement system when the voltage is increased, and the passage times are faster than ~4 μs (before which events have not yet reached the full depth). In particular, data on the smaller 7.5 nm pore (**Figure 2.8**d) show a better-resolved distribution of shallow events compared to data acquired on larger pores. On that pore, when the voltage is increased, the shallow events are compressed around ~4 μs, the minimum timescale for our measurement system to not attenuate the depth of events, and where many are missed, much like in the other data sets. On the other hand, the events from the fully formed 12-arm products continue to show a measurable reduction in the mean passage time when the voltage in increased, as in the other data sets and as is expected.

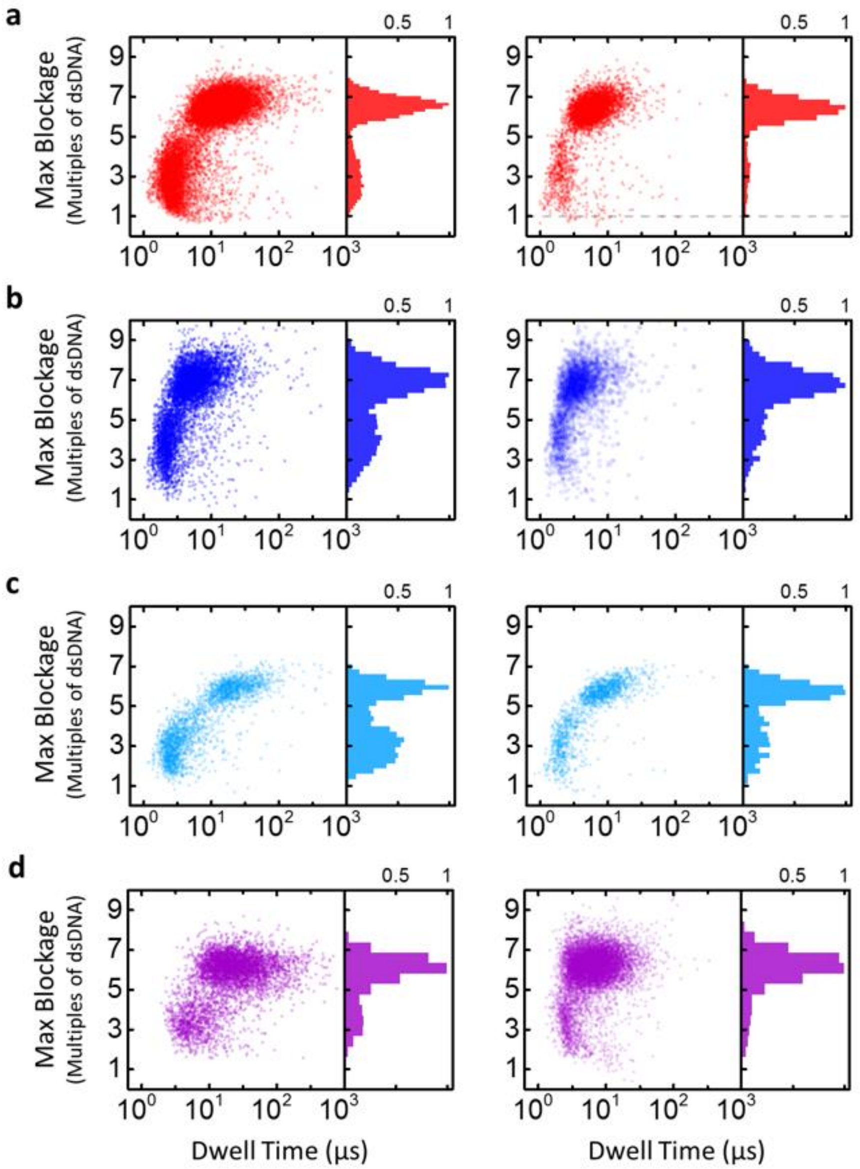

Figure 2.8. Scatter plots of 12-arm star. (a) Scatter plot of maximum blockage *versus* dwell time using an 8.8 nm pore, with an applied bias of 200 mV (left) and 300 mV (right). **(b)** Scatter plot of maximum blockage versus dwell time using a 10.5 nm pore, with an applied bias of 200 mV (left) and 250 mV (right). **(c)** Scatter plot of maximum blockage versus dwell time using an 8.7 nm pore, with an applied bias of 200 mV (left) and 300 mV (right). **(d)** Scatter plot of maximum blockage versus dwell time using a 7.5 nm pore, with an applied bias of 100 mV (left) and 200 mV (right).

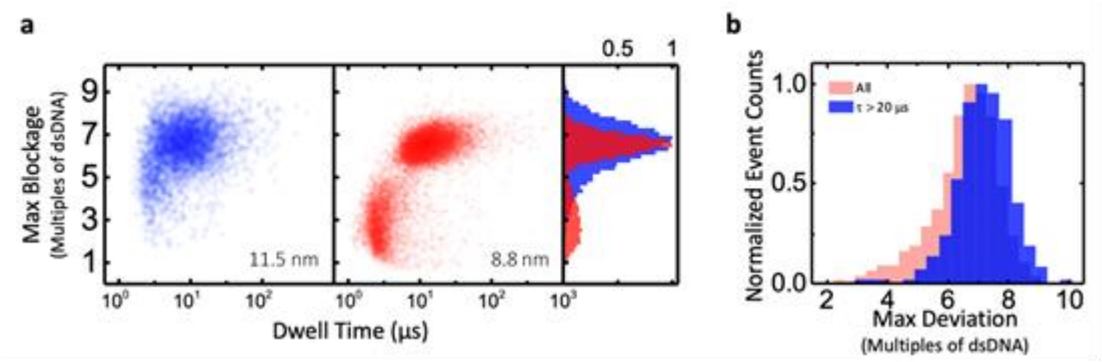

Figure 2.9. Scatter plots and histograms of the 12-arm star. (a) Scatter plots of the 12-arm star using an 8.8 nm pore (red, n = 16,822) *versus* an 11.5 nm pore (blue, n = 5,005), with an applied bias of 200 mV in symmetric 3.6 M LiCl pH 8. **(b)** Distributions of the 12-arm star on the 11.5 nm pore, entire data set (pink, n = 5,005) *versus* subset of data with events longer than 20 µs (blue, n = 583).

The scatter plot and histogram of the 12-arm star using an 8.8 nm pore (red) versus an 11.5 nm pore are shown in **Figure 2.9**a. Note that data using an 8.8 nm pore (red in **Figure 2.9**a) was collected with the 12-arm star without any purification, the low-level shallow events can be eliminated by the purification technique described above. Despite this, the distributions of the fully formed 12-arm using both 8.8 nm and 11.5 nm pore have the same mean maximum blockage. The 12-arm star on a larger pore has a shorter mean dwell time (7 ± 2 µs in an 11.5 nm pore *versus* 12 ± 2 µs in an 8.8 nm pore), which results in a higher number of poorly fitted events because many events are short-lived (<10 µs), and therefore the distribution has larger spread.

For the 12-arm star data collected on an 11.5 nm data, if we plot only the subset of events with passage times longer than 20 µs, the spread of the distribution becomes smaller in comparison to the whole data set (**Figure 2.9**b). This supports the argument that the spread in the distribution below N/2, 6 multiples of dsDNA in this case, is a result of poor fits of the short-lived events, since almost no events lasting longer than 20 μs exhibit a maximum deviation below 6x dsDNA. Here the maximum deviation is the single data point furthest away from the local open pore current in an event. The maximum deviation metric thus measures the deepest sublevel of any event that is detected by the hardware, plus contribution of noise.

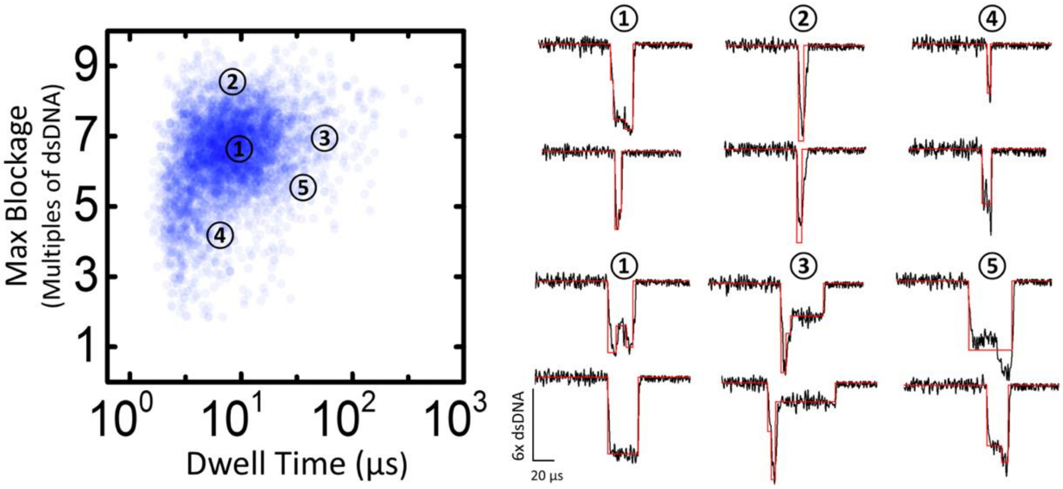

Figure 2.10. Event types of the 12-arm star. Scatter plot of the 12-arm star using an 11.5 nm pore with an applied bias of 200 mV in symmetric 3.6 M LiCl pH 8, and the current traces corresponding to different regions, with fits in red.

Figure 2.10 shows the scatter plot of the 12-arm star using an 11.5 nm pore and the current traces corresponding to each region of the scatter plot. Current traces from region 1 (events around the mean) and 3 (long-lived events) show events that are correctly fitted. Currents traces from region 4 (short-lived events below the minimal anticipated max blockage) show examples of events whose deepest levels are not fitted correctly, or the deepest levels are not resolved at all. Current traces from region 5 (long-lived events at the minimal anticipated max blockage) show examples of misfits of longer events, although the whole events are relatively long, the deepest levels are still missed by our analysis algorithm in some cases. Current traces from region 2 (events with deep blockages) show an example of a correctly fitted event and an event which is over-estimated due to fitting. In conclusion, the spread of the distribution of the star-shaped molecules are partially caused by a combination of misassembled products (very short shallow events), and the quality of the fits (under-estimation and over-estimation) of shorter events and the limitation of the resolution of our recording device.

2.5.3 Additional 4-arm and 6-arm Results

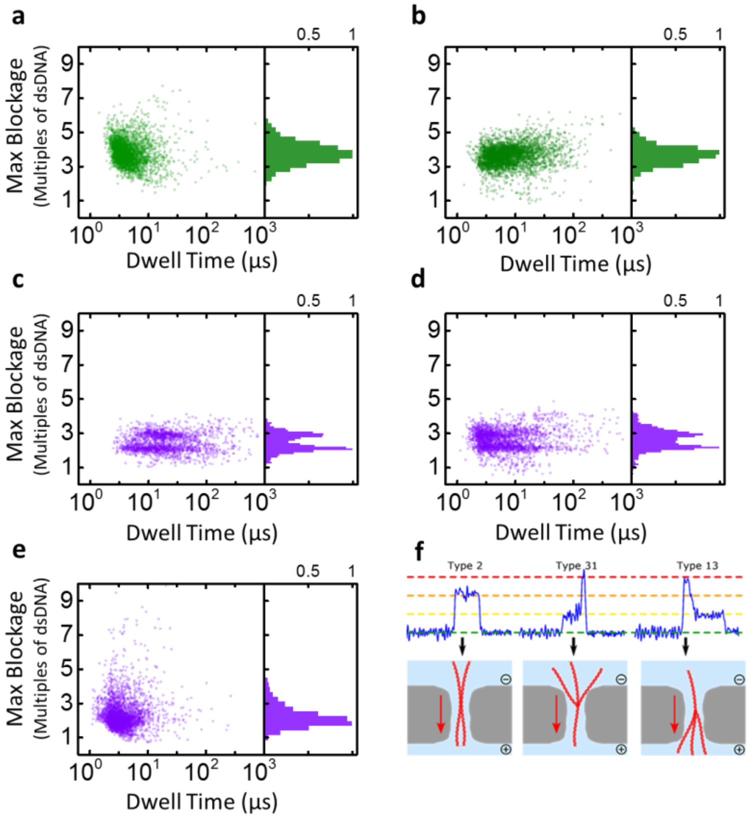

Figure 2.11. Additional 4-arm and 6-arm results. (a) Scatter plot for 6-arm star DNA of normalized maximum blockage versus dwell time in a 9.7 nm pore with an applied bias of 200 mV. **(b)** Scatter plot for 6-arm star DNA of normalized maximum blockage versus dwell time in a 7.4 nm pore with an applied bias of 200 mV. **(c)** Scatter plot for 4-arm star DNA of normalized maximum blockage versus dwell time using a 5.6 nm pore with an applied bias of 200 mV. **(d)** Scatter plot for 4-arm star DNA of normalized maximum blockage versus dwell time using a 5.6 nm pore with an applied bias of 400 mV. **(e)** Scatter plot for 4-arm star DNA of normalized maximum blockage versus dwell time using a 9 nm pore with an applied bias of 200 mV. **(f)** Example events from **(c-d)**. All experiments are performed in 3.6 M LiCl pH8 and analyzed at 500 kHz.

The gel electrophoresis results for the 6-arm dsDNA star label are shown in **Figure 2.1**b in the main manuscript, indicating correct assembly for the majority of the product. The 6-arm star labels are then characterized by solid-state nanopores, immersed in 3.6 M LiCl pH 8.0 with an applied bias of 200 mV. **Figure 2.11**a-b show the translocation characteristics of the 6-arm dsDNA star label in two different nanopores. The blockage depth histograms are fitted with a single peak Gaussian to extract the mean maximum blockage as described previously. The scatter plot from the 9.7 nm nanopore (**Figure 2.11**a) shows a mean maximum blockage of 3.7 ± 0.6 multiples of dsDNA, and the scatter plot from the 7.4 nm nanopore (**Figure 2.11**b) shows a mean maximum blockage of 3.6 ± 0.5 multiples of dsDNA. The mean maximum blockage of the 6-arm star label is more than 3x deeper than the expected blockage of dsDNA, suggesting that it is translocating most likely in a 3-arm/3-arm orientation and 4-arm/2-arm orientation, though we cannot resolve these two possibilities in the distribution, as discussed in the main text.

In contrast, the 4-arm label translocating a small 5.6 nm pore (compared to a 9.0 nm in **Figure 2.2** in Section 2.1.2) now shows two clear distinct populations in the maximum blockade distribution at an applied bias of 200 mV (**Figure 2.11**c), the deeper events have a mean maximum blockage of 2.9 ± 0.2 multiples of dsDNA indicating that the label is translocating in either a 3-arm/1-arm or the 1-arm/3-arm orientation, and the lower events have a mean maximum blockage of 2.3 ± 0.2 multiples of dsDNA indicating a 2-arm/2-arm orientation during translocation. Increasing the applied bias to 400 mV (**Figure 2.11**d), the 3-arm/1-arm population shows a mean maximum blockage of 2.9 ± 0.3 multiples of dsDNA and the 2-arm/2-arm population shows a mean maximum blockage of 2.1 ± 0.2 multiples of dsDNA. The observation of these discrete sublevels for the 4-arm label on a 5.6 nm pore, which are attributed to distinct orientations during translocation, is made possible by the small size of the pore slowing the passage of the nanostructures, restricting their conformation, and forcing specific orientations.

2.5.4 Additional 2-plex Results

In addition to the multiplexing results shown in Section 2.1.2 in **Figure 2.4**, additional 2-plex experiments were performed under similar conditions as shown in **Figure 2.12**, and without purifying the labels. The 8-arm star label shows a mean maximum blockage of 3.9 ± 0.7 multiples of dsDNA and 1.5 % of shallow events outside the Gaussian fit. The 12-arm star label shows a mean maximum blockage of 6.8 ± 0.7 multiples of dsDNA and 22.8 % of shallow events outside the Gaussian fit. These results show that we can distinguish with a confidence interval of 95 % or better 4-arm from 8-arm, and 8-arm from 12-arm. Purifying the DNA nanostructures to remove partially assembled structures would further improve the separation between the peaks (see Section 2.3.2).

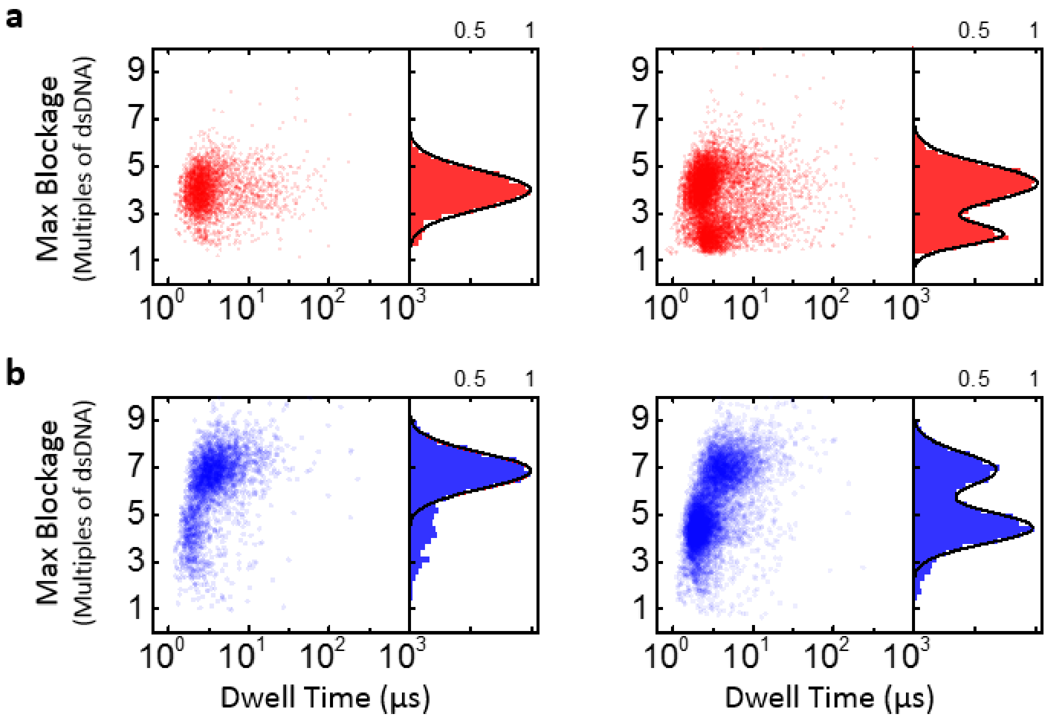

Figure 2.12. Scatter plots of 2-plexing using 8- and 12-arm stars. (a) Scatter plot of normalized maximum blockage versus dwell time for the unpurified mixture of 4-arm and 8-arm stars using a 13.4 nm pore at 200 mV in comparison with the scatter plot of 8-arm alone on the left. **(b)** Scatter plot of normalized maximum blockage versus dwell time for the unpurified mixture of 8-arm and 12-arm stars using a 10.6 nm pore at 250 mV in comparison with the scatter plot of unpurified 12-arm alone on the left. Distributions of corresponding maximum blockage are attached to each scatter plots. Experiments are performed in 3.6 M LiCl, pH 8.0, and analyzed at 500 kHz.

2.5.5 Additional Salt Asymmetry Results

Figure 2.13a shows the capture rate improvement as a function of salt concentration asymmetry for 8-arm and 12-arm dsDNA star labels for 5 different solid-state nanopores. In addition to the 200-fold increase in capture rate, an increase of up to 20-fold in the average dwell time is observed

(**Figure 2.13**b) when going from C_{trans}/C_{cis} = 3.6 M/3.6 M = 1 to C_{trans}/C_{cis} = 3.6 M/ 0.18 M = 20. Interestingly, a salt gradient in either direction ($C_{trans}/C_{cis} < 1$ and $C_{trans}/C_{cis} > 1$) appears to significantly increase the average dwell time, *i.e*. the shortest average dwell time is observed in symmetric salt. This is consistent with the salt asymmetry results for linear dsDNA by Wanunu *et al*.[65], where a 3.5x increase in average dwell time for 2,000 bp dsDNA is achieved.

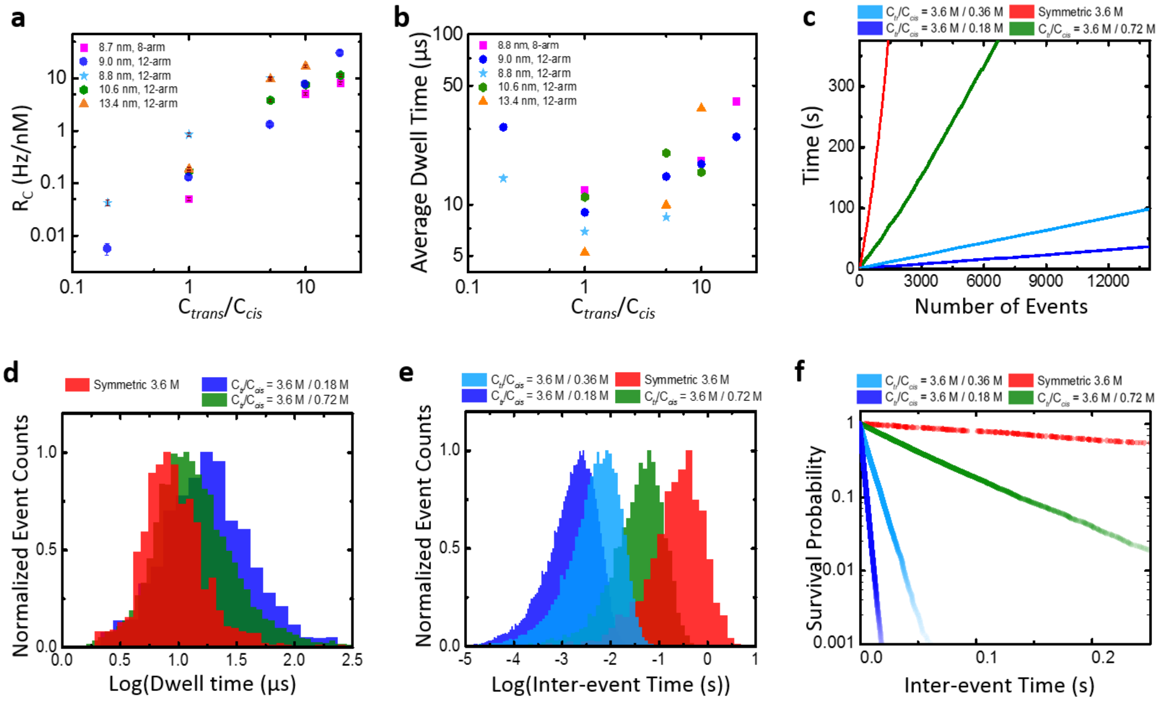

Figure 2.13. Improvement of capture rate and average dwell time for 8-arm and 12-arm star labels. (a) Capture rate *versus* salt gradient (C_{trans}/C_{cis}) on a log-log scale. **(b)** Average dwell time versus salt gradient (C_{trans}/C_{cis}) for the 12-arm star on a log-log scale. Experiments are performed with an applied bias of 200 mV in LiCl with the following ratio and absolute values of concentrations: C_{trans}/C_{cis} = 0.72 M/ 3.6 M = 0.2, C_{trans}/C_{cis} = 3.6 M/ 3.6 M = 1, C_{trans}/C_{cis} = 3.6 M/ 0.72 M = 5, C_{trans}/C_{cis} = 3.6 M/ 0.36 M = 10, C_{trans}/C_{cis} = 3.6 M/ 0.18 M = 20. **(c)** Time versus number of events for the 12-arm star for various asymmetric LiCl salt conditions. **(d)** Distribution of translocation time for the 12-arm star for symmetric 3.6 M/ 3.6 M

LiCl compared to C_{trans}/C_{cis} = 5, 10 and 20. **e)** Distribution of inter-event time for C_{trans}/C_{cis} = 10 and 20 compared to symmetric 3.6 M/3.6 M LiCl. **f)** Survival probability versus inter-event time for symmetric and asymmetric LiCl salt. All experiments in **(c,d,e,f)** are performed using a 9 nm pore with an applied bias of 200 mV.

Figure 2.13 (c), (d), (e) and **(f)** show the distribution of inter-event times and the cumulative number of events as a function of time to demonstrate that arrival time of molecules at the pore follows the expected (time-invariant) Poisson process. This suggests that the events detected are fully translocating so that no molecules are counted multiple times.

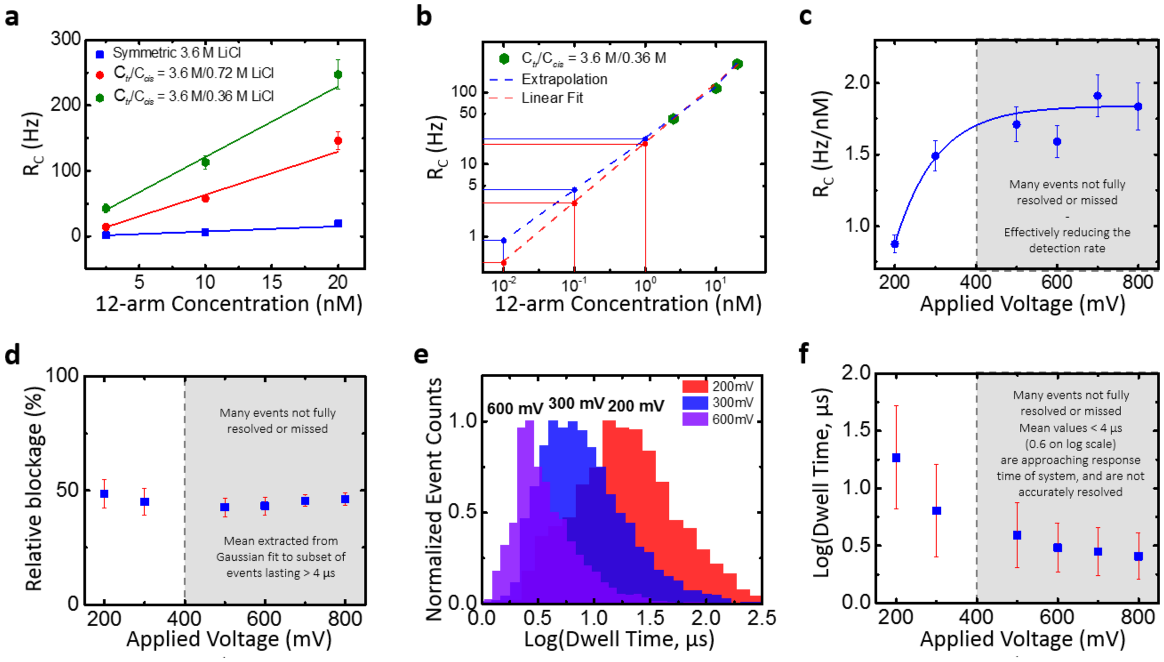

Figure 2.14. Voltage dependence of the 12-arm star in asymmetric LiCl salt conditions using a 10.3 ±0.3 nm pore. (a) Capture rate of the 12-arm star as a function of its molar concentration for symmetric and asymmetric LiCl, at 200 mV. **(b)** Extrapolation to pico-molar range (10 pM and 100 pM) for

asymmetric C_{trans}/C_{cis} = 0.36 M/3.6 M LiCl, at 200 mV. **(c, d, and f)** Capture rate, relative blockage and dwell time of the 12-arm star *versus* applied voltage in symmetric 0.72 M/0.72 M LiCl. **(e)** Distribution of dwell time for 200 mV, 300 mV and 600 mV in symmetric 0.72 M/0.72 M LiCl.

Figure 2.14a shows capture rate of the 12-arm star as a function of its concentration (from 2.5 nM to 20 nM) for symmetric 3.6 M LiCl, C_{trans}/C_{cis} = 3.6 M/0.72 M and C_{trans}/C_{cis} = 3.6 M/0.36 M. The capture rate for the 12-arm star at 10 pM can be extrapolated for the asymmetric C_{trans}/C_{cis} = 3.6 M/0.36 M case, we estimate a capture rate of 0.9 Hz and 0.4 Hz from interpolation and linear fit, respectively (**Figure 2.14**b). This shows the potential of picomolar concentration measurements while overcoming the challenges of analyzing short-lived translocation events.

Figure 2.14d shows that the relative blockage level (extracted from Gaussian fit) of the 12-arm star in symmetric 0.72 M LiCl does not appear to be affected by voltage (from 200 mV to 800 mV) and stays close to 50%, indicating that the 12-arm events are indeed translocations rather than collisions with the pore. This is supported by the fact that the average dwell time decreases with increasing voltage as shown in **Figure 2.14**e-f.

Although with a higher applied voltage, we expect the translocation time to be scale as $1/V$, the discrepancy shown in **Figure 2.14**f (at higher voltages) comes from the lack of temporal resolution of the current recording device. As the applied voltage is increased over 500 mV, the 12-arm stars translocation events become too fast and many events are missed, and it becomes more difficult fit them correctly. This is reflected on **Figure 2.14**f where the decrease in dwell time is attenuated and flattens out. Furthermore, the capture rate stops increasing once the applied voltage passes the 500 mV as shown in **Figure 2.14**c, indicating by events are more events are missed with increasing voltage above 500 mV.

2.5.6 Pore Statistics

The effective pore length were calibrated by using long linear dsDNA as a molecular ruler [129], while in 3.6M LiCl pH8. The effective pore size is calculated based on the pore conductance and the effective pore length.

Pore ID	Applied Voltage (mV)	Mean Baseline Level (nS)	Effective Pore Length (nm)	Effective Pore Size (nm)
P1	200	25.2 ± 0.4	5.5 ± 0.3	4.2 ± 0.1
P2	400	12.8 ± 0.2	10.0 ± 0.3	3.6 ± 0.1
P3	200	59.6 ± 0.4	10.9 ± 0.3	9.2 ± 0.1
P4	200	34.3 ± 0.2	11.4 ± 0.4	6.7 ± 0.1
P5	200	21.6 ± 0.2	10.8 ± 0.2	5.0 ± 0.1
P6	200	44.9 ± 0.2	12.3 ± 0.3	8.1 ± 0.1
P7	200	41.5 ± 0.2	10.3 ± 0.2	7.2 ± 0.1
P8	400	15.6 ± 0.2	10.5 ± 0.2	4.1 ± 0.1
P9	400	21.4 ± 0.1	13.9 ± 0.2	5.5 ± 0.1
P10	400	36.0 ± 0.1	13.4 ± 1.0	7.4 ± 0.1
P11	200	26.3 ± 0.2	10.9 ± 0.7	5.6 ± 0.2
P12	200	31.2 ± 0.2	8.9 ± 0.1	5.7 ± 0.1
P13	200	40.0 ± 0.2	9.6 ± 0.1	7.2 ± 0.1

P14	400	37.0 ± 0.1	9.1 ± 0.2	6.7 ± 0.1
P15	200	54.3 ± 0.3	12.8 ± 0.3	9.7 ± 0.1
P16	200	33.8 ± 0.3	11.9 ± 0.2	7.1 ± 0.1
P17	200	33.9 ± 0.2	12.2 ± 0.3	7.1 ± 0.1
P18	200	37.5 ± 0.2	12.6 ± 0.4	7.4 ± 0.1
P19	200	45.9 ± 0.4	14 ± 0.4	8.8 ± 0.1
P20	200	74.7 ± 0.5	13.3 ± 0.7	11.6 ± 0.2
P21	200	55.0 ± 0.6	12.9 ± 0.6	9.5 ± 0.2
P22	200	41.6 ± 0.4	10.7 ± 0.3	7.4 ± 0.1
P23	200	47.6 ± 0.5	13.3 ± 0.4	8.8 ± 0.1
P24	200	86.9 ± 1.4	13.3	13.4
P25	200	75.6 ± 1.6	12.5 ± 0.4	11.4 ± 0.3
P26	200	61.8 ± 0.9	12.9 ± 0.3	10.6 ± 0.2
P27	200	63.5 ± 1.5	12.8 ± 0.4	10.3 ± 0.3
P28	200	52.3 ± 1.1	12.5 ± 0.3	9.0 ± 0.2
P29	200	75.4 ± 1.3	13.8 ± 0.4	12.5 ± 0.3
P30	200	82.2 ± 1.1	12.1 ± 0.3	11.5 ± 0.3

Table 2.5. Statistics of nanopores.

2.6 Acknowledgments

We would like to acknowledge to financial support of the Natural Sciences and Engineering Research Council of Canada (NSERC). The authors would like to thank Dr. Kyle Briggs, Dr. Eric Beamish, and Dr. Daniel Tessier for helpful discussions.

Chapter 3 – Probing Translocation Properties of Helix Bundle DNA Origami Structures using Solid-State Nanopores

This chapter is submitted as:

Dynamics of Passage of DNA Nanostructures through Solid-State Nanopores Gives Insight on Complexities of Macromolecular Assembly

Liqun He,* Martin Charon,* Philipp Karau, Kyle Briggs, Vincent Tabard-Cossa

Department of Physics, University of Ottawa, Ontario, Canada

*These authors contributed equally

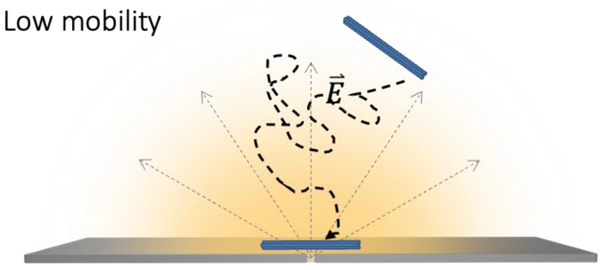

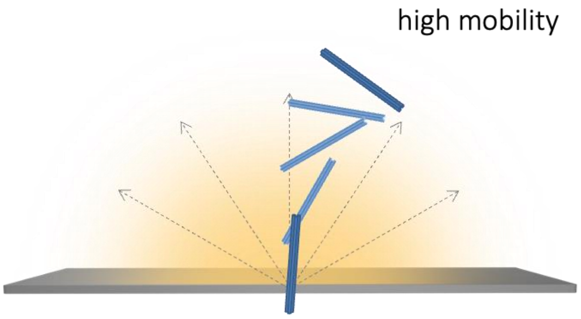

Abstract

Solid-state nanopores are emerging as versatile single-molecule sensors to electrically characterize a range of biological molecules. DNA nanostructures are self-assembled via specific base pairing of DNA, their programmability make them particularly useful for applications including biophysical studies, molecular computation and biosensing. Here, we present the use of this single-molecule approach to probe DNA nanostructures, their assembly, mechanical properties, and investigate their dynamics with varying temperature. Using controlled dielectric breakdown (CBD) fabricated solid-state nanopores, from 9 to 15 nm in diameter, we present results on the electrophoretic capture and translocation characteristics of the 3 helix-bundle (3HB) and linear double-stranded M13 origami structures (ldsM13) in comparison to double-stranded DNA (dsDNA). The rigid nature of helix-bundle structures results in long passage times and metastable states during translocation, we establish translocation profiles and discuss folding characteristics, mobility, and molecular configuration during passage under different experimental conditions. Our results indicate that when translocating single-file, the 3HB nanostructure behaves just like linear dsDNA fragments; and when the 3HB nanostructure is captured by anend, local defects along its contour length dominate the translocation dynamics. A good agreement between nanopore and gel electrophoresis was observed for both origami structures, we also discuss how the assembly, purity and stability of DNA nanostructures can be assessed using nanopore detection, and present nanopores as an alternative to gel electrophoresis. Furthermore, we observed total degradation of the origami structure after a heat shock as short as two minutes, resulting in higher order blockages

on a nanopore and faster migrating bands on gel electrophoresis, the thermal response of 3HB suggests the presence of mis-assembled products.

3.1 Introduction

Tremendous advancement has been made in the field of DNA nanotechnology since its introduction. Motivated by the numerous applications in biotechnology, a variety of 2-dimensional and 3-dimensional DNA nanostructures have been developed and studied. DNA nanostructures are finding more applications in a wide range of research fields, including single-molecule biophysics, diagnostics, and therapeutics. Douglas *et al* showed detergent-resistant DNA nanotubes can be used as liquid-crystalline medium for the structural analysis of membrane protein,[146] DNA origami can be used to aid imaging of macromolecules or serve as a constraining frame for macromolecules.[147–149] DNA nanostructures can be functionalized by using modified DNA oligonucleotides, including chemical modifications such as thiolated oligonucleotides,[150–152] photo-active and photo-cleavable groups,[153–155] and molecular modifications such as biotinylated oligonucleiotides.[156–158] DNA nanotechnology has demonstrated potential in diagnostics and therapeutics, such as a drug-delivery vehicle consists of a hollow DNA box with a controllable lid that can be opened by strand displacement.[51]

DNA origami structures are traditionally characterized using gel electrophoresis, and microscopy techniques such as transmission electron microscopy (TEM) and atomic force microscopy (AFM). Gel electrophoresis has been the gold standard for the characterization of DNA origami structures for its simplicity and quick bulk estimation about yield and purity, though it has the major drawback that it does not provide structural information. Microscopy techniques provide high resolution imaging of the sample on single-molecule level. Negative-stain TEM, a well-established diagnostic technique, where the background is stained to contrast the unstained sample specimen, is particularly useful for 3-dimensional structures,[62,63,159,160] but suffers from sample preparation complexity and deformation of the sample specimen during the experiment.[52,56,58,161] In comparison, nanopore sensing as a single-molecule platform has distinct advantages for this purpose. Nanopore sensing allows for the detection in buffer solution which preserves the structural features of the sample as opposed to immobilizing the samples on a surface. Targets can be individually measured on the single-molecule level, as the blockage depth, duration, frequency, and temporal structure of translocation events reveal information about a molecule's size and conformation.

A number of research groups have work involving sensing DNA nanostructures using solid-state nanopores. Alibakhshi *et al* studied electrophoretic transport of ring- and cube-shaped nanostructures using solid-state nanopores.[65] Bell and Kong e*t al* first used long linear dsDNA carriers that contain barcodes for multiplexed digital detection specific proteins.[68,86,87] Similar DNA nano-carrier approaches were employed by Cai and Sze *et al* for the detection proteins and antibodies.[69,85] More recently, Wang *et el* demonstrated the current enhancement of DNA helix bundle structures at low salt concentrations.[66] Beamish *et al* used solid-state nanopores to investigate the translocation properties of linear and looped nanoswitch topologies;[49] a set of short DNA nanostructures as probes which a conformational change in the presence of nucleic acid biomarkers such as microRNA or other small molecules.[162] Raveendran *et al* showed the use of aptamer functionalized 2D DNA origami featuring target-specific cavities for the detection C-reactive protein in plasma sample.[99] Similarly, in our previous work we presented multiplexed nanopore detection of star-shaped DNA nanostructures and their application to detection of low concentration of specific target proteins in a serum sample.[64,155]

Since Nadrian Seeman laid the framework for the use of DNA nanostructure in 1982, DNA has been used to construct increasingly complex shapes.[45] DNA origami is the arrangement of hundreds of oligonucleotides at specific locations to assemble a variety of nanoscale objects with nano-metre precision.[51,52,54–58,146,147,163–173] There are two main approaches to DNA origami: The multi-stranded approach, and the scaffold-based approach.[24] The multi-stranded approach makes use of the DNA complementarity rule by mixing pieces of DNA oligonucleotides which are mutually complementary in such a way as to naturally form the target shape. In 2006, Paul Rothemund introduced DNA origami for the construction of arbitrary shapes, with involves the use of a scaffold strand with a known sequence, and numerous staple strands to fold and bind the scaffold into the desired shape.[55] He fabricated large two-dimensional nanostructures by mixing hundreds of short ~40-mer oligonucleotides with a 7249 nt long sequence of M13 viral DNA, as shown in Figure 1a. This approach was further developed by Douglas *et al*, where they developed a computer-aided design (CAD) software called caDNAno.[57] This software extends DNA origami to 3D shapes, making the prototyping of DNA origami even more accessible. The basic principle of 3-dimensional DNA origami is Watson-Crick complementarity, we assembled of origami structures by mixing linearized scaffold DNA (single-stranded M13mp18) and hundreds of short oligonucleotide staple strands (~40 nt) as previously described.[52,56–58]

Synthetic DNA nanostructures, owing to the programmable nature, are well suited for probing the underlying transport properties in nanopore systems. For the purpose of this study, we prepared different structures using the scaffold approach: linear double stranded M13 (ldsM13), and 3 helix bundles (3HB), as illustrated in **Figure 3.1**a-b. We show that the nanopores are effective tools for the detection and characterization of DNA nanostructures. Signal-to-noise ratio (SNR) and time resolution have been the limiting factors in some areas of nanopore research, helix bundle structures due to their programmability, can be specifically designed to tackle these challenges. The 3HB structures provide good SNR while maintaining passage time to allow reliable detection. Using these structures, we study the translocation and folding characteristics of the helix bundle structures in various experimental conditions, while using the linear assembly as a reference point with which to interpret behavioral differences.

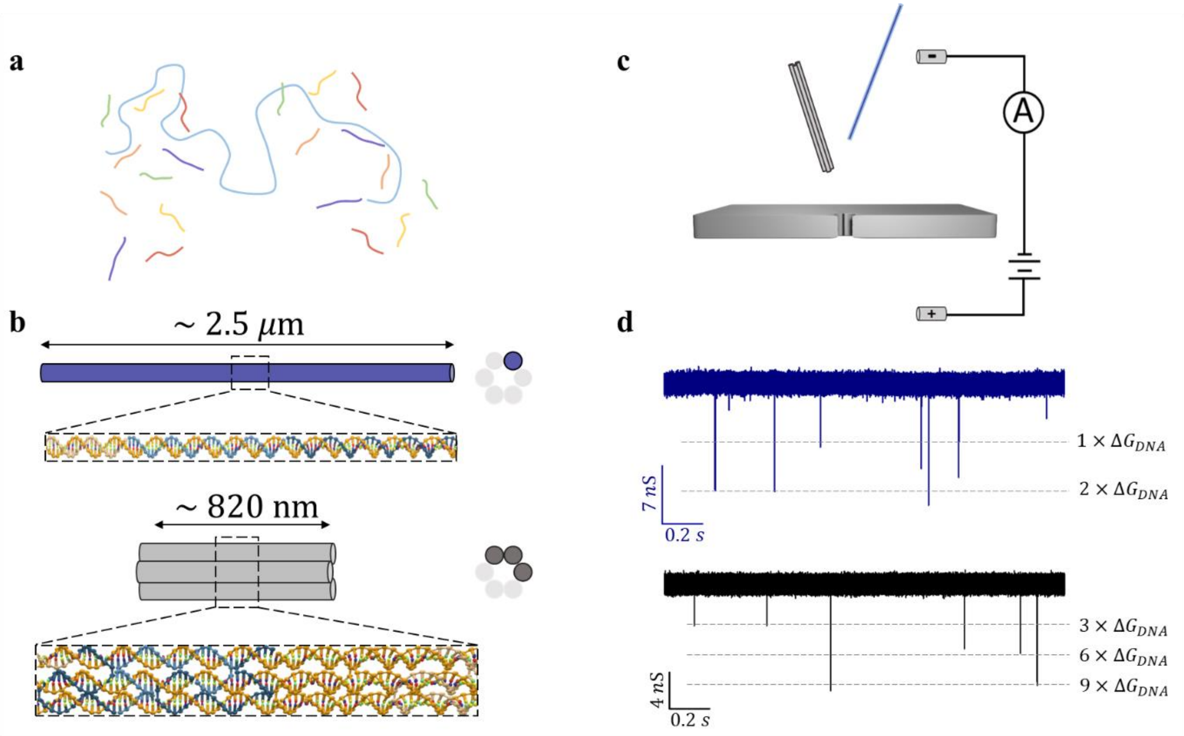

Figure 3.1. **Detection of DNA nanostructures using solid-state nanopores. (a)** Schematic of DNA helix bundle hybridization, thermal annealing of 7249 nt M13mp13 with 190 short “staple” strands. **(b)** Coarse-grained model of ldsM13 and 3HB structures using OxDNA. **(c)** Schematics of nanopore setup. **(d)** 2, and 10 second current traces of ldsM13 (blue) and 3HB (black), in 3.6 M LiCl and 1.2 M LiCl, respectively.

Experiments are performed with an applied bias of 300 mV. The current traces shown are low-pass Bessel filtered at 200 kHz. Dashed lines high multiples of single-file blockage levels.

3.2 Results and Discussion

3.2.1 Linear Assembly

An illustration of the assembly of the origami structures is shown in **Figure 3.1**a-b, the protocol is described in the Section 3.4 and Section 3.5.1; the design and sequences of the structures are given in Section 3.5.2. Once assembled, the structures were characterized by gel electrophoresis as shown in **Figure 3.7** to confirm the quality of the assembly prior to nanopore sensing. Nanopore sensing details are available in the Methods section. Origami structures were then electrophoretically driven through the nanopore, as illustrated in **Figure 3.1**c. **Figure 3.1**d show 2 second and 10 second sample current traces of the ldsM13 and 3HB structures with an applied bias of 300 mV, in 3.6 M and 1.2 M LiCl salt, respectively.

To characterize the ldsM13 assembly, molecules were passed through an 8.4 nm ± 0.2 nm nanopore in a 3.6M LiCl salt solution under a 200mV applied voltage. For comparison, 7 kbp dsDNA, whose 2.38 μm contour length is comparable to ldsM13's 2.46 μm length, was also analyzed under the same conditions. For optimal comparison, both experiments were run in succession in the same pore to avoid pore-to-pore variations. Only a 7% increase in current was observed between the 7kbp ($I_{baseline} =$ 14.45 nA, $d =$ 8.2 nm) and ldsM13 ($I_{baseline} =$ 15.50 nA, $d =$ 8.6 nm) measurements. As shown in **Figure 3.1**d, the presence of ldsM13 in solution causes transient current blockades, as expected from nanopore translocations in high salt concentration.[66] **Figure 3.2**a shows the concatenated current traces of 17 consecutive ldsM13 translocation events, and 17 consecutive 7kbp translocation events depicted in blue and red, respectively. The majority of translocation events for both 7kbp and ldsM13 display two distinct blockage sublevels, the deepest one occurring first, followed by a shallower one. This is expected from folded translocations for which molecules enter the pore not via their ends but by bending along their contour.[174,175]

Individual events were fit using custom software (see Section 3.4) to quantify the relative current blockage and duration of each sublevel identified within an event. **Figure 3.2**b shows a scatterplot of maximum blockage ΔG_{max} *versus* translocation time τ for both the ldsM13 (blue) and the 7kbp (red) translocation events. Here, maximum blockage denotes the maximum conductance blockage recorded for all the sublevels identified in a single translocation event, whereas translocation time denotes the total duration of the blockage events. Just like 7kbp, ldsM13 translocations display multiple distinct populations, easily identified by the quantized peaks of ΔG_{max} as shown in the ΔG_{max} histogram of **Figure 3.2**b. The different peaks correspond to events which at any point had multiple ldsM13 strands simultaneously inside the pore, as expected from folded translocations.[176] Fitting each blockage peak to Gaussian distributions, the most probable ΔG_{max} values identified for the single-file and folded ldsM13 populations were found to be $\Delta G_1^{M13} = 8.52\,nS$, and $\Delta G_2^{M13} = 17.38\,nS$, which are nearly indistinguishable from the 7kbp blockage values of $\Delta G_1^{7kbp} = 8.47\,nS$ and $\Delta G_1^{7kbp} = \ 17.33\,nS$. Current blockage being closely related to the cross-sectional area of translocating molecules, we thus trivially conclude that the diameters of ldsM13 assemblies and dsDNA are nearly identical.

Although both block ionic currents similarly, ldsM13 and 7kbp have significantly different translocation time distributions. To demonstrate this, the inset of **Figure 3.2** plots the histogram of the logged translocation times, only considering the translocation times of single-file events ($\Delta G_{max} < 10\ nS$). 7kbp events shows tightly distributed single-file translocation times τ_1, whose distribution is well described by a log-normal function with a mean translocation time of $\tau_1^{7kbp} = 264\ \mu s$. The distribution of single-file ldsM13 events shows a similar peak with a slightly longer mean time of $\tau_1^{M13} = 296\ \mu s$, expected from the slightly longer molecule (7249 bp vs 7000 bp), but also shows a streak of shorter translocations spanning the entire range between the log-normal peak and the current amplifier's resolution limit of $\approx 5\ \mu s$. A similar distribution is also observed for the translocation times of folded events ($\Delta G_{max} > 10\ nS$), as shown in Section 3.5.3. The fact that shorter ldsM13 translocations in the lower tail of the τ distribution have ΔG_{max} values consistent with that of dsDNA suggests that although ldsM13 molecules of the right dimensions were assembled, as demonstrated by the good agreement of ΔG_1, ΔG_2 and τ_1 values for 7kbp and ldsM13, many shorter fragments of linear assemblies can be found in solution. A similar observation and conclusion are reached by gel electrophoresis, which shows a streak of fragments migrating faster than 7kbp dsDNA.

To investigate the origin of this lower τ-tail, we assembled ldsM13 molecules without using the restriction enzyme responsible for cutting and linearizing the M13 scaffold, therefore expecting circular double-stranded M13 (cdsM13) molecules. The passage of cdsM13 through a 7.9 nm pore in 3.6 M LiCl however showed that a significant fraction of cdsM13 were linearized, with translocation times and blockages matching that of 7kbp dsDNA. In Supplementary Information Section S4, we use folding statistics to estimate that a portion of cdsM13 molecules were linearized and thus conclude that the M13 scaffold used to build both the ldsM13 and cdsM13 molecules randomly cut along its contour. This is consistent with the denaturing gel electrophoresis results shown in **Figure 3.6**. Although the origin of this randomly located cut is not further sought out in this work, we note that the combination of this randomly located scaffold break and the localized cut induced by the restriction enzyme would result in dsDNA fragments of random lengths when assembling ldsM13 molecules, thereby causing a spread of shorter translocation times, as in **Figure 3.2**b.

Using the data of **Figure 3.2**, we next attempted to gain structural information on the properly assembled ldsM13 assemblies by studying how the molecules fold inside nanopores and comparing with the similar-sized 7kbp dsDNA. To do this, we first filtered out events corresponding to fragmented ldsM13 assemblies. Although this could be roughly done by filtering based on translocation times (**Figure 3.2**b), we found that properly formed molecules could be more precisely identified and filtered on an individual basis using the sublevel-duration statistics of folded events. The filtering method used is summarized in **Figure 3.2**c, which shows a scatterplot of ldsM13 translocation time τ *versus* the corresponding folded state sublevel duration τ_{fold}, whereas the inset shows the same plot for folded 7kbp translocations. As shown for 7kbp dsDNA and as described by Mihovilovic *et al.*,[175] a downward trend is expected for τ vs τ_{fold} for linear polymers probing different folding locations along their contours. This is because folded polymer conformations reduce the end-to-end lengths of translocating polymers, and therefore polymers folding near their ends should have minimal τ_{fold} and maximal τ, whereas polymers folding near their middle should have maximal τ_{fold} and minimal τ. Because of the misassembled ldsM13 fragments however, the scatter plot for ldsM13 folded translocations in **Figure 3.2**c shows a more convoluted plot resulting from randomly fragmented translocations probing both capture locations. To extract translocations from fully assembled ldsM13 molecules, we used only the subset of events satisfying $\tau < (200\,\mu s - \tau_{fold})$. The choice of this filter is explained in more details in Section 3.5.3.

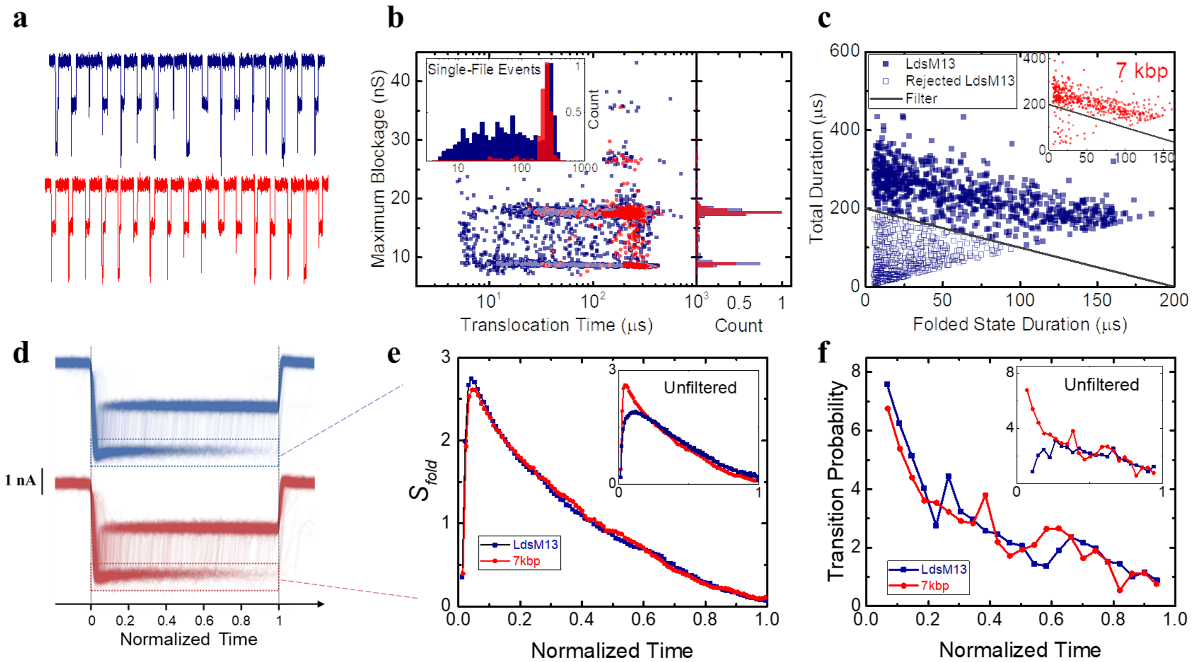

Figure 3.2. ldsM13 characterization and folding statistics. (a) Concatenated current trace of single translocation events for ldsM13 (blue) and 7kbp dsDNA (red). **(b)** Scatter plot of Maximum blockage *versus* translocation time and normalized histogram of maximum blockage level for ldsM13 (blue) and 7bkp dsDNA fragments (red), inset shows the normalized histogram of translocation time for ldsM13 (blue) and 7bkp dsDNA fragments (red). **(c)** Total translocation time *versus* folded state translocation time for ldsM13, inset show the total translocation time *versus* folded state translocation time plot for 7kbp dsDNA. **(d)** The overlayed events of for ldsM13 (blue) and 7bkp dsDNA fragments (red) on a normalized time scale. **(e)** The extracted the folded state survival probability $S_{fold\,(T)}$ for ldsM13 (blue) and 7kbp dsDNA (red). **(f)** the folded state transition probability $P_{fold(T)}$ for ldsM13 (blue) and 7kbp dsDNA (red). All experiments are done in 3.6 M LiCl, with an applied bias of 300 mV.

With most of the improperly assembled ldsM13 events filtered out, we next compared the folding statistics of ldsM13 and 7kbp dsDNA. This was achieved by overlaying the current traces of folded translocation events ($16\,nS < \Delta G_{max} < 19\,nS$), done by temporally scaling events such they begin at time $T = 0$ and end at $T = 1$, as shown in **Figure 3.2**d. From the overlaid traces, we then extracted the folded state survival probability $S_{fold}(T)$, defined as the probability that an event is still in a folded state at normalized time $T \in [0,1]$. Section 3.5.3 describes in detail how $S_{fold}(T)$ is extracted from the overlaid traces. **Figure 3.2**e plots the resulting $S_{fold}(T)$ for 7kbp dsDNA (red) and ldsM13 (blue) folded translocations, where both distributions are shown to be nearly identical. Interestingly, the $S_{fold}(T)$ distribution obtained without filtering the misassembled lsM13 events differs significantly from 7kbp dsDNA (**Figure 3.2**e inset), therefore demonstrating that polymer length plays an important role in determining how long a folded translocation remains in the folded state. Similarly, **Figure 3.2**f plots the folded state transition probability $P_{fold}(T)$ of both 7kbp and ldsM13, defined as the probability that an event transitions from folded state to single-file state at time T, calculated as $P_{fold}(T) = -dS_{fold}/dT \approx -\Delta S_{fold}/\Delta T$. **Figure 3.2**f shows again that $P_{fold}(T)$ is identical for both 7kbp and filtered ldsM13, but also that $P_{fold}(T)$ decreases monotonically with normalized time T. This indicates that the folded states are more likely to be short with respect to τ, which is consistent with previous observations showing that linear polymers prefer to enter nanopores close to their ends.[175]

3.2.2 3-Helix Bundle

To establish the nanopore translocation profiles for the 3-helix bundle structures (3HB), we ran the samples in various pore sizes (9 – 14 nm), salt concentrations (0.45 – 3.6 M LiCl), and under a wide range of voltages (100 – 900 mV). **Figure 3.3**a shows the representative current traces of 12 transient blockades of 3HB molecules in an 11.4 nm pore immersed in 0.9 M LiCl solution, under a 300 mV voltage. Half of the events in **Figure 3.3**a show two distinct blockage sublevels, the deepest one occurring first, followed by a shallower one, as expected from folded translocations, and as observed with dsDNA translocations in **Figure 3.2**a. **Figure 3.3**b shows a scatter plot of the maximum conductance blockage ΔG_{max} against the corresponding duration of each of the blockade event. The ΔG_{max} values are normalized by ΔG_{DNA}, the conductance blockage values measured from 2kbp dsDNA translocations inside the same pore as the 3HB, with $\Delta G = 1.54\,nS$ single-file and $3.18\,nS$ folded. The relative blockage level $\Delta G_{max}/\Delta G_{DNA}$ histogram in Figure 3b shows that 3HB blockades produce multiple populations easily identifiable by their maximum blockage ΔG_{max}. A first population is well described by a Gaussian distribution centered around $\Delta G_{max} = 4.76\,nS$, roughly three times that of dsDNA. This blockage depth corresponds well to the one expected from single-file translocation of properly assembled 3HB structures, whose cross-sectional area should be equivalent to that of three dsDNA strands. Two more populations at $\Delta G = 9.52\,nS$ and $15.21\,nS$, can be similarly identified with ionic blockage, whose peaks are centered near $\Delta G_{max}/\Delta G_{DNA} \approx 6$ and 9, they correspond to folded and double folded 3HB events. Given that the quantized blockage levels of 3HB blockades are multiples of $3\Delta G_{DNA}$ (or 1x ΔG_{3HB} single-file) as shown in **Figure 3.3**b, and the sequence of blockage states observed in their current traces (**Figure 3.3**a), both figures therefore suggest that 3HB molecules can bend inside nanopores, resulting in folded conformations. Moreover, we even find that 3HB molecules consistently fold over 50% more than 2kbp dsDNA, a molecule of similar length ($L_{3HB} = 0.82\,\mu m$ $versus$ $L_{2kbp} = 0.68\,\mu m$), when measured under the same experimental conditions. These conclusions are surprising considering that the triple bundle design is expected to has a persistence length three times that of double stranded DNA.[147,177–179]

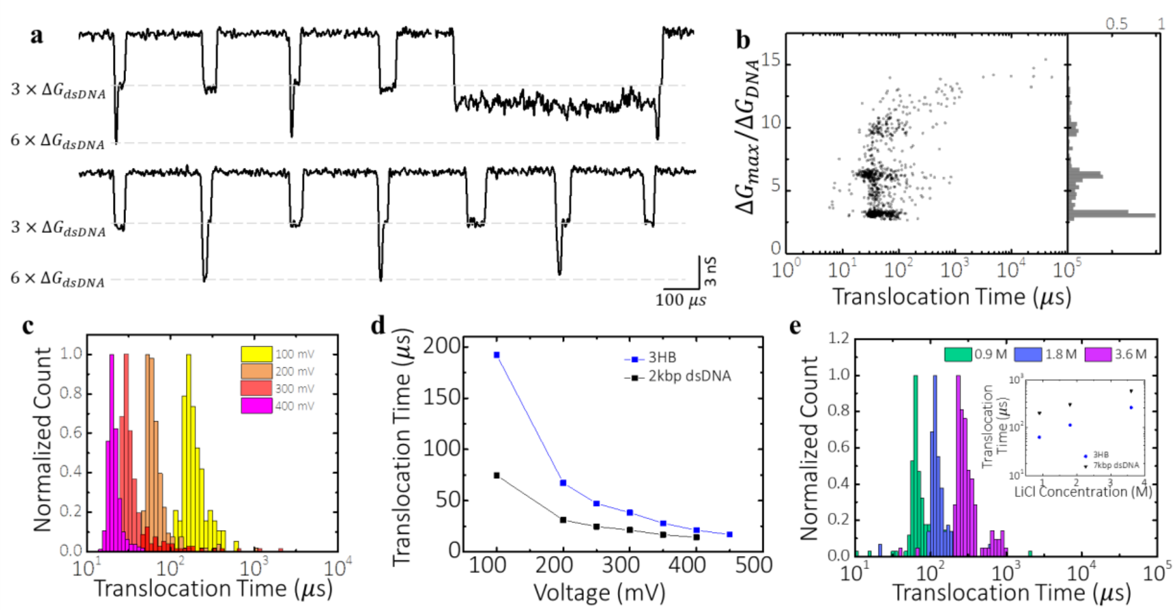

Figure 3.3. Nanopore characterization of 3HB structures. (a) Representative current traces of 3HB translocation events. **(b)** Scatter plot and histograms of normalized maximum blockage *versus* dwell time for a mixture of 3 helix bundle, in 1.2 M LiCl with an applied bias of 200 mV using a 13.2 nm pore. **(d)** Dwell time distribution of 3HB in 0.9 M LiCl using a 13.3 nm pore, with an applied bias of 100 (pink), 200 (red), 300 (orange), and 400 (yellow) mV, inset shows a semi-log plot dwell time as a function of LiCl salt concentration for 3 helix bundle and linear 2kbp dsDNA. **(e)** Dwell time distribution of 3 helix bundle in 0.9 (cyan), 1.8 (blue), and 3.6 (purple) M LiCl using a 11.4 nm pore, with an applied bias of 200 mV, inset shows a semi-log plot dwell time as a function of LiCl salt concentration for 3HB and linear 7kbp dsDNA.

Given the unexpected 3HB folding behavior outlined above, we next characterized the single-file translocation events (centered around $\Delta G_{max}/\Delta G_{DNA} = 3$) to determine if 3HB molecules were properly assembled or not, and to confirm that blockades indeed result from 3HB translocations, instead of collisions with the pore. This was first achieved by measuring the translocation times of 3HB through a 13.3 nm pore, in 0.9 M LiCl solution, under voltages ranging from 100 mV to 450 mV. The results are summarized in **Figure 3.3**c which shows 3HB translocation time distributions measured at different voltages, and in **Figure 3.3**d which plots the most probable 3HB translocation time measured at each voltage. For comparison, **Figure 3.3**d also shows the translocation time measurements of 2kbp dsDNA, which were performed in parallel with the 3HB measurements. Like 2kbp dsDNA, **Figure 3.3**d shows that 3HB translocation times reduce monotonically with voltage, as expected from molecules entering and fully traversing nanopores.

We further characterized 3HB single-file events by measuring the dependence of translocation time on salt concentration in an 11.4 nm pore, under an applied voltage of 200 mV. **Figure 3.3**e shows the histograms of the log of translocation time of 3HB single-file events in 0.9 M (cyan), 1.8 M (blue), and 3.6 M (purple) LiCl, respectively. To again compare 3HB to the well-known dsDNA translocations, the inset of Figure 3e shows the translocation time distributions measured for all three salt concentrations for 3HB and 7kbp dsDNA molecules, acquired simultaneously from a 3HB-7kbp mixture through the same pore. Like 7kbp dsDNA, 3HB structures translocate faster in lower salt concentrations. We quantify the translocations by their equivalent charge deficit (ECD), calculated as the time-integral of the difference between the current during the blockade event and the open-pore current, a quantity which represents the amount of additional charge which would have passed through the nanopore had the molecule not caused a transient blockage.[30] **Figure 3.11** shows a scatter plot of maximum blockage ΔG_{max} *versus* ECD of a mixture of 3HB and 7kbp. By fitting the ECD histograms to log-normal distributions, we found the 7kbp and 3HB populations are nearly identically centered around ECD $= 0.05$ pC. This is expected from properly assembled 3HB nanostructures since although of different dimensions, 3HB and 7bkp DNA fragments share a similar mass due to 3HB structures being assembled from a 7249 nt M13mp18 scaffold. From the combined observations that 3HB molecules block three times as much current as dsDNA, that 3HB and 7kbp dsDNA blockades result in the same ECD, and that 3HB events get faster with increasing voltages and in lower salt concentrations, we therefore conclude that 3HB transient blockades indeed result from properly assembled 3HB molecules translocating across nanopores. The results indicate that the higher blockade populations centered around 6x and 9x dsDNA correspond to folding of the 3HB molecules during population rather than multi-mers translocating, this is consistent with gel electrophoresis results shown in **Figure 3.7**.

After establishing that single-file translocations result from properly assembled 3HB molecules, we next investigated the folded 3HB translocations ($\Delta G_{max} > 3\Delta G_{DNA}$) to thoroughly characterize the transport process of 3HB assemblies through nanopores. **Figure 3.4**a plots the maximum blockage level ΔG_{max} of individual 3HB translocations *versus* the corresponding translocation times for a 13.3 nm pore in 0.9 M LiCl under biases of 200, 300 and 400 mV (data from **Figure 3.3**d). Consistent with **Figure 3.3**b, different populations can be identified based on maximum level blockage alone. Biases of 200 mV and 300 mV result in single-file translocations ΔG_{3HB} and a second population with a maximum blockage corresponding to $2\Delta G_{3HB}$. Under a $400\ mV$ applied voltage, a third population emerges, with maximum blockages centered just shy of $3\Delta G_{3HB}$. Again, quantized blockage distributions like the ones observed in **Figure 3.4**a are expected from linear polymers when nanopores are big enough to allow folded passages, *i.e.*, translocations for which a polymer enters the pore not by an end, but by bending along its contour. Since 3HB molecules should have three times the persistence length of the already rigid dsDNA ($\ell_p^{DNA} \gg d_{pore}$), seeing 3HB fold on itself more than once at 400 mV is very unexpected. To better understand the mechanism by which 3HB molecules fold inside pores, we next focused our analysis on the $2\Delta G_{3HB}$ population, *i.e.*, the events for which 3HB folds on itself only once during translocation.

The three different voltages displayed in **Figure 3.4**a show that events in the $2\Delta G_{3HB}$ population behave significantly differently than those in the single-file population. Unlike single-file translocations which strictly get faster with increasing voltages (**Figure 3.3**c-d), the mean duration of a subset of the $2\Delta G_{3HB}$ population increases when voltage is increases from 200mV to 400 mV. This behavior is typically expected from molecules colliding with nanopores, wherein molecules don’t fully enter nanopores yet still block current, until they diffuse away, and the current baseline is restored. In such cases, higher voltages make it harder for molecules to diffuse away from the pore, and therefore induce longer blockades. However, other events from the $2\Delta G_{3HB}$ population show shorter blockage times under 400 mV than under 200 mV, as expected from normal translocations. These two confounding behaviors result in a spread of blockage durations that significantly increases with voltage, as seen in **Figure 3.4**a.

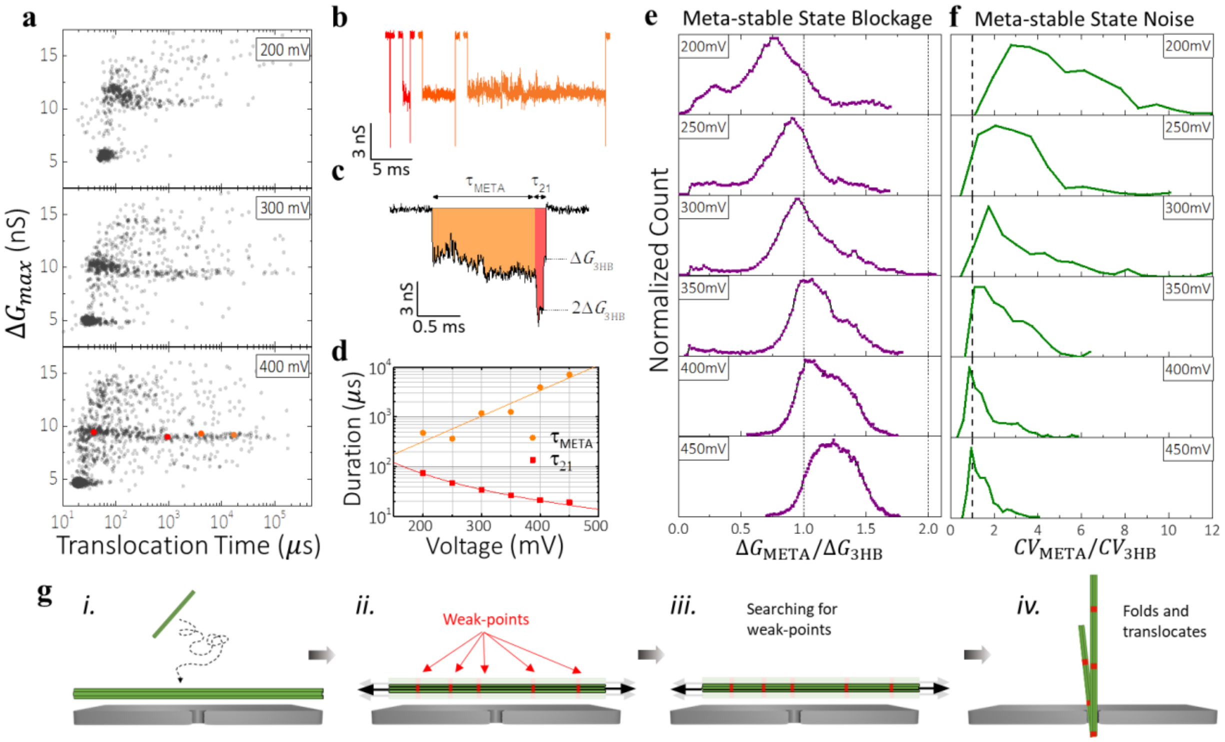

Figure 3.4. Folding statistics of 3HB translocation. (a) Scatter plots of maximum blockage level *versus* translocation time for 3HB molecules using a 13.3 nm pore in 0.9 M LiCl, with an applied bias of 200, 300, and 400 mV. **(b)** Current traces of representative events highlighting folding and events with meta-stable state, the example current traces correspond to four highlighted regions (orange/red dots) in **(a),** the 400 mV experiment. **(c)** An example current trance of a folded 3HB translocation event with meta-stable state. Orange portion represents the meta-stable state, which is followed by a folded state and single-file state shown in red. **(d)** Duration of meta-stable portion (orange) and translocation portion (red) as a function of applied voltage. **(e)** Normalized histograms of meta-stable stage blockage level, normalized by single-file 3HB translocation blockage, for 200, 250, 300, 350, 400, and 450 mV. **(f)** Normalized histograms of the metastable state blockage noise, normalized by single-file event noise for 200, 250, 300, 350, 400, and 450 mV. **(g)** Illustration of 3HB translocation process.

Good insight into the 3HB folding behavior is gained by examining the current traces from the $2\Delta G_{3HB}$ population: **Figure 3.4**b displays the traces of 4 blockade events from the $2\Delta G_{3HB}$ population which span the entire range of translocation times from the 400 mV data in Figure 4a (events highlighted in red in **Figure 3.4**a). Unlike typical folded DNA translocations which usually show a folded state followed by a single-file state, the longer blockades instead begin with a shallow blockage state, followed by a deeper one. In fact, over 90 % of events from the $2\Delta G_{3HB}$ population can be temporally truncated into three consecutive blockage states, as demonstrated in **Figure 3.4**c. The first blockage state is noisy and can last up to $10^5\ \mu s$; We label this blockage state the metastable state. The last two blockage states closely correspond to a blockage of $2\Delta G_{3HB}$ followed by a ΔG_{3HB} blockage, as expected of normal folded events.

Interestingly, the duration of the metastable state τ_{META} is strongly correlated to the total event duration τ: meta-stable states contributes the most to the total event duration. This strong correlation is further displayed in **Figure 3.13**. **Figure 3.4**d plots the voltage dependence of duration of the metastable state τ_{META} and of the final two states $\tau_{21} = \tau - \tau_{META}$ (see **Figure 3.4**c), where it is shown that τ_{21} monotonically reduces with voltages, as expected from typical translocations, whereas τ_{META} monotonically increases with voltage, as expected from collision-like events. Interestingly, the dependence of τ_{21} on voltage is well described by a power scaling law $\tau_{21} \sim x^{-1.80\Delta V}$, whereas the metastable state is better described by an exponential function $\tau_{META} = 30e^{0.012\Delta V}$. We therefore conclude that the metastable state is solely responsible for the collision-like behavior of longer blockades, and therefore for the wide duration spread observed in **Figure 3.4**a. Moreover, > 90% of events in the $2\Delta G_{3HB}$ population appear to be normally folded 3HB translocations preceded by a metastable state. Note that a small portion of folded events only have two states instead of three: the metastable state followed by a folded state $2\Delta I_{3HB}$, expected events folding near their center.

To better understand the nature and origin of the metastable state, we now report how ionic current is altered by the 3HB-induced metastable state. **Figure 3.4**e displays the histograms of the metastable state blockage currents ΔG_{META} measured at different voltages. Note that since the metastable state is noisy and spans multiple orders of magnitude in duration, the histograms were obtained by averaging the normalized raw current histograms of each individual event. Moreover, note that the ΔG_{META} histograms were normalized by the single-file blockage state ΔG_{3HB} to reduce inter-measurement variability. **Figure 3.4**e shows that the most probable $\Delta G_{META}/\Delta G_{3HB}$ value increases monotonically with voltage. When measured at 200 mV, the most probable metastable state blockage value is $\Delta G_{META}/\Delta G_{3HB} \approx 0.75$, and therefore less current is blocked than during a single-file translocation. The opposite is true for higher voltages for which $\Delta G_{META}/\Delta G_{3HB}$ is peaked around ≈ 1.25 under 450 mV. Finally, **Figure 3.4**f shows the histogram of the metastable state blockage noise CV_{META}/CV_{3HB} measured at different voltages. Here noise is quantified using the coefficient of variation $CV_{META} = \sigma_{META}/\Delta G_{META}$, *i.e.*, the ratio of the standard deviation σ_{META} and mean ΔG_{META} of the ionic blockage during the metastable state. Note that the metastable noise CV_{meta} is normalized by the single-file noise CV_{3HB} to again reduce measurement variability. **Figure 3.4**f shows that the metastable state noise reduces with increasing voltage. Interestingly, for higher voltages, the metastable state noise reduces to that of single-file 3HB translocations, as shown by the CV_{meta}/CV_{3HB} distribution centered around 1 at 450 mV. In **Figure 3.16**, it is further shown that the current blockage during the metastable state displays voltage-independent $1/f$ noise.

The voltage trends identified in **Figure 3.4** help paint a close-to-complete picture of the mechanism by which 3HB molecules fold inside nanopores. The bending and folding of 3HB molecules inside nanopores, identified by the last two blockage states (see **Figure 3.4**c), is preceded by a collision-like metastable state which lasts longer, blocks more current, and gets less noisy with larger voltages. Based on these observations, we interpret the folding steps as follows: 1) A 3HB approaches the nanopore and is not captured by an end, but instead is docked against the pore at some point along its contour; 2) Due to its high local rigidity ($\ell_{3HB} > \ell_{DNA} > d_{pore}$), the 3HB molecule does not bend inside the pore; It instead diffuses laterally, the action of which is hindered by the electric field in the vicinity of the pore; 3) A segment of weaker local rigidity along the 3HB finds the nanopore, and facilitates bending and entering inside the nanopore; 4) Normal 2-1 folded translocation occurs, wherein two 3HB segments are in the pore at once, followed by a single segment.

According to the above, the metastable state is a direct result of the docking stage in which 3HB diffuses laterally along its contour, and stronger electric fields induced by higher voltages pull the structures deeper into the pore mouth, making it harder to diffuse laterally, and therefore increasing the average time required to find a weaker spot along the 3HB contour. Note that the introduction of heterogeneous rigidity is necessary to explain the increasing metastable duration with voltage: A uniformly rigid molecule too stiff to bend instantly inside nanopores would require on average a non-zero time τ_{unif} to successfully overcome the bending energy barrier and enter the nanopore. Increasing the voltage would reduce τ_{unif} due the rigidity uniformity and to higher fields facilitating the barrier crossing. From the above folding interpretation however, 3HB molecules must diffuse an average distance δL between their initial docking points and the closest weaker spot. This would require time $\tau_{META} \sim \delta L^2 / D_{lat}(\Delta V)$, where $D_{lat}(\Delta V)$ is the lateral diffusion coefficient, which reduces exponentially with voltage according to Figure 4d. Interestingly, the idea that 3HB is docked and diffuses laterally is further supported by some blockade events displaying the metastable state followed solely by a single-file blockage state instead of a 2-1 sequence as shown in **Figure 3.18**a-i. Such events were presumably docked near their ends and diffused until their ends were captured by the pore, resulting in a single-file translocation. The mobility results help explain the origin of the docking of the 3HB, lower mobility which results in a larger portion of the molecules arriving flat at the pore mouth. Finally, note that the metastable state was observed in almost all experimental conditions tested, but was more prominent under high voltages and low salt concentrations, as shown in **Figure 3.19** and **Figure 3.20**, *i.e.*, conditions optimizing the electrophoretic response of 3HB molecules. Furthermore, we extrapolated the free-solution mobility for the 3HB molecules using various percentages of Agarose gels and confirmed that the 3HB indeed has a lower mobility compared to DNA molecules with similar length, 2kbp dsDNA, as shown in Section 3.5.5.

To examine the origin of the weak spots on the 3HB structure as well as the deeper blockade events at $9\Delta G_{DNA}$, we purposefully induced defects by introducing the samples to a heat shock: Using a thermal cycler, different samples of the same 3HB assembly batch were heated to a temperature of 65 $^{\circ}C$ for durations of 0, 30, 60, 120, 180, and 300 seconds, in order to purposefully induce 3HB defects and mis-assemblies. The samples were then snap-cooled to 4 $^{\circ}C$ to preserve the degraded state, and immediately characterized by nanopore and gel electrophoresis.

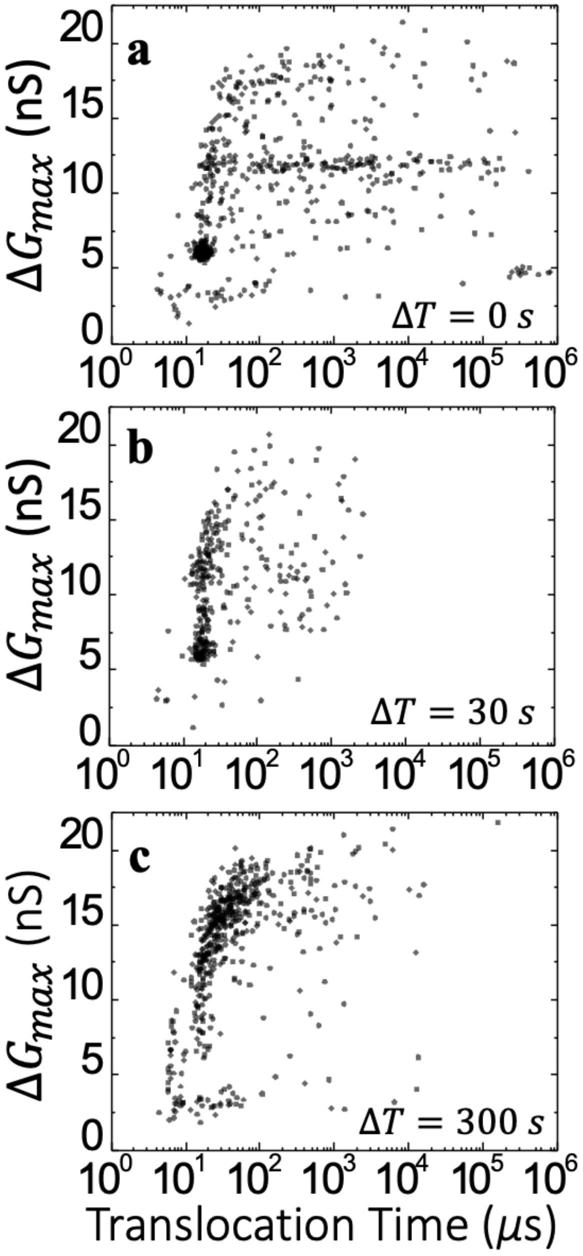

Figure 3.5. Thermal response of helix bundle nanostructures. (a-c) Scatter plots of Maximum blockage level versus translocation time of 3HB structures heated at 65 C for $\Delta T = 0$, 30, and 300 seconds, respectively. All nanopore experiments are performed using a 11.3 nm pore in 0.9 M LiCl with an applied bias of 400 mV.

Figure 3.5 shows the scatter plots of maximum blockage ΔG_{max} level *versus* translocation time of the 3HB molecules heated for $\Delta T = 0$, 30 and 300 seconds, and passing through a 9.5 nm nanopore, in 0.9M LiCl, and under a 400 mV applied voltage. The nanopore and gel electrophoresis characterization of 3HB thermal response at $\Delta T = 1$, 2, and 3 minutes are shown in Section 3.5.6. The 3HB blockades in pristine condition ($\Delta T = 0$) show blockages and translocation times consistent with that of **Figure 3.4**a: a well-defined single-file population at $\Delta G_{3HB} = 3\Delta G_{DNA}$, a wide-spread of folded-state population at $2\Delta G_{3HB}$ dur to the meta-stable states, and a $3\Delta G_{3HB}$ population corresponding to 3HB folded twice on itself. As the samples are heated, even for as short as 30 seconds, two observations can be made: first, the distinct populations begin to spread in maximum blockage level and start to become a streak of single-molecule events; and second, the long meta-stable state events disappear. When the samples are heated for longer periods of times, the trend continues, and eventually barely any single-file 3HB events remained, as shown in **Figure 3.5**a-c. The reduction and eventual disappearance of single-file passage and meta-stable events indicate that the structures degrade and become more flexible as more defects appear on the structure when heated for longer times. The nanopore results shown in **Figure 3.5** and **Figure 3.24** are consistent with gel electrophoresis results in **Figure 3.23** – as samples are heated, the 3HB band migrate faster, and more "staple" strands fall off, as the fastest migrating band gain brightness with more heat shock. Therefore, we hypothesize that the double-folded events are likely translocation events of mis-assembled 3HB structures.

3.3 Conclusion

Nanopores combined with DNA nanotechnology provides an interesting approach in biophysical studies and provides more insights in molecular transport. Here, we used measurements of ionic current to characterize transport properties of origami structures through solid-state nanopores, we identified and classified the events produced by origami structures and established a basis of probing local defects and impurities in such structures. We fully characterized and profiled both nanostructures in 0.45 to 3.6 M LiCl salt with an applied voltage from 100 to 1000 mV, using nanopores ranging from 9 to 15 nm in diameter. Specifically, we find that the ldsDNA mis-assemblies caused by random cuts in the M13mp18 scaffold result in an additional smear of shorter translocation events; the meta-stable state events present in 3HB folded events indicate the occurrence of lateral diffusion to facilitate translocation, suggesting possible local defects throughout the structure. In addition, we observed partial to total degradation of the 3HB molecules when introduced to heat for $\Delta t > 30$ seconds, this thermal response suggests mis-assembled products, although relatively rare, do make up a portion of the final products. Finally, all nanopore results collected in this study were confirmed by Agarose gel electrophoresis. Results from nanopores arrived at the same conclusion and demonstrated considerably improved sensitivity through single-molecules measurements.

3.4 Experimental Methods

3.4.1 Scaffold Preparation

The linearized M13 single-stranded DNA scaffolds were prepared from M13mp18 circular single-stranded DNA (New England Biolabs, N4040S). To attach the primer, primer strand was added in a mixture with 10 μg M13mp18 circular single-stranded DNA at a ratio of 10:1 in 1x NEB 3.1 buffer, the mixture was heated to 95 ^{o}C and slowly cooled down to room temperature in a MiniAmp Plus Thermal Cycler (ThermoFisher Scientific, #A37835). A mixture of prepared circular scaffold (with primer attached), and 10 units of HincII restriction enzyme (New England Biolabs, R0103S) in a total reaction volume of 50 μL in 1x NEB 3.1 buffer were incubated at 37 ^{o}C for 3 hours, then heat inactivated at 65 ^{o}C for 20 minutes in the thermal cycler.

The linearized products were characterized by denaturing agarose gel electrophoresis at 1% in 1x TAE buffer (40 mM Tris, 20 mM acetic acid, and 2 mM EDTA, pH 10.5). Upon completion, the agarose gel was submerged in 1xTAE buffer (40 mM Tris, 20 mM acetic acid, and 2 mM EDTA) at pH 8 and incubated on incubator at 60 RPM for an hour to bring gel pH back to 8. The gel was then submerged in 2x gel volume de-ionized water with 1x GelRed (Biotium, #41003) for 45 minutes on incubator then store at 4 ^{o}C overnight to post stain. As shown in **Figure 3.6**, linear single-stranded M13 migrate faster than circular single-stranded M13 molecules, the disappearance of circular band is an indication of complete cut. The sequence of the linearized M13 scaffold is provided in Section 3.5.1.

3.4.2 Nanostructure Assembly

For the assembly of the 3HB molecules, the scaffold (linearized M13mp18 from New England Biolabs, N4040S) was mixed with staple strands (191 staple strands for 3HB, and 181 staple strands for ldsM13) at a molar ratio of 1:10 in assembly buffer (at final 40 mM Tris, 20 mM acetic acid, 2 mM EDTA, and 16 mM $MgCl_2$, pH 8). The product is heated to 95 ^{o}C for 5 minutes, cooled to 90 ^{o}C, ramped from 90 ^{o}C to 60 ^{o}C at a rate of 0.4 ^{o}C per minute, then from 60 ^{o}C to 26 ^{o}C at a rate of 0.03 $^{\circ}C$, and snap cooled to 4 $^{\circ}C$ using minicamp Plus Thermal Cycler (ThermoFisher Scientific, #A37835). After the assembly, the nanostructures were spun down using 100 kDa Amicon Ultra-0.5 Centrifugal Filter Unit (Millipore Sigma, UFC500396), three washes with the assembly buffer were performed to completely remove excess staple strands present in the solution. Similarly, the ldsM13 molecules were assembled using 181 staple strands and linearized M13mp18 scaffold from Tilibit (Tilibit Nanosystems GmbH, M1-12) at a ratio of 5:1. The assembled products were visualized on 1% agarose gel in 1x TAE buffer (40 mM Tris, 20 mM acetic acid, and 2 mM EDTA, pH 8), as shown in 3.5.1. Generuler 1 kb plus DNA Ladder (ThermoFisher Scientific, SM1331) was used as a reference guide for nanostructure migration. GelRed (Biotium, #41003) was used for visualization of the DNA bands.

3.4.3 Nanopore Sensing

The DNA nanostructures in 1x assembly buffer were added to a LiCl solution of 0.45 M to 3.6 M for nanopore sensing, typically 5 μL of the nanostructure solution was added to 35 μL LiCl buffered with 10 mM HEPES at pH 8. Linear 2kbp (ThermoFisher Scientific, SM1701) and 7kbp (ThermoFisher Scientific, SM1741) NoLimits DNA fragments were always run prior to nanostructures or in a mixture to normalize pore geometry variations during post-processing. Samples were introduced to the *cis* side of the chip and a negative voltage was applied to the *cis* side with the *trans* side grounded. The ionic current recordings were performed in MATLAB 2013a (32-bit) using the VC100 current amplifier (Chimera Instruments) with sampling frequency of 4.17 MHz and a bandwidth of 1 MHz and were subsequently software low-pass Bessel filtered as needed.

3.4.4 Nanopore Fabrication

Nanopores were fabricated in 12 nm thick free-standing SiNx membranes (Norcada, NBPX5004Z) using controlled breakdown (CBD).[12,13,26,27] CBD was performed in 1 M KCl buffered with 10 mM HEPES at pH 8 and pores were grown to 9–12 nm in 3.6 M LiCl buffered with 10 mM HEPES at pH 8 using moderate voltage conditioning. Prior to fabrication, the chips were cleaned using air plasma for 70 seconds and painted with a layer of PDMS to reduce high-frequency noise.

3.4.5 Data Analysis

Translocation events in the recorded current traces were located and fitted using a custom implementation of the CUSUM+ algorithm.[180] A digital low-pass filter of 200 kHz was applied for the analysis unless otherwise specified. The fitted translocation events were plotted and further analyzed using the in-house analysis software Nanolyzer and OriginLab.

3.5 Supplementary Information

3.5.1 M13mp18 scaffold preparation and DNA nanostructure assembly

Scaffold Preparation

The linearized M13 single-stranded DNA scaffolds were prepared as described in the Methods Section in the main text, using M13mp18 circular single-stranded DNA (New England Biolabs, N4040S). The primer strand was added in a mixture with 10 μg M13mp18 circular single-stranded DNA at a ratio of 10:1 in 1x NEB 3.1 buffer, the mixture was heated to 95 ^{o}C and slowly cooled down to room temperature in a thermal cycler. A mixture of prepared circular scaffold (with primer attached), and 10 units of HincII restriction enzyme (New England Biolabs, R0103S) in a total reaction volume of 50 μL in 1x NEB 3.1 buffer were incubated at 37 ^{o}C for 3 hours, then heat inactivated at 65 ^{o}C for 20 minutes in a thermal cycler.

The linearized products were characterized by denaturing agarose gel electrophoresis at 1% in 1x TAE buffer (40 mM Tris, 20 mM acetic acid, and 2 mM EDTA, pH 10.5). Upon completion, the agarose gel was submerged in 1xTAE buffer at pH 8 and incubated on incubator at 60 RPM for an hour to bring gel pH back to 8. The gel was then submerged in 2x gel volume de-ionized water with 1x GelRed (Biotium, #41003) for 45 minutes on incubator then store at 4 ^{o}C overnight to post stain. As shown in **Figure 3.1**, linear single-stranded M13 (lane 3) migrate faster than circular single-stranded M13 molecules (lane 2), the disappearance of circular band is an indication of complete cut.

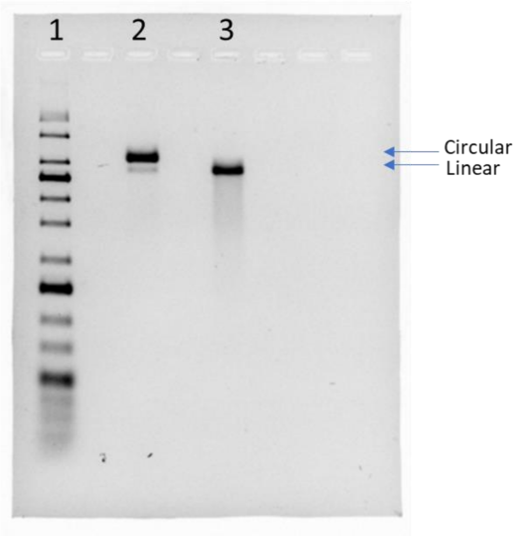

Figure 3.6. M13mp18 scaffold gel electrophoresis in denaturing gel. Lane 1: GeneRuler 1kbp plus DNA Ladder (ThermoFisher Scientific, SM1331). Lane 2: M13mp18 circular ssDNA scaffold (New England Biolabs, N4040S). Lane 3: M13mp18 linear ssDNA, digested by HincII (New England Biolabs, R0103S). The gel electrophoresis was done using 1% Agarose gel, prepared and performed in 1xTAE buffer at pH 10.5 (40 mM Tris, 20 mM acetic acid, and 2 mM EDTA, pH 10.6) on ice, with an applied voltage of 70 V.

Nanostructure assembly

Once assembled, the 3HB molecules were run on a 1% non-denaturing Agarose gel on ice, as shown in **Figure 3.7**, showing one clear band. The excess staple strands were removed by three washes using the assembly buffer (40 mM Tris, 20 mM acetic acid, 2 mM EDTA, and 16 mM MgCl2, pH 8) through 100 kDa Amicon Ultra-0.5 Centrifugal Filter Unit (Millipore Sigma, UFC500396).

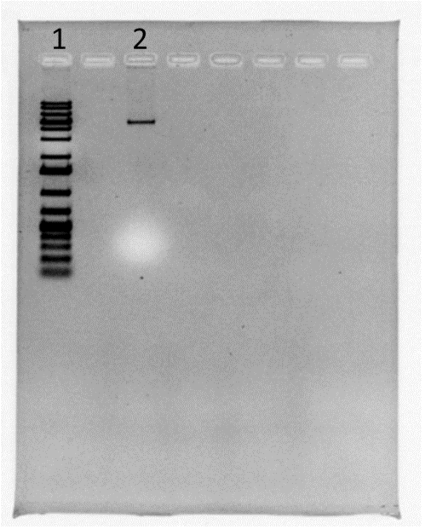

Figure 3.7. Gel electrophoresis characterization of 3HB assembly. Lane 1: Generuler 1 kb plus DNA Ladder (ThermoFisher Scientific, SM1331). Lane 2: 3HB. The gel electrophoresis was done using 1% Agarose gel, which was prepared and performed in 1xTAE buffer (40 mM Tris, 20 mM acetic acid, and 2 mM EDTA) at pH 8 on ice, with an applied voltage of 70 V.

3.5.2 Sequence and design of the assembled molecules.

The sequence of linearized M13mp18, the HincII primer sequence, a design of the molecules and the sequences of all staple strands used for both 3HB and ldsM13 are shown below.

Sequence of linearized M13mp18

The sequence of the M13mp18 scaffold is shown below, showing linearization by HincII (New England Biolabs, R0103S). The sequence with underline represents the region where the primer strand is attached. And the red sequences are the recognition site for HincII restriction enzyme.

GACCTGCAGGCATGCAAGCTTGGCACTGGCCGTCGTTTTACAACGTCGTGACTGGGAAAACCCTGGCGT
TACCCAACTTAATCGCCTTGCAGCACATCCCCCTTTCGCCAGCTGGCGTAATAGCGAAGAGGCCCGCACC
GATCGCCCTTCCCAACAGTTGCGCAGCCTGAATGGCGAATGGCGCTTTGCCTGGTTTCCGGCACCAGAA
GCGGTGCCGGAAAGCTGGCTGGAGTGCGATCTTCCTGAGGCCGATACTGTCGTCGTCCCCTCAAACTGG
CAGATGCACGGTTACGATGCGCCCATCTACACCAACGTGACCTATCCCATTACGGTCAATCCGCCGTTTG
TTCCCACGGAGAATCCGACGGGTTGTTACTCGCTCACATTTAATGTTGATGAAAGCTGGCTACAGGAAG
GCCAGACGCGAATTATTTTTGATGGCGTTCCTATTGGTTAAAAAATGAGCTGATTTAACAAAAATTTAAT
GCGAATTTTAACAAAATATTAACGTTTACAATTTAAATATTTGCTTATACAATCTTCCTGTTTTTGGGGCTT
TTCTGATTATCAACCGGGGTACATATGATTGACATGCTAGTTTTACGATTACCGTTCATCGATTCTCTTGT
TTGCTCCAGACTCTCAGGCAATGACCTGATAGCCTTTGTAGATCTCTCAAAAATAGCTACCCTCTCCGGCA
TTAATTTATCAGCTAGAACGGTTGAATATCATATTGATGGTGATTTGACTGTCTCCGGCCTTTCTCACCCT
TTTGAATCTTTACCTACACATTACTCAGGCATTGCATTTAAAATATATGAGGGTTCTAAAAATTTTTATCCT
TGCGTTGAAATAAAGGCTTCTCCCGCAAAAGTATTACAGGGTCATAATGTTTTTGGTACAACCGATTTAG
CTTTATGCTCTGAGGCTTTATTGCTTAATTTTGCTAATTCTTTGCCTTGCCTGTATGATTTATTGGATGTTA
ATGCTACTACTATTAGTAGAATTGATGCCACCTTTTCAGCTCGCGCCCCAAATGAAAATATAGCTAAACA
GGTTATTGACCATTTGCGAAATGTATCTAATGGTCAAACTAAATCTACTCGTTCGCAGAATTGGGAATCA
ACTGTTATATGGAATGAAACTTCCAGACACCGTACTTTAGTTGCATATTTAAAACATGTTGAGCTACAGC
ATTATATTCAGCAATTAAGCTCTAAGCCATCCGCAAAAATGACCTCTTATCAAAAGGAGCAATTAAAGGT
ACTCTCTAATCCTGACCTGTTGGAGTTTGCTTCCGGTCTGGTTCGCTTTGAAGCTCGAATTAAAACGCGAT
ATTTGAAGTCTTTCGGGCTTCCTCTTAATCTTTTTGATGCAATCCGCTTTGCTTCTGACTATAATAGTCAGG
GTAAAGACCTGATTTTTGATTTATGGTCATTCTCGTTTTCTGAACTGTTTAAAGCATTTGAGGGGGATTCA

ATGAATATTTATGACGATTCCGCAGTATTGGACGCTATCCAGTCTAAACATTTTACTATTACCCCCTCTGG

CAAAACTTCTTTTGCAAAAGCCTCTCGCTATTTTGGTTTTTATCGTCGTCTGGTAAACGAGGGTTATGATA

GTGTTGCTCTTACTATGCCTCGTAATTCCTTTTGGCGTTATGTATCTGCATTAGTTGAATGTGGTATTCCTA

AATCTCAACTGATGAATCTTTCTACCTGTAATAATGTTGTTCCGTTAGTTCGTTTTATTAACGTAGATTTTT

CTTCCCAACGTCCTGACTGGTATAATGAGCCAGTTCTTAAAATCGCATAAGGTAATTCACAATGATTAAA

GTTGAAATTAAACCATCTCAAGCCCAATTTACTACTCGTTCTGGTGTTTCTCGTCAGGGCAAGCCTTATTC

ACTGAATGAGCAGCTTTGTTACGTTGATTTGGGTAATGAATATCCGGTTCTTGTCAAGATTACTCTTGAT

GAAGGTCAGCCAGCCTATGCGCCTGGTCTGTACACCGTTCATCTGTCCTCTTTCAAAGTTGGTCAGTTCG

GTTCCCTTATGATTGACCGTCTGCGCCTCGTTCCGGCTAAGTAACATGGAGCAGGTCGCGGATTTCGACA

CAATTTATCAGGCGATGATACAAATCTCCGTTGTACTTTGTTTCGCGCTTGGTATAATCGCTGGGGGTCA

AAGATGAGTGTTTTAGTGTATTCTTTTGCCTCTTTCGTTTTAGGTTGGTGCCTTCGTAGTGGCATTACGTA

TTTTACCCGTTTAATGGAAACTTCCTCATGAAAAAGTCTTTAGTCCTCAAAGCCTCTGTAGCCGTTGCTAC

CCTCGTTCCGATGCTGTCTTTCGCTGCTGAGGGTGACGATCCCGCAAAAGCGGCCTTTAACTCCCTGCAA

GCCTCAGCGACCGAATATATCGGTTATGCGTGGGCGATGGTTGTTGTCATTGTCGGCGCAACTATCGGT

ATCAAGCTGTTTAAGAAATTCACCTCGAAAGCAAGCTGATAAACCGATACAATTAAAGGCTCCTTTTGGA

GCCTTTTTTTTGGAGATTTTCAACGTGAAAAAATTATTATTCGCAATTCCTTTAGTTGTTCCTTTCTATTCTC

ACTCCGCTGAAACTGTTGAAAGTTGTTTAGCAAAATCCCATACAGAAAATTCATTTACTAACGTCTGGAA

AGACGACAAAACTTTAGATCGTTACGCTAACTATGAGGGCTGTCTGTGGAATGCTACAGGCGTTGTAGT

TTGTACTGGTGACGAAACTCAGTGTTACGGTACATGGGTTCCTATTGGGCTTGCTATCCCTGAAAATGAG

GGTGGTGGCTCTGAGGGTGGCGGTTCTGAGGGTGGCGGTTCTGAGGGTGGCGGTACTAAACCTCCTGA

GTACGGTGATACACCTATTCCGGGCTATACTTATATCAACCCTCTCGACGGCACTTATCCGCCTGGTACTG

AGCAAAACCCCGCTAATCCTAATCCTTCTCTTGAGGAGTCTCAGCCTCTTAATACTTTCATGTTTCAGAAT

AATAGGTTCCGAAATAGGCAGGGGGCATTAACTGTTTATACGGGCACTGTTACTCAAGGCACTGACCCC

GTTAAAACTTATTACCAGTACACTCCTGTATCATCAAAAGCCATGTATGACGCTTACTGGAACGGTAAAT

TCAGAGACTGCGCTTTCCATTCTGGCTTTAATGAGGATTTATTTGTTTGTGAATATCAAGGCCAATCGTCT

GACCTGCCTCAACCTCCTGTCAATGCTGGCGGCGGCTCTGGTGGTGGTTCTGGTGGCGGCTCTGAGGGT

GGTGGCTCTGAGGGTGGCGGTTCTGAGGGTGGCGGCTCTGAGGGAGGCGGTTCCGGTGGTGGCTCTG

GTTCCGGTGATTTTGATTATGAAAAGATGGCAAACGCTAATAAGGGGGCTATGACCGAAAATGCCGATG

AAAACGCGCTACAGTCTGACGCTAAAGGCAAACTTGATTCTGTCGCTACTGATTACGGTGCTGCTATCGA

TGGTTTCATTGGTGACGTTTCCGGCCTTGCTAATGGTAATGGTGCTACTGGTGATTTTGCTGGCTCTAATT

CCCAAATGGCTCAAGTCGGTGACGGTGATAATTCACCTTTAATGAATAATTTCCGTCAATATTTACCTTCC

CTCCCTCAATCGGTTGAATGTCGCCCTTTTGTCTTTGGCGCTGGTAAACCATATGAATTTTCTATTGATTG

TGACAAAATAAACTTATTCCGTGGTGTCTTTGCGTTTCTTTTATATGTTGCCACCTTTATGTATGTATTTTC

TACGTTTGCTAACATACTGCGTAATAAGGAGTCTTAATCATGCCAGTTCTTTTGGGTATTCCGTTATTATT

GCGTTTCCTCGGTTTCCTTCTGGTAACTTTGTTCGGCTATCTGCTTACTTTTCTTAAAAAGGGCTTCGGTAA

GATAGCTATTGCTATTTCATTGTTTCTTGCTCTTATTATTGGGCTTAACTCAATTCTTGTGGGTTATCTCTCT

GATATTAGCGCTCAATTACCCTCTGACTTTGTTCAGGGTGTTCAGTTAATTCTCCCGTCTAATGCGCTTCC

CTGTTTTTATGTTATTCTCTCTGTAAAGGCTGCTATTTTCATTTTTGACGTTAAACAAAAAATCGTTTCTTA

TTTGGATTGGGATAAATAATATGGCTGTTTATTTTGTAACTGGCAAATTAGGCTCTGGAAAGACGCTCGT

TAGCGTTGGTAAGATTCAGGATAAAATTGTAGCTGGGTGCAAAATAGCAACTAATCTTGATTTAAGGCT

TCAAAACCTCCCGCAAGTCGGGAGGTTCGCTAAAACGCCTCGCGTTCTTAGAATACCGGATAAGCCTTCT

ATATCTGATTTGCTTGCTATTGGGCGCGGTAATGATTCCTACGATGAAAATAAAAACGGCTTGCTTGTTC

TCGATGAGTGCGGTACTTGGTTTAATACCCGTTCTTGGAATGATAAGGAAAGACAGCCGATTATTGATT

GGTTTCTACATGCTCGTAAATTAGGATGGGATATTATTTTTCTTGTTCAGGACTTATCTATTGTTGATAAA

CAGGCGCGTTCTGCATTAGCTGAACATGTTGTTTATTGTCGTCGTCTGGACAGAATTACTTTACCTTTTGT

CGGTACTTTATATTCTCTTATTACTGGCTCGAAAATGCCTCTGCCTAAATTACATGTTGGCGTTGTTAAAT

ATGGCGATTCTCAATTAAGCCCTACTGTTGAGCGTTGGCTTTATACTGGTAAGAATTTGTATAACGCATA

TGATACTAAACAGGCTTTTTCTAGTAATTATGATTCCGGTGTTTATTCTTATTTAACGCCTTATTTATCACA

CGGTCGGTATTTCAAACCATTAAATTTAGGTCAGAAGATGAAATTAACTAAAATATATTTGAAAAAGTTT

TCTCGCGTTCTTTGTCTTGCGATTGGATTTGCATCAGCATTTACATATAGTTATATAACCCAACCTAAGCC

GGAGGTTAAAAAGGTAGTCTCTCAGACCTATGATTTTGATAAATTCACTATTGACTCTTCTCAGCGTCTTA

ATCTAAGCTATCGCTATGTTTTCAAGGATTCTAAGGGAAAATTAATTAATAGCGACGATTTACAGAAGCA

AGGTTATTCACTCACATATATTGATTTATGTACTGTTTCCATTAAAAAAGGTAATTCAAATGAAATTGTTA

AATGTAATTAATTTTGTTTTCTTGATGTTTGTTTCATCATCTTCTTTTGCTCAGGTAATTGAAATGAATAAT

TCGCCTCTGCGCGATTTTGTAACTTGGTATTCAAAGCAATCAGGCGAATCCGTTATTGTTTCTCCCGATGT

AAAAGGTACTGTTACTGTATATTCATCTGACGTTAAACCTGAAAATCTACGCAATTTCTTTATTTCTGTTTT

ACGTGCAAATAATTTTGATATGGTAGGTTCTAACCCTTCCATTATTCAGAAGTATAATCCAAACAATCAG

GATTATATTGATGAATTGCCATCATCTGATAATCAGGAATATGATGATAATTCCGCTCCTTCTGGTGGTTT

CTTTGTTCCGCAAAATGATAATGTTACTCAAACTTTTAAAATTAATAACGTTCGGGCAAAGGATTTAATAC

GAGTTGTCGAATTGTTTGTAAAGTCTAATACTTCTAAATCCTCAAATGTATTATCTATTGACGGCTCTAAT

CTATTAGTTGTTAGTGCTCCTAAAGATATTTTAGATAACCTTCCTCAATTCCTTTCAACTGTTGATTTGCCA

ACTGACCAGATATTGATTGAGGGTTTGATATTTGAGGTTCAGCAAGGTGATGCTTTAGATTTTTCATTTG

CTGCTGGCTCTCAGCGTGGCACTGTTGCAGGCGGTGTTAATACTGACCGCCTCACCTCTGTTTTATCTTCT

GCTGGTGGTTCGTTCGGTATTTTTAATGGCGATGTTTTAGGGCTATCAGTTCGCGCATTAAAGACTAATA

GCCATTCAAAAATATTGTCTGTGCCACGTATTCTTACGCTTTCAGGTCAGAAGGGTTCTATCTCTGTTGGC

CAGAATGTCCCTTTTATTACTGGTCGTGTGACTGGTGAATCTGCCAATGTAAATAATCCATTTCAGACGAT

TGAGCGTCAAAATGTAGGTATTTCCATGAGCGTTTTTCCTGTTGCAATGGCTGGCGGTAATATTGTTCTG

GATATTACCAGCAAGGCCGATAGTTTGAGTTCTTCTACTCAGGCAAGTGATGTTATTACTAATCAAAGAA

GTATTGCTACAACGGTTAATTTGCGTGATGGACAGACTCTTTTACTCGGTGGCCTCACTGATTATAAAAA

CACTTCTCAGGATTCTGGCGTACCGTTCCTGTCTAAAATCCCTTTAATCGGCCTCCTGTTTAGCTCCCGCTC

TGATTCTAACGAGGAAAGCACGTTATACGTGCTCGTCAAAGCAACCATAGTACGCGCCCTGTAGCGGCG

CATTAAGCGCGGCGGGTGTGGTGGTTACGCGCAGCGTGACCGCTACACTTGCCAGCGCCCTAGCGCCC

GCTCCTTTCGCTTTCTTCCCTTCCTTTCTCGCCACGTTCGCCGGCTTTCCCCGTCAAGCTCTAAATCGGGGG

CTCCCTTTAGGGTTCCGATTTAGTGCTTTACGGCACCTCGACCCCAAAAAACTTGATTTGGGTGATGGTTC

ACGTAGTGGGCCATCGCCCTGATAGACGGTTTTTCGCCCTTTGACGTTGGAGTCCACGTTCTTTAATAGT

GGACTCTTGTTCCAAACTGGAACAACACTCAACCCTATCTCGGGCTATTCTTTTGATTTATAAGGGATTTT

GCCGATTTCGGAACCACCATCAAACAGGATTTTCGCCTGCTGGGGCAAACCAGCGTGGACCGCTTGCTG

CAACTCTCTCAGGGCCAGGCGGTGAAGGGCAATCAGCTGTTGCCCGTCTCACTGGTGAAAAGAAAAACC

ACCCTGGCGCCCAATACGCAAACCGCCTCTCCCCGCGCGTTGGCCGATTCATTAATGCAGCTGGCACGAC

AGGTTTCCCGACTGGAAAGCGGGCAGTGAGCGCAACGCAATTAATGTGAGTTAGCTCACTCATTAGGCA

CCCCAGGCTTTACACTTTATGCTTCCGGCTCGTATGTTGTGTGGAATTGTGAGCGGATAACAATTTCACA

CAGGAAACAGCTATGACCATGATTACGAATTCGAGCTCGGTACCCGGGGATCCTCTAGAGTC

Structure Design

The caDNAno designs of 3HB and ldsDNA are shown in **Figure 3.8**. Due to their length and the repetition nature, only a partial design is shown here, and the full sequences of staple strands are given later in the section. The long blue strand represents the M13mp18 scaffold, and the short, coloured strands are the staple strands, where the arrow side is the 3’ end.

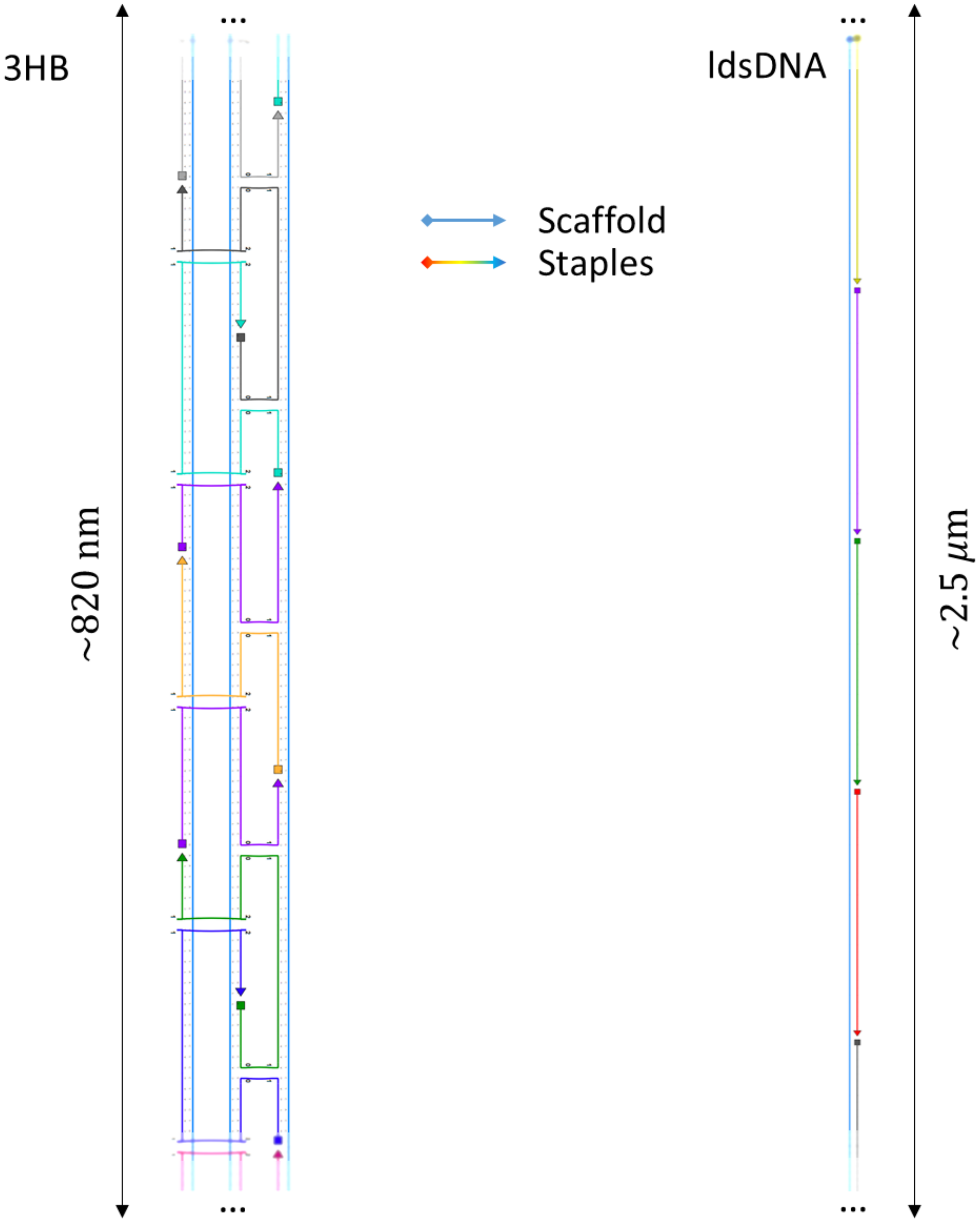

Figure 3.8. Designs of 3HB and ldsDNA molecules. Left: 3HB molecule design on a honey-comb lattice, using M13mp18 scaffold (circular, New England Biolabs, N4040S), linearized at HincII (New England Biolabs, R0103S) site, using 191 staple strands with an average oligo length of 38 nt, the 3HB has a length of approximately 820 nm. Right: ldsDNA design, using the same M13mp18 scaffold, using 181 staple strands with an average oligo length of 40 nt, the ldsDNA molecule has a length of approximately 2.5 μm.

Sequences of Staple strands

3HB

The 3HB molecules were assembled by mixing the linearized single stranded M13 scaffold with 191 staple strands at a molar ratio of 1:10 in assembly buffer (at final 40 mM Tris, 20 mM acetic acid, 2 mM EDTA, and 16 mM $MgCl_2$, pH 8). The mixture was heated to 95 $^{\mathrm{o}}C$ for 5 minutes, cooled to 90 $^{\mathrm{o}}C$, ramped from 90 $^{\mathrm{o}}C$ to 60 $^{\mathrm{o}}C$ at a rate of 0.4 $^{\mathrm{o}}C$ per minute, then from 60 $^{\mathrm{o}}C$ to 26 $^{\mathrm{o}}C$ at a rate of 0.03 $^{\mathrm{o}}C$, and snap cooled to 4 $^{\mathrm{o}}C$ using minicamp Plus Thermal Cycler (ThermoFisher Scientific, #A37835). The nanostructures were subsequently washed three times using 100 kDa Amicon Ultra-0.5 Centrifugal Filter Unit (Millipore Sigma, UFC500396) using the assembly buffer to remove the excess staple oligos. The sequences of the 3HB staple oligos are shown in **Table 3.1**.

Oligo	Sequence	Length
1	CGACGGCGTTATACACCGGAATCATAATTACTAGAAAAAG	40
2	CCCAGTCATAAAGCAGGCGTTAAATAAG	28
3	GTTGGGTAGGGCTTATACCGACCGTGTG	28
4	AAAGGGGGATGTGCATATTTAACCTAAATTTAATG	35
5	CGGTGCGCGAGCCAAGAAAACTTTTTCAAATATATGGCAGAG	42
6	AGGCTGCGCAACTGTAAAGTAAATCGCAAGACAAA	35
7	GTGCCGGACAATAAAGGTTGGGTTATATAACTATACTGTCCA	42

8	TCCAGCCAGCTTTCTAATGCATACCTTTTTAACCT	35
9	GGACGACAACAAGAAGAGTCAATAGTGAATTTATCATAGATA	42
10	TCGTAACCGTGCATTCCTAATGCTTAGATTAAGAC	35
11	TAATGGGTCTTTCCATTAATTAATTTTCCCTTAGATCAATAA	42
12	TCCGTGGGAACAAAACGGGTATTGCTTCTGTAAAT	35
13	CATTAAAGCCGTTTAATGGAAACAGTACATAAATCTCGAGAA	42
14	TGGCCTTCCTGTAGGGAATCATTCATTTGAATTAC	35
15	AACCAATAGGCTTAGAAACAAACATCAAGAAAACAAAATCAG	42
16	AAATTTTTGTTAAAAACGCGAACCTGAGCAAAAGA	35
17	ATTGTAATTGAAGCCAAGTTACAAAATCGCGCAGAACTTGCG	42
18	CAGGAAGATTGTATAGTTGCTTCGCCTGATTGCTT	35
19	TGTACCCACCAACGACAGTAACAGTACCTTTTACATTATCCT	42
20	TAATCGTAAAACTATCCAGAGGGTTTAACGTCAGA	35
21	GAGAGTCATTTATCTTTGCACGTAAAACAGAAATATAAACAG	42
22	ATCTACAAAGGCTAAAACGATGAACCTACCATATC	35
23	AAATTAATTACAGATCCTGATTGTTTGGATTATACGAAAATA	42
24	AATATGATATTCAAAACAGGGGATGGCAATTCATC	35
25	GGGTGAGGAACAAACCAGAAGGAGCGGAATTATCATAACTGA	42
26	TGAGTAATGTGTAGGAGCGCTTTTTGCGGAACAAA	35
27	TTTTTAGGCCCAATGCCCGAACGTTATTAATTTTAAAGAATT	42
28	AGCCTTTATTTCAAACAATGAACAACTCGTATTAA	35

29	AAAACATGAAAAGTACATTTGAGGATTTAGAAGTAGAAGCCC	42
30	AGAGCATAAAGCTAACAAAGTTTAGAGCCGTCAAT	35
31	GGCAAAGGAATACCAGGTTATCTAAAATATCTTTAACGCAAT	42
32	ATTAACATCCAATATGATTAAACAGTTGAAAGGAA	35
33	GAAAAGGAAATACAAATATCAAACCCTCAATCAATTTAGCAA	42
34	AGCTATATTTTCATAACATATGCATCACCTTGCTG	35
35	TTAGATATTTGTCAACAGTGCCACGCTGAGAGCCACGGAATA	42
36	CTGCGAACGAGTAGTTCATATTCAGTATTAACACC	35
37	GAAGTTTAACCGATCCGAACGAACCACCAGCAGAAAAAGGGC	42
38	TAAATATGCAACTATAAATATAAAACATCGCCATT	35
39	AATTGCTGTCACCGTTTGAATGGCTATTAGTCTTTGGTGAAT	42
40	GGTCATTTTTGCGGGGAATTAATACGTGGCACAGA	35
41	TTAGAGAAGCAAGGTGGCCAACAGAGATAGAACCCGCACCAT	42
42	ACCGGAAGCAAACTAATGAAACCAGTAATAAAAGG	35
43	TATCGCGATCAAGTTGAAATGGATTATTTACATTGTCAGTAG	42
44	ATTAAGAGGAAGCCAGACTGTACATTTTGACGCTC	35
45	TTATAGTCTTATTACCGCCAGCCATTGCAACAGGATCGGTCA	42
46	ATCAAAAATCAGGTTTCATAAGTAATATCCAGAAC	35
47	GCTTTAAGCCTCCCTCACTTGCCTGAGTAGAAGAACCACCAC	42
48	ATAAATATTCATTGCTCAGAACTTCTTTGATTAGT	35
49	TTAGACTACCAGAAAAAAGAGTCTGTCCATCACGCCCCTCAG	42

50	TTTGCCAGAGGGGGGCCGCCATAATCAGTGAGGCC	35
51	AAACCAAGCCTTGATTAGACAGGAACGGTACGCCAAGGTCAG	42
52	ATAACCCTCGTTTATAAATCCAGGAGGCCGATTAA	35
53	AAGGAATTTTACCGTATAACGTGCTTTCCTCGTTAGCGCAGT	42
54	TTCAACTAATGCAGATACATGATGGTTGCTTTGAC	35
55	GAAAGATTTTAACGCCACACCCGCCGCGCTTAATGTACTGGT	42
56	AACTAACGGAACAAAGTAACACGGTCACGCTGCGC	35
57	GGACGTTTCGGAACAGAAAGCGAAAGGAGCGGGCGGCCCCCT	42
58	TTTAAGAACTGGCTCATGAAAACGTGGCGAGAAAG	35
59	TTCAACTAGGATTAAAGGGAGCCCCCGATTTAGAGTCAAGAG	42
60	TAGTAAATTGGGCTAGTACCAAAGCACTAAATCGG	35
61	ATAAGGCATAGCCCAACCATCACCCAAATCAAGTTGGGTTGA	42
62	CAACGTAACAAAGCACCGTACAGGGCGATGGCCCA	35
63	AATCTTGACCCTCAAGAACGTGGACTCCAACGTCACCCTCAG	42
64	CATAGGCTGGCTGAAGAGCCAGGAACAAGAGTCCA	35
65	GAAAGAGAACCCATCAAAAGAATAGCCCGAGATAGGCAAGCC	42
66	TCATAAGGGAACCGAGTTTCGTCGGCAAAATCCCT	35
67	ATGTTACCAGACAGTGCCCCAGCAGGCGAAAATCCCCTGTAG	42
68	AATTGTGTCGAAATGTAACGAAGCAAGCGGTCCAC	35
69	CAAAGTATGAATTTAACAGCTGATTGCCCTTCACCCAGACGT	42
70	ACCCCCAGCGATTATGCTAAACTTTTCACCAGTGA	35

71	AGAGGCAAGGAACACGGGGAGAGGCGGTTTGCGTAGAGTGAG	42
72	CACTACGAAGGCACGAATAATATTAATGAATCGGC	35
73	GGAAGTTTCCAAAACACTGCCCGCTTTCCAGTCGGTCCAAAA	42
74	GCTTTGAGGACTAATATCGGTTCACATTAATTGCG	35
75	ACAGCATGCTTGATGCATAAAGTGTAAAGCCTGGGGAATTTC	42
76	GCGGGATCGTCACCCGACAATCACACAACATACGA	35
77	GCTGAGGCTTGCAGGGAGTTAAAGGCCCCACGCATTGTTA	40
78	CCTGTTTAGTATCATATGCCAGTGCCAAGCTTGCATGC	38
79	GCATTTTGGCCTCTTCGCTATTACGCCATAATTTATTTAGTT	42
80	GACGACGAAACCAGGCAAAGCGCCATTCAGTAATTTGTAAAT	42
81	AGTCCTGGACAGTATCGGCCTCAGGAAGATCAACAAAAATCA	42
82	TCGGCTGATAGGTCACGTTGGTGTAGATAAACCAAATCCTTG	42
83	CAAGCAATGTGAGCGAGTAACAACCCGTGCACTCAAATATAT	42
84	ATATAGAAGGAACGCCATCAAAAATAATAGCAAGCAAATTAA	42
85	GGAGGTTACGTTAATATTTTGTTAAAATCCTCCCGGGCGAAT	42
86	GAATCTTCGGTTGATAATCAGAAAAGCCTACAATTTCGGGAG	42
87	CCATATTTGGAGCAAACAAGAGAATCGATACAAAAAAGAAAT	42
88	GCAGCCTTGCCGGAGAGGGTAGCTATTTCAAAAATTTCTGAA	42
89	ACACCCTAAAGGCCGGAGACAGTCAAATGGAGAATTCATATT	42
90	GAGTTAAAACCCTCATATATTTTAAATGAACCCACAAAGTTT	42
91	TTTTTAATATGACCCTGTAATACTTTTGTCTTACCTTAGACT	42

92	AATAACGAATTAGCAAAATTAAGCAATACGAGGAAGGAGCAC	42
93	ACGTAGATGGCATCAATTCTACTAATAGCAGTATGATCTGGT	42
94	AGTTTATCATTTCGCAAATGGTCAATAAGACACCAGCAGCAA	42
95	GACATTCCATTCCATATAACAGTTGATTAAAGACAGATAAAA	42
96	TATCACCGAATATAATGCTGTAGCTCAACATTAAAAATGCGC	42
97	TACCATTGTACCTTTAATTGCTCCTTTTACCAGTATTCTGAC	42
98	CGACAGATTTTAATTCGAGCTTCAAAGCACCGTAAGCAGATT	42
99	TAGCCCCCAGAAGCAAAGCGGATTGCATGGCATTTAAAACGC	42
100	CGGAACCACAGTTCAGAAAACGAGAATGACCAGAGCTCAAAC	42
101	AGCCGCCGGATAGCGTCCAATACTGCGGGCCACCAAAATTAA	42
102	ACGATTGAATAGCGAGAGGCTTTTGCAATTGAGGCGAATCCT	42
103	CTCTGAATACGAGGCATAGTAAGAGCAAATGGAAAGAATCAG	42
104	AATAAGTTCATCAGTTGAGATTTAGGAAAGGAGTGCGCCGCT	42
105	GCCTATTGGGAAGAAAAATCTACGTTAAAGTTAATCTAGGGC	42
106	AAGGATTTTAATCATTGTGAATTACCTTAGACTCCCTTGACG	42
107	TATAAGTTTGCCCTGACGAGAAACACCAGTCGAGATTTTGGG	42
108	AACCGCCACAAGAACCGGATATTCATTAACCGCCAAAGGGCG	42
109	CAATAGGGACAGATGAACGGTGTACAGAAGGGATAGGTTGAG	42
110	CATTCCATTAGCCGGAACGAGGCGCAGATACAACGTGTTTGA	42
111	TAGTAAACAACGGAGATTTGTATCATCGGTCTTTCGCCTGGC	42
112	AATAGAAAAAGAATACACTAAAACACTCTTCAGCGTTGGGCG	42

113	AAAAGGCTCCATTAAACGGGTAAAATACGAAAATCGAAACCT	42
114	TTAAACACGGAACGAGGGTAGCAACGGCTCGAGGTGTGCCTA	42
115	AATAAACAAATTCTTACCAGTACGACGTTGTAAAA	35
116	ATAAATACAACGCTCAACAGTAACGCCAGGGTTTT	35
117	GTTTGAAAATTGAGAATCGCCTGCAAGGCGATTAA	35
118	AATTTCATCTTCTGACAACGCCAACATGGCTGGCG	35
119	GAACGCGGTAATAAGAGAATATTGGGAAGGGCGAT	35
120	GCTGATGCAAATCCCCGACAAAAGGTAAGCCATTC	35
121	CCGGCTTACAACATGTTCAGCCGGCACCGCTTCTG	35
122	TAGGTCTGAGAGACGAACGCGCCTGTTTATCGCAC	35
123	GCTGAGAAAAATAATATCCCACTGCCAGTTTGAGG	35
124	AAAACATAGCGATATTACGAGCATGTAGGGGCGCA	35
125	CGTCGCTTTATCATTCCAAGACGGCGGATTGACCG	35
126	GTGAGTGAATAACCTTAAACCAAGTACCCGGATTC	35
127	CTTTTTTTTATTTTCATCGTACCAGCTTTCATCAA	35
128	TTACATTTAACAATTTACCGCGCCCAATTCGCGTC	35
129	AGATGATTCCGGTATTCTAAGTCAGCTCATTTTTT	35
130	TATTCATTTCAATTGGCGTTTTAGCGAATCGCATT	35
131	TGAATACCTTAAATCAAGATTAAGCAAATATTTAA	35
132	AAACAATAACGGATATTTTGCACCCAGCCCAAAAA	35
133	TGAATATCTAACGAGCGTCTTGCATGTCAATCATA	35

134	TGCGTAGATTTTCACCTAATTTGCCAGTTGAACGG	35
135	AAAATTACCAATCCAAATAAGTCAGGTCATTGCCT	35
136	TAATGGAAGGGTTATTTTTGTTTAACGTTTGAGAG	35
137	AATATAAGAGAATAACATAAACCGTTCTAGCTGAT	35
138	CCTGATTATCAGATAAGCGCATTAGACGCACCATC	35
139	GAAACCAGTCAGAGGGTAATTGTAAAGATTCAAAA	35
140	GAGTAACATTATCAAATATCAGAGAGATCAATGCC	35
141	ATCCTTTAATAAGAGCAAGAACGCAAGGATAAAAA	35
142	TTACAAACAATTCGAATAGCAATAGCTACGGGAGA	35
143	AGATAATAAGCAGATAGCCGAAATCGGTTGTACCA	35
144	TAACAACTAATAGATACCAGAAGGAAACAAGCCTC	35
145	TTGAGGACAAAAGAACTGGCAAATCATACAGGCAA	35
146	CAGTTGGCAAATCAGACTCCTTATTACGTAGTAGC	35
147	AACCTCATACATAAAGGTGGCTTGGGGCGCGAGCT	35
148	ATGAAAAATCTAAAAAAAGAAACGCAAACCTGTTT	35
149	GCCTGCACAATCAATAGAAAAATTTAGTTTGACCA	35
150	CAGAGGTGAGGCGGGGTTTACCAGCGCCCCCAATT	35
151	AAAAATATGAGGGAGGGAAGGAAGTACGGTGTCTG	35
152	GAACTGATAGCCCTTGACGGAAATTATTCATGTTT	35
153	CAATATTACTTGAGCCATTTGATGGCTTAGAGCTT	35
154	CTGAAAGCGTAAGAGAGCCAGCAAAATCGATAAGA	35

155	GACATTCCCGGAAACGTCACCCCAACAGGTCAGGA	35
156	CACCAGTCACACGACCATCGATAGCAGCGAACCAG	35
157	AATCGTCTTGCCTTTAGCGTCCGAAAGACTTCAAA	35
158	TCATGGAAATACCTAGCGCGTTTTCATCCAAAAAG	35
159	AATATTAGCGTTTGCCATCTTCTTTACCCTGACTA	35
160	TATCGGCCTTGCTGTCAAAATCACCGGAACCATAA	35
161	AATAACATCAGAGCCGCCACCAATCCCCCTCAAAT	35
162	CCGTTGTAGCAATACCGCCACCCTCAGAAATCGTC	35
163	ACCGAGTCCACCACCAGAGCCTAATAGTAAAATGT	35
164	GAGAAGTGTTTTTAGCATTGACAGGAGGAAGAAGT	35
165	AGGGATTTATTCACAAACAAACCAGACGACGATAA	35
166	AGCGGGAGCTAAACTCATTAAAGCCAGACACTATC	35
167	GAGCACGTTCCAGTAAGCGTCATACATAACGCCAA	35
168	ACAGGGCGCGTACTGCTTTTGATGATACTACCACA	35
169	GTAACCAGGGTCAGTGCCTTGCATTATTACAGGTA	35
170	GCTGGCAAGTGTAGGTGCCCGTATAAACTAAAACG	35
171	GAAGGGACTATTATTCTGAAACATTATACCAGTCA	35
172	GGGAAAGCCGGCGAGTATTAAGAGGCTGATGCGAT	35
173	AACCCTAGCGGGGTTTTGCTCTGAGATGGTTTAAT	35
174	GTCGAGGTGCCGTAGGCGGATAAGTGCCGAACGAG	35
175	CTACGTGGGAATAGGTGTATCTGCTCATTCAGTGA	35

176	AAAAACCGTCTATCTCAGGAGGTTTAGTCCCAAAT	35
177	CTATTAAGAACCGCCACCCTCCCTTCATCAAGAGT	35
178	TGTTGTTCCAGTTTCCACCCTCATTTTCCCAGGCG	35
179	TATAAATGTACCGTAACACTGAACTGACCAACTTT	35
180	TGGTGGTTCCGAAATCACCAGTACAAACCGGTCAA	35
181	GCTGGTTCCCTCATAGTTAGCCCGCGACCTGCTCC	35
182	CCTGAGAGAGTTGCTCTAAAGTTTTGTCCCTGATA	35
183	GACGGGCTCTGTATGGGATTTTACCAAGCGCGAAA	35
184	CCAGGGTGGTTTTTCAACTTTCAACAGTATCTTTG	35
185	CAACGCGACTAAAGGAATTGCCAACCTAAAACGAA	35
186	GTCGTGCCAGCTGCAATTTTTTCACGTTGTAATGC	35
187	TTGCGCTGGAGCCTTTAATTGAGACTTTTTCATGA	35
188	ATGAGTGAGCTAACTTATCAGCTTGCTTTACAGAG	35
189	GCCGGAAACCGATAGTTGCGCCTCAGCAGCGAAAG	35
190	TCCGCTCACAATTCGACAACAACCATCGCGCTTTT	35
191	TAGCTGTTTCCTGTGTGAAATAACCGATATATTCGGTC	38
Primer for HincII	CTGCAGGTCGACTCTAGAGG	20

Table 3.1. Staple strand sequences for 3HB, and primer sequence for HincII restriction enzyme.

ldsM13

The ldsM13 molecules were assembled in a similar manner: by mixing the linearized single stranded M13 scaffold with 181 staple strands at a molar ratio of 1:10 in assembly buffer (at final 40 mM Tris, 20 mM acetic acid, 2 mM EDTA, and 16 mM $MgCl_2$, pH 8). The mixture was thermal annealed, and snap cooled to 4 ^{o}C using minicamp Plus Thermal Cycler (ThermoFisher Scientific, #A37835). The nanostructures were subsequently washed three times using 100 kDa Amicon Ultra-0.5 Centrifugal Filter Unit (Millipore Sigma, UFC500396) using the assembly buffer to remove the excess staple oligos. The sequences of the 3HB staple oligos are shown in **Table 3.2**.

Oligo	Sequence	Length
1	GACTCTAGAGGATCCCCGGGTACCGAGCTCGAATTCGTAATCATG	45
2	GTCATAGCTGTTTCCTGTGTGAAATTGTTATCCGCTCACA	40
3	ATTCCACACAACATACGAGCCGGAAGCATAAAGTGTAAAG	40
4	CCTGGGGTGCCTAATGAGTGAGCTAACTCACATTAATTGC	40
5	GTTGCGCTCACTGCCCGCTTTCCAGTCGGGAAACCTGTCG	40
6	TGCCAGCTGCATTAATGAATCGGCCAACGCGCGGGGAGAG	40
7	GCGGTTTGCGTATTGGGCGCCAGGGTGGTTTTTCTTTTCA	40
8	CCAGTGAGACGGGCAACAGCTGATTGCCCTTCACCGCCTG	40
9	GCCCTGAGAGAGTTGCAGCAAGCGGTCCACGCTGGTTTGC	40
10	CCCAGCAGGCGAAAATCCTGTTTGATGGTGGTTCCGAAAT	40
11	CGGCAAAATCCCTTATAAATCAAAAGAATAGCCCGAGATA	40
12	GGGTTGAGTGTTGTTCCAGTTTGGAACAAGAGTCCACTAT	40

13	TAAAGAACGTGGACTCCAACGTCAAAGGGCGAAAAACCGT	40
14	CTATCAGGGCGATGGCCCACTACGTGAACCATCACCCAAA	40
15	TCAAGTTTTTTGGGGTCGAGGTGCCGTAAAGCACTAAATC	40
16	GGAACCCTAAAGGGAGCCCCCGATTTAGAGCTTGACGGGG	40
17	AAAGCCGGCGAACGTGGCGAGAAAGGAAGGGAAGAAAGCG	40
18	AAAGGAGCGGGCGCTAGGGCGCTGGCAAGTGTAGCGGTCA	40
19	CGCTGCGCGTAACCACCACACCCGCCGCGCTTAATGCGCC	40
20	GCTACAGGGCGCGTACTATGGTTGCTTTGACGAGCACGTA	40
21	TAACGTGCTTTCCTCGTTAGAATCAGAGCGGGAGCTAAAC	40
22	AGGAGGCCGATTAAAGGGATTTTAGACAGGAACGGTACGC	40
23	CAGAATCCTGAGAAGTGTTTTTATAATCAGTGAGGCCACC	40
24	GAGTAAAAGAGTCTGTCCATCACGCAAATTAACCGTTGTA	40
25	GCAATACTTCTTTGATTAGTAATAACATCACTTGCCTGAG	40
26	TAGAAGAACTCAAACTATCGGCCTTGCTGGTAATATCCAG	40
27	AACAATATTACCGCCAGCCATTGCAACAGGAAAAACGCTC	40
28	ATGGAAATACCTACATTTTGACGCTCAATCGTCTGAAATG	40
29	GATTATTTACATTGGCAGATTCACCAGTCACACGACCAGT	40
30	AATAAAAGGGACATTCTGGCCAACAGAGATAGAACCCTTC	40
31	TGACCTGAAAGCGTAAGAATACGTGGCACAGACAATATTT	40
32	TTGAATGGCTATTAGTCTTTAATGCGCGAACTGATAGCCC	40
33	TAAAACATCGCCATTAAAAATACCGAACGAACCACCAGCA	40

34	GAAGATAAAACAGAGGTGAGGCGGTCAGTATTAACACCGC	40
35	CTGCAACAGTGCCACGCTGAGAGCCAGCAGCAAATGAAAA	40
36	ATCTAAAGCATCACCTTGCTGAACCTCAAATATCAAACCC	40
37	TCAATCAATATCTGGTCAGTTGGCAAATCAACAGTTGAAA	40
38	GGAATTGAGGAAGGTTATCTAAAATATCTTTAGGAGCACT	40
39	AACAACTAATAGATTAGAGCCGTCAATAGATAATACATTT	40
40	GAGGATTTAGAAGTATTAGACTTTACAAACAATTCGACAA	40
41	CTCGTATTAAATCCTTTGCCCGAACGTTATTAATTTTAAA	40
42	AGTTTGAGTAACATTATCATTTTGCGGAACAAAGAAACCA	40
43	CCAGAAGGAGCGGAATTATCATCATATTCCTGATTATCAG	40
44	ATGATGGCAATTCATCAATATAATCCTGATTGTTTGGATT	40
45	ATACTTCTGAATAATGGAAGGGTTAGAACCTACCATATCA	40
46	AAATTATTTGCACGTAAAACAGAAATAAAGAAATTGCGTA	40
47	GATTTTCAGGTTTAACGTCAGATGAATATACAGTAACAGT	40
48	ACCTTTTACATCGGGAGAAACAATAACGGATTCGCCTGAT	40
49	TGCTTTGAATACCAAGTTACAAAATCGCGCAGAGGCGAAT	40
50	TATTCATTTCAATTACCTGAGCAAAAGAAGATGATGAAAC	40
51	AAACATCAAGAAAACAAAATTAATTACATTTAACAATTTC	40
52	ATTTGAATTACCTTTTTTAATGGAAACAGTACATAAATCA	40
53	ATATATGTGAGTGAATAACCTTGCTTCTGTAAATCGTCGC	40
54	TATTAATTAATTTTCCCTTAGAATCCTTGAAAACATAGCG	40

55	ATAGCTTAGATTAAGACGCTGAGAAGAGTCAATAGTGAAT	40
56	TTATCAAAATCATAGGTCTGAGAGACTACCTTTTTAACCT	40
57	CCGGCTTAGGTTGGGTTATATAACTATATGTAAATGCTGA	40
58	TGCAAATCCAATCGCAAGACAAAGAACGCGAGAAAACTTT	40
59	TTCAAATATATTTTAGTTAATTTCATCTTCTGACCTAAAT	40
60	TTAATGGTTTGAAATACCGACCGTGTGATAAATAAGGCGT	40
61	TAAATAAGAATAAACACCGGAATCATAATTACTAGAAAAA	40
62	GCCTGTTTAGTATCATATGCGTTATACAAATTCTTACCAG	40
63	TATAAAGCCAACGCTCAACAGTAGGGCTTAATTGAGAATC	40
64	GCCATATTTAACAACGCCAACATGTAATTTAGGCAGAGGC	40
65	ATTTTCGAGCCAGTAATAAGAGAATATAAAGTACCGACAA	40
66	AAGGTAAAGTAATTCTGTCCAGACGACGACAATAAACAAC	40
67	ATGTTCAGCTAATGCAGAACGCGCCTGTTTATCAACAATA	40
68	GATAAGTCCTGAACAAGAAAAATAATATCCCATCCTAATT	40
69	TACGAGCATGTAGAAACCAATCAATAATCGGCTGTCTTTC	40
70	CTTATCATTCCAAGAACGGGTATTAAACCAAGTACCGCAC	40
71	TCATCGAGAACAAGCAAGCCGTTTTTATTTTCATCGTAGG	40
72	AATCATTACCGCGCCCAATAGCAAGCAAATCAGATATAGA	40
73	AGGCTTATCCGGTATTCTAAGAACGCGAGGCGTTTTAGCG	40
74	AACCTCCCGACTTGCGGGAGGTTTTGAAGCCTTAAATCAA	40
75	GATTAGTTGCTATTTTGCACCCAGCTACAATTTTATCCTG	40

76	AATCTTACCAACGCTAACGAGCGTCTTTCCAGAGCCTAAT	40
77	TTGCCAGTTACAAAATAAACAGCCATATTATTTATCCCAA	40
78	TCCAAATAAGAAACGATTTTTTGTTTAACGTCAAAAATGA	40
79	AAATAGCAGCCTTTACAGAGAGAATAACATAAAAACAGGG	40
80	AAGCGCATTAGACGGGAGAATTAACTGAACACCCTGAACA	40
81	AAGTCAGAGGGTAATTGAGCGCTAATATCAGAGAGATAAC	40
82	CCACAAGAATTGAGTTAAGCCCAATAATAAGAGCAAGAAA	40
83	CAATGAAATAGCAATAGCTATCTTACCGAAGCCCTTTTTA	40
84	AGAAAAGTAAGCAGATAGCCGAACAAAGTTACCAGAAGGA	40
85	AACCGAGGAAACGCAATAATAACGGAATACCCAAAAGAAC	40
86	TGGCATGATTAAGACTCCTTATTACGCAGTATGTTAGCAA	40
87	ACGTAGAAAATACATACATAAAGGTGGCAACATATAAAAG	40
88	AAACGCAAAGACACCACGGAATAAGTTTATTTTGTCACAA	40
89	TCAATAGAAAATTCATATGGTTTACCAGCGCCAAAGACAA	40
90	AAGGGCGACATTCAACCGATTGAGGGAGGGAAGGTAAATA	40
91	TTGACGGAAATTATTCATTAAAGGTGAATTATCACCGTCA	40
92	CCGACTTGAGCCATTTGGGAATTAGAGCCAGCAAAATCAC	40
93	CAGTAGCACCATTACCATTAGCAAGGCCGGAAACGTCACC	40
94	AATGAAACCATCGATAGCAGCACCGTAATCAGTAGCGACA	40
95	GAATCAAGTTTGCCTTTAGCGTCAGACTGTAGCGCGTTTT	40
96	CATCGGCATTTTCGGTCATAGCCCCCTTATTAGCGTTTGC	40

97	CATCTTTTCATAATCAAAATCACCGGAACCAGAGCCACCA	40
98	CCGGAACCGCCTCCCTCAGAGCCGCCACCCTCAGAACCGC	40
99	CACCCTCAGAGCCACCACCCTCAGAGCCGCCACCAGAACC	40
100	ACCACCAGAGCCGCCGCCAGCATTGACAGGAGGTTGAGGC	40
101	AGGTCAGACGATTGGCCTTGATATTCACAAACAAATAAAT	40
102	CCTCATTAAAGCCAGAATGGAAAGCGCAGTCTCTGAATTT	40
103	ACCGTTCCAGTAAGCGTCATACATGGCTTTTGATGATACA	40
104	GGAGTGTACTGGTAATAAGTTTTAACGGGGTCAGTGCCTT	40
105	GAGTAACAGTGCCCGTATAAACAGTTAATGCCCCCTGCCT	40
106	ATTTCGGAACCTATTATTCTGAAACATGAAAGTATTAAGA	40
107	GGCTGAGACTCCTCAAGAGAAGGATTAGGATTAGCGGGGT	40
108	TTTGCTCAGTACCAGGCGGATAAGTGCCGTCGAGAGGGTT	40
109	GATATAAGTATAGCCCGGAATAGGTGTATCACCGTACTCA	40
110	GGAGGTTTAGTACCGCCACCCTCAGAACCGCCACCCTCAG	40
111	AACCGCCACCCTCAGAGCCACCACCCTCATTTTCAGGGAT	40
112	AGCAAGCCCAATAGGAACCCATGTACCGTAACACTGAGTT	40
113	TCGTCACCAGTACAAACTACAACGCCTGTAGCATTCCACA	40
114	GACAGCCCTCATAGTTAGCGTAACGATCTAAAGTTTTGTC	40
115	GTCTTTCCAGACGTTAGTAAATGAATTTTCTGTATGGGAT	40
116	TTTGCTAAACAACTTTCAACAGTTTCAGCGGAGTGAGAAT	40
117	AGAAAGGAACAACTAAAGGAATTGCGAATAATAATTTTTT	40

118	CACGTTGAAAATCTCCAAAAAAAAGGCTCCAAAAGGAGCC	40
119	TTTAATTGTATCGGTTTATCAGCTTGCTTTCGAGGTGAAT	40
120	TTCTTAAACAGCTTGATACCGATAGTTGCGCCGACAATGA	40
121	CAACAACCATCGCCCACGCATAACCGATATATTCGGTCGC	40
122	TGAGGCTTGCAGGGAGTTAAAGGCCGCTTTTGCGGGATCG	40
123	TCACCCTCAGCAGCGAAAGACAGCATCGGAACGAGGGTAG	40
124	CAACGGCTACAGAGGCTTTGAGGACTAAAGACTTTTTCAT	40
125	GAGGAAGTTTCCATTAAACGGGTAAAATACGTAATGCCAC	40
126	TACGAAGGCACCAACCTAAAACGAAAGAGGCAAAAGAATA	40
127	CACTAAAACACTCATCTTTGACCCCCAGCGATTATACCAA	40
128	GCGCGAAACAAAGTACAACGGAGATTTGTATCATCGCCTG	40
129	ATAAATTGTGTCGAAATCCGCGACCTGCTCCATGTTACTT	40
130	AGCCGGAACGAGGCGCAGACGGTCAATCATAAGGGAACCG	40
131	AACTGACCAACTTTGAAAGAGGACAGATGAACGGTGTACA	40
132	GACCAGGCGCATAGGCTGGCTGACCTTCATCAAGAGTAAT	40
133	CTTGACAAGAACCGGATATTCATTACCCAAATCAACGTAA	40
134	CAAAGCTGCTCATTCAGTGAATAAGGCTTGCCCTGACGAG	40
135	AAACACCAGAACGAGTAGTAAATTGGGCTTGAGATGGTTT	40
136	AATTTCAACTTTAATCATTGTGAATTACCTTATGCGATTT	40
137	TAAGAACTGGCTCATTATACCAGTCAGGACGTTGGGAAGA	40
138	AAAATCTACGTTAATAAAACGAACTAACGGAACAACATTA	40

139	TTACAGGTAGAAAGATTCATCAGTTGAGATTTAGGAATAC	40
140	CACATTCAACTAATGCAGATACATAACGCCAAAAGGAATT	40
141	ACGAGGCATAGTAAGAGCAACACTATCATAACCCTCGTTT	40
142	ACCAGACGACGATAAAAACCAAAATAGCGAGAGGCTTTTG	40
143	CAAAAGAAGTTTTGCCAGAGGGGGTAATAGTAAAATGTTT	40
144	AGACTGGATAGCGTCCAATACTGCGGAATCGTCATAAATA	40
145	TTCATTGAATCCCCCTCAAATGCTTTAAACAGTTCAGAAA	40
146	ACGAGAATGACCATAAATCAAAAATCAGGTCTTTACCCTG	40
147	ACTATTATAGTCAGAAGCAAAGCGGATTGCATCAAAAAGA	40
148	TTAAGAGGAAGCCCGAAAGACTTCAAATATCGCGTTTTAA	40
149	TTCGAGCTTCAAAGCGAACCAGACCGGAAGCAAACTCCAA	40
150	CAGGTCAGGATTAGAGAGTACCTTTAATTGCTCCTTTTGA	40
151	TAAGAGGTCATTTTTGCGGATGGCTTAGAGCTTAATTGCT	40
152	GAATATAATGCTGTAGCTCAACATGTTTTAAATATGCAAC	40
153	TAAAGTACGGTGTCTGGAAGTTTCATTCCATATAACAGTT	40
154	GATTCCCAATTCTGCGAACGAGTAGATTTAGTTTGACCAT	40
155	TAGATACATTTCGCAAATGGTCAATAACCTGTTTAGCTAT	40
156	ATTTTCATTTGGGGCGCGAGCTGAAAAGGTGGCATCAATT	40
157	CTACTAATAGTAGTAGCATTAACATCCAATAAATCATACA	40
158	GGCAAGGCAAAGAATTAGCAAAATTAAGCAATAAAGCCTC	40
159	AGAGCATAAAGCTAAATCGGTTGTACCAAAAACATTATGA	40

160	CCCTGTAATACTTTTGCGGGAGAAGCCTTTATTTCAACGC	40
161	AAGGATAAAAATTTTTAGAACCCTCATATATTTTAAATGC	40
162	AATGCCTGAGTAATGTGTAGGTAAAGATTCAAAAGGGTGA	40
163	GAAAGGCCGGAGACAGTCAAATCACCATCAATATGATATT	40
164	CAACCGTTCTAGCTGATAAATTAATGCCGGAGAGGGTAGC	40
165	TATTTTTGAGAGATCTACAAAGGCTATCAGGTCATTGCCT	40
166	GAGAGTCTGGAGCAAACAAGAGAATCGATGAACGGTAATC	40
167	GTAAAACTAGCATGTCAATCATATGTACCCCGGTTGATAA	40
168	TCAGAAAAGCCCCAAAAACAGGAAGATTGTATAAGCAAAT	40
169	ATTTAAATTGTAAACGTTAATATTTTGTTAAAATTCGCAT	40
170	TAAATTTTTGTTAAATCAGCTCATTTTTTAACCAATAGGA	40
171	ACGCCATCAAAAATAATTCGCGTCTGGCCTTCCTGTAGCC	40
172	AGCTTTCATCAACATTAAATGTGAGCGAGTAACAACCCGT	40
173	CGGATTCTCCGTGGGAACAAACGGCGGATTGACCGTAATG	40
174	GGATAGGTCACGTTGGTGTAGATGGGCGCATCGTAACCGT	40
175	GCATCTGCCAGTTTGAGGGGACGACGACAGTATCGGCCTC	40
176	AGGAAGATCGCACTCCAGCCAGCTTTCCGGCACCGCTTCT	40
177	GGTGCCGGAAACCAGGCAAAGCGCCATTCGCCATTCAGGC	40
178	TGCGCAACTGTTGGGAAGGGCGATCGGTGCGGGCCTCTTC	40
179	GCTATTACGCCAGCTGGCGAAAGGGGGATGTGCTGCAAGG	40
180	CGATTAAGTTGGGTAACGCCAGGGTTTTCCCAGTCACGAC	40

181	GTTGTAAAACGACGGCCAGTGCCAAGCTTGCATGCCTGCAGGTC	44
Primer for HincII	CTGCAGGTCGACTCTAGAGG	20

Table 3.2. Staple strand sequences for ldsM13, and primer sequence for HincII restriction enzyme.

3.5.3 Analysis of double stranded M13

Circular dsM13 - Random cutting / Yield estimates

As predicted and confirmed on denaturing gel electrophoresis, M13mp18 scaffolds come in circular, but a portion of the molecules are randomly broken due to handling during the processing. In order to assess the quality of the M13mp18 scaffold and the origin of the wide distribution of translocation time of the ldsM13 results shown in **Figure 3.2** in the main text, the assembly of the ldsM13 was performed using uncut M13mp18 scaffold, thus expecting circular double stranded M13 (cdsM13). Upon assembly, we passed the cdsM13 molecules through a 7.9 nm pore and plotted the maximum blockage *versus* translocation time as well as minimum blockage *versus* translocation time.

Figure 3.9a shows the maximum blockage of the cdsM13 *versus* translocation time, the first two populations are fitted to have $\Delta G = 6.12\, nS$ and $12.40\, nS$, the lower blockade population corresponds to linear molecule passage single-file passage while the higher blockade population could be both linear molecule folding and circular molecule single-file passage. When a linear molecule (ldsM13) is passing through, we expect the blockage levels to be $6.12\, nS$ for single-file and folded levels to be multiples of $6.12\, nS$; While we expect the cdsM13 blockage levels to be multiples of $2 \times 6.12\, nS$. Therefore, the population centered around $6.12\, nS$ is solely a result of randomly broken scaffold. However, the randomly broken ones can also produce folded level blockages, thus a minimum blockage plot might provide more insight on the yield estimate.

Figure 3.9b shows the minimum blockage of the cdsM13 *versus* translocation time, the first two populations are fitted to have $\Delta G = 6.07\ nS$ and $12.40\ nS$. Since the minimum blockage levels are plotted, a linear molecule folded event such as the ones shown in **Figure 3.2** of the main texts, would produce a minimum blockage level at $\Delta G = 6.07\ nS$, since all intact circular molecules should produce blockage levels of minimum two times that. Therefore, under the assumption that all events are correctly fitted, the population centered around $\Delta G = 6.07\ nS$ should be all linear molecules. We estimate, from the minimum blockage histogram, roughly 54.7 % of the events are from linear molecules. This number is not consistent with the gel electrophoresis estimates of roughly 20 %, however, this nanopore result is in good agreement with gel results that a fraction of the scaffold is randomly broken and it serves as a good confirmation.

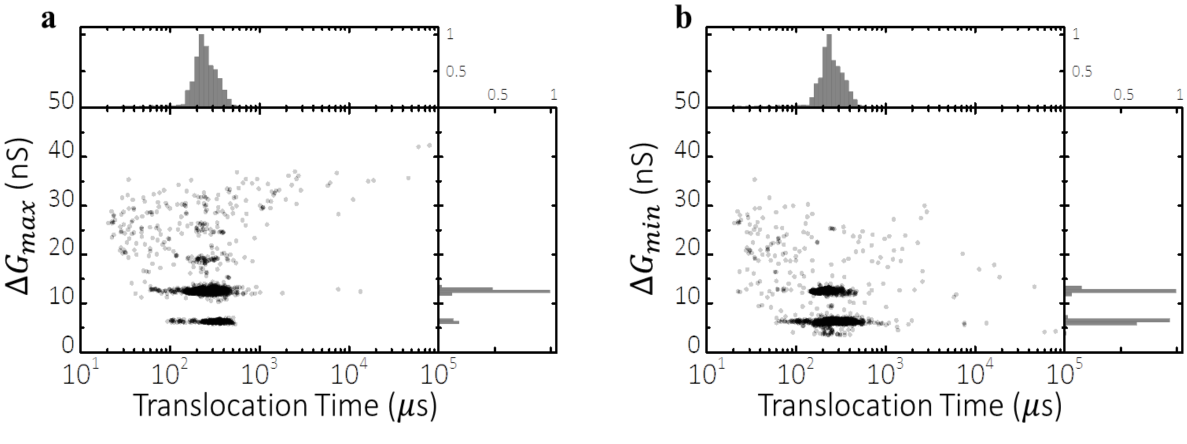

Figure 3.9. Scatter plots of dsM13 assembly using uncut M13mp18. (a) Scatter plot of maximum blockage *versus* translocation time, with histograms of maximum blockage and translocation time. **(b)** Scatter plot of minimum blockage *versus* translocation time, with histograms of minimum blockage and

translocation time. The nanopore experiments were done in 3.6 M LiCl using a 7.9 nm pore with an applied bias of 300 mV.

Filtering fragmented ldsM13 segments

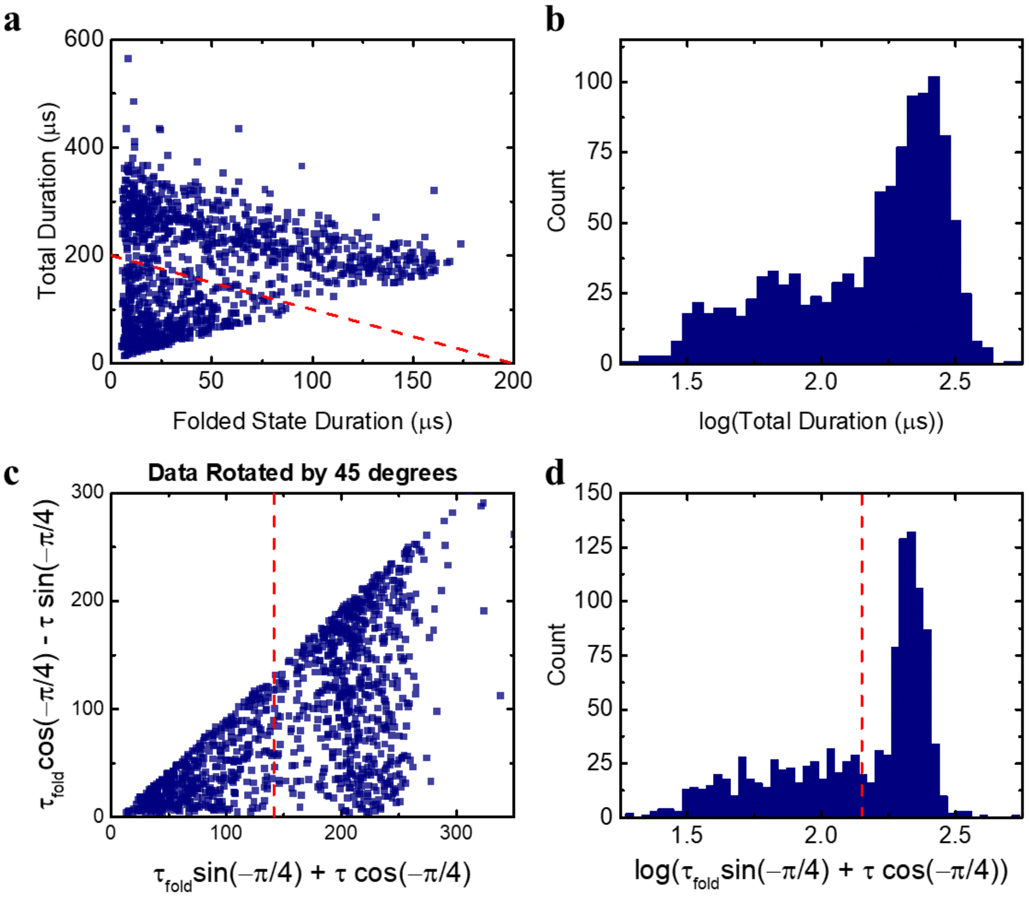

Figure 3.10. Filtering of ldsM13 events. (a) Total translocation time *versus* folded portion of folded events. **(b)** Histogram of the log of total translocation time of folded events. **(c-d)** The data from **(a-b)** rotated by 45 degrees. The experiment was performed using an 8.4 nm pore, in 3.6 M LiCl, with an applied bias of 300 mV.

Just like **Figure 3.2**c of the main text, **Figure 3.10**a shows the total duration of folded ldsM13 events plotted against the respective folded state duration of each individual ldsM13 folded translocations in an 8.4 nm pore, in 3.6M LiCl, under a 300 mV bias. **Figure 3.10**b shows the corresponding distribution of translocation times. Filtering misassembled ldsM13 fragments solely based on translocation times cannot be done precisely, since the translocation time distribution is a convolution of molecules folding at different locations along their contour, and of different lengths passing through the pore. To address this, a filter of the form $\tau = \left(200\ \mu s - \tau_{fold}\right)$ was used instead, as displayed by the red dashed line in **Figure 3.10**a. **Figure 3.10**c-d justifies the use of this filter by plotting the data from **Figure 3.10**a rotated by 45 degrees, and the corresponding x-axis ($\tau_{fold}\sin(-\pi/4) + \tau\cos(-\pi/4)$) distribution, respectively, showing a better separation between folded and misassembled ldsM13 events.

3.5.4 More 3HB results

In a mixture with dsDNA of various lengths

The 3HB molecules were run on 13.2 nm pore in a mixture with 7kbp dsDNA. **Figure 3.11** shows a scatter plot of maximum blockage ΔG_{max} *versus* ECD of a mixture of 3HB and 7kbp. By fitting the ECD histograms to log-normal distributions, we found the 7kbp and 3HB populations are nearly identically centered around ECD $= 0.05\ pC$. This is expected from properly assembled 3HB nanostructures since although of different dimensions, 3HB and 7bkp DNA fragments share a similar mass due to 3HB structures being assembled from a 7249 nt M13mp18 scaffold.

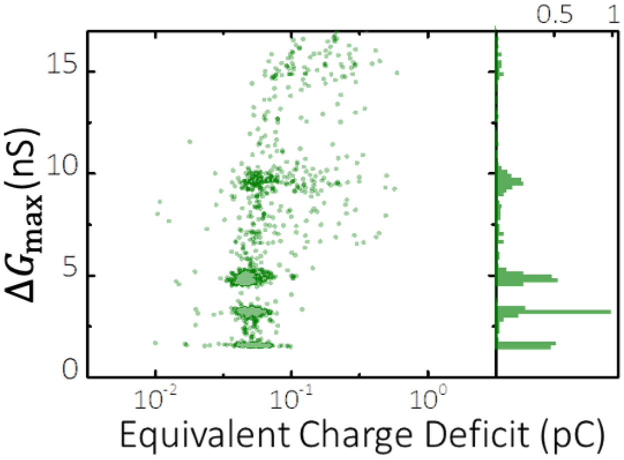

Figure 3.11. In a mixture with 7kbp. A Scatter plot and histogram of maximum blockage level *versus* equivalent charge deficit (ECD) for 3HB in a mixture with 7kbp dsDNA Fragments using a 13.2 nm pore in 0.9 M LiCl with an applied bias of 300 mV

Similarly, the 3HB were run in a mixture with other types of dsDNA such as 2kbp dsDNA fragments using a 13.3 nm pore in 0.9 M LiCl, and 10kbp dsDNA fragments using a 24 nm pore in 0.72 M LiCl. As shown in **Figure 3.12**, since the ECD is a measure of total additional charge through the nanopore, the smaller molecule 2kbp, although similar length, produced a population on with smaller ECD and a larger molecule 10kbp produced a larger ECD.

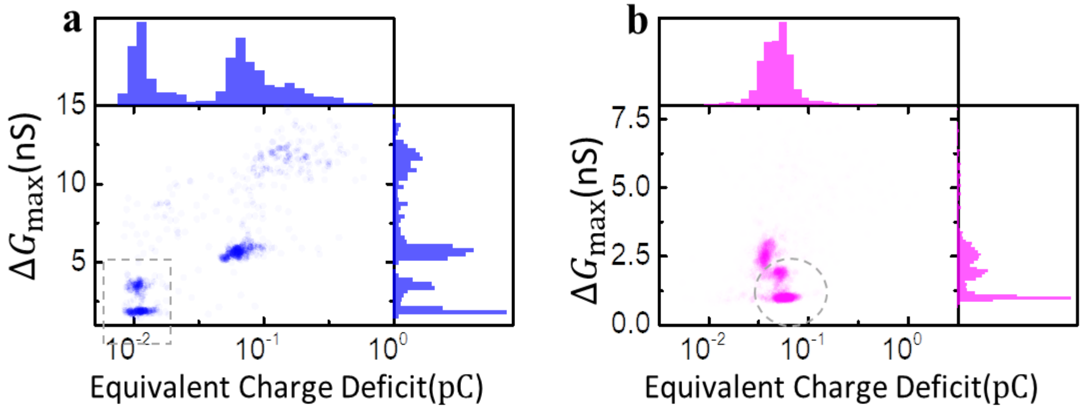

Figure 3.12. 3HB in a mixture with dsDNA fragments of various lengths. (a) 3HB in a mixture with 2kbp dsDNA fragments using a 13.3 nm pore in 0.9 M LiCl with an applied bias of 200 mV. **(b)** 3HB in a mixture with 10kbp dsDNA fragments using a 24 nm pore in 0.72 M LiCl with an applied bias of 200 mV.

Correlation of meta-stable state duration and total translocation time

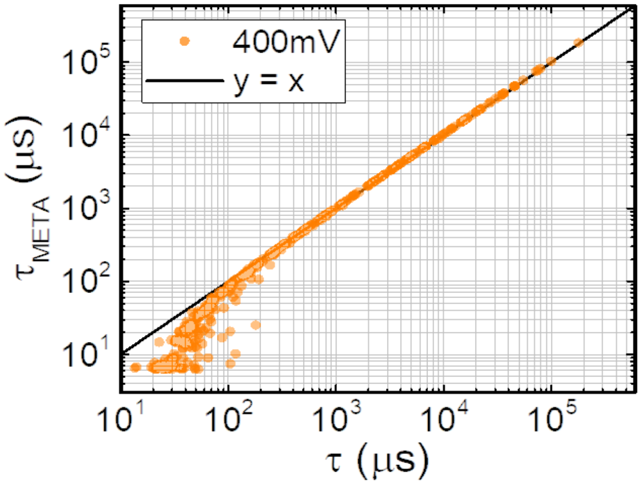

Figure 3.13. Correlation of meta-stable state duration ans total translocation time. Metastable durations *versus* total translocation time for 3HB molecules on a log-log plot. Experiment was done using a 13.3 nm pore in 0.9 M LiCl, with an applied bias of 400 mV.

Blockage *versus* translocation time of last two states

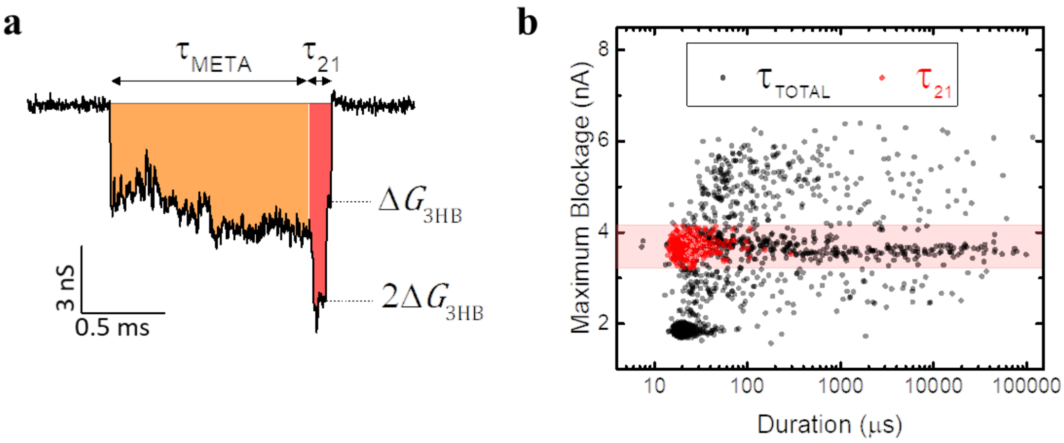

Figure 3.14. Blockage *versus* translocation time of the last two states. (a) Current trace of a 3HB even with meta-stable state. **(b)** Maximum blockage *versus* translocation time of total translocation times τ_{total} and of folded event duration τ_{21}. In plotting τ_{21}, the metastable state contribution to total translocation times is omitted, and so the wide spread of τ_{total} is removed. As a result, the temporal distribution of τ_{21} with the single-file τ_{total} distribution, further supporting the interpretation that events with $\Delta G_{max} = 2\Delta G_{3HB}$ are indeed folded translocation events preceeded by a metastable state. The experiment was performed using a 13.3 nm pore in 0.9 M LiCl, with an applied bias of 400 mV.

Meta-stable state duration distributions under different voltages

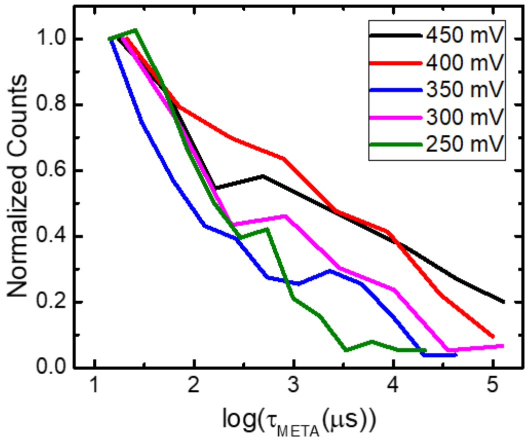

Figure 3.15. Meta-stable state duration distributions under different voltages. Distribution of meta-stable state durations τ_{META} measured at different voltages, in a 13.3 nm nanopore, in 0.9 M LiCl. The distributions are normalized such that the count at the smallest τ_{META} bin is 1.

PSD of meta-stable state

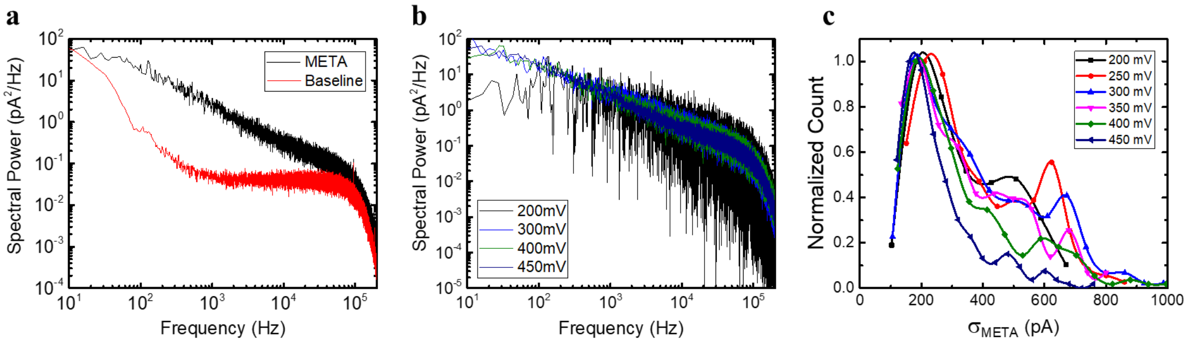

Figure 3.16. PSD of meta-stable state. Spectral Power *versus* Frequency comparison of **(a)** the meta-stable state and the baseline ionic current, and **(b)** the meta-stable state current measured under different voltages. **(c)** Distribution of the standard deviation of individual meta-stable state current traces. Results were obtained from a 13.3 nm pore, in 0.9 M LiCl.

Figure 3.16a plots and compares the Power Spectral Densities (PSD) of the ionic current traces of the open-pore baseline and of the metastable states: $1/f$ noise dominates the meta-stable state PSD for the entire bandwidth used, unlike the baseline current. Note that the PSD traces for the metastable state were obtained by concatenating the zeroed meta-stable traces, after which the spectral power was calculated over the entire concatenated trace. Interestingly, **Figure 3.16**b shows that the metastable state PSD traces are independent of the applied voltage. Given that the current's root mean square (RMS) is equivalent to the integral of PSDs, **Figure 3.16**b interestingly suggests that the RMS of meta-stable states is voltage independent. To confirm this, Figure S11c plots the normalized histograms of the meta-stable state current standard deviation $\sigma_{META} = \langle [I_{META} - \langle I_{META} \rangle]^2 \rangle^{1/2}$, measured for each individual event. Consistent with **Figure 3.16**b, **Figure 3.16**c shows that for every measured voltage, the most probable σ_{META} value is $\approx 200\ pA$.

Meta-stable state 3HB translocation events

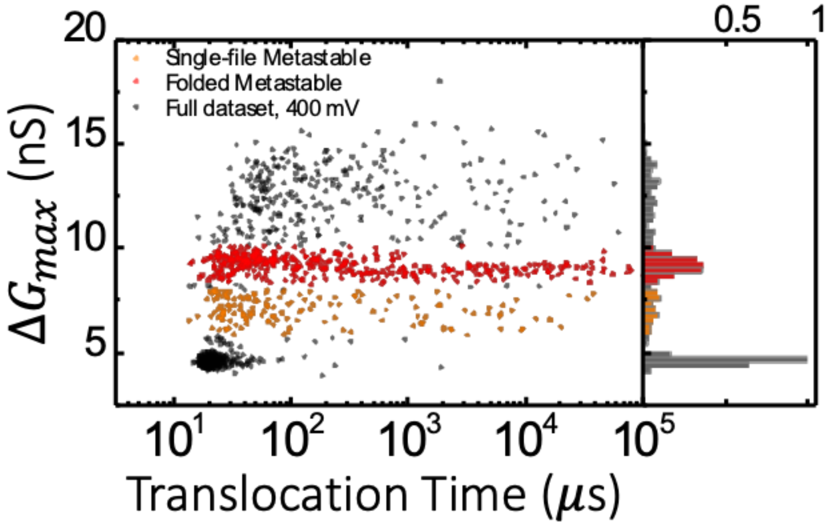

Figure 3.17. A scatter plot of maximum blockage *versus* translocation time and a histogram of maximum blockage distribution for 3HB molecules. The events with meta-stable states are highlighted: **(i)** meta-stable followed by a single-file translocation. **(ii)** meta-stable state followed by a folded translocation. The experiment was perform using a 13.3 nm pore in 0.9 M LiCl, with an applied bias of 400 mV.

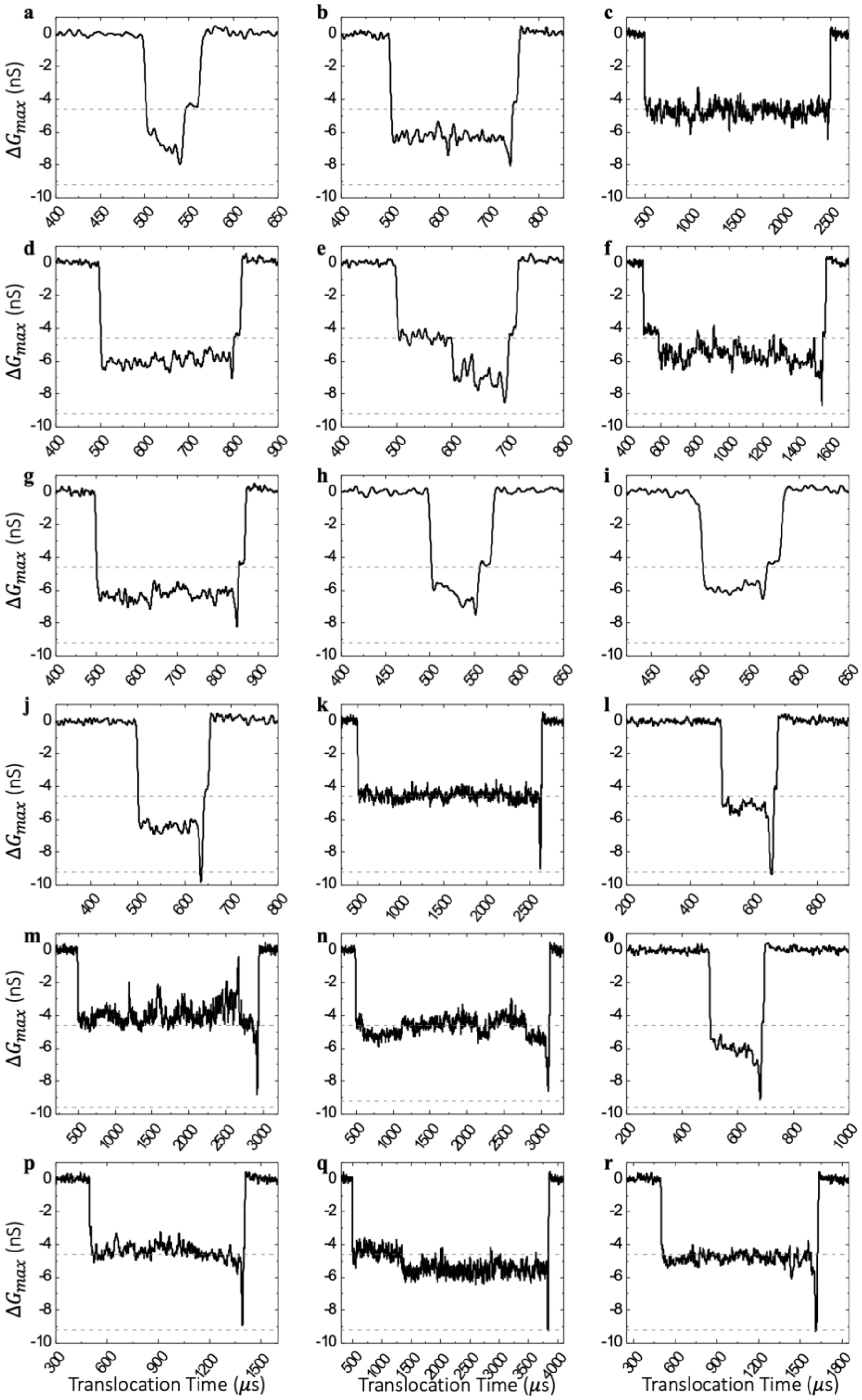

Figure 3.18. Current traces of 3HB events with meta-stable states. (a-i) 3HB current traces of meta-stable state followed by single-file translocation. **(j-r)** 3HB current traces of meta-stable state followed by

folded translocation. All experiments performed in 0.9 M LiCl, with an applied bias of 400 mV. The grey dash lines correspond to $\Delta G_{max} = \Delta G_{3HB}$, and $\Delta G_{max} = 2\Delta G_{3HB}$.

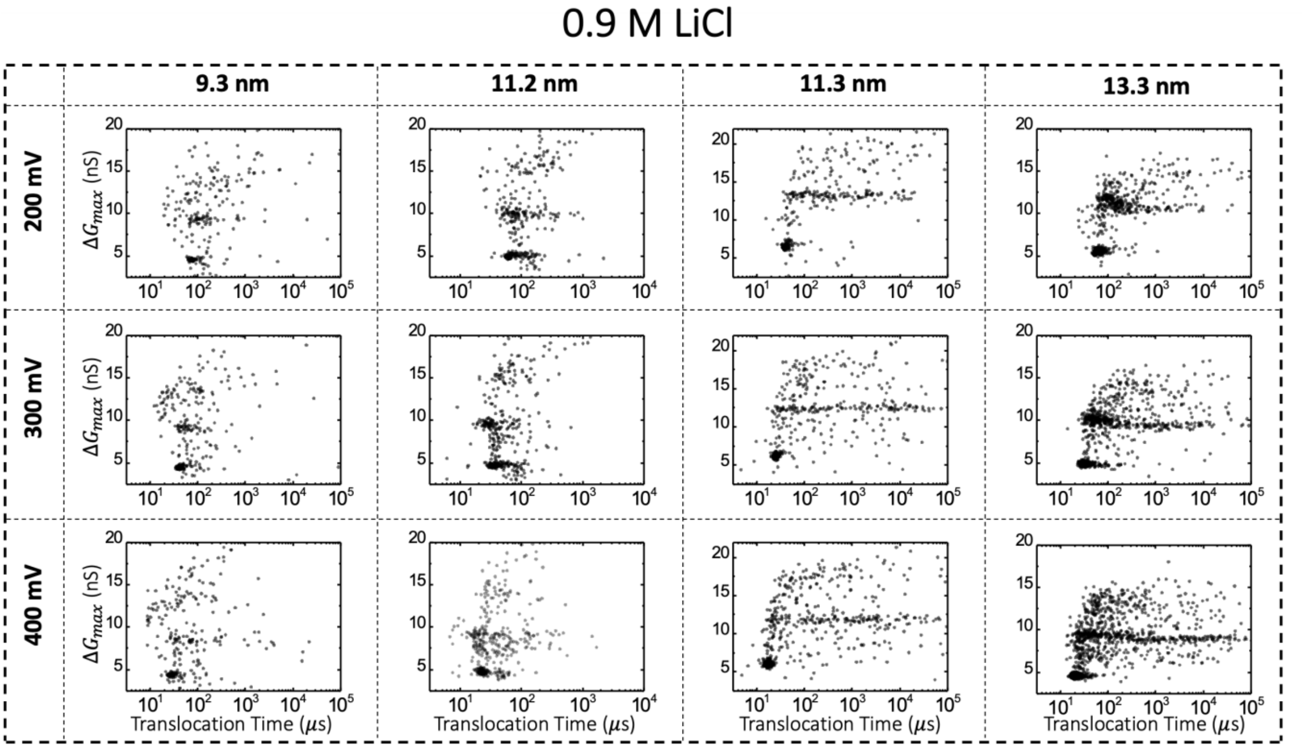

Figure 3.19. Scatter plots of 3HB translocation events in 0.9 M LiCl under various applied biases and using nanopores of different sizes.

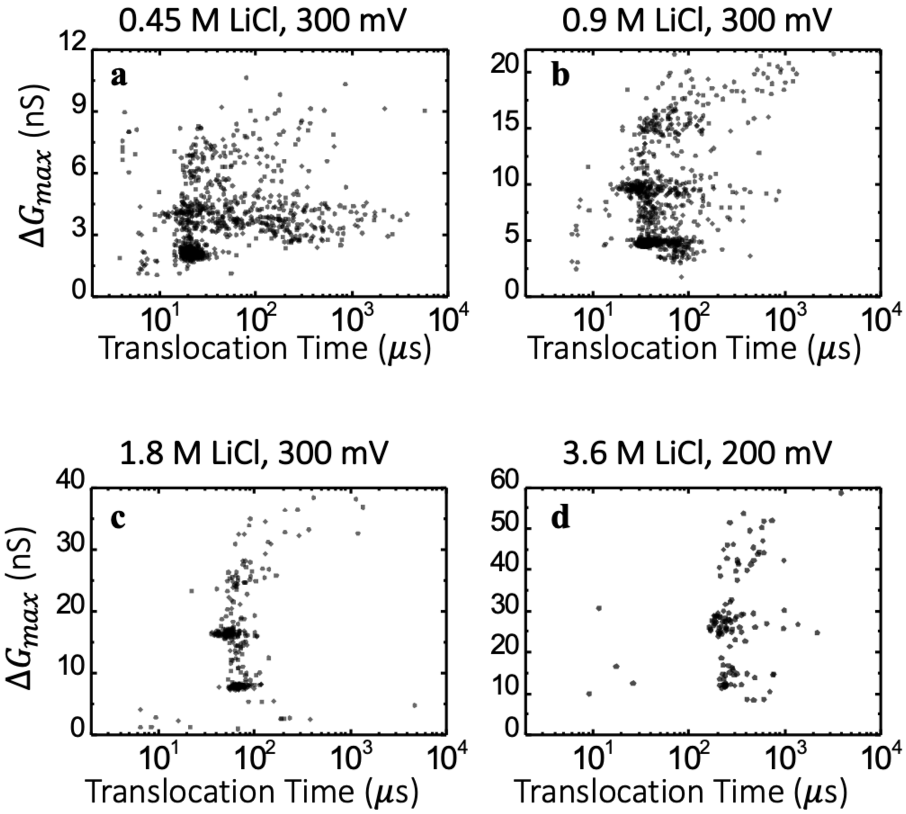

Figure 3.20. Scatter plots of 3HB translocation events using the same 11.2 nm pore in different concentrations of LiCl salt. (a-c) Under 300 mV in 0.45, 0.9, and 1.8 LiCl salt. **(d)** Under 200 mV in 3.6 M LiCl salt.

3.5.5 Mobility extraction from Agarose gel electrophoresis

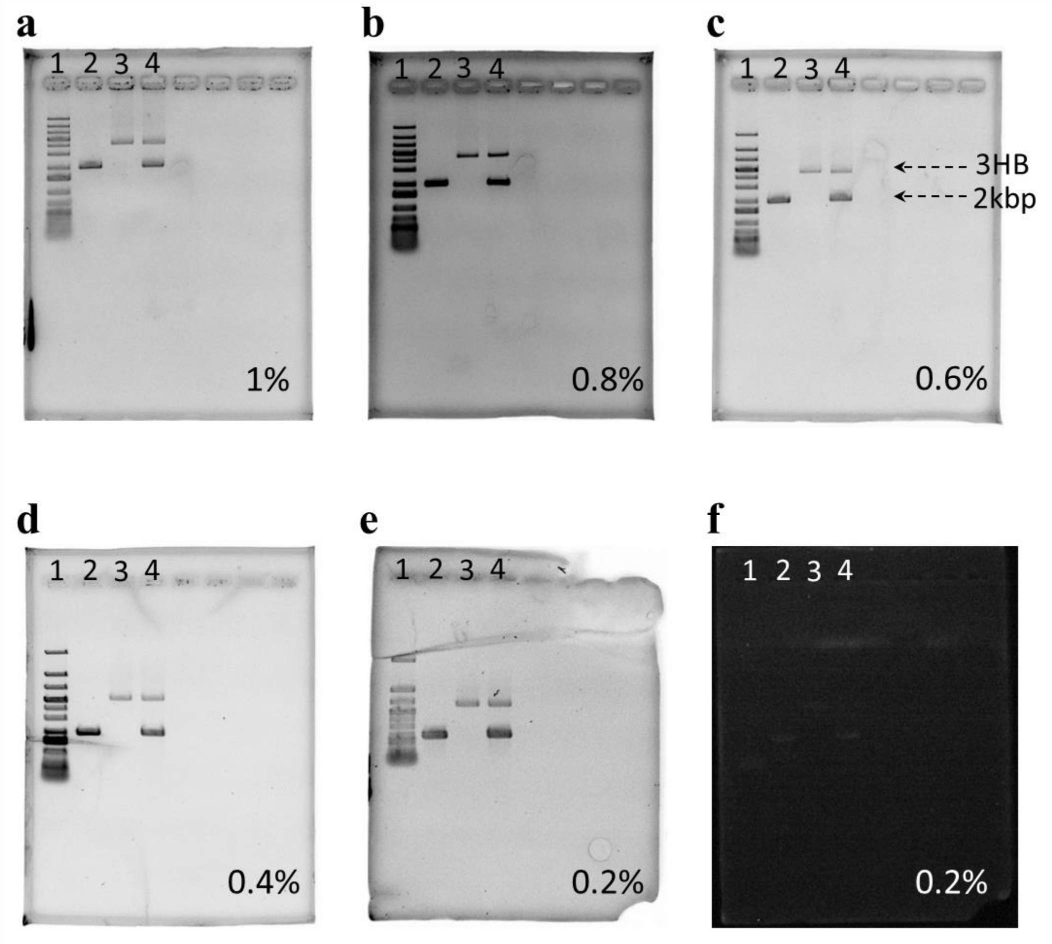

Figure 3.21. Extrapolation of 3HB mobility using 0.2 – 1 % Agarose. (a-e) Gel electrophoresis of 2kbp dsDNA fragments (ThermoFisher Scientific, SM1701) and 3HB in 0.2 – 1 % Agarose gels, post-stained using 1x GelRed (Biotium, #41003). **(f)** Gel electrophoresis of 2kbp dsDNA fragments and 3HB in 0.2 % Agarose gel with no staining. Lane 1: Generuler 1 kb plus DNA Ladder (ThermoFisher Scientific, SM1331). Lane 2: 2kbp dsDNA Fragments. Lane 3: 3HB molecules. Lane 4: mixture of 3HB and 2kbp dsDNA fragments. All experiments were performed in 1xTAE buffer (40 mM Tris, 20 mM acetic acid, and 2 mM EDTA) under 70 V for an hour.

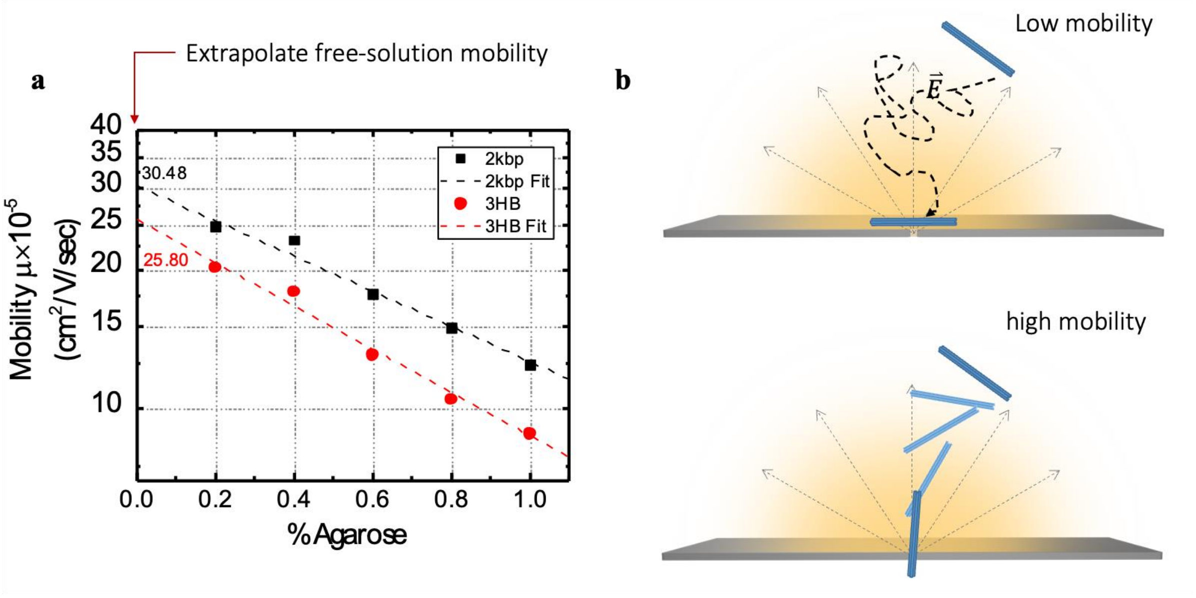

Figure 3.22. Extrapolation of free-solution mobility for 3HB. Extrapolation of the free-solution mobility for 3HB and 2kbp as a comparison, using agarose gels from 0.2 – 2 %. The experiments were performed in 1x TAE buffer, and post-stained using GelRed (Biotium, #41003).

3.5.6 Thermal experiments

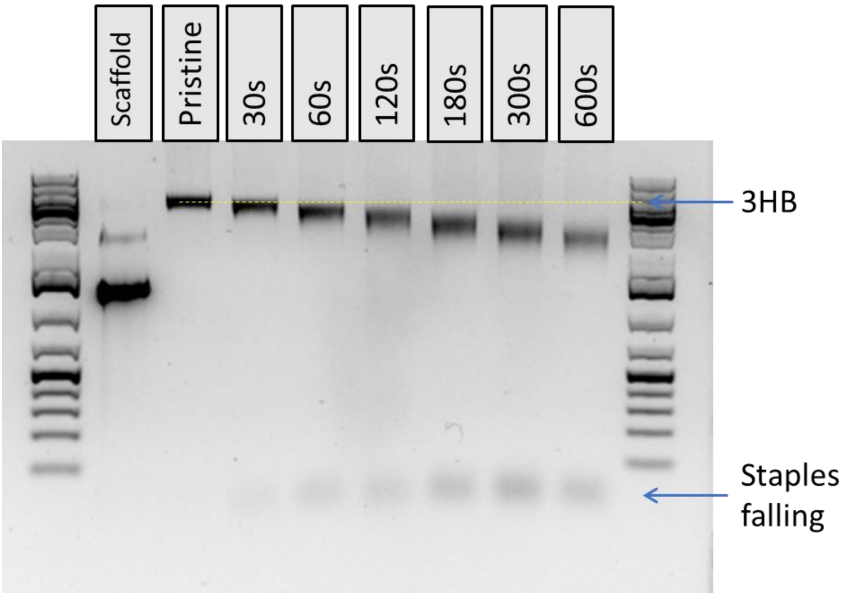

Figure 3.23. Gel electrophoresis of thermal degradation of 3HB. The assembled 3HB structures were heated to 65 degrees for 0, 30, 60, 120, 180, 300, and 600 seconds and snap cooled to 4 degrees, and ran on a 1 % Agarose gel in 1xTAE buffer (40 mM Tris, 20 mM acetic acid, and 2 mM EDTA) with an applied voltage of 70 V. From left: ladder, M13mp18 scaffold, pristine 3HB, heated for 30, 60, 120, 180, 300, and 600 seconds, and ladder. Generuler 1 kb plus DNA Ladder (ThermoFisher Scientific, SM1331).

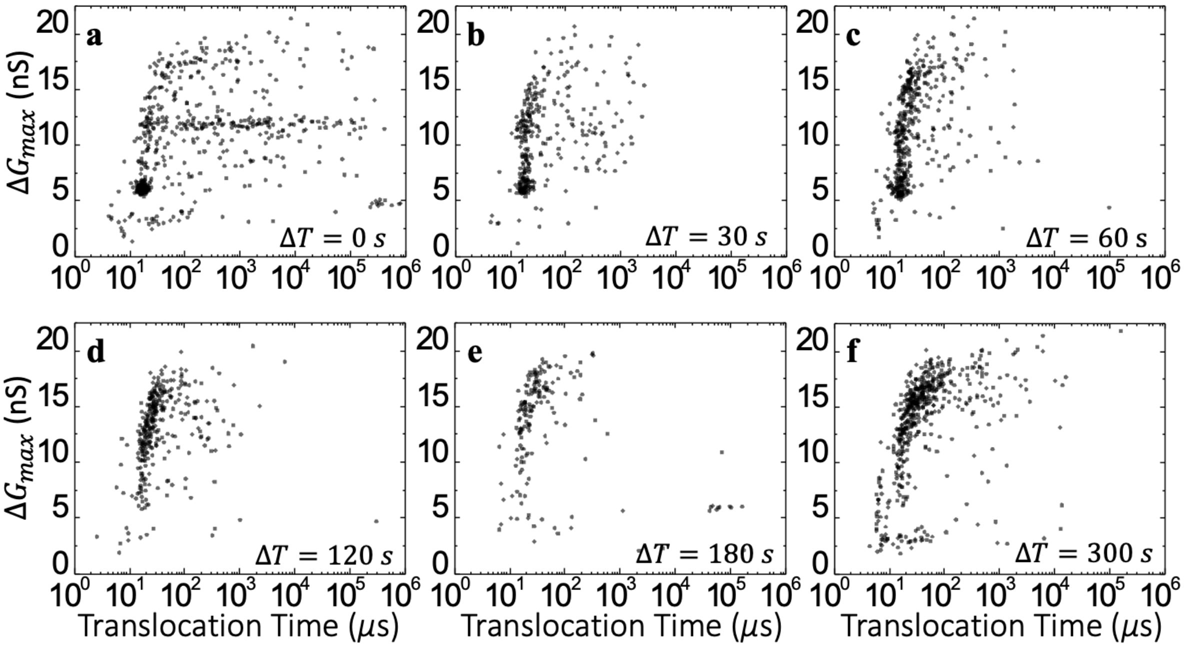

Figure 3.24. Thermal response of 3HB nanostructures. Scatter plots of maximum blockage *versus* translocation time of 3HB structures heated at 65 degrees for $\Delta T = 0, 30, 60, 120, 180$, and 300 seconds, respectively. Single-file 3HB events produce a maximum blockage level of $\sim 6\,nS$. All nanopore experiments are performed using a 11.3 nm pore, in 0.9 M LiCl with an applied bias of 400 mV.

Chapter 4 – Digital Biosensing using Solid-State Nanopores

This chapter is published as:

Digital Immunoassay for Biomarker Concentration Quantification using Solid-State Nanopores

Liqun He,* Daniel R. Tessier,* Kyle Briggs, Matthaios Tsangaris, Martin Charron, Erin M. McConnell, Dmytro Lomovtsev, and Vincent Tabard-Cossa

Department of Physics, University of Ottawa, Ottawa, Canada

*These authors contributed equally

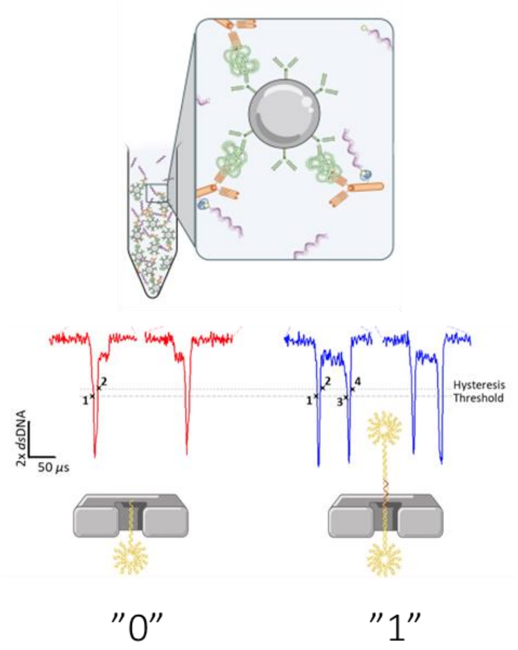

Adapted with permission from [L. He, D. R. Tessier, K. Briggs, M. Tsangaris, M. Charron, E. M. McConnell, D. Lomovtsev, and V. Tabard-Cossa, "Digital immunoassay for biomarker concentration quantification using solid-state nanopores," *Nature Communications*, **12**, 5348, 2021]

Abstract

Single-molecule counting is the most accurate and precise method for determining the concentration of a biomarker in solution and is leading to the emergence of digital diagnostic platforms enabling precision medicine. In principle, solid-state nanopores—fully electronic sensors with single-molecule sensitivity—are well suited to the task. Here we present a digital immunoassay scheme capable of reliably quantifying the concentration of a target protein in complex biofluids that overcomes specificity, sensitivity, and consistency challenges associated with the use of solid-state nanopores for protein sensing. This is achieved by employing easily-identifiable DNA nanostructures as proxies for the presence ("1") or absence ("0") of the target protein captured via a magnetic bead-based sandwich immunoassay. As a proof-of-concept, we demonstrate quantification of the concentration of thyroid-stimulating hormone from human serum samples down to the high femtomolar range. Further optimization to the method will push sensitivity and dynamic range, allowing for development of precision diagnostic tools compatible with point-of-care format.

4.1 Introduction

The nanopore field has seen tremendous progress in the last two decades, from the direct detection of single molecules to the realization of nanopore sequencing of nucleic acids, and more recently, the fingerprinting of amino acids.[6,128,181–188] One of the many promises of nanopores formed in solid-state membranes is to one day impact *in vitro* diagnostic (IVD) medical devices through the rapid and sensitive quantification of specific disease biomarker molecules in a point-of-need format. Solid-state nanopores possess attributes that make them good candidates for this type of application, including the ability to tailor pore size to suit the target of interest; robust supporting membranes suitable for a range of operating conditions; and ease of integration with microfluidics and electronics in dense arrays. Unfortunately, progress towards diagnostics applications has been slow, due to a host of challenges. For example, many clinically relevant biomolecules are proteins, which are not always compatible with the high salt concentration conditions that provide optimal signal-to-noise ratio (SNR) in solid-state nanopore devices. Transport properties of proteins through the nanopore are complex and fast, resulting in challenging detection and analysis issues.[79,189] Solid-state nanopores in their native state lack specificity to recognize a protein of interest without additional functionalization[82,84,190,191] and are prone to clogging and producing a high rate of false positives, particularly in complex biological fluids like serum that contain many different proteins. Finally, even when fabricated with sub-nanometer precision,[13,32] solid-state nanopores exhibit pore-to-pore variability in their capture characteristics and transport properties induced by minute geometric and surface charge variations which are not currently controllable, making generalization of results between nanopores a significant analysis challenge.[44,132] This reproducibility issue is a bottleneck for the development of technologies based on solid-state nanopores that often goes unaddressed.

Despite these challenges, a handful of recent studies have attempted to develop solid-state nanopore-based methods for specific target protein detection.[69,85–87,98,99,192–195] Keyser and coworkers first showed how DNA nanotechnology can be used to create long linear dsDNA carriers that contain short protrusions as barcodes that hold receptors to carry specific proteins, thereby enabling multiplexed digital detection.[68,86] Similar DNA nanocarrier schemes were employed by the groups of Edel and Ivanov to detect proteins and antibodies[69,85] from serum, while

Morin *et al.*[128] used a modified peptide nucleic acid molecule[124,196] that sequence-specifically inserts into the DNA scaffold to form a triple strand, and that can bind to a target antibody. While promising, these nanocarrier approaches have a sensitivity that is fundamentally limited by the affinity of the receptor (antibody or aptamer) to the protein of interest and will not be able to detect biomarkers in the fM range far below the typical dissociation constant for the interaction. In addition, the size of the target must generally be comparable or larger than that of the receptor to produce easily distinguishable signals between the target bound and unbound states in the absence of additional labelling, often restricting the choice of receptors to aptamers, usually with reduced affinity compared to antibodies. Furthermore, the high salt concentrations in which nanopores typically operate optimally must be balanced with the lower salt concentrations necessary to maintain a good affinity. Finally, the folding of long nanocarriers translocating the pore complicates analysis and can lead to ambiguous and false positive signals.[99]

Alternatively, in an effort to push the limit of detection, Chuah *et al.* used nanoparticles decorated with antibodies specific to their target to intentionally clog a large array of nanopores that are also decorated with antibodies, resulting in irreversible clogs being representative of a positive signal.[197] These proof-of-concept results represent early nanopore-based challengers to traditional methods of protein detection.

Many diseases, such as hypo/hyperthyroidism,[198] many forms of cancer,[199,200] infectious diseases such as tuberculosis,[201,202] neurodegenerative diseases such as Alzheimer's[111] and multiple sclerosis,[203–205] and even traumatic brain injuries,[108] are often heralded by the presence of low concentrations (~fM-pM) of specific protein biomarkers in blood samples. However, traditional analog ELISA equipped with intensity-based optical readout, long the workhorse for protein detection, is often insufficiently sensitive to quantify the relevant concentrations.[109] This is due in part to the affinity of antibodies, since the dissociation constants for the available antibodies are typically larger than the clinically relevant concentration of the target in blood samples, and in part to the inadequate SNR of standard optical readouts.[107,108]

In order to reach the required level of sensitivity while preserving specificity, digital immunoassay schemes are being developed that are able to overcome the limits imposed by both analog optical readout and relatively weak antibody pairings.[107,108] Some of these schemes are based on the use of paramagnetic micron-sized beads decorated with hundreds of thousands of capture antibodies,[152] effectively turning each bead into a capture antibody with a significantly higher *on*-rate than that of individual antibodies, but while the same *off*-rate is maintained. [206,207] In one method, this is followed by partitioning of beads into individually optically addressable microwells for digital readout of the fraction of beads with bound targets, overcoming analog error modes by transitioning to a digital scheme while still using optical detection.[108,112] These digital optical schemes have demonstrated impressive sensitivity down to the fM and even aM range for some exceptional antibody/antigen pairings,[108,208] but could be ill-suited for point-of-care use or future integration into wearable sensors due to the large form factor and complex optics needed for fluorescent readout. Nanopore sensors with their intrinsically single-molecule resolution and purely electrical readout, are viewed as an attractive alternative to optical detection schemes for digital diagnostics technologies, that offer a demonstrated path toward miniaturization and portability.[4] In this work, we employ DNA nanostructures as the basis for a digital counting scheme, to realize a robust solid-state nanopore electrical detection method. Using the characteristic electrical profiles of our DNA nanostructures combined with traditional bead-based sandwich immunoassays, we demonstrate the ability to quantify concentrations of a target protein from a serum sample. The proposed assay overcomes the specificity, sensitivity, precision, and consistency challenges associated with solid-state nanopore sensors for protein sensing from complex biological samples while using a digital readout scheme to overcome systematic error sources otherwise present. It provides a method by which to consistently measure target protein concentrations extracted from human serum against much higher concentrations of nonspecific background molecules from the femtomolar to the nanomolar (nM) range for a single nanopore sensor, in a format that is amenable to parallelization to increase sensitivity, precision and speed while allowing for the possibility of miniaturization for point-of-care use.

We demonstrate the utility of the method by measuring the concentration of thyroid-stimulating hormone (TSH), a staple biomarker for hypo/hyperthyroidism.[198] TSH is frequently used as a proof-of-concept target in model research assays and in the design of biosensors with optical, electrochemical, or electrical readouts,[209,210] since its clinically relevant concentration covers a large range and it is considered a good test case assay for new technologies since existing ELISA tests for TSH are particularly performant. The results presented here on TSH are generalizable to a framework that can be applied to any target protein/antibody pairing without needing to compromise on the nanopore sensing performance. To ensure consistency of results between many different solid-state nanopores we apply our recently reported method of controlled counting, allowing for direct comparison and consistent calibration between different nanopores.[44] Our results, acquired on 15 nanopores, 200 experiments, and $>10^5$ single-molecule events demonstrate that protein concentrations measured using this nanopore digital counting technique are accurate, precise, and robust, forming the basis for versatile biomarker quantification strategy.

4.2 Results and Discussion

4.2.1 Digital Assay Design

The quantification of specific protein concentrations from biological samples (e.g., serum) with solid-state nanopores requires precise, accurate, and robust electrical identification of these targets on a single molecule (*i.e*. digital) basis from a complex background. To enable digital detection with solid-state nanopores for precise and consistent target concentration measurements, we designed a pair of double stranded DNA (dsDNA) nanostructures in the shape of shooting stars that can be bound pairwise via a complementary single stranded DNA (ssDNA) junction strand to form an easily distinguishable dumbbell shaped nanostructure, as illustrated in **Figure 4.1**. We refer to these shooting star-like DNA nanostructures as probes (P-1 and P-2) when they are unbound, and as dumbbells (DB) when they are linked by the junction strand.

P-1 and P-2 are composed of 12-arm dsDNA stars with 11 arms 25 bp in length, and a 12th arm consisting of either a 175 bp (P-1) or a 150 bp (P-2) linear dsDNA tail. At the end of this extended arm is a 25 nt ssDNA region that is complementary to half of the junction strand (**Figure 4.5** in Section 4.5.1) which allows a P-1 and a P-2 probe to bind together to form a dumbbell-like structure (**Figure 4.1** and **Figure 4.6**). A description of probe assembly and purification can be found in Section 4.5.1 and 4.5.2.

Using the components identified above, our assay adapts a sandwich immunoassay scheme to enable digital detection with a nanopore, as depicted in **Figure 4.1**. Briefly, we employed magnetic isolation to efficiently capture target proteins onto antibody-coated paramagnetic micron-sized beads[44] and to facilitate the necessary washes to remove background molecules and dissociate nonspecifically bound complexes. Secondary detection antibodies bioconjugated with streptavidin, were then added to sandwich each target between the pair of high affinity antibodies. After equilibration and washing, short pieces of 50 nt biotinylated ssDNA (the junction strand) were added, which bind to the detector antibody and label each target. These junction strands have a photocleavable linker inserted between the biotin and the oligonucleotide sequence. Following additional washing to remove the excess unbound junction strands, the full immunoassay mixture was exposed to UV light to cleave the junction strands from the beads and release them into the solution in proportion to the concentration of bound targets. The beads were magnetically immobilized, and the supernatant containing the cleaved junction strands was recovered. The recovered supernatant was incubated with known concentration of probes and then mixed with a high concentration salt solution for nanopore sensing. A more detailed description of the assay steps and components is provided in the Methods section.

Following nanopore analysis, the translocations of unpaired probes were classified on a single-molecule basis as a “0”, while the translocations of dumbbells are classified as a “1”, thus converting the electrical nanopore signal into a digital count.

In this scheme, junction strands serve as proxies for the target proteins, and for a fixed probe concentration, the fraction of dumbbells formed can be calibrated to report on the original concentration of target proteins in a clinically relevant sample. As expected from controlled counting,[44] the use of relative counts of each population eliminates the error from varying intra- and inter-nanopore properties, allowing for highly reproducible assay performance between different nanopores.

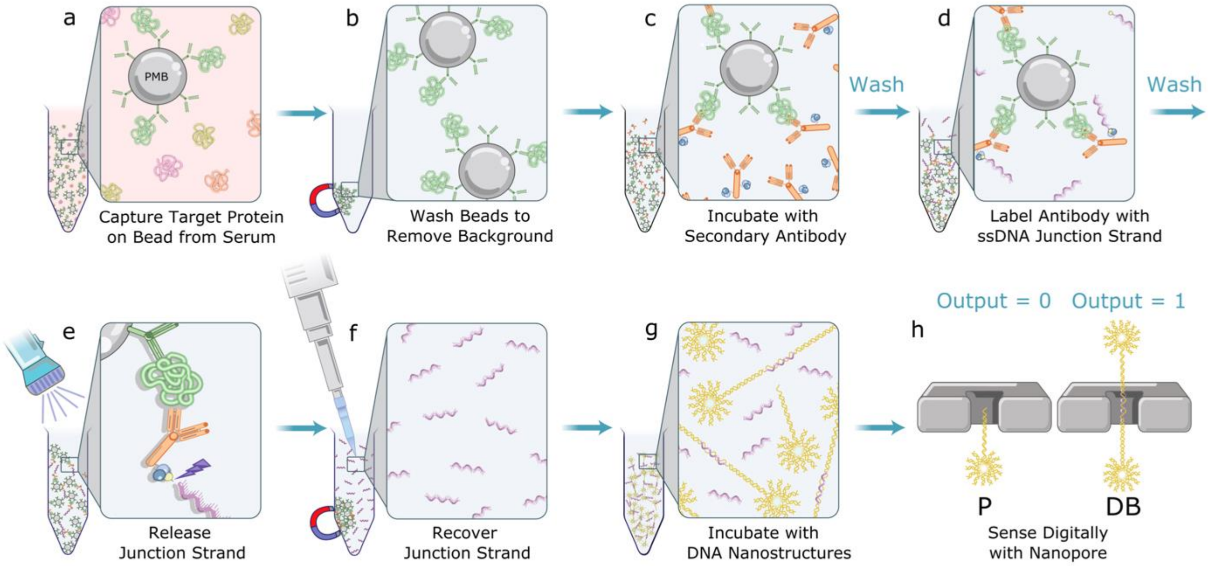

Figure 4.1. Schematic illustration of the digital immunoassay workflow with nanopore electrical detection. (a) Paramagnetic beads (PMBs) conjugated with antibodies efficiently capture specific target protein in serum sample; **(b)** PMBs are pelleted and immobilized with a magnet and supernatant is removed to eliminate unbound molecules; **(c)** PMBs are resuspended and incubated with secondary antibody conjugated with streptavidin; **(d)** Following a wash the immuno-sandwich structure is incubated with biotinylated-ssDNA junction strand; **(e)** Following another wash the solution is exposed to UV light to release the junction strand; **(f)** PMBs are pelleted and immobilized with a magnet and the supernatant containing the junction strand is recovered with a pipette; **(g)** Shooting star-like DNA probes are added to the solution containing recovered junction strand leading to assembly of a dumbbell-like DNA nanostructure; **(h)** Digital nanopore sensing to determine the fraction of probes to dumbbells.

4.2.2 Nanopore characterization of DNA nanostructures

In previous work, we showed that short, multi-arm dsDNA stars produce robust and easily identifiable signals.[49,64,126,129,162,211] Here, we further modified the star nanostructures, extending one of the arms to form a linkage for the tail section of the probe, and added an internal carbon spacer in the middle of each star oligo's sequence to relax the otherwise highly charged and sterically stressed core of the 12-arm star structure, to help facilitate translocation through nanopores. The resulting nanostructure provides a characteristic electrical signature when translocating a nanopore (**Figure 4.2**). Differences in nanopore sensing profiles between the probes P-1 and P-2, due to 25 bp difference in the length of the tail, were not distinguishable.

Figure 4.2 shows the nanopore translocation characteristics of probes and dumbbells. As expected, **Figure 4.2**b shows the most commonly observed nanopore signal of the probes, which involves a deep blockage level 6x deeper than dsDNA alone, corresponding to the body of the star.[64] We normalized the nanopore current signal by the blockage produced by the unfolded translocation of 2 kbp linear dsDNA to remove the effects of any variations in pore geometry and operating conditions between experiments,[64] thus facilitating comparison between experiments on different pores as detailed in Section 4.5. These deep, 6x dsDNA, blockages are often (>90%) followed by a shallower 1x dsDNA blockage level corresponding to the tail, though bandwidth limitations sometimes (<10%) preclude resolving the tail part of the event. The mean translocation time was 27 ± 2 µs, though probe events do occasionally approach the 200 kHz bandwidth limit of the digital low-pass filter applied during the analysis. While this bandwidth limitation might in other contexts be problematic, the depth of the blockages ensures sufficient SNR to identify the event even if the signal is somewhat attenuated.[39,212] In contrast, **Figure 4.2**b shows that when the dumbbells translocate, they produce two deep blockages separated by a shallower blockage level indicative of the linear dsDNA section between the two 12-arm DNA stars, with a mean passage time of 70 ± 2 µs. We observed a slight shift in maximum blockage level (**Figure 4.2**c-d) between the probes and the dumbbells since each dumbbell event produces two deep blockage levels and there is therefore a higher probability that at least one will be well-resolved, and the full blockage level correctly fitted. The presence or absence of this second, deep blockage level is confirmation of the presence of a junction strand in the sample.

In order to distinguish event types, we employed a simple threshold-crossing scheme detailed in Section 4.5.3. Briefly, we counted the number of times the current trace in the event crossed a set of thresholds indicative of the transition between 1x dsDNA and 6x dsDNA blockage levels. With the threshold set to 2.5x dsDNA, a shooting star event registers 2 threshold-crossings, while a dumbbell event registers 4 threshold-crossings, as shown in **Figure 4.2**b and **Figure 4.8**. The analysis of translocation events of the probes and dumbbells separately show that while the assembly into a dumbbell has only a mild effect on the passage time, the shape of the events is easily distinguishable. When using purified probes in the absence of junction strands we observed a false positive rate of <2%, primarily driven by either analysis artefacts or the binding of misassembled probe pairs (**Figure 4.9** and **Figure 4.14**). The latter is possible for example if both the probes P-1 and P-2 are missing the last two staple strands on the tip of their tails, in which case the probe pair overhang sequences are complementary and could form the dumbbell structure with a slightly shorter linkage in the absence of the junction strand. Future work will aim at resolving this by either having unique sequences for each staple in the entire tail on the respective probes, by increasing binding strength of the tail staples using longer sequences, and/or modifying the design of the DNA nanostructure labels.

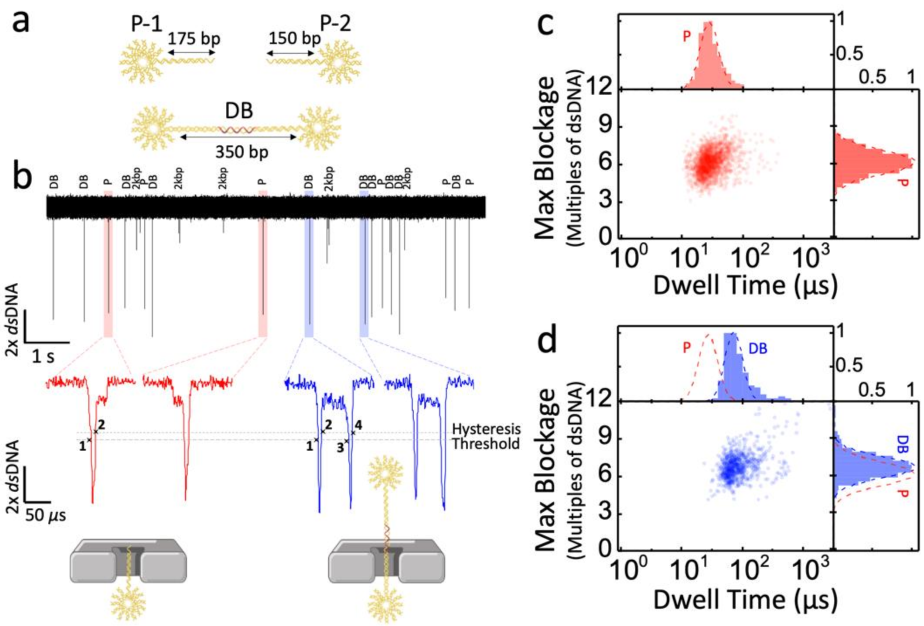

Figure 4.2. Nanopore translocation characteristics of the shooting stars probes and the dumbbells. (a) Artistic representation of the shooting star probes (P-1 and P-2) and the dumbbell (DB). **(b)** 10 seconds current trace of a mixed population of both DNA nanostructures and 2kbp dsDNA calibrator, with representative current traces showing individual translocation events corresponding to probes (left, red) and dumbbells (right, blue). Scatter plots and histograms of maximum blockage *versus* dwell time of the shooting star probes **(c)** and dumbbell **(d)**. The fit to the probe distribution (P, red dash line) is overlayed with the dumbbell distribution to facilitate comparison between the two populations. Experiments are performed on an 11.5 nm pore in 3.2 M LiCl pH 8 with an applied bias of 100 mV. Displayed current traces are low-pass Bessel filtered at 500 kHz.

4.2.3 Nanopore Digital Response Characterization

To investigate and validate the dose response of our digital assay, we first characterized the response of the nanopore sensor as a function of different mixtures of known concentrations of junction strand and probes. For this, we fixed the concentration of both probes P-1 and P-2 at 20 nM and varied the concentration of the junction strand, from 0.2 nM (ratio of 0.01:1, junction strand to probe pair) to 400 nM (20:1). **Figure 4.3**a-c show the scatter plots of the maximum blockage depth *versus* dwell time for all single-molecule events recorded for three junction strand to probe pair ratios (0.025:1, 1:1, and 10:1). The corresponding scatter plots for all concentrations are shown in **Figure 4.13**. As expected, with increasing junction strand concentration below the fixed probe pair concentration, we observed a linear increasing fraction of events attributed to the passage of dumbbell nanostructures, reaching a maximum at a ratio of 1, before the relative number of dumbbells linearly decreased again. This linear dose response is plotted in semi-log scale in **Figure 4.3**d.

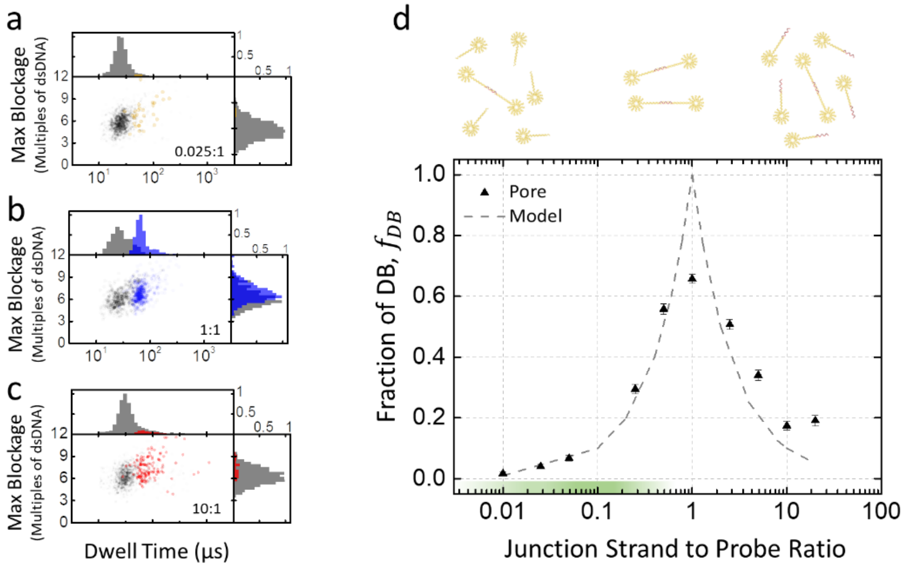

Figure 4.3. Dose response of the junction strand to shooting star probes ratio from 0.01:1 to 20:1. (a-c) Scatter plots and histograms of maximum blockage *versus* dwell time (log scale), junction strand concentrations shown **(a)** 500 pM (ratio 0.025:1); **(b)** 20 nM (ratio 1:1); and **(c)** 200 nM (ratio 10:1).

Shooting star probes P-1 and P-2 are fixed at 20 nM in all three cases. Dumbbell events called using the thresholding algorithm are shown in color, while probe events are shown in grey. **(d)** Linear dose response on a log scale for junction strand concentration ranging from 200 pM to 400 nM and shooting star probes fixed at 20 nM, with ~1100 single-molecule events at each concentration. Dashed line depicts prediction from model of binding kinetics. The optimal operating range (0.01 to 0.5) is highlighted in green on the *x*-axis. Experiments are performed in 3.2 M LiCl pH 8, at 100 mV using a 12 nm pore, with the analysis threshold set to 2.5x dsDNA all experiments are low-pass Bessel filtered at 200 kHz for analysis. Error bars are calculated as described in Equation 4.3.

To understand this non-monotonic response, we developed a simple computational model that assumes irreversible first-order binding kinetics of junction strands to probes. This model predicts that the fraction of dumbbells formed at equilibrium will be in proportion to the ratio of junction strands to probe pairs when there are fewer junction strands than probe pairs, and the inverse ratio in the opposite case, that is,

$$f_{DB}(x) = \min(x, x^{-1}) \qquad 4.1$$

where f_{DB} denotes the fraction of dumbbell events and x the ratio of junction strand (proxy for protein) concentration (c_{Js}) to each shooting star probe pair concentration ($c_{P1} = c_{P2}$), that is, $x = \frac{c_{Js}}{c_{P1}} = \frac{c_{Js}}{c_{P2}}$.

This linear behavior can be understood readily by a simple intuitive argument. Assuming irreversible binding, if there are more probe pairs than junction strands ($x < 1$), every junction strand that binds one of the probes will eventually be able to find another of the matching pair with which to bind, leading to one dumbbell per junction strand (*i.e.*, $f_{DB} = x$), depicted in **Figure 4.3**d as the green section of the junction strand to probe ratio range. On the other hand, if there are more junction strands than probes ($x > 1$), probes will get capped and be unable to find a binding partner with a free binding site, with the probability of capping occurring before binding a partner being in proportion to the ratio of concentrations in the first-order approximation that diffusion times are not rate-limiting. This is in reasonably close agreement with our experimental results when $x \neq 1$, as can be seen in **Figure 4.3**d. In this regime the model predicts a linear increase in probe capping or linear decrease in the dumbbell fraction as we increase the junction concentration (*i.e.*, $f_{DB} = x^{-1}$). The experimental data suggest that there is a limit at which the dumbbell fraction still occurs, nearing 20%, even in the presence of overwhelming numbers of junction strands. Because of this limit the range of excess junction strands to probes should be avoided for quantification. While the expected peak at $x = 1$ is present in the experimental data, in contrast to the prediction of our computational model, the experimental data shows that the dumbbell fraction only reaches a plateau of about 60%. During assembly of dumbbells particularly as concentration ratios near parity, it was noted that as expected from hybridization kinetics,[213] the incubation times required to reach binding saturation are quite long due to progressive depletion of binding species as the reaction progresses. However, this underperformance of binding near the peak cannot be explained by short incubation times, since the reaction would have run past completion well before the experiments in **Figure 4.3**d were conducted. To validate this dose response, we have also the same samples characterized by gel electrophoresis, which show good agreement with the nanopore results (see **Figure 4.10**).

The more likely explanation is that a fraction of the shooting star probes in our purified stocks were or became misassembled while stored, either prior to use or during manipulation ahead of nanopore sensing. This a common issue with multi-component DNA nanostructures[64] which introduces potential false negatives in the analysis, as discussed in more detail in Section 4.5.3. To support the hypothesis that our DNA nanostructure can incur partial disassembly post purification, we characterized samples of fully assembled dumbbells that were purified by gel band extraction. The data is shown in **Figure 4.11** and reveals that up to 20% of the single molecule events do not generate the electrical signature of 4 threshold crossings expected for the translocation of the dumbbell (**Figure 4.2**b). While further investigation is required to better understand the stability of these DNA nanostructures and determine their shelf life and optimal storage conditions, the presence of misassembled nanostructures is controlled by performing a calibration curve and serum sample testing with a single batch of probes.

Proper performance of the digital assay also requires setting the junction strand to probe ratios between 0.01 and 0.5 to maintain the dumbbell assembly in the optimal range (linear dose response). For junction strand to probe ratios well below 1 ($x \leq 0.5$) the assay should perform as expected even in the presence of up to 20% of mis-assembly, but nearing ratios of 1 ($x > 0.5$) this issue becomes limiting and results in a reduced precision. It is therefore important, both from a timing and accuracy perspective, to ensure that the concentration of shooting star probes chosen to be such that the ratio of junction strands to probes is below 0.5. This is also where the hybridization reaction is fastest.[213] The lower limit of ~0.01 is currently set by the presence of false positives at a rate of <2%, though we hope to push this limit down by improving the DNA nanostructure design. This 0.01 to 0.5 regime is highlighted in green in **Figure 4.3**d and defines the dynamic range for a given probe concentration. We expect that the current ~50-fold dynamic range of this assay scheme can be extended to ~2–3-log by improving the DNA nanostructure labels, or to an arbitrarily wide range of clinically relevant biomarker concentrations by incubating the unknown concentration of junction strands (proxies for protein) with different fixed concentrations of probes in parallel. For example, splitting the sample volume and testing it against three different probe concentrations could, in principle, provide a 5-log dynamic range. Likewise, the sensitivity of this assay, currently limited by the lower bound of the concentration ratio of junction strand to probe, $x = \frac{c_{JS}}{c_P} \approx 0.01$, can be adjusted to accommodate any desired concentration range at the cost of linearly increasing the detection time of a single nanopore sensor as concentrations are reduced, though this increase in counting time can be offset through parallelization with an array of pores and other strategies that increase nanopore capture rate.[37] The limit of detection, while fixed by the parameters of a particular assay and the choice of probe concentration, can therefore be controlled by the counting time of the nanopore and for a fixed measurement time can be improved by speeding up the detection through parallelization, amplification, preconcentration, or capture rate enhancement schemes.[37,44,64,65,67,68,214–217]

4.2.4 Nanopore Digital Immunoassay for TSH

To reliably quantify the concentration of thyroid-stimulating hormone (TSH) in human sera, our proof-of-concept protein target, we performed calibration curves using the full assay workflow presented in **Figure 4.1** and validated the reproducibility of the assay by testing the inter-pore variability. A five-point calibration curve was constructed using known concentrations of recombinant TSH (rTSH) (0.00, 0.15, 0.30, 0.60, and 1.2 nM) suspended in sample diluent (**Figure 4.4**a). Note that after release of the junction strand (proxy for protein, **Figure 4.1**f), a final concentration step was applied to the supernatant, increasing the concentration by ~17-fold before incubating for dumbbell assembly with a fixed 20 nM probe concentration (**Figure 4.1**g). This particular probe concentration was selected in order to operate the assay in the optimal range of junction strand to probe ratio previously discussed for **Figure 4.3**d, and to limit the single nanopore recording time to minutes to count a statistically significant number of single molecules.

Figure 4.4a presents the analyzed nanopore data, showing the fraction of dumbbell formed, f_{DB}, as a function of the initial spiked rTSH concentration in each of the calibrators. The calibrators were run on three different nanopores: a 10 nm (pore 1, magenta diamonds), an 11.5 nm (pore 2, blue triangles) and a 12 nm (pore 3, cyan circles). The calibration curve for the fraction of dumbbell events ranges on average from ~3% (blank) to ~40% (1.2 nM). The calibrators exhibit a linear trend as expected and overlap within their error bar for all three pores, highlighting the pore-to-pore reproducibility of our digital immunoassay scheme for pores sizes in this range. The straight line shown in **Figure 4.4**a is a linear fit to the calibration points for pore 3. For the different pores tested, the blank sample shows a background level varying from 2.5% to 3.4%. We had previously observed a <2% false positive rate from dumbbells formed from purified probes in the absence of junction strand (see **Figure 4.14**), which we attributed to analysis artefacts and the agglomeration of misassembled probe pairs. We therefore assign this additional ~1% to the values of the blank due to non-specific binding during the immunoassay, most likely of the secondary antibody to the beads not removed during washes. Limits of detection (LoD) were determined for each calibration curve at 2.5 standard deviations (s.d.) above background (blank) as commonly done.[108] LoD determined from the three pore runs were averaged for an overall mean LoD of ~20 pM for these particular choice of assay workflow and parameters.

The grey squares in **Figure 4.4**a represent the idealized values of the five rTSH calibrators for junction strand to probe ratios of 0:1, 0.125:1, 0.25:1, 0.5:1 and 1:1 as interpolated from **Figure 4.3**d. These interpolated values of the ratios assume no losses due to disassociation of the components from the immunoassay during the wash steps, nor of reagents from sticking to tubes walls, and a 1:1 labeling of the detection antibodies with junction strands (*i.e.* a perfect translation of each protein target to exactly one junction strand). Since losses are to be expected throughout the assay,[218] we empirically estimate these losses by comparing the interpolated values to our experimentally observed values. The difference in dumbbell fraction seen in **Figure 4.4**a indicate that we are on average recovering half as many junction strands as there are target proteins present.

Next, we investigated the accuracy of the nanopore digital signal with clinically relevant biological samples and validated the reproducibility for protein concentration quantification in these conditions. To accomplish this, we spiked 0.48 nM of rTSH into a human serum sample, with a predetermined undetectable level of TSH (see Methods section) and measured it on the three different pores as above. Linear fits to the calibration points for each pore are used as calibration curves to convert the observed fraction of dumbbell into the concentration of TSH originally present in the human serum sample ($i.e.$, $C_{protein} = f_{DB}/\text{slope}_{cal.}$). **Figure 4.4**b shows that the observed fraction of dumbbell formed are $19 \pm 2\%$, $19 \pm 2\%$, and $19.2 \pm 0.9\%$, corresponding to 0.54 ± 0.04, 0.61 ± 0.05, and 0.59 ± 0.03 nM of rTSH, respectively. These triplicate measurements are in good agreement with one another. Interestingly, the quantified concentrations of TSH are systematically higher than the spiked concentration of 0.48 nM. The spike recovery analysis shows that we have a recovery of 121 ± 5 %, which is close to the acceptable range of 80-120%.[219] We attribute discrepancies here to nonspecific binding and matrix effects in the presence of serum since the calibration curves were constructed from spiked rTSH in sample diluent. In future work, we anticipate that matrix effects can be normalized by running the calibration curve in TSH depleted serum or could be reduced by further increasing the dilution factor of the sample from 4× to ≥10×.[219] Additional data sets of calibration curves and serum measurements on two other pores using a different reagent batch yielded similar results as shown in **Figure 4.15** in Section 4.5.4. Nanopore assay results were further validated by gel electrophoresis (see **Figure 4.16** and **Figure 4.17** in Section 4.5.4), and five additional measurements of rTSH in human serum sample from 0.15 nM to 1.2 nM are shown in **Figure 4.18** in Section 4.5.4.

To further improve the sensitivity of our digital immunoassay and lower the LoD for a fixed nanopore counting time of a few minutes, we implemented an amplification scheme to detect rTSH down to the high femtomolar range. To achieve a ~100× amplification, we replaced the biotinylated ssDNA junction strand with a detection complex composed of 30 nm gold nanoparticles decorated with detector antibodies and hundreds of junction strands following protocols by Mirkin & co.[152,220] This effectively translates one protein into hundreds of ssDNA junction strands instead of a single one as illustrated in **Figure 4.4**c. Amplification experiments were carried out using the same assay workflow. This time, we measured concentrations of spiked rTSH in human serum samples at 0.8 pM, 1.6 pM, 3.2 pM, 6.4 pM, and 12.8 pM. **Figure 4.4**d shows the detected fraction of dumbbell formed of 7.5 ±0.9%, 12 ±1%, 16 ±2%, 24 ±2%, and 41 ±2%, with a blank serum measured at 2.9 ±0.6%. LoD for the particular parameters of this amplified digital assay is calculated to be 385 fM. Additionally, we performed a homebrew ELISA employing the same workflow and reagents as our nanopore digital assay to validate the performance of our assay components with an optical readout (See **Figure 4.19** in Section 4.5.4).

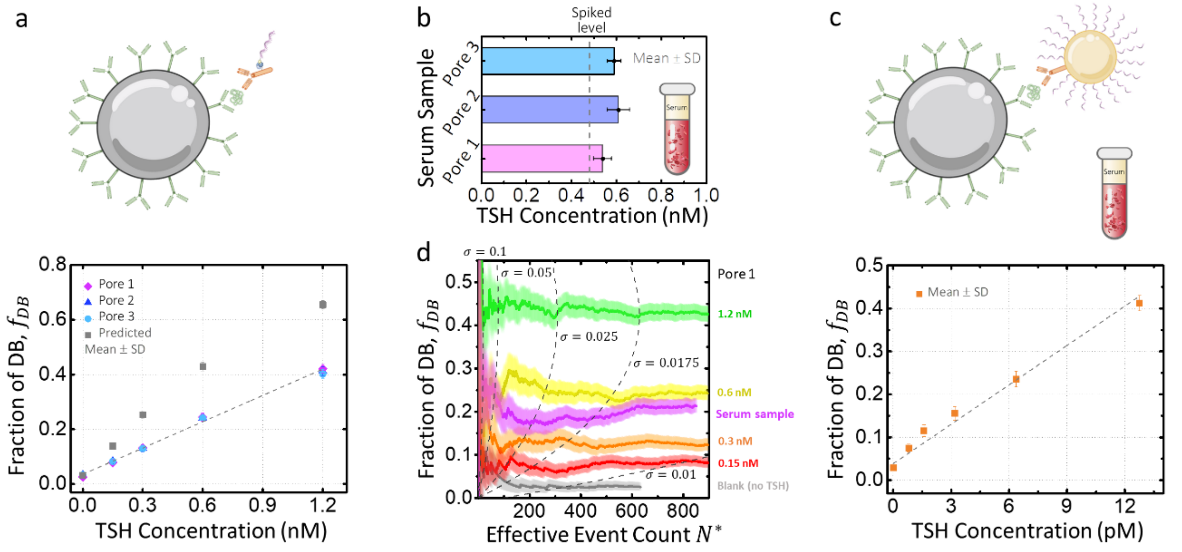

Figure 4.4. TSH assay calibration curve and TSH serum sample concentration quantification using solid-state nanopore digital detection. (a) TSH calibration curve concentration, 0 (blank), 0.15 nM, 0.3 nM, 0.6 nM, and 1.2 nM, repeated on pore 1 (10 nm, magenta diamonds, $N = 1251$, 1247, 1750, 1301, and 1239 single-molecule events), pore 2 (11.5 nm, blue triangles, $N = 1120$, 1911, 1286, 1097, and 1103 single-molecule events), pore 3 (12 nm, cyan circles, $N = 1817$, 1736, 2079, 2699, and 2140 single-molecule events), and fractions interpolated from data in **Figure 4.3**d (grey squares). The error bars represent one standard deviation following Equation 4.3. **(b)** 0.48 nM TSH spiked serum as measured by the assay on the same three pores, with $N = 1522$, 1602, 1103 single-molecule events. **(c)** Results of assay with the gold nanoparticle amplification scheme for TSH spiked in serum at 0.8 pM, 1.6 pM, 3.2 pM, 6.4 pM, and 12.8 pM on a 12.2 nm pore (orange squares, $N = 1785$, 1524, 980, 1177, 865, and 945 single-molecule events). **(d)** Fraction of dumbbell events as a function of the effective event count $N^* = N_{DB} + N_P/2$ detected for dumbbells and probes on pore 1. The colored bands represent one standard deviation, and the dashed lines represent the values of N^* needed for a given dumbbell fraction f_{DB} to have $\sigma_f = 0.1$, 0.05, 0.025, 0.0175, and 0.01. The probes P-1 and P-2 are fixed at 20 nM for 1:1 assay and 15 nM for the

amplification assay. Experiments are performed in 3.2 M LiCl in a mixture with 2 kbp linear dsDNA at 100 mV and an intra-crossings threshold of 2.5x dsDNA, all experiments are low-pass Bessel filtered at 200 kHz for analysis.

Since the speed at which single molecules are counted is dictated by the capture rate of the nanopore (a Poisson process),[44] the evolution of dumbbell fraction as a function of cumulative number of events offers insights into the assay time needed to accurately identify a particular concentration with a desired level of precision. Standard error propagation gives the mean and standard deviation of the dumbbell fraction $f_{DB} \pm \sigma_f$ as:

$$f_{DB} = \frac{N_{DB}}{N^*} \tag{4.2}$$

$$\sigma_f = \sqrt{\frac{f_{DB}(1 - f_{DB})\left(1 - \frac{f_{DB}}{2}\right)}{N^*}} \tag{4.3}$$

$$N^* = N_{DB} + \frac{N_P}{2} \tag{4.4}$$

where N_{DB} is the number of “1” events (dumbbells) and N_P is the number of “0” events (probes), assuming Poisson error on both N_{DB} and N_P, i.e., that the standard deviation of each is equal to its square root. N^* is the effective event count. Note the factor of 2 is included to pair probe events for the sake of comparison to the dumbbell fraction.

Like the standard error of a Poisson process or the standard deviation of a capture rate, the uncertainty in the ratio of two Poisson processes scales inversely with the square root of the total event count. In the limit of f_{DB} approaching either extreme of 0 or 1, where one event type dominates the counting, the numerator of Equation 4.3 approaches zero, and the uncertainty on f_{DB} is small and relatively insensitive to total event count as a result. Although intermediate values of f_{DB} show higher uncertainty for a given event count, σ_f can be reduced greatly by recording more events.

The effective event count, N^*, required to determine the fraction of events which are counted as "1" (here dumbbells) accurately within a pre-determined error of $\pm\sigma_f$ depends on the value of the dumbbell fraction f_{DB} itself. **Figure 4.4**d shows the evolution of the multiple measured dumbbell fractions of pore 1, as a function of the effective event count with respective error bars plotted following Equation 4.3. **Figure 4.4**d shows that at least 129, 173, 262, and 307 effective event counts are required to obtain an absolute uncertainty of σ_f = 0.025 (2.5%), for TSH concentrations of 0.15 nM, 0.3 nM, 0.6 nM and 1.2 nM, respectively. The minimal event count needed to distinguish two different concentrations also depends on the respective values of f_{DB}.[221,222]

4.3 Conclusions

Our discussion has thus far pertained only to the number of single-molecule translocations (counts) instead of measurement time.[44] Under our experimental conditions and with the TSH concentration ranges presented, the DNA nanostructures have a capture rate of ~1 Hz nM^{-1} on a single 10 nm nanopore, resulting in sensing times on the order of tens of minutes required for precisions of $\sigma_f \approx 0.01$. Evidently, the time to response of the nanopore sensor can be reduced or the sensitivity and precision of the digital immunoassay increased by counting single molecules more rapidly in a fixed time. We have shown the sensitivity of our digital nanopore assay can be significantly improved by amplification, yet in this configuration it is still limited by measurement time. As discussed previously, using a lower probe concentration can reduce the sensitivity by an equal factor at the cost of proportionally increasing the counting time unless the detection rate is accelerated by a combination of parallelization (array of pores), preconcentration, or capture rate enhancement schemes. See Section 4.5.5 for an example of the latter strategy. In the idealized limit of rapid nanopore detection, the enhancement factor of the K_D by the magnetic bead coated antibody and non-specific interactions would ultimately become the limiting factors.

We have shown that solid-state nanopores can be used as precise and specific digital sensors for magnetic bead-based sandwich immunoassays, using DNA nanostructures as proxies for the presence or absence of a specific target protein. We were able to accurately and most importantly consistently quantify the concentration of spiked protein in human serum in the high fM to the low nM range, overcoming several of the major challenges associated with using solid-state nanopores to quantify concentrations of biomolecular targets in complex biological samples. This represents a ~1,000× improvement in sensitivity compared to the previous nanopore studies quantifying protein concentration from serum.[69,85,99] This digital scheme, based on the electrical counting of single-molecules, is an effective solution to the pore-to-pore consistency issue that has been slowing the development of bioassays on solid-state nanopores. The shooting star nanostructures used here give a high SNR of 20 (at 200 kHz), while using high recording bandwidth to better resolve translocation events. The advantages of the antibody-coated magnetic bead approach compared to DNA nanocarrier schemes is that the affinity (more precisely the *on*-rate, k_{on}) of the magnetic-bead antibody complex to capture protein targets are enhanced by a factor equal to the number of antibodies present on the bead surface, essentially turning each bead into a much more efficient antibody and enabling fM sensitivity.[110] The selectivity is also increased by washing away background molecules and non-specifically bound objects, leaving only molecules of interest to translocate through the pore, thereby reducing false positives.

The next foci for performance optimization for our proposed assay are to increase the dynamic range and to further decrease the limit of detection while reducing the assay time to <1h. Both dynamic range and limit of detection can, in principle, be arbitrarily extended by varying the probe concentration but are practically limited here by the measurement time. As discussed previously, the current optimal dynamic range spans a ratio of junction strand (proxy for protein) to probe of ~0.01 to ~0.5, and for probe concentrations below <10 nM the incubation time required to hybridize the junction strand to two nanostructured probes to assemble the dumbbells becomes much too long (days) to be of practical use.[213] To tackle this timescale problem, techniques to control and increase the rate of nucleic acid hybridization reactions, such as isotachophoresis,[223] could be employed to extend the dynamic range from 10 nM down to the fM levels. Combined with the strategies for improving the rate of single-molecule counts by a nanopore already discussed (parallelization, amplification, pre-concentration, and capture rate enhancement schemes), we expect the proposed solid-state nanopore-based digital immunoassays scheme to reach low fM levels with a ~3-log dynamic range to undertake relevant clinical applications.

4.4 Experimental Methods

4.4.1 Probe and Dumbbell Assembly.

Probes are composed of oligos purchased from Integrated DNA Technologies. Oligo sequence information is available in **Table 4.1**. Probe 1 was assembled using the 12-star oligos and extension oligos A to G. Probe 2 was assembled using the 12-star oligos and extension oligos A to F’.

Equimolar concentrations (final concentration of 0.3 μM for each oligo in a total reaction volume of 360 μL) of all oligos were added in assembly buffer of 1x TAEMg (40 mM Tris, 20 mM acetic acid, 2 mM EDTA, and 12.5 mM magnesium acetate, pH 8), heated to 95°C for 5 min, cooled to 90°C, ramped down from 90°C at a rate of 0.4°C min^{-1} to 60 $°C$, from 60°C to 26°C at a rate of 0.03°C min^{-1}, and snap cooled to 4°C in MiniAmp Plus Thermal Cycler (ThermoFisher Scientific, #A37835). After assembly probes were visualized on 2% agarose gel in 0.5x TBE buffer, pH 8.2 (Fisher Scientific, BP1333-1). Generuler 1kb plus DNA ladder (ThermoFisher Scientific, SM1331) was used as a reference guide for nanostructure migration. GelRed (Biotium, #41003) was used for visualization of the DNA bands on all agarose and PAGE gels.

Probe batches were divided and loaded in multiple lanes on four 5% Mini-PROTEAN TBE polyacrylamide pre-cast gels (BioRad, 4565013). The band of interest was excised, and gel extracted using a custom gel extraction apparatus. Purified probe concentrations were estimated using optical density measurements made on a Take3 micro-volume plate and EPOC 2 spectrophotometer (BioTek, BTEPOCH2).

In order to assemble dumbbells directly, probe concentration was fixed at 20 nM and an increasing concentration of junction strands was added, ranging from 0.2 nM (0.01:1 junction:probe) to 400 nM (20:1 junction:probe), incubated for 2 days at room temperature (22ºC) with a total volume of 35 μL in 1x TAEMg buffer.

4.4.2 Assay Components

A step-by-step protocol describing the assay procedure can be found in Appendix A at Protocol Exchange[155]. 2.7 μm diameter paramagnetic beads were conjugated with mouse monoclonal anti human TSH beta subunit capture antibody (Fitzgerald Industries International, 10C-CR2151M4). Conjugation was performed in accordance to SIMOA Homebrew Assay Development Kit procedures (Quanterix, 101354). 0.3 mg/mL (28x dilution) TSH antibody was incubated with 1.4×10^9 beads. A non-competing detection antibody-streptavidin conjugation was done with mouse anti human TSH beta subunit detection antibody (Maine Biotechnology Services, MAB130P) and conjugated to streptavidin (1.6x dilution) using a Streptavidin Conjugation Kit (Abcam, ab102921).

For the assay calibration curve, 7.2×10^7 bead-capture antibody conjugates were mixed with varying amounts of recombinant TSH (rTSH) (BiosPacific, J11030) at concentrations of 0, 0.15, 0.3, 0.6 and 1.2 nM in 1x sample/detector diluent (Quanterix, 101359) for a total volume of 500 μL (volume used for all assay steps unless otherwise noted) and incubated for 1hr at room temperature (RT), 22ºC. To keep beads in suspension, tubes were placed on a 360° Multi-Functional Tube Rotator (VWR, PTR-35). All subsequent incubations and washes (>30 seconds) were performed on the rotator. For the 480 pM rTSH spiked serum sample a similar mixture was applied but with a 4x diluted serum (125 μL). De-identified human serum samples were purchased from BioIVT and collected from consented donors under IRB-approved protocols following BioIVT standard operating procedures and tested for TSH on an in house TSH assay (homebrew) using the SiMoA platform (HD-1 Analyzer, Quanterix). TSH levels in the samples used are below the lower limit of detection (LoD 0.18 fM), therefore undetectable in our nanopore assay. A 4x dilution was applied to the serum sample to reduce matrix effects.[224] For the amplification assay measurements, identical procedure was followed: 10^7 bead-capture antibody conjugates were mixed with varying amounts of recombinant TSH at concentrations of 0, 0.8, 1.6, 3.2, 6.4, and 1.2 pM in 4x diluted serum of total volume of 650 μL, and washes were done with 200 μL 1x wash buffer instead. After initial incubation, three wash steps were performed by magnetically immobilizing the paramagnetic beads, removing the supernatant, and resuspending in 1x wash buffer 1 (Quanterix, 100486), with 5-, 10-, and 15-minutes intervals between each wash. Following washes, the immobilized beads are removed from the magnet and the pellet is resuspended in 500 μL 1x sample/detector diluent containing 6 nM of detection antibody-streptavidin conjugate and incubated for 1hr at RT. For the amplification assay, the gold nanoparticle amplification complex was added and incubated. After incubation, three 30 seconds washes with 1x wash buffer were performed to remove any unbound detection antibody. To complete the immunoassay sandwich for all samples, 12 nM of biotinylated ssDNA junction strand were added and incubated in 1x sample/detector diluent for 15 minutes at RT. To remove any excess of unbound junction strands, three 30 seconds washes using 1x wash buffer were performed, followed by buffer exchange to 1x TAEMg with 0.1% Tween-20. **Figure 4.14** in Section 4.5.4 demonstrates that the presence of Tween-20 in the 1x TAEMg and 0.1% release/assembly buffer does not appear to affect nanopore background or assembly.

For the gold nanoparticle (AuNP) amplification complex, 30 nm standard gold nanoparticles (1 OD, Cytodiagnostics, G-30-20) were prepared following the protocols developed by Mirkin & co[152,220] as well as manufacturer technical notes. 0.1 M borate buffer was added to a total of 1 mL of 30 nm stock AuNP to adjust pH to 9.0, followed by the addition of 4 μg of detection antibody (Maine Biotechnology Services, MAB130P). After a 30-minute incubation, 25 μL of 30 μM reduced DNA oligos were added and incubated for 1 hour. The solution was then salt-aged 0.15 M NaCl over the course of 3 hours at room temperate with gentle vortexing, and further incubated at 4 ^{o}C overnight. 50 μL of 10% BSA was added to the solution and incubated for 20 minutes to passivate and stabilize the AuNP. The final solution was centrifuged at 4,500g for 15 minutes, and the supernatant was removed. This wash step was repeated 3 times and final complex was resuspended in 200 μL of 1xPBS with 0.025% Tween 20.

All samples were exposed to UV using a 3W LED flashlight (LIGHTFE, UV301D) at a distance of 1 cm for 20 minutes to cut the photocleavable linker present at the 5' end of the junction strand and release it from the immuno-sandwich. For the amplification assay, the junction strands are released by an incubation of 45 minutes in 0.2 M DTT (Dithiothreitol, ThermoFisher Scientific, A39255) and 0.3M NaH_2PO_4 buffer. Junction strands were recovered by magnetically immobilizing the remaining immuno-complex and recovering the supernatant with a pipette. To match the sensing range of the nanopore, a concentration step was performed to reduce the volume from 500 μL to 30 μL using Amicon Ultra-0.5 Centrifugal Filter Unit (Millipore Sigma, UFC500396). This yields an approximately 16.7x concentration increase of the junction strand into the low nM range for optimal nanopore sensing. Dumbbells were assembled simply by adding the probes to the junction mixture at a concentration final of 20 nM each (15 nM in case of the amplification assay) and incubating for two days. Note that shorter dumbbell assembly incubation times can be employed when the junction to probe ratio is far from 1 in either direction, however, two days was used to ensure complete assembly at the 1:1 ratio and avoid timing-related errors during proof-of-concept measurements. Further discussion regarding DB assembly time can be found in **Figure 4.10** in Section 4.5.3).

4.4.3 Nanopore Fabrication

Nanopores were fabricated in 12 nm thick free-standing SiN_x membranes (Norcada, NBPX5004Z) using controlled breakdown (CBD).[12,13] CBD was performed in 1M KCl buffered with 10 mM HEPES at pH 8 and pores were grown to 9 nm to 12 nm in 3.6 M LiCl buffered with 10 mM HEPES at pH 8 using moderate voltage conditioning.[12,28] Prior to fabrication, the chips were cleaned using air plasma for 70 seconds and painted with a layer of PDMS to reduce high-frequency noise.

4.4.4 Nanopore Sensing

The DNA nanostructures (in 1x TAEMg pH 8) were diluted a final concentration of 3.2 M LiCl for nanopore sensing, where 5 µL of the nanostructure of was added to 35 µL 3.6 M LiCl buffered with 10 mM HEPES at pH 8. Linear 2kbp dsDNA fragments (ThermoFisher Scientific, SM1701) were always added to the mixture of nanostructure sample as a molecular ruler (with final concentration of 2.4 nM) to normalize away pore geometry variations during post-processing. Samples were introduced to the *cis* side of the chip and a negative voltage was applied to the *cis* side with the *trans* side grounded. The ionic current recordings were performed in MATLAB 2013a (32-bit) using the VC100 current amplifier (Chimera Instruments) with sampling frequency of 4.17 MHz and a bandwidth of 1 MHz and were subsequently software low-pass Bessel filtered as needed. The raw data files are accessible via Federated Research Data Repository: https://doi.org/10.20383/102.0483

4.4.5 Data Analysis

Nanopore signals were analyzed using a custom implementation of the CUSUM+ algorithm,[55,56] which is freely available online[180] (https://www.github.com/shadowk29/CUSUM). A digital low-pass filter of 200 kHz was applied unless otherwise specified. Dumbbells events were distinguished using threshold crossing, with events containing exactly 4 threshold crossings identified as dumbbells, and exactly 2 threshold crossings as probes. Events with any other count of threshold crossings were rejected from analysis. Note that bandwidth limitations occasionally cause one pair of threshold crossings to be missed, resulting in a false negative. While improvements to analysis will be able to somewhat mitigate this issue going forward, in general, the proportion of events in this category are relatively consistent between pores and can be calibrated into the measurement with minimal loss of precision and accuracy. Examples of all observed event types are shown in Supplementary Notes 3. ImageJ was used for band intensity in gel images, OriginLab for plotting data.

4.4.6 Data Availability

Raw data supporting the immunoassay results within this paper are accessible via Federated Research Data Repository: https://doi.org/10.20383/102.0483. Any other data including validation and repeated experiments are available from the corresponding author upon reasonable request due to limited storage available. All processed data are provided in the Source Data file.

4.4.7 Code Availability

Nanopore data analysis was done using in-house program available at https://www.github.com/shadowk29/CUSUM

4.5 Supplementary Information

4.5.1 Design and Sequences for DNA Nanostructures

12-Arm relaxed core shooting stars probes (P-1 and P-2)			Bases (#)	GC Content (%)
Star oligos				
1	5'	AGGCACAGCTATAATAACGCAATCC/iSp18/TCTCCGGCCTCAAACTACTTTACCT	50	46
2	5'	AGGTAAAGTAGTTTGAGGCCGGAGA/iSp18/CCGAATGGAGTCTGTTCTCGACGCT	50	52
3+	5'	CAATTCTACTAATAGGAATTCGATTAGCGTCGAGAACAGACTCCATTCGG/iSp18/ACAAGTAC GAACCAACTTAGGACCT	75	43
4	5'	AGGTCCTAAGTTGGTTCGTACTTGT/iSp18/GGTCATCGTGGCGTACCATATACCT	50	48
5	5'	AGGTATATGGTACGCCACGATGACC/iSp18/TCTTCGATCTACCCGATAGGCTCCT	50	52
6	5'	AGGAGCCTATCGGGTAGATCGAAGA/iSp18/CGTACAGGTGTGACTTGAATTTGCT	50	48
7	5'	AGCAAATTCAAGTCACACCTGTACG/iSp18/AGTGTTAGAATACAACAAGCGACCT	50	42
8	5'	AGGTCGCTTGTTGTATTCTAACACT/iSp18/GCATCTCATACGACAGCATCCGACT	50	46
9	5'	AGTCGGATGCTGTCGTATGAGATGC/iSp18/TGAGCACGGAACTGTCAACCTTGCT	50	52
10	5'	AGCAAGGTTGACAGTTCCGTGCTCA/iSp18/CGTTCATTAAGATAAATCTGATCCT	50	42
11	5'	AGGATCAGATTTATCTTAATGAACG/iSp18/ACTATGACTGCTACATGCACTTCCT	50	38
12	5'	AGGAAGTGCATGTAGCAGTCATAGT/iSp18/GGATTGCGTTATTATAGCTGTGCCT	50	44
Extension oligos common to P-1 and P-2				
A	5'	AATCGAATTCCTATTAGTAGAATTGATGCCACCTCATCAGCTCGCGTCCG	50	46
B	5'	AACCTGTGTACGACTTAGATCTGTACGGACGCGAGCTGATGAGGTGGCAT	50	52
C	5'	TACAGATCTAAGTCGTACACAGGTTGCCTGAGTTGTGCGACGACGTCAGA	50	50
D	5'	CCGTAGCTGGACGTAGCGTGACCATTCTGACGTCGTCGCACAACTCAGGC	50	60
E	5'	ATGGTCACGCTACGTCCAGCTACGGGCAGAATTGGGAATCAACTGTTACA	50	50
P-1 specific extension oligo				
F	5'	GACGGTGTCTGGAAGTCTCACAGCATGTAACAGTTGATTCCCAATTCTGC	50	48
G	5'	TGCTGTGAGACTTCCAGACACCGTCCTTTAGTTGCATATAAGCTTCATGT	50	44

P-2 specific extension oligo				
F'	5'	CTACGTTCCTGGGTGACGAGCGTACTGTAACAGTTGATTCCCAATTCTGC	50	48
Dumbbell Junction oligo				
Junction	5'	/5PCBio/GTACGCTCGTCACCCAGGAACGTAGACATGAAGCTTATATGCAACTAAAG	50	46

Table 4.1. Shooting Star and Dumbbell assembly oligo sequences.

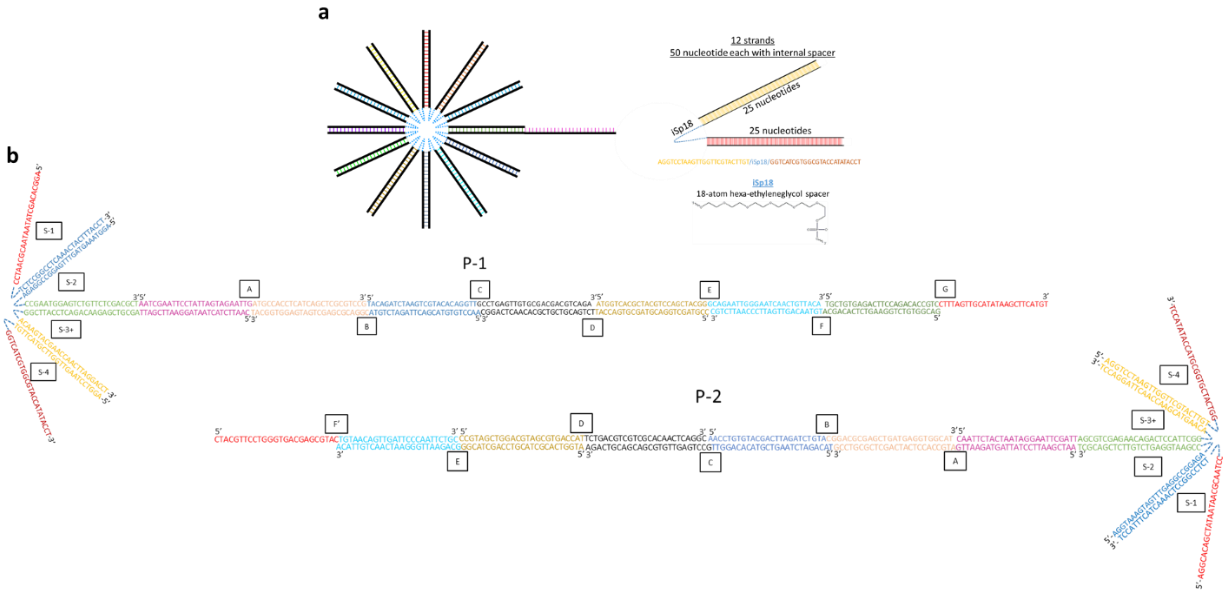

Figure 4.5. Shooting star probes (P-1 and P-2) design. (a) Schematic representation of the star portion of the DNA probes. The star structure is composed of eleven 50 nucleotide oligos each containing a hexa-ethyleneglycol spacer (EG6) in the middle of the sequence after the first 25 nt. Oligo 3+ has an additional 25 nt ssDNA overhang **(b)** Schematic representation of the shooting star probes. The tail strands attach to the 25 nt ssDNA overhang present on strand (3+) upon which hybridize 7 staggering 50nt sequence staple strands (A-G) for the P-1 or 6 staggering 50nt sequence staple strands (A-F') for the P-2.

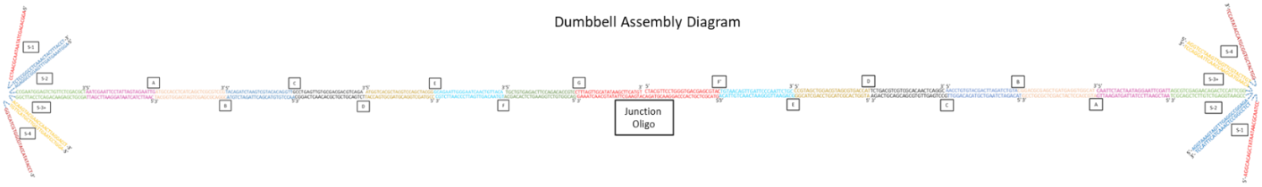

Figure 4.6. Dumbbell assembly diagram. The shooting stars probes (P-1 and P-2) are joined together by a 50 nt junction oligo. Junction oligo halves are complementary to the respective 25 nt overhang present on the shooting star probe pair.

4.5.2 DNA Nanostructure Assembly and Purification

A typical batch of shooting star assemblies can be visualized in **Figure 4.7**. Initial shooting star assembly parameters were based on previous work from He *et al. 2019.*[64] Assembly of the shooting star probes were further optimized by varying the heat source (thermocycler vs heat block), incubation time, and oligo concentration. The optimized protocol is described in the Methods section of the main text. **Figure 4.7** lanes 4 and 5 show the crude assemblies of the P-1 and P-2 respectively. Due to the increase DNA nanostructure complexity, the top bright band corresponds to the fully formed shooting star probes. Even though it is the dominant band, it only makes up 20-30% of the total population, as measured through gel electrophoresis band density estimates. This leaves a significant portion of the nanostructures as misassembled products that have the potential to cause false positives and false negatives during nanopore sensing. Because of this, all nanostructures employed for nanopore experiments are purified by gel extraction (described in

Section 4.2 and Appendix A), which increases the fraction of correct shooting star assemblies to 80-90%. Pure products can be visualized in **Figure 4.7** lanes 2 and 3. Agarose gel extraction yielded better recovery after purification, however, the gel introduced further which caused pore clogging.

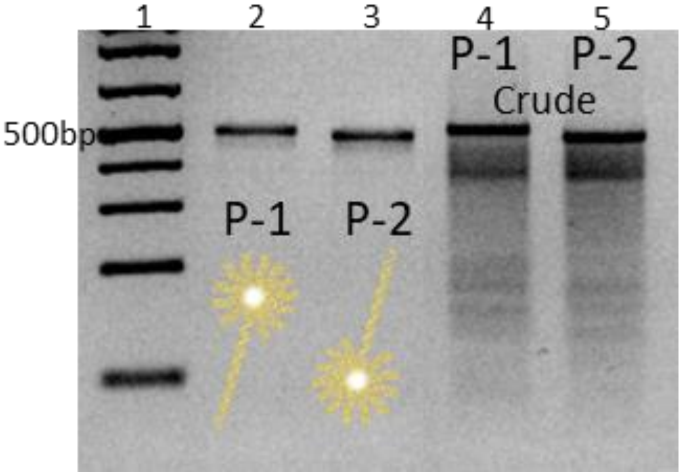

Figure 4.7. Agarose gel (2%) of shooting star probes P-1 and P-2 assemblies and purification. Lane 1: GeneRuler 1kb Plus DNA Ladder (ThermoFisher Scientific, SM1331), from bottom 75, 200, 300, 400, 500, 700, 1000, 1500, 2000, 3000, 4000, 5000, 7000, 10000, and 20000 bp, lane 2: gel extracted P-1, lane 3: gel extracted P-2, lane 4: crude P-1 and lane 5: crude P-2.

4.5.3 Dumbbell Event Detection

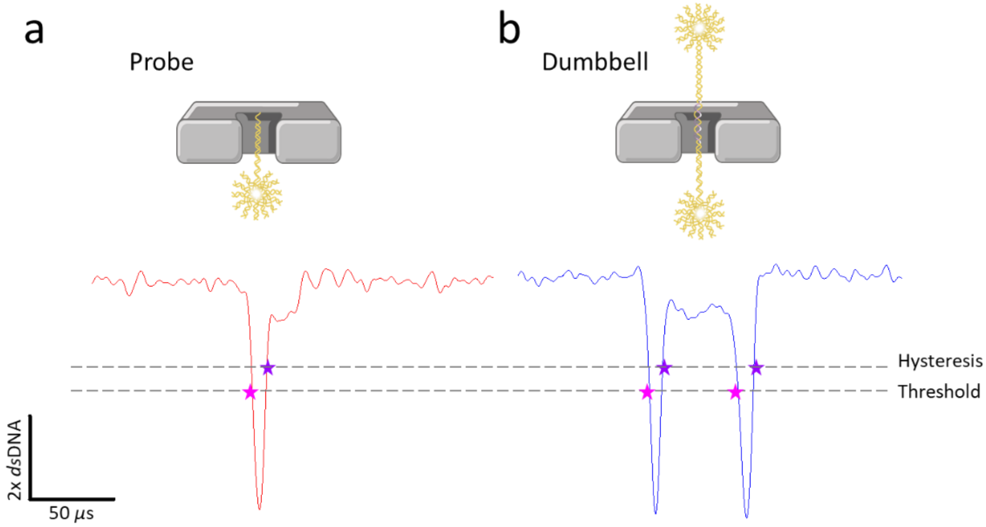

Figure 4.8. Dumbbell detection using threshold crossing scheme.

(a) A shooting star probe event registers 2 intra-crossings. **(b)** A dumbbell event registers 4 intra-crossings. The threshold is set to 2.5x dsDNA unless otherwise specified. To avoid triggering on noise, the threshold that indicates the return to baseline is closer to the baseline than the threshold that indicates the start of the deep part of the event (hysteresis).

Translocation events in the current recordings are analyzed using a custom version of the CUSUM+ algorithm[39,212], and a simple threshold-crossing algorithm is used to label events as being due to dumbbell or shooting star probe translocation. Data analysis is performed with a digital low-pass Bessel filtered at 200 kHz. A shooting star probe event contains two threshold crossings and a dumbbell event contains four threshold crossings. The threshold to indicate the start of a deeper sub event is set to 2.5x the average linear dsDNA blockage for that pore, normalized to the local baseline current, while the threshold to indicate the end of that sub event is set to 6x baseline standard deviations.

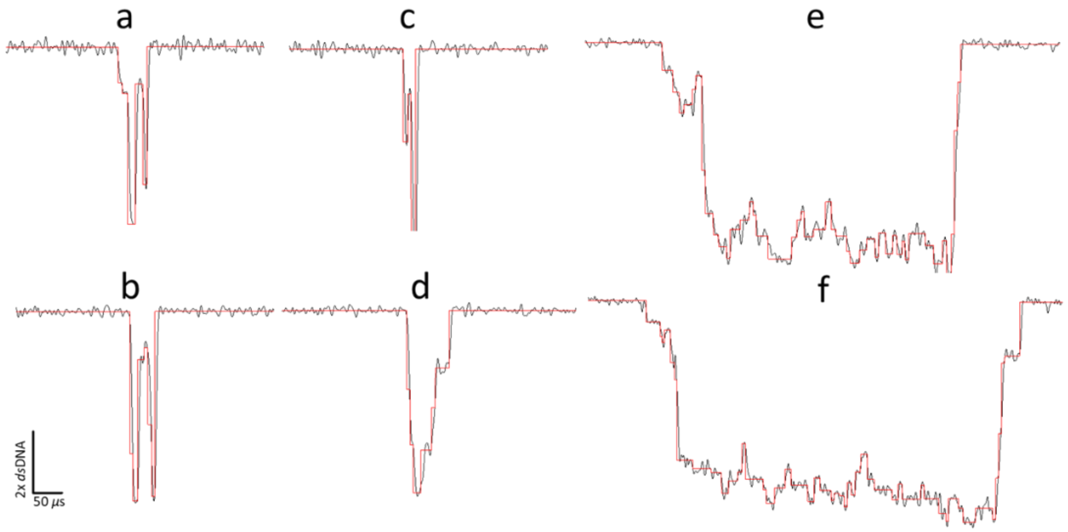

Figure 4.9. Example current traces of false positive events. (a-b) Current traces showing two distinct peaks, representing shooting star probe pairs connected by a dsDNA, indicating formation of DB due to non-specific binding. **(c)** Example current trace of an event with one peak significantly shallower than the other, representing a shooting star event with a folded extension tail, resulting in false positive. **(d-f)** Current traces of shooting stars performed using an 11 nm pore, with an applied bias of 100 mV.

The progression of the dumbbell assembly (10 nM junction ssDNA to 20 nM shooting star probes occurs quickly from 30 minutes to 4 hours, at which point it starts to level off, reaching a plateau at the 2-day mark and remaining at the plateau until beyond the 10-day mark. Interestingly, we do not observe any increase in dumbbell fraction during the nanopore sensing experiments even at short incubation times. Evidently, the dumbbell formation does not take place at an appreciable rate in the nanopore running buffer of 3.2 M LiCl, for the “0.5-hr” experiment in particular in

Figure 4.10c (red). The dumbbell fraction stabilizes to 17 % during the nanopore sensing time of 20 minutes (total of 50 minutes since the start of incubation) rather than increasing towards the 25 % observed in to the "1-hr" experiment. Nanopore sensing was not performed on samples incubated longer than 10 days. Reductions in the required incubation time can be achieved by ensuring an excess of shooting stars over junctions.

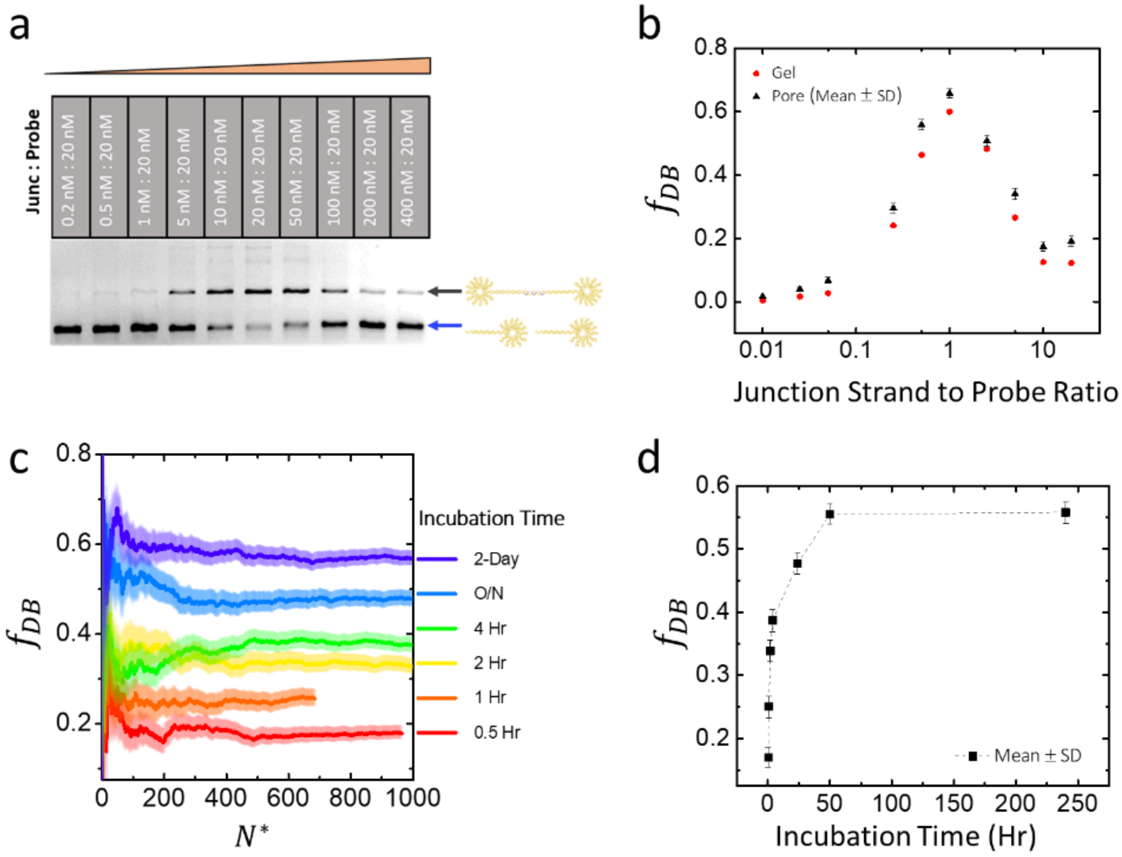

Figure 4.10. Dose response and time dependence of dumbbell assembly. (a) Gel electrophoresis (2% agarose) of dumbbells formation and remaining shooting star probes as junction concentration increases. **(b)** Comparison of dose response with junction concentration ranging from 0.2 nM to 400 nM (junction to shooting star probes ratio of 0.01:1 to 20:1) between nanopore sensing with N = ~1100 single-molecule

events at each concentration and gel band densitometry. **(c)** The time response of dumbbell events fraction f_{DB} for incubation time of 30 minutes to 2 days. **(d)** Dumbbell events fraction f_{DB} as a function of incubation time. The sample (10 nM junction ssDNA and 20 nM shooting star probes) is prepared in 1xTAEMg with a total volume of 35 μL, and 5 μL is sequentially taken from the sample and subjected to nanopore sensing after incubations of 0.5, 1, 2, 4, 24 (O/N), and 48 hours. The error bars represent one standard deviation following Equation 4.3 of the main text. All experiments are performed using an 11.3 nm pore, with an applied bias of 100 mV and the intra-crossings threshold set to 2.5x dsDNA.

Even when gel extracted purified dumbbell, 100% positive events is not attainable. **Figure 4.11**a shows a scatter plot of the purified dumbbell in which a small fraction of the shooting star or non-dumbbell events is still present. The threshold is set to multiples of the standard deviation of the local segment of the current baseline, making it a dynamic value which depends on the baseline value and noise. **Figure 4.11**b shows that the standard deviation of the baseline is indeed fluctuating. **Figure 4.11**c shows the gel electrophoresis results obtained using purified dumbbells, confirming the existence of impurities.

Two different batches of dumbbells are gel extracted and sensed on two different pores, as shown in **Figure 4.11**d-e, registering 81 ± 2 % and 84 ± 3 % dumbbells (instead the expected 100 %) using 13.6 and 12.7 nm pores. Potential contributing factors specific to the nanopore, include changes in baseline current, over-/under-crossing of the threshold and potential mechanical damage during translocation. In the case of over-crossing, the “dip” is higher than the set threshold (2.5x dsDNA), as shown in **Figure 4.11**g, resulting in the false negative event, while in the case of under-crossing, one of the stars in a dumbbell molecule translocates too fast and is not fully resolved by the recording device, resulting in one of the peaks having a blockage lower than the set threshold (2.5x dsDNA), as shown in **Figure 4.11**h (false negative). Another potential source of error would be partial degradation of the fully formed dumbbell nanostructure post purification. Evidence of this can be seen on the agarose gel (**Figure 4.11**c) as multiple faint bands below the purified dumbbell bright band.

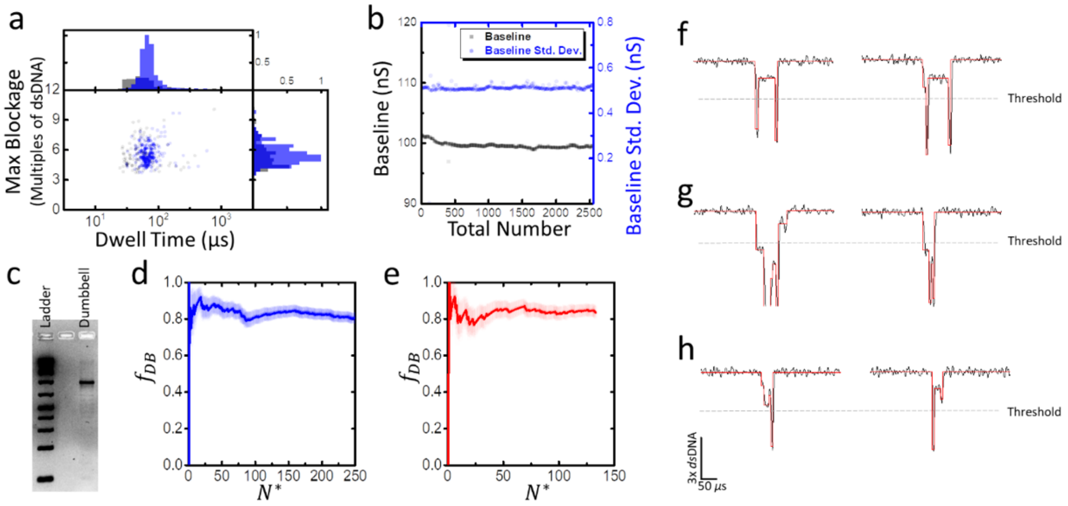

Figure 4.11. Purified dumbbell translocation characteristics. (a) Scatter plot and projected histograms of dwell time distribution and maximum blockage distribution of purified dumbbell (DB) using a 13.6 nm pore. **(b)** Baseline (black, left axis) and the standard deviation of the baseline (blue, right axis) versus total number of events of the purified DB profile shown in **(a)**. **(c)** Gel electrophoresis of purified DB batch 1 using 2 % Agarose gel in 0.5x TBE with an applied voltage of 100 V. Lane 1: GeneRuler 1kb Plus DNA Ladder (ThermoFisher Scientific, SM1331), from bottom 75, 200, 300, 400, 500, 700, 1000, 1500, 2000, 3000, 4000, 5000, 7000, 10000, and 20000 bp. **(d-e)** Time response of purified DB batch 1 and batch 2 using a 13.6 nm pore (blue) and a 12.7 nm pore (red) respectively. **(f-h)** Example current traces (black) and their fits (red) representing good crossing, over crossing, and under crossing. All experiments are performed in 3.2 M LiCl with an applied bias of 100 mV.

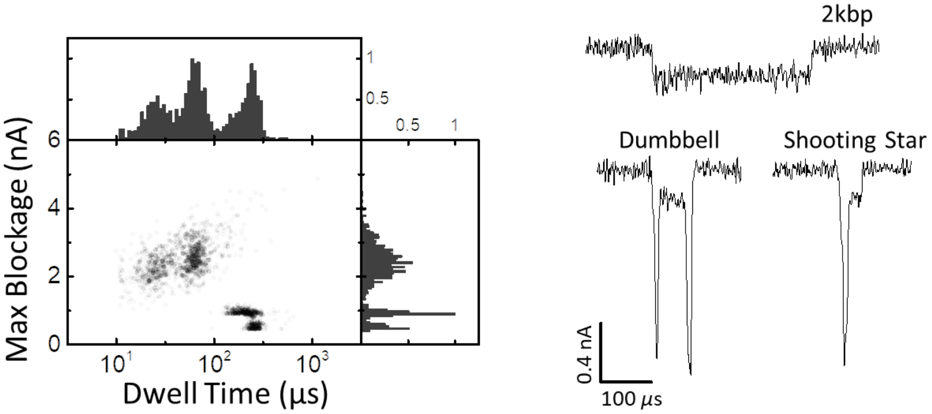

Figure 4.12. Scatter plot and current traces of shooting star probes and dumbbell. Scatter plot and projected histograms of dwell time distribution and maximum blockage distribution of a mixture of nanostructures (shooting star, dumbbell, and 2kbp dsDNA) and their representative current traces. The nanopore experiment is performed using a 12 nm pore, in 3.2 M LiCl, with an applied bias of 100 mV and the intra-crossings threshold set to 2.5x dsDNA.

Figure 4.12 shows a scatter plot of maximum blockage (in nA) *versus* dwell time of shooting star, dumbbell, and 2kbp dsDNA. In the main article, we use the unit of dsDNA which refers to the current blockage level of 2kbp dsDNA, all experiments were done with linear 2kbp DNA in the mixture, they were added as a molecular ruler to help reduce pore-to-pore and experiment-to-experiment variance in current blockage level, to ensure consistency in the threshold-crossing algorithm.

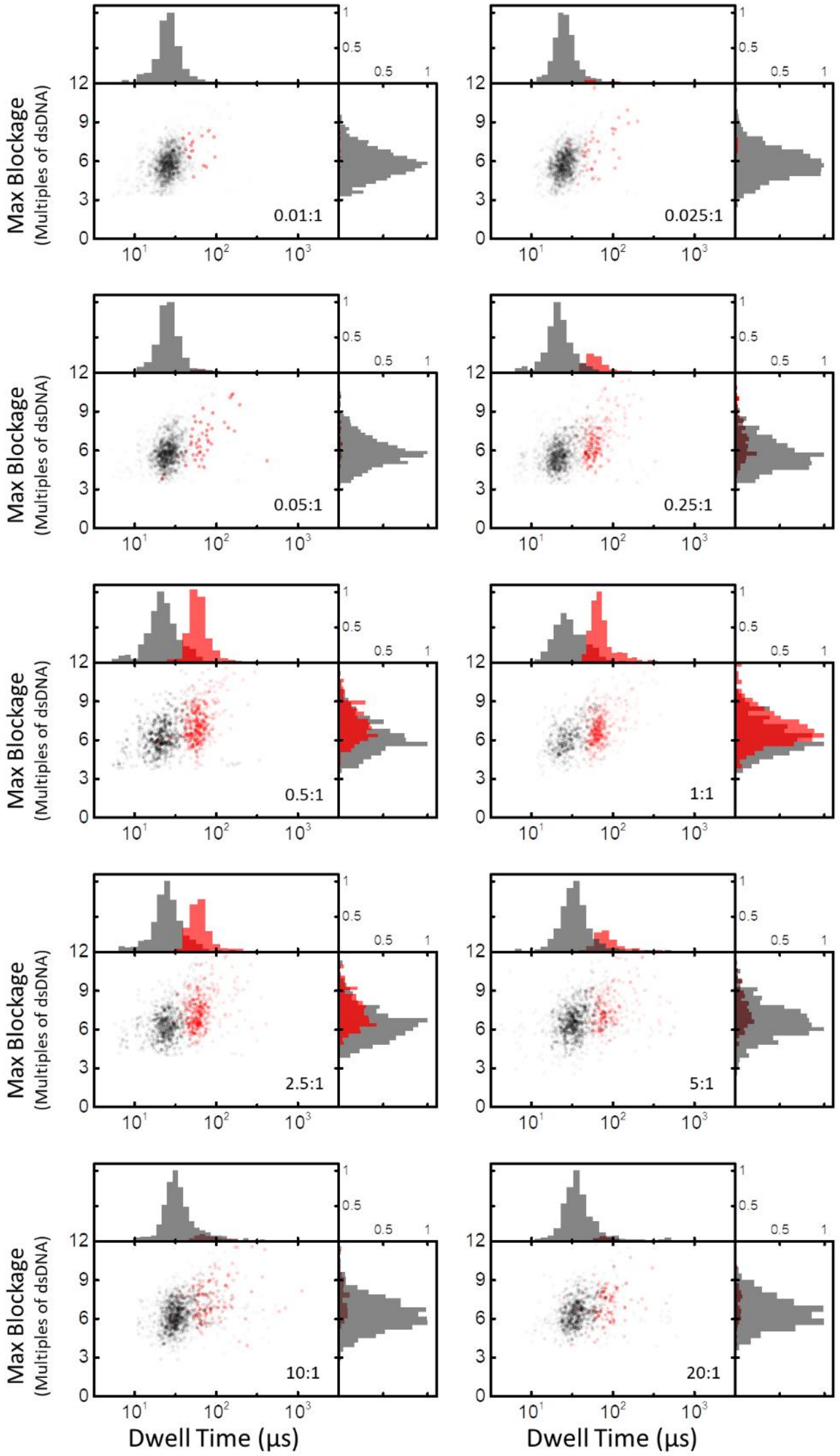

Figure 4.13. Scatter plots of dose response experiments. Scatter plots and histograms of maximum blockage *versus* dwell time (log scale) of dose response in **Figure 4.3**, of junction strand to shooting star

ratio from 0.01:1 to 20:1, showing 1639, 1524, 1268, 1337, 917, 882, 964, 1019, 1270, and 853 single-molecule events, respectively. Dumbbell events (red) are separated from shooting star events (dark grey) using the threshold-crossing algorithm.

4.5.4 Additional TSH Immunoassay Results

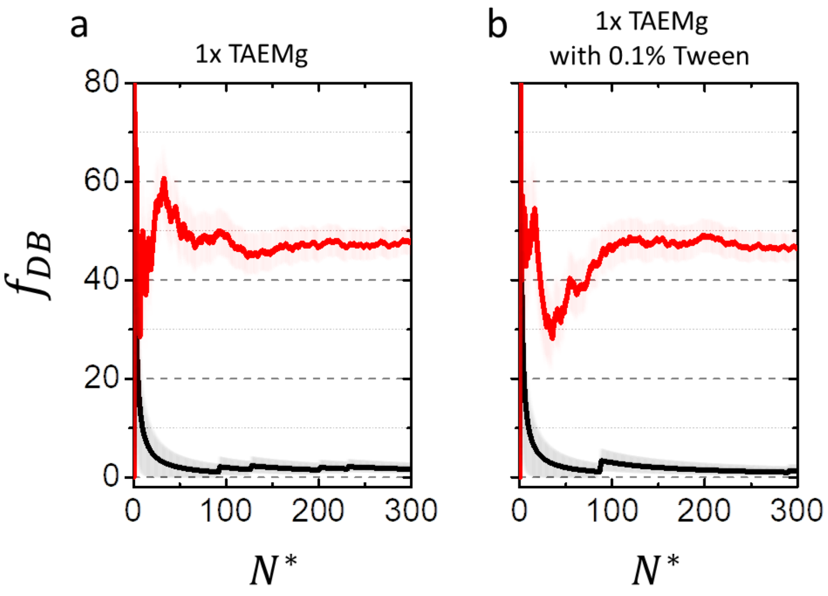

Figure 4.14. Assay buffer test and the effect on dumbbell assembly and nanopore detection. Time response of dumbbell formation with (red) and without (black) the junction ssDNA in **(a)** 1x TAEMg **(b)** 1x TAEMg with 0.1% tween 20. All four experiments are performed in 3.2 M LiCl with applied bias of 100 mV using an 11 nm pore, a 20 nM to 20 nM junction to shooting star ratio was used, with the threshold set to 2.5x dsDNA.

The use of tween-20 in the final steps of the assay during release of the junction strand significantly reduces assay components sticking to the tube walls. To ensure that the surfactant used during the assay steps does not affect nanopore performance, a set of comparison experiments are carried out. The samples are: 1) Mixture of equimolar P-1 and P-2 at 20 nM in 1xTAEMg. 2) Mixture of equimolar P-1 and P-2 at 20 nM with 20 nM junction ssDNA. 3) Mixture of equimolar P-1 and P-2 at 20 nM in 1xTAEMg plus 0.1 % tween-20. 4) Mixture of equimolar P-1 and P-2 at 20 nM with 20 nM junction ssDNA plus 0.1 % tween. All four samples are sensed on an 11 nm pore under the same experimental conditions. A background of 1.7% and 1.4% dumbbell events are detected for samples 1 and 3, while 47.1% and 46.7% are detected for samples 2 and 4, as shown in **Figure 4.14**. We observe that 0.1% tween has no effect the assembly of dumbbells, and it does not induce additional background, as identical results are reported in **Figure 4.14** with and without 0.1% tween-20. Furthermore, 0.1% tween has no measurable effect on nanopore sensing performance.

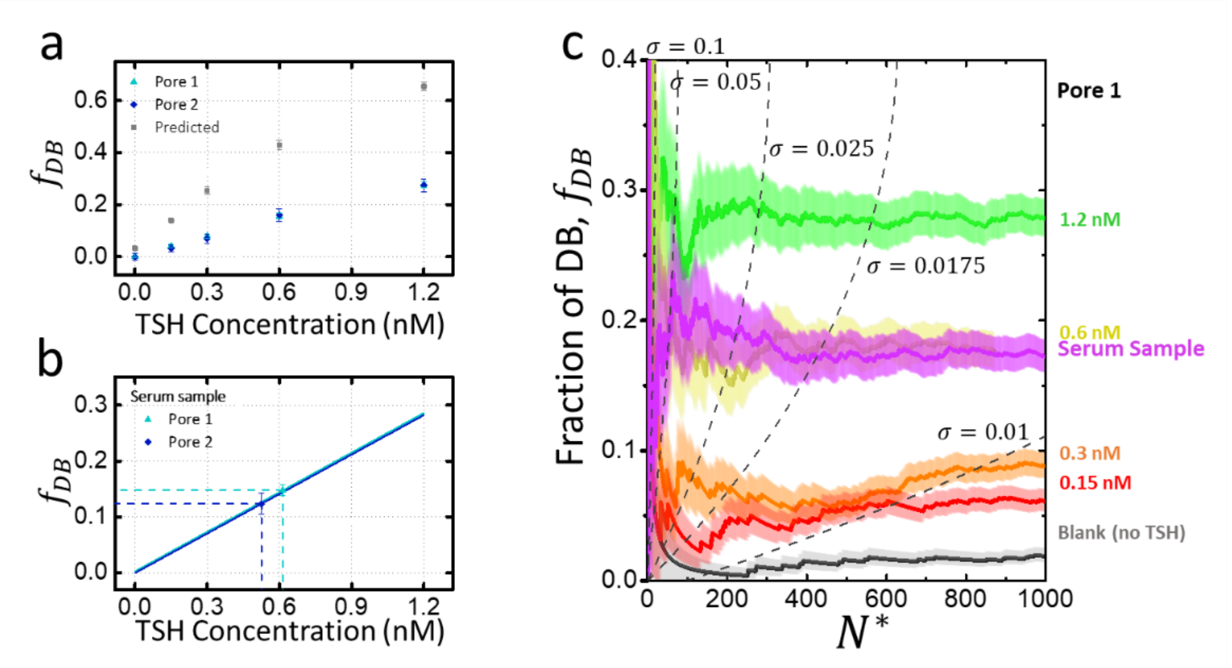

Figure 4.15. TSH assay calibration curve and TSH serum sample quantification using solid-state nanopores with a different batch of reagents. (a) TSH calibration curve concentration, blank 0, 0.15 nM, 0.30 nM, 0.60 nM, and 1.2 nM, repeated using pore 1 (12.5 nm) and pore 2 (14 nm). **(b)** 0.48 nM TSH spiked serum on the same pores. **(c)** The time response of the assay calibration points, fraction of dumbbells (DB) events as a function of effective event count detected using a 10 nm pore. The colored bands represent one standard deviation. The end points of each calibration point with two standard deviations are projected on the right. The time response of serum sample spiked with 0.48 nM TSH, repeated using pore 1 (12.5 nm). The probes P-1 and P-2 are fixed at 20 nM. All experiments are performed in 3.2 M LiCl in a mixture with 2kbp dsDNA standard with an applied bias of 100 mV and the intra-crossings threshold set to 2.5x dsDNA.

The TSH assay repeats are conducted using a different batch of reagents on pore 1 (12.5 nm) and pore 2 (14 nm) as shown in **Figure 4.15**. Following the assay scheme, the ssDNA junctions released from the sandwich assay corresponding to 0, 0.15, 0.3, 0.6 and 1.2 nM TSH concentrations are collected and mixed with shooting star pairs at a fixed concentration of $c_1 = c_2 = 20$ nM. A 5-point calibration curve is then constructed, as shown in **Figure 4.13**. Backgrounds of 2% and 5% positive events are detected in the blank sample (subtracted from calibration points) using the 12.5 nm and 14 nm pore, respectively. A serum sample spiked with 0.48 nM TSH was then sensed on the 2 pores, measuring 17 $\pm$1% and 17 $\pm$2% positive events respectively. Since the calibration curve shows a linear dose response, we interpolate a target to probe ratio of 0.51 and 0.44, corresponding to 10.2 nM and 8.7 nM junctions in the mixture with shooting star probes and predicting the initial target TSH concentration in the assay to be 0.61 $\pm$0.03 and 0.53 nM $\pm$0.08, respectively. **Figure 4.15**c shows that at least 67, 113, 196 and 279 effective event counts are required to obtain an absolute uncertainty of σ_f = 0.025 (2.5%), for TSH concentrations of 0.15 nM, 0.3 nM, 0.6 nM and 1.2 nM, respectively.

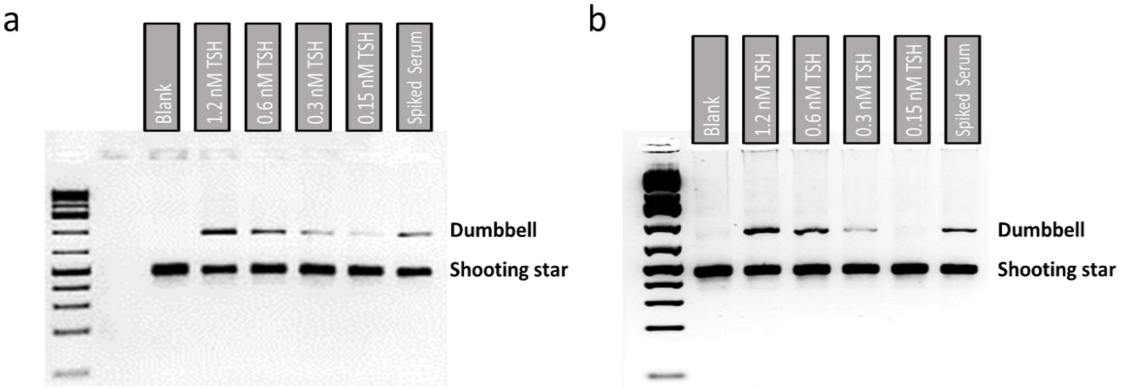

Figure 4.16. Dumbbell formation as a function of target protein concentration using 2 % Agarose gel. (a-b) TSH assay samples from left to right: blank (no TSH), 1.2, 0.6, 0.3, 0.15 nM TSH, and 0.48 nM TSH

spiked serum sample. **(a)** Same samples as the nanopore TSH assay shown in Figure 4 of the main article. Lane 1: GeneRuler 1kb Plus DNA Ladder (ThermoFisher Scientific, SM1331), from bottom 75, 200, 300, 400, 500, 700, 1000, 1500, 2000, 3000, 4000, 5000, 7000, 10000, and 20000 bp.

Figure 4.16 shows gel electrophoresis of the both TSH assay demonstrated in main text **Figure 4.4** in Section 4.2, and in **Figure 4.15**, confirming our observations from the nanopore sensing in which we can observe 1) the blank, no visible dumbbell band (nanopore false positive, signal to noise of dumbbell like DNA nanostructures), 2) 1.2 nM to 0.15 nM TSH calibrators, a decreasing amount of dumbbell products and 3) the 0.48 nM TSH spiked serum, the dumbbell band intensity appears as it should between the 0.6 nM and 0.3 nM calibrators bands intensities.

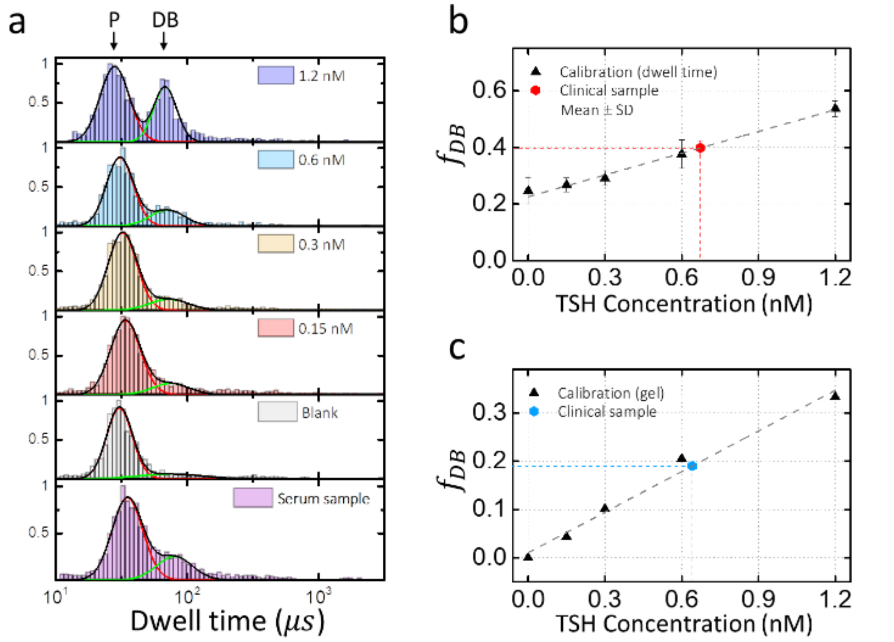

Figure 4.17. Additional analysis of TSH assay. (a) Histograms of nanopore dwell time distribution. Calibration curves of TSH concentration of blank, 0.15, 0.3, 0.6, and 1.2 nM, are constructed using **(b)**

Gaussian fits of dwell time distribution, with $N = 1251, 1247, 1750, 1301, 1239$, and 1522 single-molecule events, error bars represent one standard deviation from the Gaussian fits, and **(c)** Relative gel electrophoresis band intensity. Serum sample spiked with 0.48 nM TSH are measured and plotted using both methods. All nanopore experiments are performed using a 10 nm pore in 3.2 M LiCl with an applied bias of 100 mV. Gel electrophoresis is performed using 2% Agarose in 0.5x TBE buffer at 100 V.

Although the use of threshold crossings using nanopores has shown great consistency and reproducibility, we also compare to a few other methods of quantification. Here, besides using the threshold technique as presented **Figure 4.4** in Section 4.2, we extracted DB fraction by Gaussian fitting the dwell time distribution and relative gel electrophoresis band intensity for the same data set. **Figure 4.17**a shows the histogram of dwell time distributions of TSH concentration of blank, 0.15, 0.3, 0.6, and 1.2 nM, and serum sample spiked with 0.48 nM TSH. A calibration curve of dumbbell formation *versus* TSH concentration is constructed by comparing dwell time distribution, as shown in **Figure 4.17**b, the serum sample spiked with 0.48 nM TSH is then plotted and extrapolated from the fit, measuring 0.67 nM. Similarly, by comparing gel electrophoresis intensities of bands from **Figure 4.16** for different TSH concentrations, the same 5-point calibration curve is constructed as shown in **Figure 4.17**c. The serum sample spiked with 0.48 nM TSH is performed on the same gel, extrapolating the DB fraction obtained from gel electrophoresis in **Figure 4.17**c, it measures 0.64 nM. The alternative methods of dwell time distribution analysis and gel band intensity analysis predict TSH initial concentrations of 0.67 and 0.64 nM, comparable to the nanopore results obtained using threshold crossing (0.54, 0.61, and 0.59 nM using 10, 11.5, and 12 nm pores, respectively, as shown in **Figure 4.4** in Section 4.2).

Although the dwell time analysis yielded similar results and gel band analysis yield similar results, the two alternative methods have their limitations. The nanopore-based dwell time distribution analysis relies on the correct fitting of the histograms, and this can be particularly troublesome for lower concentrations. The calibration curve in **Figure 4.17**b levels off at low concentrations and the dose response appears to be no longer in a linear regime, making the dwell time analysis method suffer from reductions of the dynamic range, limit of detection, and sensitivity compared to the threshold crossing method (**Figure 4.4** in Section 4.2). Gel band intensity analysis provides accurate and consistent results but requires a relatively large amount of sample for lower concentration limits compared to threshold crossing. Meanwhile, nanopore-based threshold crossing method can reliably detect and distinguish dumbbell from shooting star on a single-molecule basis at low concentrations, which practically allows for real time analysis as it only requires a few hundred single molecule events (5 minutes of nanopore sensing) to generate statistically meaningful results.

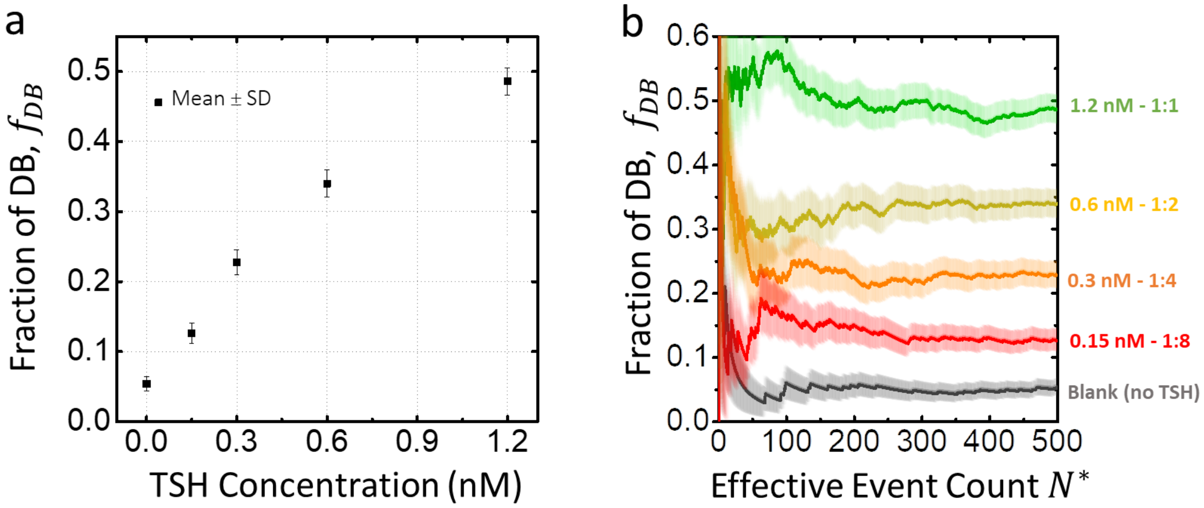

Figure 4.18. Additional TSH measurements in human serum sample. (a) TSH calibration curve concentration, 0 (blank), 0.15 nM, 0.3 nM, 0.6 nM, and 1.2 nM, with $N = 973, 936, 887, 821$, and 1337 single-molecule events. The error bars represent one standard deviation following Equation 4.3 of Section 4.1. **(b)** Fraction of dumbbell events as a function of the effective event count $N^* = N_{DB} + N_P/2$ detected for dumbbells and probes. Experiments are performed in 4x diluted human serum and sensed using a 12 nm pore in 3.2 M LiCl at 100 mV. Intra-crossings threshold is set 2.5x dsDNA, all experiments are low-pass Bessel filtered at 200 kHz for analysis.

Additionally, we repeated our nanopore assay and performed five additional measurements of rTSH in human serum sample from 0.15 nM to 1.2 nM using a 12 nm pore, as shown in **Figure 4.18**. We performed a homebrew ELISA assay employing the same workflow and reagents as our nanopore assay to validate our method. To do so, we replaced the biotinylated junction strand with a commercial biotinylated-HRP. Compared to the detection range (~0.1 – 70 pM) of the commercially available ELISA for TSH (ThermoFisher Scientific), our homebrew ELISA preformed as expected, allowing us to detect low (0.8 pM), medium (3.2 pM) and high (12.7 pM) concentrations that corresponded with our nanopore assay as shown in **Figure 4.19**. Note that the homebrew ELISA was carried out using the same nanopore assay workflow, which was not optimized for optical readouts.

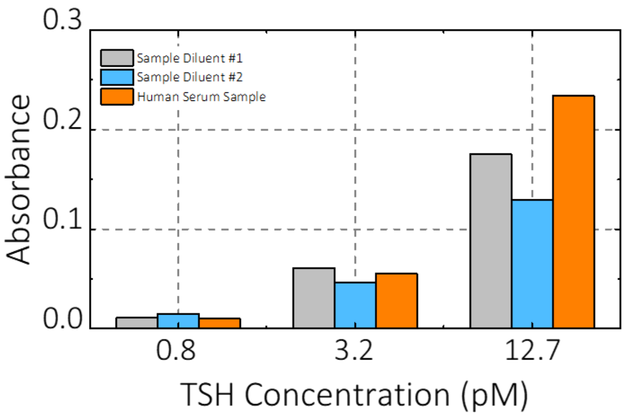

Figure 4.19. Validation of assay components by comparison of signal in sample diluent and low-mid-high values in human serum at nanopore assay concentrations.

Commercial biotinylated HRP was used to produce an optical readout, with same assay components and steps scaled down to volumes compatible with a 96 well plate and a 24-magnet base. The values presented have been corrected by subtracting the absorbance of the blank. Briefly, primary antibody coated magnetic beads were washed with sample diluent then combined with TSH in either sample diluent (SD) or 1 in 4 diluted human serum sample and allowed to incubate for 1.5 hours at room temperature (RT) with gentle agitation. The beads were washed three times for 5, 10, then 15 minutes, then were incubated with the secondary antibody in sample diluent for 1 hour at RT. Following 3 quick washes, the beads were incubated with biotinylated HRP (ThermoFisher Scientific, 432040) for 15 min at RT. Following a final 3 quick washes the presence of TSH was indicated by incubation with TMB ELISA Substrate (fast kinetics ab171524) for 17.5

min then stopped using 450 nm Stop Solution for TMB Substrate (Abcam, ab171529). The absorbance at 450 nm was read using a BioTek EPOC 2 spectrophotometer (Biotek, BTEPOCH2).

4.5.5 Additional Nanopore Characterization of Nanostructures

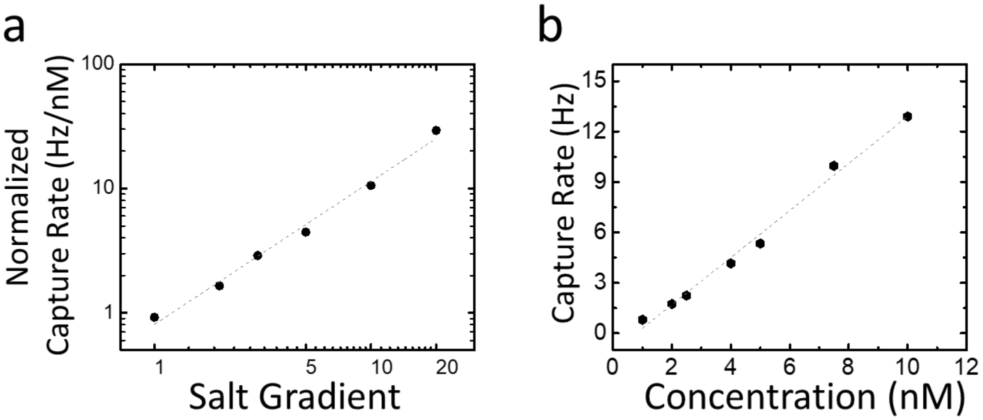

Figure 4.20. Nanopore capture rate analysis of shooting star probes. (a) Normalized capture rate of shooting stars as a function of salt gradient, with C_{cis} = 0.18, 0.36, 0.72, 1.2, 1.8, and 3.6 M LiCl and C_{trans} fixed at 3.6 M LiCl. **(b)** The capture rate of shooting star as a function of shooting star concentration. All experiments are performed using an 8.5 nm pore with an applied bias of 200 mV.

Following the previous work in salt asymmetry,[37,64] the capture rate of the shooting star can be improved while increasing the translocation time and maintaining a high SNR. The normalized capture rate is increased from 0.9 Hz/nM in symmetric salt ($C_{cis} = C_{trans}$ = 3.6 M LiCl) to 29 Hz/nM with the use of a 20x salt gradient (C_{cis} = 0.18 M LiCl and C_{trans} = 3.6 M LiCl) using an 8.5 nm pore as shown in **Figure 4.20**a. Moreover, **Figure 4.20**b shows the capture rate of shooting star as a function of its concentration, the capture rate of shooting star exhibits a linear response to the concentration of the molecule.

4.6 Acknowledgements

The authors would like to thank John Pezacki, Mark Hayden, Craig Jeffrey and Jeffrey Huff for fruitful discussions. The authors would like to acknowledge the support of the Natural Sciences and Engineering Research Council of Canada (NSERC), through funding from grant #CRDPJ 530554-18, and the National Institutes of Health, through funding from grant R01 EB031581.

Chapter 5 – Summary and Outlook

Summary

Since nanopore sensors were conceptualized three decades ago,[4] their development and applications have been explored and improved tremendously.[181,225–227] Nanopores have gained attention as single-molecule counters to electrically detect a range of biological molecules in a handheld format, but challenges remain before nanopore diagnostics can be truly useful. The aim of this thesis was to develop reliable labels for nanopore detection and to implement them in an assay setting on a solid-state nanopore platform. Towards this objective, I attempted to address some of the challenges in the field, namely, sensitivity and specificity. I developed a nanopore-based digital assay that utilizes the programmability of DNA nanostructures. I studied several nanostructures and assessed their potential as DNA proxy labels, finalized on one candidate molecule that has reliable capture by a nanopore while providing a fantastic SNR, and allows multiplexed detection. This allowed me to implement a bead-based assay using nanopore readout to quantify a target protein down to high femtomolar sensitivity. The work presented in this thesis falls into two main categories: characterization of DNA nanostructures using solid-state nanopores; and the development of a digital nanopore assay.

Chapter 1 – As a walkthrough of the concepts employed during my PhD study, Chapter 1 of this thesis cover a brief introduction of the main areas in my research, namely the fabrication and instrumentation of nanopores, DNA origami detection using nanopores, and bead-based digital assay using nanopores. I therefore go through each of the key elements of my PhD research. A nanopore is a nanometre-sized aperture in a thin membrane. Molecules of interest are captured and driven by an applied voltage across the pore, which reveals information about the molecule’s size, shape, charge, and conformation. The nanopores used in this thesis were solid-state nanopores fabricated using a technique called controlled dielectric breakdown (CBD), developed by the Tabard-Cossa Lab at the University of Ottawa. In passing, I would like to mention that I made at least 260 pores during the course of my PhD. In section 1.1, I discussed nanopore instrumentation and nanopore signal classification, as well as other nanopore concepts such as capture rate.

Another common denominator of this thesis, and a primary tool of interest throughout my study, is DNA nanotechnology. DNA origami structures were studied on their own and used as building blocks in an assay. Gel electrophoresis and microscopy techniques being the go-to when it comes to characterizing nanostructures. More recently, however, research groups have begun studying nanostructures using nanopores, as they offer interesting insights about the molecules of interest on a single-molecule level, and it preserves their natural state in buffer solution without the need to immobilize the molecules on a surface. In chapter 1.2, I presented some examples of what researchers have been able to do when combining nanopores and DNA nanotechnology, whether as a tool to study capture and translocation or as a reporting molecule in an assay.

To be practically useful in an assay setting, nanopore sensing schemes must overcome a number of hurdles, as discussed in chapter 1.3. For instance, as the transport properties of most protein molecules through solid-state nanopores are fast and unreliable, solid-state nanopores suffer from their lack of specificity for protein recognition. Solid-state nanopores in their natural state are ill suited to sensing proteins directly without surface functionalization. They are also vulnerable to clogging and are likely to produce unacceptably high false positives due to the inability to distinguish targets of interest from background molecules present in biofluids. In addition, many clinically relevant proteins are not always compatible with nanopore operating conditions, e.g., the high salt concentration needed to maintain SNR. In chapter 1.3, I discussed some of the successful attempts at nanopore protein detection by other groups, the most commonly used approach being the nanocarrier, where the target protein is bound to the DNA nanocarrier via an aptamer specific to that particular protein. Later in the chapter, I presented our approach to solve these challenges by adapting a bead-based assay to the nanopore system.

Chapter 2 – Early detection of disease biomarkers at the point of need could revolutionize medical diagnostics. When it comes to solid-state nanopore sensors, the specificity of the ionic current trace and the detection rate of the target molecule in a complex sample remain issues to be resolved if nanopores are to enable this vision. In Chapter 2, I showed the capture and translocation characteristics of star-shaped DNA nanostructures to evaluate their potential as surrogate labels for biomarkers of interest. The nanostructures are designed to be easily synthesized, fast capture, and reliably multiplexed based on conductance blockages. When more arms are introduced to the nanostructures, we can increase the nanopore signal-to-noise ratio (SNR) in a controllable manner for a range of pore sizes. The N-arm stars produce conductance blockages that increase linearly with the number of arms, and I demonstrated conductance-based multiplexed detection of three such nanostructures. The translocation characteristics of 4-, 6-, 8-, and 12-arm star-shaped DNA were repeated for 30 different nanopores ranging in size from 4 nm to 13 nm, producing unique electrical signatures. The observed maximum blockage of the star-shaped molecules follows a predictable trend according to the passage geometry during translocation. These DNA nanostructures demonstrate great potential to be used in a blockade-based 3-plex detection scheme.

Finally, the much-improved SNR facilitates detection in highly asymmetric salts. I demonstrated a capture rate enhancement of two orders of magnitude while maintaining the nanopore's temporal and ionic signals using the 12-arm star. These properties make the star-shaped molecules very promising candidates as proxy labels to be implemented in ultra-sensitive single-molecule solid-state nanopore-based assays. In fact, in Chapter 4 I used these labels in a digital assay scheme, etc.

Chapter 3 – Nanopores combined with DNA nanotechnology provides an interesting approach and provides more insights on the dynamics of passage of DNA nanostructures. In Chapter 3, I showed results on the translocation characteristics and folding statistics of the 3 helix-bundle (3HB) and linear double-stranded M13 origami structures (ldsM13). The rigid nature of helix-bundle structures results in long passage times and metastable states during translocation, I built translocation profiles of the nanostructures and discussed their folding characteristics, mobility, and molecular configuration during passage under different experimental conditions. The results shown in Chapter 3 suggest that the 3HB nanostructure behaves just like linear dsDNA fragments when translocating single file through a nanopore; local defects exist, and when the 3HB nanostructure is not captured by an end, local defects along its contour length dominate the translocation dynamics. The consistency between nanopore and gel electrophoresis was observed for both origami structures, I discussed potentially using nanopores to assess the assembly, purity and stability of DNA nanostructures, and how it can be assessed as an alternative to gel electrophoresis. Furthermore, when introduced to a heat shock of 65 degrees for various amounts of time, surpingly the nanostructures immediately begin to degrade. A total degradation of the origami structure after just two minutes, results in higher order blockages on a nanopore which correspond well with the faster migrating bands on gel electrophoresis. This thermal response of 3HB suggests the presence of mis-assembled products.

Chapter 4 – In recent years, motivated by the need for novel digital diagnostic technologies, the biosensing field has seen important advances on nanopore detection of proteins in clinically relevant samples.[69,99,155] In Chapter 4, building on work presented in Chapter 2 and publications from 2019 to 2021,[64,155,162] that characterized the capture and translocation of specific DNA nanostructures, and advances made in controlled counting to precisely measure the concentration of a target,[44] and the fabrication tools solid-state nanopores by controlled breakdown (CBD).[12,13,26] I developed a versatile nanopore-based digital immunoassay scheme capable of reliably measuring the concentration of a specific target protein in serum. I employed a magnetic bead-based sandwich immunoassay upstream of nanopore-based electrical sensing. This scheme converts the target protein into proxy labels configured as 12-arm star DNA nanostructures to quantify its presence ("1") or absence ("0"), providing a strong SNR and high accuracy to quantify the biomarker concentration. These proxy labels allow for an automatable signal analysis method to digitally classify electrical signatures from the different translocating DNA nanostructures, eliminating manual classification and user biases. These attributes help overcome the main challenges associated with the use of solid-state nanopores for reliable, ultra-sensitive protein concentration quantification in complex biological samples: (1) the specificity, the ability to tell apart the target signal from background molecules present in biofluids; (2) the consistency of nanopore electrical detection between pores of varying geometry. To demonstrate the ability of the nanopore digital scheme to quantify in the picomolar to nanomolar range, with high precision, biomarkers from serum samples, I used thyroid-stimulating hormone (TSH). TSH was chosen since it is frequently used as a proof-of-concept target during assay development.

Using the nanopore-based amplification assay, a 10 – 100x improvement in sensitivity was achieved compared to the previous nanopore studies[69,85,98,99] sensing proteins from serum. Compared to DNA nanocarrier approaches discussed in section 1.3, the magnetic bead-based digital immunoassay scheme allows for the use of high affinity antibodies to capture protein targets. Furthermore, the assay conditions can be optimized solely for specific protein capture without having to worry about nanopore performance, whereas DNA nanocarrier schemes require mixing serum with sensing solution, which is neither optimized for highest affinity binding to targets nor for best nanopore sensing conditions. Finally, due to the magnetic nature of beads, which facilitate washes, background molecules are eliminated prior to sensing, leaving molecules of interest to translocate through the pore. This significantly increases selectivity and is ideal for quantifying biomarkers from complex biological samples.

Outlook

Chapter 2 – An ideal label for nanopore sensing in a digital assay should demonstrate reproducible, and consistent performance. Despite the success of the fabrication of the nanopore by controlled dielectric breakdown (CBD) discussed in Chapter 1 and the improvement in signal-to-noise ratio (SNR) and capture rate made using star-shaped DNA nanostructures discussed in Chapter 2, reliable translocation of the stars remained a challenge. This was largely due to frequent clogging of the nanopore. To put it in perspective, the 12-arm star has a diameter of 17 nm while a typical nanopore used in the study was between 9-12 nm in diameter. Nanopores of this size were used because of the limitations high-bandwidth current amplifier employed in my thesis, even if these were the state-of-the-art. Indeed, larger pores would not only lead to translocations too close to the bandwidth (1 MHz) of the current amplifier but generate current levels too high (>20 nA) and thus saturating it. Consequently, the nanostructure must deform and reorient itself to translocate, and this "squeezing" tend to result in permanent clogs of the nanopore. One could argue that this clogging issue could be solved by simply using nanostructures with shorter arms but similarly to the issue with using larger pores, some degree of interaction between the nanopore and the nanostructure is needed to maintain the temporal resolution and consistent blockage levels. In Chapter 2, I showed that short, multi-arm dsDNA stars produce robust and easily identifiable signals. For the work showed in Chapter 4, I further modified the star-shaped nanostructures, extending one of the arms to form a linkage for the tail section of the probe, and added an internal carbon spacer in the middle of each star oligo's sequence as illustrated in **Figure 5.1**.

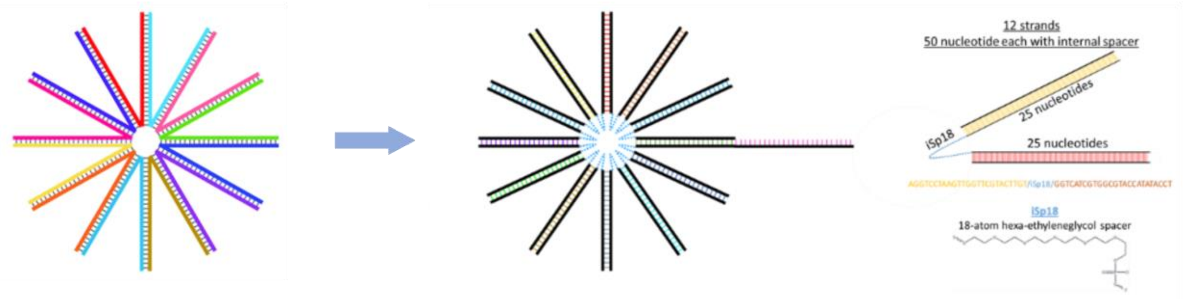

Figure 5.1. The 12-arm star *versus* the relaxed core 12-arm star. The 12-arm star *versus* the relaxed core 12-arm star.

The internal hexa-ethyleneglycol spacer has been shown to add flexibility within an oligo.[228,229] The 18-atom spacer used is the longest spacer arm available that can be added to an oligo by IDT (a company providing nucleic acid synthesis services). The internal spacers are believed to have helped relax the otherwise highly charged and sterically stressed core of the 12-arm star structure, thus facilitating translocation through nanopores. As a result, with the use of the relaxed core star-shaped structures, all the nanopores used for the work presented in Chapter 4 lasted through whole sets of experiments, this also eliminated pore-to-pore variance for each of the experiments. Notably, none of the nanopores gave up mid-experiment and I was able to collect hundreds of thousands of single-molecule translocation events with each pore.

Another challenge with the use of DNA nanostructures on nanopores is the assembly yield, it is safe to say none of the DNA self-assembly gives 100% yield. Generally speaking, it follows the trend that the simpler the structure the higher the assembly yield becomes. At the same time, when designing labels, not only do researchers need to keep the main objectives such as high SNR in mind, but the assembly yield also plays a role in label design. Impurities of the DNA nanostructures can cause issues in the downstream applications, such as clogging of the nanopores and reporting molecule binding to the impurities. In some case like the 12-arm star with the extension tail, the assembly yield was barely 50% as shown in **Figure 5.2**a. In my mind, there are two approaches, first one being to use the nanostructures as-is (meaning without any additional purification steps) and try to distinguish the mis-assemblies from the correctly assembled products during nanopore sensing. The major advantage of this approach is its simplicity, no post processing is needed after the assembly and the nanostructures are ready for use. However, the most obvious drawback is that the translocation signatures from correct and mis-assembled products can heavily overlap. As shown in **Figure 5.2**a, it is not so easy to tell apart with high confidence. Another disadvantage with this approach is that if the nanostructures are going to be used as probes in an assay like the scheme presented in Chapter 4, the mis-assemblies may contain binding sites which will compete with the correctly assembled products and potentially introduce false positives. The effect of having impurities has been simulated by Dr. Kyle Briggs in his recent publication,[230] which shows it is impossible to reach 100% hybridization with even a small fraction of mis-assembled products in the mixture. Therefore, we decided to tackle this issue by purifying the nanostructures.

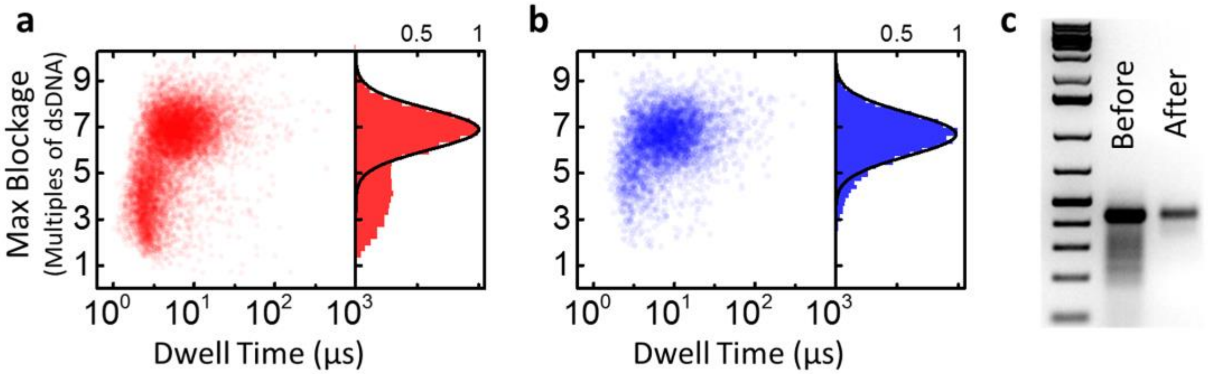

Figure 5.2. Purification results of 12-arm. (a) Scatter plot of unpurified 12-arm star showing 29% shallow events. **(b)** Scatter plot of purified 12-arm star with 7% shallow events. Both experiments are performed in LiCl pH 8.0, using the same pore of 11.5 nm in diameter with an applied bias of 200 mV. **(c)** Gel electrophoresis results in 2% agarose gel in 1xTAE, from left to right: GeneRuler 1 kb Plus DNA Ladder (Thermo Scientific, SM1331), 12-arm star following assembly, and 12-arm star after purification. On the ladder lane of the gel image shows from bottom to top: 200, 300, 400, 500, 700, 1000, 1,500 bp, etc.

When it comes to purifying DNA nanostructures, the most common technique is perhaps gel electrophoresis to separate structures by length followed by its extraction from the gel.[52,56,61] Agarose gel extraction is the gold standard in the field of DNA nanotechnology, the purification consists of three main steps: (1) performing gel electrophoresis with the appropriate amount of products loaded, ideally as much as possible without saturating the bands; (2) visualizing, identifying and excising of the desired bands; (3) eluting the DNA from the gel into a solution, typically done by dissolving the DNA-containing gel using a specific buffer. Agarose gel extraction is a well-established technique, and there are several kits commercially available, such as QIAquick Gel Extraction Kit (Qiagen, 28706X4), Freeze ‘N Squeeze DNA Gel Extraction Spin Columns (Bio-Rad, 7326165), and BluePippin (Sage Science, BLU0001). At the time, I thought these would only take a few days or weeks to purify my DNA nanostructures for nanopore sensing, but little did I know that the compatibility of the resulting extract with the nanopore was going to be a huge challenge. Indeed, the Agarose gel extraction worked great but failed at the nanopore sensing stage, as the pore immediately clogged. The exact reasons why it caused the nanopores to clog remain unclear, but it was concluded from the later tests that anything that had been in the same buffer with Agarose gel would result in a clog. My hypothesis is that uncross-linked agarose polymers would get extracted at the same time as the DNA nanostructures and would then be pulled in the pore by electrophoretic forces. Luckily, I was able to develop an in-house gel extraction system with my colleagues from the lab, which is based on polyacrylamide gel electrophoresis (PAGE). The details of the extraction protocols are given in Appendix A. As shown in **Figure 5.3**, the purification removes the impurities, which helps maximize binding and minimize false positive events when used in the work presented in Chapter 4.

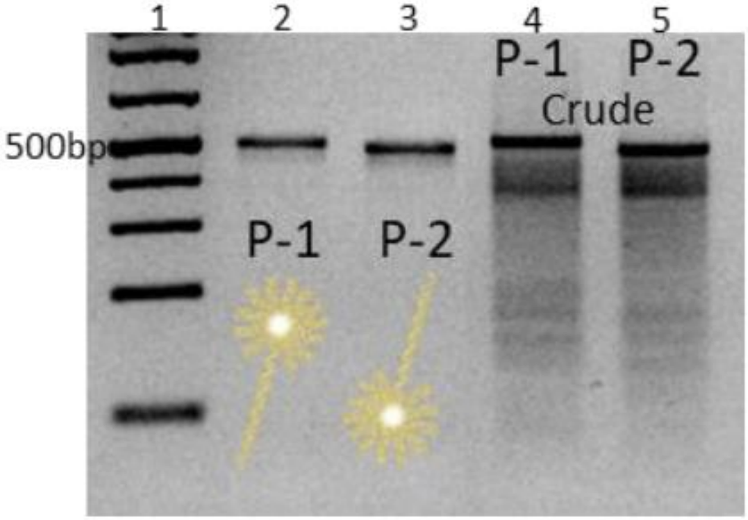

Figure 5.3. Agarose gel (2%) of shooting star probes P-1 and P-2 assemblies and purification. Lane 1: GeneRuler 1kb Plus DNA Ladder (ThermoFisher Scientific, SM1331), from bottom 75, 200, 300, 400, 500, 700, 1000, 1500, 2000, 3000, 4000, 5000, 7000, 10000, and 20000 bp, lane 2: gel extracted P-1, lane 3: gel extracted P-2, lane 4: crude P-1 and lane 5: crude P-2.

Despite the improvements in yield using the PAGE-based purification, the entire process remain incredibly time consuming – to gather enough purified products for a full set of experiments using this technique typically requires pooling the products of 50+ lanes with each lane loaded to its full capacity due to the massive losses during the process, that is 6 consecutive PAGE gel extractions for one experiment. Thus, there is a need to a more efficient system. This can be achieved by mass parallelization of PAGE and automation of the process, a fully automated PAGE-based system capable of running the purification with very little supervision much similar the (expensive) Bluepippin could address the ease-to-use issue.

Chapter 4 – To be truly clinically relevant, several issues still need to be resolved, particularly where assay time, dynamic range, and multiplexing are concerned. The assay scheme in its current form is complex and time consuming. One drawback that comes with the bead-based assay - the number of steps, can be addressed by automating the incubations and washes (as is done in the commercial Quanterix HD-1 Analyzer using robotic liquid handlers – alternatively more compact digital droplet systems could be used). However, in the scheme showcased in Chapter 4, the rate limiting step is the incubation step of the junction strand with the DNA nanostructures to produce the digital signal. Indeed, DNA hybridization takes times (up to 48 hours to reach equilibrium at 1:1 ratio of junction strands to probe). This is a two-step hybridization, namely, the junction (linker strand) must find and bind to both P-1 and P-2 probes, which exponentially increases hybridization time. For this reason, in Chapter 4, I limited the dynamic range of my assay to 0.5 ratio to limit the assay time. However, to resolve the turnaround time issue better, one could employ quencher strand (complimentary the binding sites on the probes) at an excess, for instance, the quencher strand is added at the fixed assay time of two hours. Upon the addition of such molecule, one could effectively quench all unbound probes by capping their binding sites with excess quencher strands. Alternatively, a new probe design which can undergo shape transformation in one-step with the presence of the junction strand could dramatically reduce assay time.

Using antibody-coated beads multiplies the on rate of the capture antibody and reduces the K_D proportionately, so the assay does not suffer from the limitation by the dissociation constant of a single antibody or aptamer, which otherwise limits the sensitivity to a small range around the K_D value. The sensitivity of the approach discussed in Chapter 4 is, however, limited only by nanopore measurement time. As discussed, the error bar of dumbbell (DB) fraction decreases with more translocation events, thus, to measure at much lower concentrations one would need to collect significantly more single-molecule events on a nanopore. This can be achieved by one of following approaches: (1) record for 5 hours per experiment, which is not practically in a clinical setting; (2) a capture rate increase scheme using salt asymmetry, which has been shown to increase capture rate by one order of magnitude without sacrificing temporal resolution;[37,64,139] (3) pre-concentration of the molecules at nanopore mouth as demonstrated by Edel and coworkers.[216] (4) parallelization of nanopores, solid-state nanopores are fabricated on a substrate that can be significantly upscaled on a wafer-scale and individually addressable pores. By parallelizing the pore detection, we could reach fM sensitivity for proteins and aM for nucleic acid targets. In contrast, schemes that employ a single receptor to bind a target are limited to a small target concentration range around the K_D for the receptor, making them incompatible with low-abundance biomarker detection.

Appendix A

Digital Immunoassay Protocol for Solid-State Nanopore Sensing

Liqun He, Daniel R. Tessier, Kyle Briggs, Matthaios Tsangaris, Martin Charron, Erin M. McConnell, Dmytro Lomovtsev, and Vincent Tabard-Cossa*

Department of Physics, University of Ottawa, Ottawa, Canada

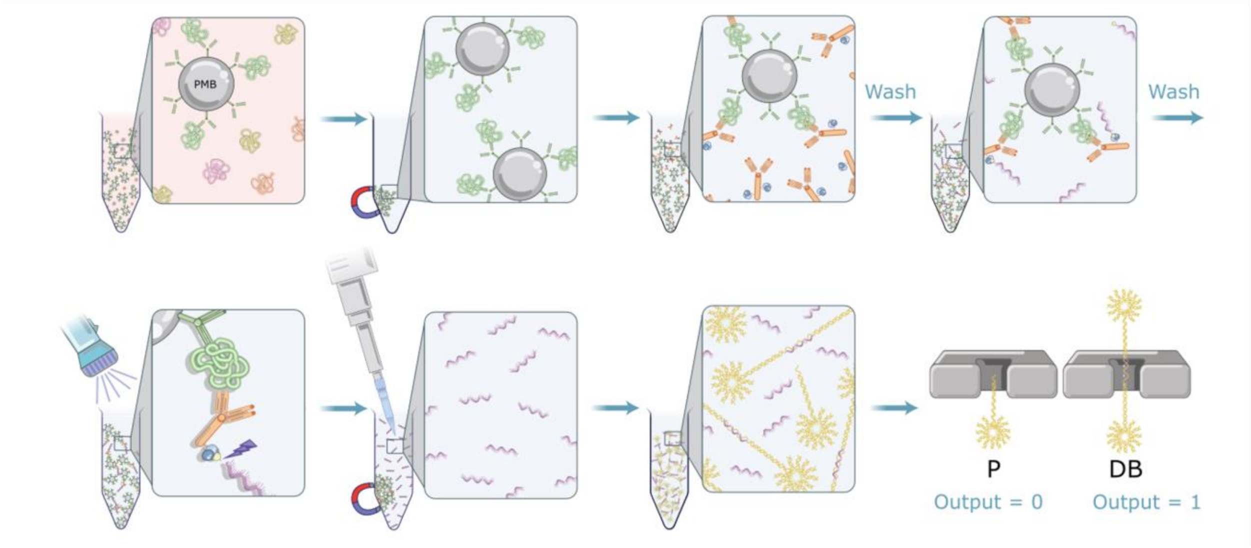

Adapted with permission from [L. He, D. R. Tessier, K. Briggs, M. Tsangaris, M. Charron, E. M. McConnell, D. Lomovtsev, and V. Tabard-Cossa, “Digital Immunoassay Protocol for Solid-State Nanopore Sensing,” *Protoc. Exch.*, 2022]

Abstract

The ability to digitally count single molecules enables accurate and precise determination of the concentration of a disease biomarker. Owing to their intrinsic single-molecule sensitivity and fully electronic detection capability, solid-state nanopores show great promise for this task toward point-of-care diagnostic applications. Here, we describe the protocols for implementing a magnetic bead-based immunoassay strategy coupled with digital detection and downstream solid-state nanopore electrical readout. The digital scheme employs DNA nanostructures, as proxy labels for the presence ("1") or absence ("0") of the target protein. We provide step-by-step protocols for assembling and purifying DNA nanostructures; Preparing magnetic beads decorated with capture antibodies; Conjugating secondary detection antibodies to bind the DNA label; Functionalizing gold nanoparticles; and running the full assay where thyroid stimulating hormone (TSH) from human serum samples is quantified down to the femtomolar range. The protocols and assay scheme presented herein are easily generalized to the quantification of a wide range of target proteins, by selecting the appropriate antibody pair.

Reagents

- SiN_x membranes (Norcada, NBPX5004Z)
- SYLGARD 184 Silicone Elastomer Kit (Dow Chemical Company, 4019862)
- Potassium chloride (Fisher Scientific, P217-500)
- Lithium Chloride (Fisher Scientific, L121-500)
- Lithium Hydroxide Anhydrous (Fisher Scientific, L128-500)
- HEPES (Fisher Scientific, BP310100)

- Agarose (Fisher Scientific, BP160500)
- Mini-PROTEAN TBE precast gels (Bio-rad, 4565013)
- Mini-PROTEAN TGX gels (Bio-rad, 456-1093)
- NoLimits 2kbp dsDNA fragments (ThermoFisher Scientific, SM1701)
- GeneRuler 1kbp plus DNA ladder (ThermoFisher Scientific, SM1331)
- DNA Gel Loading Dye 6X (ThermoFisher Scientific, R0611)
- Carboxylated paramagnetic beads 2.7 µm (Quanterix, 103612)
- EDC (ThermoFisher Scientific, A35391)
- Sample/detector diluent (Quanterix, 101359)
- Wash buffer 1 (Quanterix, 100486)
- Mouse monoclonal anti human TSH beta subunit capture antibody (Fitzgerald Industries International, 10C-CR2151M4)
- Anti-human TSH beta subunit detection antibody (Maine Biotechnology Services, MAB130P)
- Streptavidin Conjugation Kit (Abcam, ab102921)
- Recombinant TSH (rTSH) (BiosPacific, J11030)
- Serum samples (BioIVT, BRH1391829 – BRH1391838)
- DTT (Dithiothreitol) (ThermoFisher Scientific, A39255)
- Ultramer/HPLC purified DNA oligos with modifications (Integrated DNA technologies)
- Standard 30 nm gold nanoparticles (Cytodiagnostics, G-30-20)
- Tween-20 (Sigma-Aldrich, P1379-100ML)
- Bovine serum albumin (Proliant Biologicals, 68100-100G)

- Bead Wash Buffer (Quanterix, 101355)
- Bead Blocking Buffer (Quanterix, 101356)
- Bead Diluent (Quanterix, 100458)
- Bead Conjugation Buffer (Quanterix, 101357)
- 6x Loading Buffer (ThermoFisher Scientific, R0611)
- 5x TAEMg pH 8 (200 mM Tris, 100 mM Acetic acid, 10 mM EDTA, and 62.5 mM $MgCl_2$)
- 10x TBE buffer (ThermoFisher Scientific, V36401)
- 10x Tris/Glycine Buffer (Bio-Rad, 1610734)

Equipment

- 3W LED flashlight (LIGHTFE, UV301D)
- 3 kDa Amicon Ultra-0.5 Centrifugal Filter Unit (Millipore Sigma, UFC500396)
- 100 kDa Amicon Ultra-0.5 Centrifugal Filter Unit (Millipore Sigma, UFC510096)
- D-Tube Dialyzer Maxi, MWCO 6-8 kDa (Millipore, 71509-3)
- Illustra NAP-5 columns (GE Healthcare, 17185601)
- Multi-Functional Tube Rotator (VWR, PTR-35).
- Gel imaging workstation (Azure biosystems, C150).
- MiniAmp Plus Thermal Cycler (Applied Biosystems, A37834).
- VWR Mini Centrifuge (VWR, 76269-064)

Figures

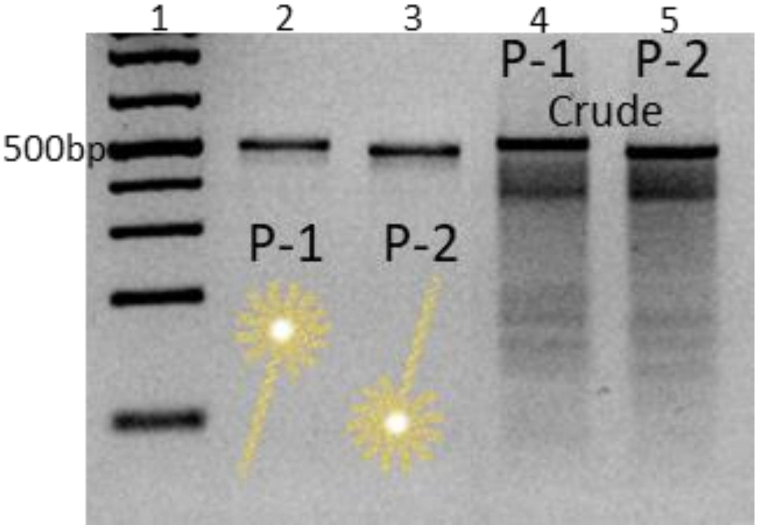

Figure A.1. Agarose gel electrophoresis probes assemblies and purification.

Agarose gel electrophoresis (2%) of shooting star probes assemblies and purification. Lane 1: GeneRuler 1kb Plus DNA Ladder (ThermoFisher Scientific, SM1331), from bottom 75, 200, 300, 400, 500, 700, 1000, 1500, 2000, 3000, 4000, 5000, 7000, 10000, and 20000 bp, lane 2: gel extracted P-1, lane 3: gel extracted P-2, lane 4: crude P-1 and lane 5: crude P-2.

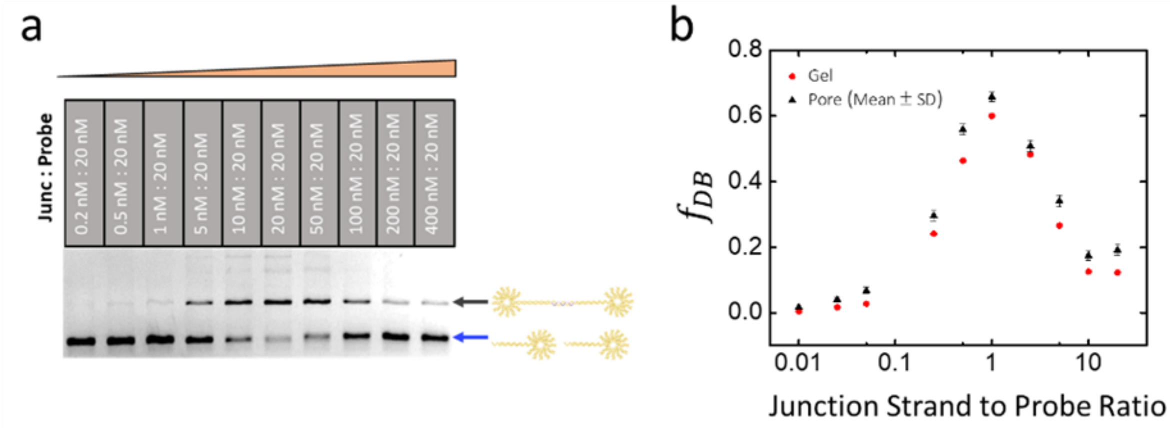

Figure A.2. Dose response and time dependence of dumbbell assembly.

(a) Gel electrophoresis (2% agarose) of dumbbells formation and remaining shooting star probes as junction concentration increases. **(b)** Comparison of dose response with junction concentration ranging from 0.2 nM to 400 nM (junction to shooting star probes ratio of 0.01:1 to 20:1) between nanopore sensing and gel band densitometry

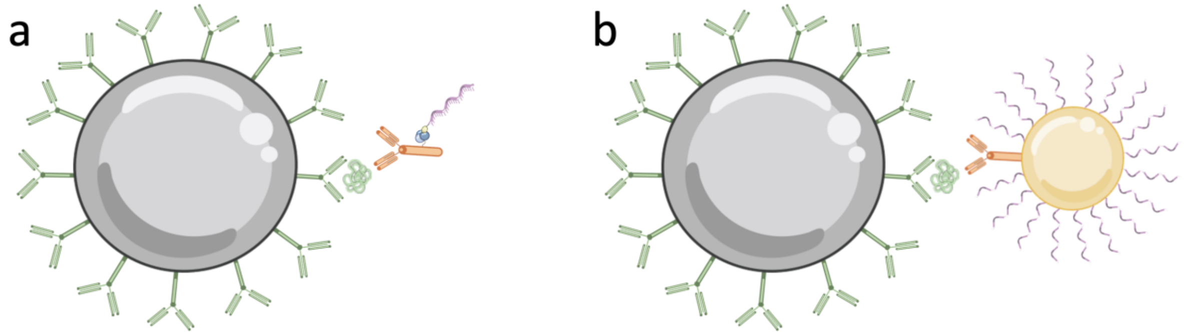

Figure A.3. Schematic illustration of 1 to 1 assay and amplification assay.

(a) 2.7 μm PMB coated with detection Ab, target protein, and detection Ab conjugated with 50 nt photocleavable junction strand. **(b)** 2.7 μm PMB coated with detection Ab, target protein, and detection complex consists of 30 nm gold nanoparticles decorated with 50 nt junction strands and detection Ab.

Table 1. Shooting Star and Dumbbell assembly oligo sequences

12-Arm relaxed core shooting stars probes (P-1 and P-2)			Bases (#)	GC Content (%)
Star oligos				
1	5'	AGGCACAGCTATAATAACGCAATCC/iSp18/TCTCCGGCCTCAAACTACTTTACCT	50	46
2	5'	AGGTAAAGTAGTTTGAGGCCGGAGA/iSp18/CCGAATGGAGTCTGTTCTCGACGCT	50	52
3+	5'	CAATTCTACTAATAGGAATTCGATTAGCGTCGAGAACAGACTCCATTCGG/iSp18/ACAAGTACGAACCAACTTAGGACCT	75	43
4	5'	AGGTCCTAAGTTGGTTCGTACTTGT/iSp18/GGTCATCGTGGCGTACCATATACCT	50	48
5	5'	AGGTATATGGTACGCCACGATGACC/iSp18/TCTTCGATCTACCCGATAGGCTCCT	50	52
6	5'	AGGAGCCTATCGGGTAGATCGAAGA/iSp18/CGTACAGGTGTGACTTGAATTTGCT	50	48
7	5'	AGCAAATTCAAGTCACACCTGTACG/iSp18/AGTGTTAGAATACAACAAGCGACCT	50	42
8	5'	AGGTCGCTTGTTGTATTCTAACACT/iSp18/GCATCTCATACGACAGCATCCGACT	50	46
9	5'	AGTCGGATGCTGTCGTATGAGATGC/iSp18/TGAGCACGGAACTGTCAACCTTGCT	50	52
10	5'	AGCAAGGTTGACAGTTCCGTGCTCA/iSp18/CGTTCATTAAGATAAATCTGATCCT	50	42
11	5'	AGGATCAGATTTATCTTAATGAACG/iSp18/ACTATGACTGCTACATGCACTTCCT	50	38
12	5'	AGGAAGTGCATGTAGCAGTCATAGT/iSp18/GGATTGCGTTATTATAGCTGTGCCT	50	44
Extension oligos common to P-1 and P-2				
A	5'	AATCGAATTCCTATTAGTAGAATTGATGCCACCTCATCAGCTCGCGTCCG	50	46
B	5'	AACCTGTGTACGACTTAGATCTGTACGGACGCGAGCTGATGAGGTGGCAT	50	52
C	5'	TACAGATCTAAGTCGTACACAGGTTGCCTGAGTTGTGCGACGACGTCAGA	50	50
D	5'	CCGTAGCTGGACGTAGCGTGACCATTCTGACGTCGTCGCACAACTCAGGC	50	60
E	5'	ATGGTCACGCTACGTCCAGCTACGGGCAGAATTGGGAATCAACTGTTACA	50	50
P-1 specific extension oligo				
F	5'	GACGGTGTCTGGAAGTCTCACAGCATGTAACAGTTGATTCCCAATTCTGC	50	48
G	5'	TGCTGTGAGACTTCCAGACACCGTCCTTTAGTTGCATATAAGCTTCATGT	50	44
P-2 specific extension oligo				
F'	5'	CTACGTTCCTGGGTGACGAGCGTACTGTAACAGTTGATTCCCAATTCTGC	50	48
Dumbbell Junction oligo				

Junction	5'	/5PCBio/GTACGCTCGTCACCCAGGAACGTAGACATGAAGCTTATATGCAACTAAAG	50	46

Table 1: Shooting Star and Dumbbell assembly oligo sequences. The star structure is composed of eleven 50 nucleotide oligos each containing a hexa-ethyleneglycol spacer (EG6) in the middle of the sequence after the first 25 nt. Oligo 3+ has an additional 25 nt ssDNA. The tail strands attach to the 25 nt ssDNA overhang present on strand (3+) upon which hybridize 7 staggering 50nt sequence staple strands (A-G) for the P-1 or 6 staggering 50nt sequence staple strands (A-F') for the P-2. Junction oligo halves are complementary to the respective 25 nt overhang present on the shooting star probe pair.

Assay Procedure

DNA Nanostructure Assembly

1. Add 12 μL of each oligo (stock: 100 μM) for P1 (Star oligo 1 – 12, Extension oligo A – E, F, and G) and P2 (Star oligo 1 – 12, Extension oligo A – E, and F') in separate tubes, 72 μL of 5x TAEMg buffer and deionized water to reach a total reaction volume of 360 μL with a final concentration of 3.3 μM for each oligo in 1x TAEMg (40 mM Tris, 20 mM acetic acid, 2 mM EDTA, and 12.5 mM magnesium acetate, pH 8).
2. Vortex the samples, divide and transfer each sample into 4 PCR tubes, and place the samples in a thermal cycler such as the MiniAmp Plus Thermal Cycler (Applied Biosystems, A37834).
3. Incubate samples at 95 ^{o}C for 5 minutes then cool to 90 ^{o}C. Ramp down from 90 ^{o}C to 60 ^{o}C at 0.4 ^{o}C/min, 60 ^{o}C to 26 ^{o}C at 0.03 ^{o}C /min, then snap cooled to 4 ^{o}C indefinitely.

4. Prepare 50 mL 0.5x TBE in an Erlenmeyer flask, weigh out and add 1 g of agarose to the 0.5x TBE buffer to make 2 % gel, and microwave for 15-30 seconds at a time for approximately 2 minutes and 30 seconds until the agarose is completely dissolved. Let the agarose cool, add 5 μL of 10,000x GelRed to agarose solution, and gently mix to avoid creating bubbles. Pour the agarose solution into the gel tray, insert comb, and let agarose solidify for 20 minutes. Note: the volume of agarose and gel stain needed depends on the size of the gel plate used. For this protocol a gel tray with the following dimensions (10 cm x 7 cm) was used.
5. Pool the DNA nanostructure probes from the four PCR tubes after the assembly, mix 0.5 μL of each DNA nanostructure probe with 9.5 μL of deionized water and 2 μL of 6x Loading buffer (ThermoFisher Scientific, R0611) for gel characterization. Load the samples on 2 % agarose gel, run the gel at 70 V for approximately 1 hour, and visualize on Gel imaging workstation (Azure biosystems, C150). The remaining probe can be stored at 4 ^{o}C.

DNA Nanostructure Purification

1. Take 90 μL of assembled probe (P1/P2), add 14 μL of 5x TAEMg, 15 μL of 10x GelRed, 25 μL of 6x Loading Buffer (ThermoFisher Scientific, R0611), and 26 μL of deionized water. Vortex the samples and load into wells of 5% Mini-PROTEAN TBE polyacrylamide pre-cast gels (BioRad, 4565013). Run the gel in 0.5x TBE buffer at 100 V on ice for 3 hours.
2. Take the gels out of cassettes and visualize using gel imager (Azure biosystems, C150) UV plate.

3. Identify the band of interest and excise with a razor blade.
4. Place the excised gel slices (containing products of interest) in custom extraction apparatus or D-Tube Dialyzer Maxi (MWCO 6-8 kDa, Millipore, 71509-3) tubes, and apply 100 V in 1x TBE buffer to electrophoretically extract the DNA samples out of the gel slices.
5. Take the supernatant (0.5 mL to 3 mL) from the extraction tubes, and perform buffer exchange into 1x TAEMg using 100 kDa Amicon Ultra-0.5 Centrifugal Filter Units (Millipore Sigma, UFC510096). This should concentrate the sample into ~ (35 μL).

Quantification of Nanoprobes

6. Quantify the purified probes by taking 2 μL of the sample and performing nucleic acid concentration measurements using a UV-Visible spectrophotometer for small sample volumes such as the Take3 micro-volume plate accessory of the EPOC 2 spectrophotometer (BioTek, BTEPOCH2).
7. Take equimolar concentrations of purified DNA nanostructure probes, where the probe concentrations are fixed at either 15 nM or 20 nM, and add various amounts of junction strands, ranging from 0.2 nM (0.01:1 junction:probe) to 400 nM (20:1 junction:probe) for dumbbell assembly.
8. Incubate for up to two days (48 h) at room temperature.
9. Confirm the quality of dumbbell formation on 2% agarose gel as shown in Figure 1.

Nanopore Characterization Measurements

10. Take 4 μL of the assembled dumbbell samples, add 35.5 μL of 3.6 M LiCl and 0.5 μL 2kbp dsDNA fragments (ThermoFisher Scientific, SM1701).
11. Vortex the sample and load it into the nanopore flow cell (*cis* side)[12,64].

12. Apply -100 mV and sense on a nanopore for 10 - 30 minutes, anticipated results are shown in Figure 2.

Paramagnetic Bead Ab Conjugation

1. Add 234 μg of primary antibody (Fitzgerald Industries International, 10C-CR2151M4) to 100 kDa Amicon Ultra-0.5 Centrifugal Filter Unit (Millipore Sigma, UFC510096).
2. Add Bead Conjugation Buffer (Quanterix, 101357) to the filter unit to reach a final volume of 500 μL.
3. Centrifuge at 14,000 g for 5 minutes, discard flow-through, and wash the samples by adding 450 μL Bead Conjugation Buffer.
4. Repeat the 450 μL washes three times.
5. Invert the filter unit membrane and centrifuge into a new tube at 1,000 g for 2 minutes.
6. Rinse the filter unit membrane by adding another 50 μL of Bead Conjugation Buffer, centrifuge at 1,000 g for 2 minutes into the same tube.
7. Collect the sample and measure the protein concentration using the Take3 micro-volume plate accessory of the EPOC 2 spectrophotometer (BioTek, BTEPOCH2).
8. Add enough Bead Conjugation Buffer to dilute the sample to 0.3 mg/mL.
9. Store the antibody sample on ice.
10. Take 300 μL (8.5 x 10^8) of carboxylated paramagnetic beads sized 2.7 μm (Quanterix, 103612) and resuspend by vortexing.
11. Briefly centrifuge the sample using the pulse spin setting of a small 8 sample rotor bench top centrifuge and place solution on magnet for > 1 minute, remove supernatant.

12. Add 600 μL of the Bead Wash Buffer (Quanterix, 101355), and vortex to resuspend beads.
13. Repeat 600 μL washes three times using Bead Wash Buffer ensuring to vortex the beads each time, then remove the buffer after the samples have been placed on the magnet for >1 min.
14. Add 600 μL of Bead Conjugation Buffer (Quanterix, 101357), vortex to resuspend beads, then use the magnet to retain the beads and remove the buffer.
15. Repeat 600 μL washes three times using Bead Conjugation Buffer (Quanterix, 101357) ensuring to vortex the beads each time, then remove the buffer after the samples have been placed on the magnet for >1 min.
16. Add 570 μL of the Bead Conjugation Buffer and store on ice.
17. Add 100 μL of the Bead Conjugation Buffer to 1 mg vial of EDC (ThermoFisher Scientific, A35391), close lid and vortex.
18. Add 30 μL of the EDAC to the washed paramagnetic beads and incubate on shaker (VWR, PTR-35) for 30 minutes to allow for bead activation.
19. Pulse spin using tabletop centrifuge (VWR, 76269-064), and wash activated paramagnetic beads with 600 μL Bead Conjugation Buffer (Quanterix, 101357), then place on magnet for >1 min and remove supernatant.
20. Add prepared buffer exchanged primary antibody to activated paramagnetic beads.
21. Incubate for 2 hours on shaker.
22. Pulse spin, place paramagnetic bead/primary antibody solution on magnet, collect supernatant and label as “supernatant”.
23. Perform one wash with 600 μL Bead Wash Buffer (Quanterix, 101355), collect supernatant and label as “wash 1”.

24. Measure protein concentrations of supernatant and wash 1 using EPOC 2 spectrophotometer (BioTek, BTEPOCH2). Compare values to total amount of antibody loaded to estimate total antibody coated and percentage antibody coated.
25. Perform another wash with Bead Wash Buffer (Quanterix, 101355), then discard the supernatant.
26. Add 600 μL of Bead Blocking Buffer (Quanterix, 101356) and incubate for 30 minutes on Multi-Functional Tube Rotator (VWR, PTR-35) at 5 rpm to keep particles in suspension.
27. Perform one wash using 600 μL of Bead Wash Buffer (Quanterix, 101355).
28. Perform two more washes using 600 μL of Bead Diluent (Quanterix, 100458), resuspend in 600 μL Bead Diluent and store at 4 ^{o}C.

Secondary Antibody Streptavidin Conjugation

1. Take 62.5 μL (100 μg) of secondary antibody (Maine Biotechnology Services, MAB130P) and add 37.5 μL of 1x PBS to have secondary antibody at 1 μg/μL in 100 μL.
2. Add 10 μL of Modifier reagent (Abcam, ab102921) to 100 μL of secondary antibody.
3. Add the above 100 μL sample to lyophilized Streptavidin Mix (Abcam, ab102921), pipette up and down to have material fully dissolved.
4. Incubate at room temperature for 3 hours.
5. Add 10 μL of Quencher (Abcam, ab102921) to the reaction.
6. Incubate at room temperature for 30 minutes.
7. Confirm the quality of the conjugation using native gel, Mini-PROTEAN TGX gels (Bio-rad, 456-1093) in 1x Tris/Glycine Buffer at 100 V
8. Store at 4 ^{o}C.

Assay Procedure

1. Take 72 μL (7.2×10^7) of prepared bead-capture antibody conjugates, add Sample Diluent (Quanterix, 101359) to a total volume of 500 μL.
2. Place the tube on the magnet, and remove supernatant.
3. Perform two more 500 μL washes.
4. Add various amounts (0.8 fM to 1.2 nM) of recombinant TSH (rTSH) (BiosPacific, J11030) and bring the volume up to 500 μL using Sample Diluent or diluted human serum sample.
5. Incubate for 1 hour at room temperature on Multi-Functional Tube Rotator (VWR, PTR-35) at 5 rpm.
6. Place the tube on the magnet for >1 min, and remove the supernatant.
7. Add 500 μL of Wash Buffer 1 (Quanterix, 100486), and incubate for 5 minutes on Multi-Functional Tube Rotator (VWR, PTR-35) at 5 rpm.
8. Place the tube on the magnet for >1 min, and remove the supernatant.
9. Add 500 μL of Wash Buffer 1 (Quanterix, 100486), and incubate for 10 minutes on Multi-Functional Tube Rotator (VWR, PTR-35) at 5 rpm.
10. Place the tube on the magnet for >1 min, and remove the supernatant.
11. Add 500 μL of Wash Buffer 1 (Quanterix, 100486), and incubate for 15 minutes on Multi-Functional Tube Rotator (VWR, PTR-35) at 5 rpm.
12. Place the tube on the magnet for >1 min, and remove the supernatant.
13. Resuspend in 500 μL of Sample Diluent (Quanterix, 101359) containing 6 nM secondary antibody-streptavidin conjugate. OPTION 1: for the amplification assay, add 10 μL of

AuNP amplification complex to a final volume of 50 μL in Sample Diluent (Quanterix, 101359).

14. Incubate for 1 hour on Multi-Functional Tube Rotator (VWR, PTR-35) at 5 rpm at room temperature.
15. Perform three 30 sec washes with 1x Wash Buffer 1 (Quanterix, 100486), and resuspend in 500 μL of Sample Diluent (Quanterix, 101359). OPTION 1: for theamplification assay, skip this step.
16. Add 12 nM of biotinylated ssDNA junction strand. OPTION 1: for the amplification assay, skip this step.
17. Incubate for 15 min at room temperature on Multi-Functional Tube Rotator (VWR, PTR-35) at 5 rpm. OPTION 1: for the amplification assay, skip this step.
18. Perform three 30 sec washes with 1x Wash Buffer 1 (Quanterix, 100486), and resuspend in 500 μL of 1x TAEMg buffer containing 0.025 % Tween-20. OPTION 1: for the amplification assay, resuspend in 20 μL of 1x PBS containing0.025 % Tween-20.
19. Apply UV using a 3W LED flashlight (LIGHTFE, UV301D) at a distance of 1 cm for 20 minutes to release the ssDNA junction strand. OPTION 1: for the amplification assay, release the junction strand by incubation for 45 minutes in 0.2 M DTT (ThermoFisher Scientific, A39255) and 0.3M NaH_2PO_4 buffer in a final volume of 30 μL.
20. Place the samples on the magnet for >1 min and transfer the supernatant to 3 kDa Amicon Ultra-0.5 Centrifugal Filter Unit (Millipore Sigma, UFC500396).
21. Perform buffer exchange and concentrate the ssDNA junction strands into 35 μL of 1x TAEMg containing 0.025 % Tween-20.
22. Add the purified shooting star probes at either 15 or 20 nM final concentrations.

23. Incubate at room temperate for up to 2 days for dumbbell assembly.

OPTION 1: Gold Nanoparticle Amplification Scheme

DTT Reduction

1. Take thiolated ssDNA oligos and perform three washes of 1x PBS using 3 kDa Amicon Ultra-0.5 Centrifugal Filter Unit (Millipore Sigma, UFC500396) to have final concentration of 10 μM in 1x PBS.
2. Prepare 0.3 M NaH_2PO_4 containing0.2 M DTT solution (ThermoFisher Scientific, A39255).
3. Mix 250 μL of the buffer exchanged DNA oligo and 250 μL of 0.3 M NaH_2PO_4 and 0.2 M DTT.
4. Incubate at room temperature for 2 hours (unless otherwise stated incubations were done at room temperature on the benchtop.).
5. Take a NAP-5 column (GE Healthcare, 17185601), remove all caps and let storage buffer flow through.
6. Equilibrate the NAP-5 column with 10 mL deionized water.
7. Add the reduced DNA sample to the column and allow sample to fully enter membrane.
8. Place column on top of a new tube.
9. Add 1 mL deionized water to elute purified sample.
10. Reduce the volume to 200 μL using 3 kDa Amicon Ultra-0.5 Centrifugal Filter Unit (Millipore Sigma, UFC500396), confirm and adjust the final concentration of the sample to to 25 μM with deionized water.
11. Split the sample into 50 μL aliquots and store at -20 C.

Preparation of Amplification complex. (AuNP Functionalization with antibody and ssDNA oligos)

1. Take 960 μL of 30 nm AuNP (Cytodiagnostics, G-30-20), add 40 μL 0.1 M borate buffer to adjust the solution to pH 9.
2. Add 4 μg of secondary antibody (Maine Biotechnology Services, MAB130P) to a 1.7 mL tube, and add the adjusted AuNP solution to the tube with the secondary antibody[152,220].
3. Incubate at room temperature for 30 minutes.
4. Add 25 μL of reduced ssDNA oligos and incubate for 1 hour.
5. Salt age to a final concentration of 0.15 M NaCl by adding 6 additions of 1 M NaCl every 30 min.
6. Incubate at 4 ^{o}C overnight (optional pause point).
7. Add 50 μL of 10 % BSA and incubate for 5 minutes.
8. Centrifuge at 4,500 g for 15 minutes. Discard the supernatant.
9. Add 950 μL of 1x PBS containing0.025 % v/v Tween-20, resuspend by gentle shaking or vortexing.
10. Repeat steps 8 – 9 two times.
11. Add 150 μL of 1x PBS containing0.025 % v/v Tween-20.
12. Store at 4 ^{o}C.

Time Taken

1. Paramagnetic bead preparation: 5 hours
2. DNA nanostructure assembly: overnight

3. DNA nanostructure purification: 5 hours
4. Secondary antibody streptavidin conjugation: 4 hours
5. DTT reduction: 3 hours
6. Amplification complex preparation: 5 hours
7. Assay workflow: 4 hours
8. Dumbbell formation: up to 2 days
9. Nanopore sensing: 10 – 20 minutes per sample

References

1. Cherf, G. M. *et al.* Automated forward and reverse ratcheting of DNA in a nanopore at 5-Å precision. *Nat. Biotechnol. 2012 304* **30**, 344–348 (2012).
2. Suzuki, Y. Advent of a new sequencing era: long-read and on-site sequencing. *J. Hum. Genet. 2020 651* **65**, 1–1 (2020).
3. Hu, Z.-L., Huo, M.-Z., Ying, Y. I.-L. & Long, Y.-T. Biological Nanopore Approach for Single-Molecule Protein Sequencing. *Angew. Chemie* **133**, 14862–14873 (2021).
4. Deamer, D., Akeson, M. & Branton, D. Three decades of nanopore sequencing. *Nature Biotechnology* vol. 34 518–524 (2016).
5. Xue, L. *et al.* Solid-state nanopore sensors. *Nat. Rev. Mater. 2020 512* **5**, 931–951 (2020).
6. Dekker, C. Solid-state nanopores. *Nat. Nanotechnol.* **2**, 209–215 (2007).
7. Bell, N. A. W. *et al.* Multiplexed ionic current sensing with glass nanopores. *Lab Chip* **13**, 1859–1862 (2013).
8. Perry, D., Momotenko, D., Lazenby, R. A., Kang, M. & Unwin, P. R. Characterization of Nanopipettes. *Anal. Chem.* **88**, 5523–5530 (2016).
9. Steinbock, L. J. *et al.* Probing DNA with micro- and nanocapillaries and optical tweezers. *J. Phys. Condens. Matter* **22**, 454113 (2010).
10. Karhanek, M., Kemp, J. T., Pourmand, N., Davis, R. W. & Webb, C. D. Single DNA Molecule Detection Using Nanopipettes and Nanoparticles. *Nano Lett.* **5**, 403–407 (2005).
11. Li, J. *et al.* Ion-beam sculpting at nanometre length scales. *Nat. 2001 4126843* **412**, 166–169 (2001).
12. Waugh, M. *et al.* Solid-state nanopore fabrication by automated controlled breakdown. *Nat.*

Protoc. **15**, 122–143 (2020).

13. Kwok, H., Briggs, K. & Tabard-Cossa, V. Nanopore Fabrication by Controlled Dielectric Breakdown. *PLoS One* **9**, e92880 (2014).
14. Garaj, S. *et al.* Graphene as a subnanometre trans-electrode membrane. *Nat. 2010 4677312* **467**, 190–193 (2010).
15. Macha, M., Marion, S., Nandigana, V. V. R. & Radenovic, A. 2D materials as an emerging platform for nanopore-based power generation. *Nat. Rev. Mater. 2019 49* **4**, 588–605 (2019).
16. Umehara, S., Karhanek, M., Davis, R. W. & Pourmand, N. Label-free biosensing with functionalized nanopipette probes. *Proc. Natl. Acad. Sci. U. S. A.* **106**, 4611–4616 (2009).
17. Actis, P., Mak, A. C. & Pourmand, N. Functionalized nanopipettes: Toward label-free, single cell biosensors. *Bioanal. Rev.* **1**, 177–185 (2010).
18. Shao, Y. & Mirkin, M. V. Fast kinetic measurements with nanometer-sized pipets. Transfer of potassium ion from water into dichloroethane facilitated by dibenzo-18-crown-6. *J. Am. Chem. Soc.* **119**, 8103–8104 (1997).
19. Gibb, T. R., Ivanov, A. P., Edel, J. B. & Albrecht, T. Single molecule ionic current sensing in segmented flow microfluidics. *Anal. Chem.* **86**, 1864–1871 (2014).
20. Weit, C., Bard, A. J. & Feldberg, S. W. Current Rectification at Quartz Nanopipet Electrodes. *Anal. Chem.* **69**, 4627–4633 (1997).
21. Steinbock, L. J., Steinbock, J. F. & Radenovic, A. Controllable shrinking and shaping of glass nanocapillaries under electron irradiation. *Nano Lett.* **13**, 1717–1723 (2013).
22. Bell, N. A. W. *et al.* DNA origami nanopores. *Nano Lett.* **12**, 512–517 (2012).
23. Wei, R. *et al.* DNA Origami Gatekeepers for Solid-State Nanopores. *Angew. Chemie Int.*

Ed. **51**, 4864–4867 (2012).

24. Fragasso, A. *et al.* Reconstitution of Ultrawide DNA Origami Pores in Liposomes for Transmembrane Transport of Macromolecules. *ACS Nano* **15**, 12768–12779 (2021).
25. Storm, A. J., Chen, J. H., Ling, X. S., Zandbergen, H. W. & Dekker, C. Fabrication of solid-state nanopores with single-nanometre precision. *Nat. Mater. 2003 28* **2**, 537–540 (2003).
26. Briggs, K. *et al.* Kinetics of nanopore fabrication during controlled breakdown of dielectric membranes in solution. *Nanotechnology* **26**, 084004 (2015).
27. Carlsen, A. T., Briggs, K., Hall, A. R. & Tabard-Cossa, V. Solid-state nanopore localization by controlled breakdown of selectively thinned membranes. *Nanotechnology* **28**, 085304 (2017).
28. Beamish, E., Kwok, H., Tabard-Cossa, V. & Godin, M. Precise control of the size and noise of solid-state nanopores using high electric fields. *Nanotechnology* **23**, 405301 (2012).
29. Kowalczyk, S. W., Grosberg, A. Y., Rabin, Y. & Dekker, C. Modeling the conductance and DNA blockade of solid-state nanopores. *Nanotechnology* **22**, 315101 (2011).
30. Verschueren, D. V., Jonsson, M. P. & Dekker, C. Temperature dependence of DNA translocations through solid-state nanopores. *Nanotechnology* **26**, (2015).
31. Hall, J. E. Access resistance of a small circular pore. *J. Gen. Physiol.* **66**, 531–532 (1975).
32. Briggs, K., Kwok, H. & Tabard-Cossa, V. Automated Fabrication of 2-nm Solid-State Nanopores for Nucleic Acid Analysis. *Small* **10**, 2077–2086 (2014).
33. Chen, P. *et al.* Probing Single DNA Molecule Transport Using Fabricated Nanopores. *Nano Lett.* **4**, 2293–2298 (2004).
34. Ando, G., Hyun, C., Li, J. & Mitsui, T. Directly observing the motion of DNA molecules near solid-state nanopores. *ACS Nano* **6**, 10090–10097 (2012).

35. Muthukumar, M. Theory of capture rate in polymer translocation. *J. Chem. Phys.* **132**, 195101 (2010).

36. Muthukumar, M. *Polymer Translocation*. (CRC PRESS, 2011).

37. Wanunu, M., Morrison, W., Rabin, Y., Grosberg, A. Y. & Meller, A. Electrostatic focusing of unlabelled DNA into nanoscale pores using a salt gradient. *Nat. Nanotechnol.* **5**, 160–165 (2010).

38. Tabard-Cossa, V. Instrumentation for Low-Noise High-Bandwidth Nanopore Recording. *Eng. Nanopores Bioanal. Appl. A Vol. Micro Nano Technol.* 59–93 (2013) doi:10.1016/B978-1-4377-3473-7.00003-0.

39. Briggs, K. Solid-State Nanopores: Fabrication, Application, and Analysis. (PhD thesis, University of Ottawa, 2018).

40. Gershow, M. & Golovchenko, J. A. Recapturing and trapping single molecules with a solid-state nanopore. *Nat. Nanotechnol.* **2**, 775–779 (2007).

41. Rowghanian, P. & Grosberg, A. Y. Electrophoretic capture of a DNA chain into a nanopore. *Phys. Rev. E* **87**, 042722 (2013).

42. Grosberg, A. Y. & Rabin, Y. DNA capture into a nanopore: Interplay of diffusion and electrohydrodynamics. *J. Chem. Phys.* **133**, 165102 (2010).

43. Meller, A. & Branton, D. Single molecule measurements of DNA transport through a nanopore. *Electrophoresis* **23**, 2583–2591 (2002).

44. Charron, M., Briggs, K., King, S., Waugh, M. & Tabard-Cossa, V. Precise DNA Concentration Measurements with Nanopores by Controlled Counting. *Anal. Chem.* **91**, 12228–12237 (2019).

45. Seeman, N. C. Nucleic acid junctions and lattices. *J. Theor. Biol.* **99**, 237–247 (1982).

46. Hansen, C. H., Yang, D., Koussa, M. A. & Wong, W. P. Nanoswitch-linked immunosorbent assay (NLISA) for fast, sensitive, and specific protein detection. *Proc. Natl. Acad. Sci. U. S. A.* **114**, 10367–10372 (2017).

47. Shrestha, P. *et al.* Single-molecule mechanical fingerprinting with DNA nanoswitch calipers. *Nat. Nanotechnol. 2021 1612* **16**, 1362–1370 (2021).

48. Koussa, M. A., Halvorsen, K., Ward, A. & Wong, W. P. DNA nanoswitches: a quantitative platform for gel-based biomolecular interaction analysis. *Nat. Methods 2014 122* **12**, 123–126 (2014).

49. Beamish, E., Tabard-Cossa, V. & Godin, M. Programmable DNA Nanoswitch Sensing with Solid-State Nanopores. *ACS Sensors* **4**, 2458–2464 (2019).

50. Shen, B. *et al.* Plasmonic nanostructures through DNA-assisted lithography. *Sci. Adv.* **4**, (2018).

51. Andersen, E. S. *et al.* Self-assembly of a nanoscale DNA box with a controllable lid. *Nat. 2009 4597243* **459**, 73–76 (2009).

52. Castro, C. E. *et al.* A primer to scaffolded DNA origami. *Nat. Methods 2011 83* **8**, 221–229 (2011).

53. Lottspeich, F. & Engels, J. W. Techniques for the Hybridization and Detection of Nucleic Acids. in *Bioanalytics : analytical methods and concepts in biochemistry and molecular biology* 719–754 (Wiley, 2018).

54. Saccà, B. & Niemeyer, C. M. DNA Origami: The Art of Folding DNA. *Angew. Chemie Int. Ed.* **51**, 58–66 (2012).

55. Rothemund, P. W. K. Folding DNA to create nanoscale shapes and patterns. *Nature* **440**, 297–302 (2006).

56. Douglas, S. M. *et al.* Self-assembly of DNA into nanoscale three-dimensional shapes. *Nature* **459**, 414–418 (2009).

57. Douglas, S. M. *et al.* Rapid prototyping of 3D DNA-origami shapes with caDNAno. *Nucleic Acids Res.* **37**, 5001–5006 (2009).

58. Dietz, H., Douglas, S. M. & Shih, W. M. Folding DNA into twisted and curved nanoscale shapes. *Science (80-.).* **325**, 725–730 (2009).

59. Kim, D. N., Kilchherr, F., Dietz, H. & Bathe, M. Quantitative prediction of 3D solution shape and flexibility of nucleic acid nanostructures. *Nucleic Acids Res.* **40**, 2862–2868 (2012).

60. Martin, T. G. & Dietz, H. Magnesium-free self-assembly of multi-layer DNA objects. *Nat. Commun. 2012 31* **3**, 1–6 (2012).

61. Bellot, G., McClintock, M. A., Lin, C. & Shih, W. M. Recovery of intact DNA nanostructures after agarose gel–based separation. *Nat. Methods 2011 83* **8**, 192–194 (2011).

62. De Carlo, S. & Harris, J. R. Negative staining and cryo-negative staining of macromolecules and viruses for TEM. *Micron* **42**, 117–131 (2011).

63. Harris, J. R. & De Carlo, S. Negative Staining and Cryo-negative Staining: Applications in Biology and Medicine. *Methods Mol. Biol.* **1117**, 215–258 (2014).

64. He, L., Karau, P. & Tabard-Cossa, V. Fast capture and multiplexed detection of short multi-arm DNA stars in solid-state nanopores. *Nanoscale* **11**, 16342–16350 (2019).

65. Alibakhshi, M. A. *et al.* Picomolar Fingerprinting of Nucleic Acid Nanoparticles Using Solid-State Nanopores. *ACS Nano* **11**, 9701–9710 (2017).

66. Wang, V., Ermann, N. & Keyser, U. F. Current Enhancement in Solid-State Nanopores

Depends on Three-Dimensional DNA Structure. *Nano Lett.* **19**, 5661–5666 (2019).

67. Chen, K. *et al.* Digital Data Storage Using DNA Nanostructures and Solid-State Nanopores. *Nano Lett.* **19**, 1210–1215 (2019).

68. Bell, N. A. W. & Keyser, U. F. Digitally encoded DNA nanostructures for multiplexed, single-molecule protein sensing with nanopores. *Nat. Nanotechnol.* **11**, 645–651 (2016).

69. Sze, J. Y. Y. Y., Ivanov, A. P., Cass, A. E. G. G. & Edel, J. B. Single molecule multiplexed nanopore protein screening in human serum using aptamer modified DNA carriers. *Nat. Commun.* **8**, 1552 (2017).

70. Schmid, S., Stömmer, P., Dietz, H. & Dekker, C. Nanopore electro-osmotic trap for the label-free study of single proteins and their conformations. *Nat. Nanotechnol. 2021 1611* **16**, 1244–1250 (2021).

71. Burns, J. R., Stulz, E. & Howorka, S. Self-assembled DNA nanopores that span lipid bilayers. *Nano Lett.* **13**, 2351–2356 (2013).

72. Schmid, S. & Dekker, C. The NEOtrap – en route with a new single-molecule technique. *iScience* **24**, 103007 (2021).

73. Seifert, A. *et al.* Bilayer-spanning DNA nanopores with voltage-switching between open and closed state. *ACS Nano* **9**, 1117–1126 (2015).

74. Burns, J. R. *et al.* Lipid-Bilayer-Spanning DNA Nanopores with a Bifunctional Porphyrin Anchor. *Angew. Chemie Int. Ed.* **52**, 12069–12072 (2013).

75. Tripathi, P. *et al.* Electrical unfolding of cytochrome c during translocation through a nanopore constriction. *Proc. Natl. Acad. Sci. U. S. A.* **118**, 2022 (2021).

76. Carlsen, A. & Tabard-Cossa, V. Mapping shifts in nanopore signal to changes in protein and protein-DNA conformation. *Proteomics* **2021**, 2100068 (2021).

77. Zahid, O. K., Wang, F., Ruzicka, J. A., Taylor, E. W. & Hall, A. R. Sequence-Specific Recognition of MicroRNAs and Other Short Nucleic Acids with Solid-State Nanopores. *Nano Lett.* **16**, 2033–2039 (2016).

78. Freedman, K. J., Bastian, A. R., Chaiken, I. & Kim, M. J. Solid-State Nanopore Detection of Protein Complexes: Applications in Healthcare and Protein Kinetics. *Small* **9**, 750–759 (2013).

79. Plesa, C. *et al.* Fast Translocation of Proteins through Solid State Nanopores. *Nano Lett.* **13**, 658–663 (2013).

80. Larkin, J., Henley, R. Y., Muthukumar, M., Rosenstein, J. K. & Wanunu, M. High-Bandwidth Protein Analysis Using Solid-State Nanopores. *Biophys. J.* **106**, 696–704 (2014).

81. Wanunu, M. & Meller, A. Chemically modified solid-state nanopores. *Nano Lett.* **7**, 1580–1585 (2007).

82. Yusko, E. C. *et al.* Controlling protein translocation through nanopores with bio-inspired fluid walls. *Nat. Nanotechnol.* **6**, 253–260 (2011).

83. Awasthi, S. *et al.* Polymer Coatings to Minimize Protein Adsorption in Solid-State Nanopores. *Small Methods* **4**, 2000177 (2020).

84. Yusko, E. C. *et al.* Real-time shape approximation and fingerprinting of single proteins using a nanopore. *Nat. Nanotechnol.* **12**, 360–367 (2017).

85. Cai, S., Sze, J. Y. Y., Ivanov, A. P. & Edel, J. B. Small molecule electro-optical binding assay using nanopores. *Nat. Commun.* **10**, 1797 (2019).

86. Kong, J., Bell, N. A. W. & Keyser, U. F. Quantifying Nanomolar Protein Concentrations Using Designed DNA Carriers and Solid-State Nanopores. *Nano Lett.* **16**, 3557–3562

(2016).

87. Bell, N. A. W. & Keyser, U. F. Specific Protein Detection Using Designed DNA Carriers and Nanopores. *J. Am. Chem. Soc.* **137**, 2035–2041 (2015).

88. Armbruster, D. A. & Pry, T. Limit of Blank, Limit of Detection and Limit of Quantitation. *Clin. Biochem. Rev.* **29**, S49 (2008).

89. Lister, A. S. Validation of HPLC Methods in Pharmaceutical Analysis. *Sep. Sci. Technol.* **6**, 191–217 (2005).

90. Betz, J. M., Brown, P. N. & Roman, M. C. Accuracy, precision, and reliability of chemical measurements in natural products research. *Fitoterapia* **82**, 44–52 (2011).

91. Gamba, J. The Role of Transport Phenomena in Whispering Gallery Mode Optical Biosensor Performance. (PhD thesis, California Institute of Technology, 2012).

92. Rogers, J. K., Taylor, N. D. & Church, G. M. Biosensor-based engineering of biosynthetic pathways. *Curr. Opin. Biotechnol.* **42**, 84–91 (2016).

93. Wei, B. *et al.* Engineering Biosensors with Dual Programmable Dynamic Ranges. *Anal. Chem.* **90**, 1506–1510 (2018).

94. Danzer, K. Selectivity and specificity in analytical chemistry. General considerations and attempt of a definition and quantification. *Fresenius' J. Anal. Chem. 2001 3695* **369**, 397–402 (2001).

95. Szurdoki, F., Michael, K. L. & Walt, D. R. A Duplexed Microsphere-Based Fluorescent Immunoassay. *Anal. Biochem.* **291**, 219–228 (2001).

96. Frutiger, A. *et al.* Nonspecific Binding - Fundamental Concepts and Consequences for Biosensing Applications. *Chem. Rev.* **121**, 8095–8160 (2021).

97. Kong, J., Zhu, J. & Keyser, U. F. Single molecule based SNP detection using designed DNA

carriers and solid-state nanopores †. *Chem. Commun.* (2016) doi:10.1039/C6CC08621G.

98. Kong, J., Zhu, J., Chen, K. & Keyser, U. F. Specific Biosensing Using DNA Aptamers and Nanopores. *Adv. Funct. Mater.* **29**, 1807555 (2019).

99. Raveendran, M., Lee, A. J., Sharma, R., Wälti, C. & Actis, P. Rational design of DNA nanostructures for single molecule biosensing. *Nat. Commun.* **11**, 4384 (2020).

100. Nelson, D. L., Cox, M. M. & Hoskins, A. A. Protein function. in *Lehninger principles of biochemistry* (W H FREEMAN, 2021).

101. Landry, J. P., Ke, Y., Yu, G. L. & Zhu, X. D. Measuring affinity constants of 1450 monoclonal antibodies to peptide targets with a microarray-based label-free assay platform. *J. Immunol. Methods* **417**, 86–96 (2015).

102. Jenison, R. D., Gill, S. C., Pardi, A. & Polisky, B. High-Resolution Molecular Discrimination by RNA. *Science (80-.).* **263**, 1425–1429 (1994).

103. Thevendran, R. & Citartan, M. Assays to Estimate the Binding Affinity of Aptamers. *Talanta* **238**, 122971 (2022).

104. Engvall, E. & Perlmann, P. Enzyme-Linked Immunosorbent Assay, Elisa. *J. Immunol.* **109**, (1972).

105. Schmidt, S. D., Mazzella, M. J., Nixon, R. A. & Mathews, P. M. Aβ measurement by enzyme-linked immunosorbent assay. *Methods Mol. Biol.* **849**, 507–527 (2012).

106. Huang, C. Y. *et al.* A highly efficient bead extraction technique with low bead number for digital microfluidic immunoassay. *Biomicrofluidics* **10**, 011901 (2016).

107. Walt, D. R. Optical Methods for Single Molecule Detection and Analysis. *Anal. Chem.* **85**, 1258–1263 (2013).

108. Wilson, D. H. *et al.* The Simoa HD-1 Analyzer: A Novel Fully Automated Digital

Immunoassay Analyzer with Single-Molecule Sensitivity and Multiplexing. *J. Lab. Autom.* **21**, 533–547 (2016).

109. Rosi, N. L. & Mirkin, C. A. Nanostructures in biodiagnostics. *Chem. Rev.* **105**, 1547–62 (2005).

110. Rissin, D. M. *et al.* Single-molecule enzyme-linked immunosorbent assay detects serum proteins at subfemtomolar concentrations. *Nat. Biotechnol.* **28**, 595–599 (2010).

111. Li, D. & Mielke, M. M. An Update on Blood-Based Markers of Alzheimer's Disease Using the SiMoA Platform. *Neurol. Ther.* **8**, 73–82 (2019).

112. Kelley, S. O. *et al.* Advancing the speed, sensitivity and accuracy of biomolecular detection using multi-length-scale engineering. *Nat. Nanotechnol.* **9**, 969–980 (2014).

113. Gooding, J. J. & Gaus, K. Single-Molecule Sensors: Challenges and Opportunities for Quantitative Analysis. *Angew. Chemie Int. Ed.* **55**, 11354–11366 (2016).

114. He, L. *et al.* Digital immunoassay for biomarker concentration quantification using solid-state nanopores. *Nat. Commun. 2021 121* **12**, 1–11 (2021).

115. Quick, J. *et al.* Real-time, portable genome sequencing for Ebola surveillance. *Nature* **530**, 228–232 (2016).

116. Bayley, H. Nanopore sequencing: from imagination to reality. *Clin. Chem.* **61**, 25–31 (2015).

117. Koo, B., Yorita, A. M., Schmidt, J. J. & Monbouquette, H. G. Amplification-free, sequence-specific 16S rRNA detection at 1 aM. *Lab Chip* **18**, 2291–2299 (2018).

118. Zahid, O. K., Zhao, B. S., He, C. & Hall, A. R. Quantifying mammalian genomic DNA hydroxymethylcytosine content using solid-state nanopores. *Nat. Publ. Gr.* 4–9 (2016) doi:10.1038/srep29565.

119. Wang, F. *et al.* Solid-State Nanopore Analysis of Diverse DNA Base Modifications Using a Modular Enzymatic Labeling Process. *Nano Lett.* **17**, 7110–7116 (2017).

120. Zhang, Y., Rana, A., Stratton, Y., Czyzyk-krzeska, M. F. & Esfandiari, L. Sequence-Speci fi c Detection of MicroRNAs Related to Clear Cell Renal Cell Carcinoma at fM Concentration by an Electroosmotically Driven Nanopore-Based Device. (2017) doi:10.1021/acs.analchem.7b01944.

121. Lin, Y., Ying, Y.-L., Shi, X., Liu, S.-C. & Long, Y.-T. Direct sensing of cancer biomarkers in clinical samples with a designed nanopore. *Chem. Commun.* **53**, 11564–11567 (2017).

122. Squires, A. H., Atas, E. & Meller, A. Genomic Pathogen Typing Using Solid-State Nanopores. *PLoS One* **10**, e0142944 (2015).

123. Shim, J. *et al.* Nanopore-Based Assay for Detection of Methylation in Double-Stranded DNA Fragments. *ACS Nano* **9**, 290–300 (2015).

124. Singer, A., Rapireddy, S., Ly, D. H. & Meller, A. Electronic Barcoding of a Viral Gene at the Single-Molecule Level. *Nano Lett.* **12**, 1722–1728 (2012).

125. Morin, T. J. *et al.* Nanopore-Based Target Sequence Detection. *PLoS One* **11**, 1–21 (2016).

126. Beamish, E., Tabard-Cossa, V. & Godin, M. Identifying Structure in Short DNA Scaffolds Using Solid-State Nanopores. *ACS Sensors* **2**, 1814–1820 (2017).

127. Guo, Q., Kong, T., Su, R., Zhang, Q. & Cheng, G. Noise spectroscopy as an equilibrium analysis tool for highly sensitive electrical biosensing. *Appl. Phys. Lett.* **101**, 93704 (2012).

128. Morin, T. J. *et al.* A handheld platform for target protein detection and quantification using disposable nanopore strips. *Sci. Rep.* **8**, 14834 (2018).

129. Karau, P. & Tabard-Cossa, V. Capture and Translocation Characteristics of Short Branched DNA Labels in Solid-State Nanopores. *ACS Sensors* **3**, 1308–1315 (2018).

130. Wang, X. & Seeman, N. C. Assembly and Characterization of 8-Arm and 12-Arm DNA Branched Junctions. *J. Am. Chem. Soc.* **129**, 8169–8176 (2007).

131. Carson, S., Wick, S. T., Carr, P. A., Wanunu, M. & Aguilar, C. A. SI: Direct Analysis of Gene Synthesis Reactions Using Solid-State Nanopores. *ACS Nano* (2015).

132. Briggs, K. *et al.* DNA Translocations through Nanopores under Nanoscale Preconfinement. *Nano Lett.* **18**, 660–668 (2018).

133. Carson, S., Wilson, J., Aksimentiev, A. & Wanunu, M. Smooth DNA transport through a narrowed pore geometry. *Biophys. J.* **107**, 2381–2393 (2014).

134. Misiunas, K., Ermann, N. & Keyser, U. F. QuipuNet: convolutional neural network for single-molecule nanopore sensing. (2018) doi:arXiv:1803.10653v2.

135. Charron, M., Philipp, L., He, L. & Tabard-Cossa, V. Elucidating the dynamics of polymer transport through nanopores using asymmetric salt concentrations. *Nano Res. 2022 1511* **15**, 9943–9953 (2022).

136. Wadsworth, I. D. & Hall, A. R. Effects of symmetric and asymmetric salt conditions on a selective solid-state nanopore assay. *Nano Res. 2022 1511* **15**, 9936–9942 (2022).

137. He, Y. *et al.* Mechanism of How Salt-Gradient-Induced Charges Affect the Translocation of DNA Molecules through a Nanopore. *Biophys. J.* **105**, 776–782 (2013).

138. Squires, A. & Meller, A. DNA capture and translocation through nanoscale pores - A fine balance of electrophoresis and electroosmosis. *Biophys. J.* **105**, 543–544 (2013).

139. Charron, M., Philipp, L., He, L. & Tabard-Cossa, V. Elucidating the Dynamics of Polymer Transport through Nanopores using Asymmetric Salt Concentrations. *ChemRxiv* (2021) doi:10.26434/CHEMRXIV-2021-8WM8V.

140. Bello, J. *et al.* Increased dwell time and occurrence of dsDNA translocation events through

solid state nanopores by LiCl concentration. 1082–1090 (2019) doi:10.1002/elps.201800426.

141. Tabard-Cossa, V., Trivedi, D., Wiggin, M., Jetha, N. N. & Marziali, A. Noise analysis and reduction in solid-state nanopores. *Nanotechnology* **18**, 305505 (2007).

142. Kowalczyk, S. W., Wells, D. B., Aksimentiev, A. & Dekker, C. Slowing down DNA translocation through a nanopore in lithium chloride. *Nano Lett.* **12**, 1038–1044 (2012).

143. Forstater, J. H. *et al.* MOSAIC: A Modular Single Molecule Analysis Interface for Decoding Multi-state Nanopore Data. *Anal. Chem.* **88**, 11900–11907 (2016).

144. Balijepalli, A. *et al.* Quantifying Short-Lived Events in Multistate Ionic Current Measurements. *ACS Nano* **8**, 1547–1553 (2015).

145. Sun, Y., Sriramajayam, K., Luo, D. & Liao, D. J. A Quick, Cost-Free Method of Purification of DNA Fragments from Agarose Gel. **22**, 93–95 (2012).

146. Douglas, S. M., Chou, J. J. & Shih, W. M. DNA-nanotube-induced alignment of membrane proteins for NMR structure determination. *Proc. Natl. Acad. Sci. U. S. A.* **104**, 6644–6648 (2007).

147. Liedl, T., Högberg, B., Tytell, J., Ingber, D. E. & Shih, W. M. Self-assembly of three-dimensional prestressed tensegrity structures from DNA. *Nat. Nanotechnol. 2010 57* **5**, 520–524 (2010).

148. Gu, H., Yang, W. & Seeman, N. C. DNA scissors device used to measure mutS binding to dna mis-pairs. *J. Am. Chem. Soc.* **132**, 4352–4357 (2010).

149. Chhabra, R., Sharma, J., Liu, Y. & Yan, H. Addressable molecular tweezers for DNA-templated coupling reactions. *Nano Lett.* **6**, 978–983 (2006).

150. Englisch, U. & Gauss, D. H. Chemically Modified Oligonucleotides as Probes and

Inhibitors. *Angew. Chemie Int. Ed. English* **30**, 613–629 (1991).

151. Wilner, O. I. & Willner, I. Functionalized DNA nanostructures. *Chem. Rev.* **112**, 2528–2556 (2012).

152. Nam, J. M., Thaxton, C. S. & Mirkin, C. A. Nanoparticle-based bio-bar codes for the ultrasensitive detection of proteins. *Science (80-.).* **301**, 1884–1886 (2003).

153. Kielkopf, C. L., Erkkila, K. E., Hudson, B. P., Barton, J. K. & Rees, D. C. Structure of a photoactive rhodium complex intercalated into DNA. *Nat. Struct. Biol. 2000 72* **7**, 117–121 (2000).

154. Evans, R. K., Johnson, J. D. & Haley, B. E. 5-Azido-2'-deoxyuridine 5'-triphosphate: A photoaffinity-labeling reagent and tool for the enzymatic synthesis of photoactive DNA. *Proc. Natl. Acad. Sci. U. S. A.* **83**, 5382–5386 (1986).

155. He, L. *et al.* Digital Immunoassay Protocol for Solid-State Nanopore Sensing. *Protoc. Exch.* (2021).

156. Conrad, F. & Krupp, G. A solid phase method for mapping restriction sites. *Nucleic Acids Res.* **20**, 6423–6424 (1992).

157. Hultman, T., Stahl, S., Homes, E. & Uhlén, M. Direct solid phase sequencing of genomic and plasmid DNA using magnetic beads as solid support. *Nucleic Acids Res.* **17**, 4937–4946 (1989).

158. Misra, R. R., Chiang, S. Y. & Swenberg, J. A. A comparison of two ultrasensitive methods for measuring 1,N6-etheno-2'- deoxyadenosine and 3,N4-etheno-2'-deoxycytidine in cellular DNA. *Carcinogenesis* **15**, 1647–1652 (1994).

159. Woeste, S. & Demchick, P. New version of the negative stain. *Appl. Environ. Microbiol.* **57**, 1858–1859 (1991).

160. Stirling, J. W., Curry, A. & Eyden, B. Diagnostic electron microscopy : a practical guide to tissue preparation and interpretation. (2013).

161. Dey, S. *et al.* DNA origami. *Nat. Rev. Methods Prim. 2021 11* **1**, 1–24 (2021).

162. Beamish, E., Tabard-Cossa, V. & Godin, M. Digital counting of nucleic acid targets using solid-state nanopores. *Nanoscale* **12**, 17833–17840 (2020).

163. Andersen, E. S. *et al.* DNA origami design of dolphin-shaped structures with flexible tails. *ACS Nano* **2**, 1213–1218 (2008).

164. Ke, Y. *et al.* Scaffolded DNA origami of a DNA tetrahedron molecular container. *Nano Lett.* **9**, 2445–2447 (2009).

165. Liu, W., Zhong, H., Wang, R. & Seeman, N. C. Crystalline two-dimensional DNA-origami arrays. *Angew. Chemie - Int. Ed.* **50**, 264–267 (2011).

166. Han, D., Pal, S., Liu, Y. & Yan, H. Folding and cutting DNA into reconfigurable topological nanostructures. *Nat. Nanotechnol. 2010 510* **5**, 712–717 (2010).

167. Endo, M., Katsuda, Y., Hidaka, K. & Sugiyama, H. Regulation of DNA methylation using different tensions of double strands constructed in a defined DNA nanostructure. *J. Am. Chem. Soc.* **132**, 1592–1597 (2010).

168. Endo, M., Sugita, T., Katsuda, Y., Hidaka, K. & Sugiyama, H. Programmed-assembly system using DNA jigsaw pieces. *Chem. - A Eur. J.* **16**, 5362–5368 (2010).

169. Kuzuya, A. & Komiyama, M. Design and construction of a box-shaped 3D-DNA origami. *Chem. Commun.* 4182–4184 (2009) doi:10.1039/B907800B.

170. Endo, M., Hidaka, K., Kato, T., Namba, K. & Sugiyama, H. DNA prism structures constructed by folding of multiple rectangular arms. *J. Am. Chem. Soc.* **131**, 15570–15571 (2009).

171. Ke, Y. *et al.* Multilayer DNA origami packed on a square lattice. *J. Am. Chem. Soc.* **131**, 15903–15908 (2009).

172. Pound, E., Ashton, J. R., Becerril, H. A. & Woolley, A. T. Polymerase chain reaction based scaffold preparation for the production of thin, branched DNA origami nanostructures of arbitrary sizes. *Nano Lett.* **9**, 4302–4305 (2009).

173. Qian, L. *et al.* Analogic China map constructed by DNA. *Chinese Sci. Bull. 2006 5124* **51**, 2973–2976 (2006).

174. Storm, A. J., Chen, J. H., Zandbergen, H. W. & Dekker, C. Translocation of double-strand DNA through a silicon oxide nanopore. *Phys. Rev. E - Stat. Nonlinear, Soft Matter Phys.* **71**, 051903 (2005).

175. Mihovilovic, M., Hagerty, N. & Stein, D. Statistics of DNA capture by a solid-state nanopore. *Phys. Rev. Lett.* **110**, 028102 (2013).

176. Li, J., Gershow, M., Stein, D., Brandin, E. & Golovchenko, J. A. DNA molecules and configurations in a solid-state nanopore microscope. *Nat. Mater. 2003 29* **2**, 611–615 (2003).

177. Lee, J. Y. *et al.* Rapid Computational Analysis of DNA Origami Assemblies at Near-Atomic Resolution. *ACS Nano* **15**, 1002–1015 (2021).

178. Kauert, D. J., Kurth, T., Liedl, T. & Seidel, R. Direct mechanical measurements reveal the material properties of three-dimensional DNA origami. *Nano Lett.* **11**, 5558–5563 (2011).

179. Lee, C., Kim, K. S., Kim, Y. J., Lee, J. Y. & Kim, D. N. Tailoring the Mechanical Stiffness of DNA Nanostructures Using Engineered Defects. *ACS Nano* **13**, 8329–8336 (2019).

180. Briggs, K. CUSUM v3.3.3 Nanopore Analysis Software Suite. (2020) doi:10.5281/zenodo.595675.

181. Wanunu, M. Nanopores: A journey towards DNA sequencing. *Physics of Life Reviews* vol. 9 125–158 (2012).

182. Branton, D. *et al.* The potential and challenges of nanopore sequencing. *Nat. Biotechnol.* **26**, 1146–1153 (2008).

183. Manrao, E. A. *et al.* Reading DNA at single-nucleotide resolution with a mutant MspA nanopore and phi29 DNA polymerase. *Nat. Biotechnol.* **30**, 349–353 (2012).

184. Laszlo, A. H. *et al.* Decoding long nanopore sequencing reads of natural DNA. *Nat. Biotechnol.* **32**, 829–833 (2014).

185. Derrington, I. M. *et al.* Nanopore DNA sequencing with MspA. *Proc. Natl. Acad. Sci.* **107**, 16060–16065 (2010).

186. Varongchayakul, N., Song, J., Meller, A. & Grinstaff, M. W. Single-molecule protein sensing in a nanopore: a tutorial. *Chem. Soc. Rev.* **47**, 8512–8524 (2018).

187. Kolmogorov, M., Kennedy, E., Dong, Z., Timp, G. & Pevzner, P. A. Single-molecule protein identification by sub-nanopore sensors. *PLOS Comput. Biol.* **13**, e1005356 (2017).

188. Ouldali, H. *et al.* Electrical recognition of the twenty proteinogenic amino acids using an aerolysin nanopore. *Nat. Biotechnol. 2019 382* **38**, 176–181 (2019).

189. Fragasso, A., Pud, S. & Dekker, C. 1/ f noise in solid-state nanopores is governed by access and surface regions. *Nanotechnology* **30**, 395202 (2019).

190. Houghtaling, J. *et al.* Estimation of Shape, Volume, and Dipole Moment of Individual Proteins Freely Transiting a Synthetic Nanopore. *ACS Nano* **13**, 5231–5242 (2019).

191. Eggenberger, O. M., Ying, C. & Mayer, M. Surface coatings for solid-state nanopores. *Nanoscale* **11**, 19636–19657 (2019).

192. Robertson, J. W. F. & Reiner, J. E. The Utility of Nanopore Technology for Protein and

Peptide Sensing. *Proteomics* **18**, 1–14 (2018).

193. Li, W. *et al.* Single Protein Molecule Detection by Glass Nanopores. *ACS Nano* **7**, 4129–4134 (2013).

194. Rivas, F. *et al.* Label-free analysis of physiological hyaluronan size distribution with a solid-state nanopore sensor. *Nat. Commun. 2018 91* **9**, 1–9 (2018).

195. Sethi, K. *et al.* Direct Detection of Conserved Viral Sequences and Other Nucleic Acid Motifs with Solid-State Nanopores. *ACS Nano* **15**, 8474–8483 (2021).

196. Singer, A. *et al.* Nanopore Based Sequence Specific Detection of Duplex DNA for Genomic Profiling. *Nano Lett.* **10**, 738–742 (2010).

197. Chuah, K. *et al.* Nanopore blockade sensors for ultrasensitive detection of proteins in complex biological samples. *Nat. Commun.* **10**, 2109 (2019).

198. Sheehan, M. T. Biochemical Testing of the Thyroid: TSH is the Best and, Oftentimes, Only Test Needed – A Review for Primary Care. *Clin. Med. Res.* **14**, 83–92 (2016).

199. Hepner, A. *et al.* Serum Neurofilament Light, Glial Fibrillary Acidic Protein and Tau Are Possible Serum Biomarkers for Activity of Brain Metastases and Gliomas. *World J. Oncol.* **10**, 169–175 (2019).

200. Campesato, L. F. *et al.* Comprehensive cancer-gene panels can be used to estimate mutational load and predict clinical benefit to PD-1 blockade in clinical practice. *Oncotarget* **6**, 34221–34227 (2015).

201. Ahmad, R. *et al.* A rapid triage test for active pulmonary tuberculosis in adult patients with persistent cough. *Sci. Transl. Med.* **11**, 8287 (2019).

202. Llibre, A. *et al.* Plasma Type I IFN Protein Concentrations in Human Tuberculosis. *Front. Cell. Infect. Microbiol.* **9**, (2019).

203. Thebault, S. *et al.* High serum neurofilament light chain normalizes after hematopoietic stem cell transplantation for MS. *Neurol. Neuroimmunol. NeuroInflammation* **6**, (2019).

204. Srpova, B. *et al.* Serum neurofilament light chain reflects inflammation-driven neurodegeneration and predicts delayed brain volume loss in early stage of multiple sclerosis. *Mult. Scler.* **27**, 52–60 (2020).

205. Ferraro, D. *et al.* Plasma neurofilaments correlate with disability in progressive multiple sclerosis patients. *Acta Neurol. Scand.* **141**, 16–21 (2020).

206. Chang, L. *et al.* Single molecule enzyme-linked immunosorbent assays: Theoretical considerations. *J. Immunol. Methods* **378**, 102–115 (2012).

207. François, P. & Zilman, A. Physical approaches to receptor sensing and ligand discrimination. *Curr. Opin. Syst. Biol.* **18**, 111–121 (2019).

208. Ma, F., Li, Y., Tang, B. & Zhang, C. Fluorescent Biosensors Based on Single-Molecule Counting. *Acc. Chem. Res.* **49**, 1722–1730 (2016).

209. Park, S. *et al.* Combined Signal Amplification Using a Propagating Cascade Reaction and a Redox Cycling Reaction for Sensitive Thyroid-Stimulating Hormone Detection. *Anal. Chem.* **91**, 7894–7901 (2019).

210. Gutiérrez-Sanz, Ó., Andoy, N. M., Filipiak, M. S., Haustein, N. & Tarasov, A. Direct, Label-Free, and Rapid Transistor-Based Immunodetection in Whole Serum. *ACS Sensors* **2**, 1278–1286 (2017).

211. Karau, P. DNA Labels for Improved Detection and Capture with Solid-State Nanopores. (MSc thesis, University of Ottawa, 2018).

212. Forstater, J. H. J. H. *et al.* MOSAIC: A modular single-molecule analysis interface for decoding multistate nanopore data. *Anal. Chem.* **88**, 11900–11907 (2016).

213. Zhang, J. X. *et al.* Predicting DNA hybridization kinetics from sequence. *Nat. Chem.* **10**, 91–98 (2018).

214. Tahvildari, R., Beamish, E., Tabard-Cossa, V. & Godin, M. Integrating nanopore sensors within microfluidic channel arrays using controlled breakdown. *Lab Chip* **15**, 1407–1411 (2015).

215. Varongchayakul, N., Hersey, J. S., Squires, A., Meller, A. & Grinstaff, M. W. A Solid-State Hard Microfluidic–Nanopore Biosensor with Multilayer Fluidics and On-Chip Bioassay/Purification Chamber. *Adv. Funct. Mater.* **28**, 1804182 (2018).

216. Freedman, K. J. *et al.* Nanopore sensing at ultra-low concentrations using single-molecule dielectrophoretic trapping. *Nat. Commun.* **7**, 10217 (2016).

217. Quick, J. *et al.* Multiplex PCR method for MinION and Illumina sequencing of Zika and other virus genomes directly from clinical samples. *Nat. Protoc.* **12**, 1261–1276 (2017).

218. Sista, R. S. *et al.* Heterogeneous immunoassays using magnetic beads on a digital microfluidic platform. *Lab Chip* **8**, 2188–2196 (2008).

219. Andreasson, U. *et al.* A Practical Guide to Immunoassay Method Validation. *Front. Neurol.* **6**, 179 (2015).

220. Hill, H. D. & Mirkin, C. A. The bio-barcode assay for the detection of protein and nucleic acid targets using DTT-induced ligand exchange. *Nat. Protoc.* **1**, 324–336 (2006).

221. Park, T. *et al.* Bayesian Estimation of Hardness Ratios: Modeling and Computations. *Astrophys. J.* **652**, 610–628 (2006).

222. Griffin, T. Distribution of the Ratio of Two Possion Random Variables. (MSc thesis, Texas Tech University, 1992).

223. Bercovici, M., Han, C. M., Liao, J. C. & Santiago, J. G. Rapid hybridization of nucleic acids

using isotachophoresis. *Proc. Natl. Acad. Sci.* **109**, 11127–11132 (2012).

224. Zhang, H., Zhao, Q., Li, X.-F. & Le, X. C. Ultrasensitive assays for proteins. *Analyst* **132**, 724 (2007).

225. He, Y., Tsutsui, M., Zhou, Y. & Miao, X. S. Solid-state nanopore systems: from materials to applications. *NPG Asia Mater. 2021 131* **13**, 1–26 (2021).

226. Lee, K. *et al.* Recent Progress in Solid-State Nanopores. *Adv. Mater.* **30**, 1704680 (2018).

227. Shi, X. *et al.* A nanopore-powered DNA turbine. *ArXiv* (2022).

228. Salunkhe, M., Wu, T. & Letsinger, R. L. Control of Folding and Binding of Oligonucleotides by Use of a Nonnucleotide Linker. *J. Am. Chem. Soc.* **114**, 8768–8772 (1992).

229. Dolinnaya, N. G. *et al.* Oligonucleotide circularization by template-directed chemical ligation. *Nucleic Acids Res.* **21**, 5403–5407 (1993).

230. Briggs, K., Bouhamidi, M. Y., He, L. & Tabard-Cossa, V. Efficient Simulation of Arbitrary Multicomponent First-Order Binding Kinetics for Improved Assay Design and Molecular Assembly. *ACS Meas. Sci. Au* **2**, 139–146 (2021).